

Calculation of NMR Parameters in a Modern Relativistic Density Functional Framework: Theory, Implementation, and Application

Zur Erlangung des akademischen Grades eines

DOKTORS DER NATURWISSENSCHAFTEN

(Dr. rer. nat.)

von der KIT-Fakultät für Chemie und Biowissenschaften

des Karlsruher Instituts für Technologie (KIT)

genehmigte

DISSERTATION

von

M.Sc. Yannick Joel Franzke

1. Referent: apl. Prof. Dr. Florian Weigend
2. Referent: Prof. Dr. Filipp Furche
Tag der mündlichen Prüfung: 19.07.2021

Für Andrea und Joshua

Kurzfassung

In dieser Arbeit wird die relativistische Theorie der exakten Entkopplung (engl. *exact two-component theory*, X2C) auf chemische Verschiebungen und Kopplungskonstanten der Atomkerne in der Kernspinresonanz-Spektroskopie (engl. *nuclear magnetic resonance*, NMR) angewandt, um damit Spektren von Molekülen mit schweren Elementen zu interpretieren und vorherzusagen. Da der NMR-Abschirmungstensor und der Kopplungstensor von der Elektronendichte in Kernnähe abhängt, wird für die akkurate Berechnung eine relativistische Allelektronentheorie benötigt. In X2C wird die relativistische Entkopplung in einer Matrixform realisiert, wobei unkontrahierte oder primitive Basisfunktionen genutzt werden, was zu erhöhten Dimensionen führt. Ebenso müssen für die Ableitungen der Entkopplungsmatrix für NMR-Parameter Antwortgleichungen erster und zweiter Ordnung gelöst werden. Dies führt folglich zu einem hohen Rechenaufwand. In dieser Arbeit wird die diagonale, lokale Näherung der unitären Entkopplung (engl. *diagonal local approximation to the unitary decoupling transformation*, DLU) für NMR-Parameter hergeleitet und in einen Computercode implementiert. Diese Näherung reduziert den Rechenaufwand um eine Potenz ohne dabei zu einem nennenswerten Verlust an Genauigkeit zu führen. Die Antwortgleichungen werden nur innerhalb der atomaren Blöcke gelöst, sodass der Rechenaufwand für die Ein- und Zweielektronen-Terme balanciert wird.

Das Modell der endlich ausgedehnten Atomkerne wird für das skalare Potential und das Vektorpotential genutzt, da gerade die Fermi-Kontakt-Wechselwirkung der NMR-Kopplungskonstanten stark auf die Elektronendichte am Kernort reagiert. Insbesondere für die sechste Periode ist dieses Modell von Bedeutung und muss für eine genaue Berechnung berücksichtigt werden. Ebenso wird die Optimierung von Basissätzen auf Grundlage der analytischen Ableitungen erst mit diesem Modell möglich. Für die chemische Verschiebung werden optimierte Basissätze auf *double*-, *triple*-, und *quadruple- ζ* Niveau präsentiert. Somit wird X2C zusammen mit den etablierten Näherungen für die Zweielektronen-Integrale zu einem nützlichen Werkzeug für die Berechnung der NMR-Spektren von Hauptgruppen- und Übergangsmetall-Verbindungen.

Die Elektronenkorrelation wird im Rahmen der Dichtefunktionaltheorie (DFT) bis zur vierten Stufe der Jakobsleiter zum exakten Funktional berücksichtigt, d.h. bis zu (lokalen) Hybridfunktionalen. Die paramagnetische Stromdichte wird hierbei für die kinetische Energiedichte genutzt, um einen eichinvarianten Formalismus zu gewährleisten. Im Rahmen dieser Arbeit werden die ersten formal eichinvarianten Berechnungen von NMR-Kopplungen mit entsprechenden Funktionalen präsentiert. Die Implementierung nutzt einen verallgemeinerten Algorithmus zur Lösung der Antwortgleichungen, der für beliebige Eigenschaften gültig ist. Es werden nur die für die Eigenschaft spezifischen Integrale benötigt. Die Effekte des *Hamiltonian*, des Basissatzes und der Dichtefunktional-Näherungen werden über das Periodensystem evaluiert.

Die entwickelte Theorie und die Implementierung werden auf organometallische Phosphorverbindungen angewandt und so die Phosphor-Metall $p\pi-p\pi$ Bindung erklärt. Darüber hinaus konnte die Aromatizität des rein metallischen Clusters $[\text{Th}@\text{Bi}_{12}]^{4-}$ auf Basis einer Analyse der magnetisch induzierten Stromdichte und experimenteller Befunde bestätigt werden. Nach heutigem Stand ist dies die größte rein metallische aromatische Verbindung. Im Zuge dieser Analyse wurden die Ringströme aller bekannten rein metallischen Aromaten und der typischen organischen Aromaten sowie der Heteroaromaten berechnet. Ein Vergleich mit dem Ringstrom des Clusters $[\text{Th}@\text{Bi}_{12}]^{4-}$ zeigt, dass dieser einen großen Strom für 2π -Elektronen aufweist. Daher erweitert $[\text{Th}@\text{Bi}_{12}]^{4-}$ das Konzept der π -Aromatizität und verschiebt dessen Grenzen.

Abstract

Herein, the relativistic exact two-component (X2C) theory is applied to the nuclear magnetic resonance (NMR) shifts and indirect spin–spin coupling constants to interpret and predict the spectra of molecules containing heavy elements. As the NMR shielding and coupling tensor depend on the electron density in the vicinity of the nuclei, its calculations requires an all-electron relativistic description. In X2C, the relativistic decoupling is carried out in a matrix form employing uncontracted or primitive basis functions, which increases the corresponding dimensions. Furthermore, it is necessary to solve response equations for the derivative of the decoupling matrix to calculate the NMR properties. Therefore, X2C comes with high computational demands. In this work, the diagonal local approximation to the unitary decoupling transformation (DLU) is derived and implemented for NMR shifts and coupling constants. This approximation reduces the computation times by one power without significant loss of accuracy and allows for routine applications with moderate computational costs. In DLU, the response equations of the relativistic decoupling matrix must be solved within the atomic blocks only. In contrast to the full X2C approach, the one and two-electron part are balanced in terms of computation time.

Furthermore, the finite nucleus model is used for both the scalar and the vector potential as especially the Fermi-contact interaction for NMR coupling constants is very sensitive towards the electron density at the nucleus. In particular for the sixth row of the periodic table of elements, the finite nuclear size effects need to be considered to obtain accurate results. Moreover, the finite nucleus model allows to optimize basis sets based on analytical energy gradients and the variational principle. Tailored basis sets are presented for NMR shifts at double, triple, and quadruple- ζ quality. Together with well-established approximations of the two-electron terms, X2C therefore becomes a valuable tool which can be used to predict and interpret the NMR spectra of main-group and transition-metal systems.

Electron correlation is treated within a density functional framework. Density functional approximations up to the fourth rung of Jacob’s ladder are employed, i.e. (local) hybrid density functionals. To arrive at a gauge-invariant formalism for the NMR parameters, the paramagnetic current density is used for all kinetic-energy-dependent functionals. Therefore, this work presents the first gauge-invariant calculations of NMR coupling constants at the meta-generalized gradient approximation and local hybrid functional level of theory. The implementation utilizes a generalized solver for response equations, which is able to calculate arbitrary molecular properties if the required integrals are provided. The impact of the relativistic Hamiltonian, the basis set, and the density functional approximation is assessed throughout the periodic table of elements.

The developed computational methodology is applied to organometallic phosphorous compounds and the phosphorous-metal $p\pi$ – $p\pi$ bond is rationalized. Moreover, the implementation allowed to confirm the all-metal aromaticity of the $[\text{Th}@\text{Bi}_{12}]^{4-}$ cluster based on a magnetically induced current density analysis and experimental findings. To date, this is the largest all-metal aromatic compound. The ring currents of all known metal aromatic systems and the typical organic all-carbon aromatic molecules and the heteroaromatic compounds are calculated and compared to the ring current of $[\text{Th}@\text{Bi}_{12}]^{4-}$. Notably, $[\text{Th}@\text{Bi}_{12}]^{4-}$ sustains a substantial ring current for 2 π -electrons and is therefore pushing the limits of π -aromaticity.

Contents

Kurzfassung	iii
Abstract	v
1 Introduction	1
2 Fundamentals of Exact Two-Component Theory	5
2.1 Notation	5
2.2 Dirac–Hamilton Operator	5
2.3 Pauli Equation and Non-Relativistic Limit	8
2.4 Restricted Kinetic Balance Condition and Basis Set Expansion	10
2.5 Exact Decoupling of the Dirac Hamiltonian in a Matrix Representation	12
2.6 Consequences of the Relativistic One-Electron Ansatz for Many-Electron Systems	14
2.7 Local Approximations of the X2C Hamiltonian	15
2.8 Reduction to a Scalar-Relativistic One-Component Hamiltonian	17
3 Fundamentals of Two-Component Hartree–Fock and Density Functional Theory	19
3.1 Gaussian Atom-Centered Basis Sets	19
3.2 Two-Component Hartree–Fock Theory	21
3.3 Approximations of the Two-Electron Integrals	23
3.4 Two-Component Density Functional Theory and Kohn–Sham Equations	24
3.5 Density Functional Approximations	26
3.5.1 Local Spin-Density Approximation	27
3.5.2 Generalized Gradient Approximation	27
3.5.3 Meta-Generalized Gradient Approximation	27
3.5.4 Global and Range-Separated Hybrid Density Functionals	28
3.5.5 Local Hybrid Density Functionals	29
4 NMR Shieldings and Shifts in Scalar-Relativistic X2C Theory	35
4.1 NMR Shielding Tensor, Vector Potential, and Gauge-Including Atomic Orbitals	35
4.2 Restricted Magnetic Balance Condition and Diamagnetic Contribution	38
4.3 Derivatives of the X2C Hamiltonian and Scalar-Relativistic Approximation	40
4.3.1 Magnetic Field Derivatives	41
4.3.2 Magnetic Moment Derivatives	44
4.3.3 Mixed Derivatives	44
4.4 Response Equations for the Derivatives of the Decoupling Matrix	45
4.4.1 First Derivatives	45
4.4.2 Second Derivatives	49
4.5 Sylvester Matrix Equations for the Derivatives of the Renormalization Matrix	51
4.6 DLU-X2C for NMR Shifts	53
4.7 Coupled-Perturbed Hartree–Fock and Kohn–Sham Equations	57
4.8 Magnetically Induced Current Densities	59

5	Quasirelativistic NMR Indirect Spin–Spin Coupling Constants	63
5.1	Definition and Balance Condition	63
5.2	Derivatives of the X2C Hamiltonian	66
5.2.1	First Derivatives of the X2C Hamiltonian	66
5.2.2	Second Derivatives of the X2C Hamiltonian	68
5.3	Local Approximation of the X2C Hamiltonian	69
5.4	Comparison to the Non-Relativistic Integral Derivatives	72
6	Generalized Solver for Two-Component Response Equations	75
7	Generalization of meta-GGA and Local Hybrid Functionals for Gauge Invariance	81
7.1	Gauge-Dependence of the Kinetic Energy Density	81
7.2	Gauge-Invariant Formalism for NMR Shifts and Couplings	82
8	Development of Tailored Basis Sets	87
8.1	Analytical Gradients and Symmetry Exploitation	87
8.2	Optimized Basis Sets for NMR Shieldings and Shifts	90
8.2.1	Analysis of Deficits and Development of Optimized Basis Sets	91
8.2.2	Comparison to Other Relativistic All-Electron Basis Sets	95
8.2.3	Comparison to Non-Relativistic NMR-Optimized Basis Sets	98
9	Assessment of the Accuracy of Relativistic Hamiltonians	101
9.1	NMR Shieldings and Shifts	101
9.1.1	Demonstration of Gauge-Origin and Translation Invariance	101
9.1.2	Organometallic Main-Group Alkynyls	102
9.1.3	Xenon Fluorides	103
9.1.4	Transition-Metal Oxo Compounds	105
9.1.5	Tungsten Compounds	106
9.1.6	Demonstration of Efficiency	107
9.2	NMR Indirect Spin–Spin Coupling Constants	109
9.2.1	Tetrel Molecules and Hydrogen Halides	109
9.2.2	Organometallic Main-Group Alkynyls	113
9.2.3	Tin Compounds	115
9.2.4	Application to Palladium and Platinum Complexes	117
9.2.5	Demonstration of Efficiency	119
10	Assessment of the Accuracy of Density Functional Approximations	123
10.1	NMR Indirect Spin–Spin Coupling Constants	124
10.2	NMR Shieldings and Shifts	126
10.2.1	NMR Shielding Constants of Organic Compounds	126
10.2.2	^1H and ^{13}C NMR Shifts of Organic Compounds	128
10.2.3	NMR Shifts of Transition-Metal Oxo Compounds	129
10.2.4	NMR Shifts of Xenon Fluorides	130
10.2.5	NMR Shifts of Tungsten Compounds	132
10.2.6	Summary	134
11	Application to Phosphinidenide Complexes	135
12	Application to All-Metal Aromaticity	141
12.1	Aromaticity and IUPAC Criteria	141
12.2	Pushing the Limits of Aromaticity with $[\text{Th}@\text{Bi}_{12}]^{4-}$	145
12.3	Ring Currents and NICS of $[\text{K}_2\text{Zn}_{20}\text{Bi}_{16}]^{6-}$	152

13 Summary and Conclusions	155
A Appendix	157
A.1 Integral Evaluation in the Finite Nucleus Model	157
A.2 Expectation Values in X2C and DLU-X2C	163
A.2.1 Electronic Moments: Dipole and Quadrupole Moment	164
A.2.2 Magnetic Dipole Moment of the Electron	165
A.2.3 Nuclear Electric Field Integrals	166
A.3 Static Polarizabilities in X2C and DLU-X2C	167
A.4 Recontracted pcSseg-4 Basis Set for As	169
A.5 NMR Shielding Constants and Shifts of the Organometallic Main-Group Molecules	170
A.6 NMR Shielding Constants of Xenon and the Xenon Fluorides	172
A.7 NMR Shielding Constants of Transition-Metal Oxo Compounds	173
A.8 NMR Shielding Constants of Tungsten Compounds	174
A.9 PBE Results for the NMR Coupling Constants of Alkynyl Compounds	175
A.10 PBE Results for the NMR Coupling Constants of Alkynyl Compounds with X2C-Optimized Structures	176
List of Figures	177
List of Tables	179
Acronyms and Symbols	181
Permissions to Print	191
List of Publications	193
Bibliography	195
Acknowledgments	219

1 Introduction

Nuclear magnetic resonance (NMR) spectroscopy is key to the analysis of newly synthesized compounds in organic and inorganic chemistry.^[1–3] NMR spectroscopy can be carried out in all phases but is most commonly done for molecules in solution. The respective NMR spectra consist of two main parameters. On the one hand, the NMR shift, δ , determining the position of the signal. On the other hand, the NMR coupling constant, J , describing the splitting of the signal due to the coupling of the nuclear magnetic moments. NMR spectra are regularly interpreted using reference databases,^[3–5] semi-empirical methods, or quantum chemical calculations.^[6–10] Organic compounds are routinely analyzed with the first two approaches due to the vast amount of available data. In contrast, the amount of data is limited in inorganic chemistry—in particular for molecules containing heavy elements or for metal clusters. Therefore, quantum chemical calculations are indispensable in the interpretation of NMR spectra of such compounds.^[11–15] To ensure the applicability of quantum chemical methods to large molecules, an efficient implementation is highly important. Yet, such an implementation has not been presented for heavy elements. Therefore, an efficient computational methodology will be developed in this work. In addition to structure determination, quantum chemical studies of NMR parameters may also be used to study the electron delocalization and the aromaticity of organic and inorganic compounds based on magnetically induced ring currents.^[16–19] In a simple picture, placing a molecule with delocalized electrons into a magnetic field causes the electrons to move according to Ampère’s circuital law. Magnetically induced ring currents allow to assign the degree of aromaticity for both organic and inorganic compounds based on theoretical considerations. Generally, the accuracy of a quantum chemical calculation mainly depends on the employed Hamiltonian, the method to treat electron correlation, and the basis set used in the expansion of the quantum mechanical operators.

Most quantum chemical calculations are based on the Schrödinger equation of quantum mechanics.^[20–23] However, the Schrödinger Hamiltonian is insufficient for compounds consisting of heavy elements. In such systems, the electrons move at a speed close to the speed of light and therefore the theory of special relativity^[24] needs to be considered. Thus, the Schrödinger equation is replaced by the Dirac equation,^[25] which is a (4×4) matrix equation, or an effective relativistic Hamiltonian as the basis for quantum chemistry.^[26–36] The difference between the results obtained with the Schrödinger and the Dirac equation, respectively, are described as relativistic effects. Most prominent of which are probably the color of gold,^[37,38] the high voltage of the lead-acid battery in conventional cars,^[39] and the melting point of mercury.^[40,41] Relativistic effects are commonly partitioned into scalar-relativistic and spin-orbit effects. The first describe the contraction of the density due to the mass-velocity relation^[42] whereas the latter refer to the splitting of energy levels due to magnetic induction. For instance, spin-orbit interactions lift the degeneracy of the three p states, denoted by angular momentum quantum number $l = 1$, with respect to the magnetic quantum number, m_l . Note that these effects are not accessible in experimental studies as it is not possible to “turn off relativity”. A common way to introduce relativistic effects in calculations are effective core potentials (ECPs).^[43–45] ECPs introduce an effective nuclear charge and replace the core electrons with a relativistic pseudo potential. For instance, an ECP60 for mercury^[46] means that the inner 60 electrons are “cut out” and modeled by a pseudo potential. These pseudo potentials are fitted to explicit relativistic calculations based on the Dirac equation or approximations thereof. Using ECPs results in a modified Schrödinger equation, in which only the nuclear potential and the number of electrons are replaced. Consequently, the computational demands are essentially the same as for the non-relativistic ansätze and the results are

sufficient for many molecular properties, which are dominated by the valence electrons. However, NMR properties depend on the density in the vicinity of the nuclei. Thus, an all-electron relativistic treatment is vital for accurate predictions. Four-component (4c) or so-called “fully” relativistic approaches make direct use of the Dirac equation^[47,48] and have been already applied to NMR spectroscopy.^[49–64] Due to the (4×4) structure of the Dirac equation, the computational costs are significantly increased compared to the non-relativistic Schrödinger equation or ECP-based methodologies. Furthermore, the Dirac equation not only describes electrons but also the corresponding antiparticles, the positrons. The latter are of minor importance in chemistry. Therefore, already in the 1950s Foldy and Wouthuysen^[65] suggested to decouple the electronic and the positronic states by block-diagonalization with a unitary transformation to obtain a quasirelativistic two-component (2c) approach. However, no analytical closed form of such a unitary transformation matrix is known.^[66] Consequently, approximations for the unitary transformation were suggested. In Douglas–Kroll–Hess (DKH) theory,^[67–69] the decoupling is achieved by a sequence of unitary transformations, trying to remove the off-diagonal elements order by order. In the limit of an infinite number of unitary transformations, this will yield an exact decoupling.^[70,71] The matrix elements are evaluated using a resolution of the identity in the momentum space. This makes the calculation of magnetic properties problematic or at least significantly more involved than energy calculations as the momentum is generalized to account for the vector potential of the magnetic field and the magnetic moment of the nuclei.^[72–74] Another approximate quasirelativistic theory is the zeroth-order regular approximation (ZORA),^[75–78] which was also applied to NMR spectroscopy.^[79–83] However, ZORA is less accurate than high-order DKH and partly relies on error cancellation.^[84] For instance, the NMR shielding constants itself show a rather large deviation to the 4c results. While it is not possible to derive an analytical closed form of the unitary transformation, it is possible to exactly decouple the electronic and the positronic states in a matrix representation with a (finite) basis set expansion.^[85–92] This is based on the pioneering work of Dyall for the normalized elimination of the small component (NESC).^[93–96] In such an exact two-component (X2C) ansatz, the matrix representation of the Dirac–Hamilton operator is diagonalized to arrive at an electrons-only equation. To yield computational benefits, this procedure is only applied to the one-electron Dirac Hamiltonian. The quasirelativistic X2C Hamiltonian is not only formally more accurate than ZORA or DKH theory but also allows for a rather straightforward evaluation of analytical derivatives for molecular properties.^[97,98] This was recently carried out for NMR shielding constants and shifts.^[99–103] Despite these significant formal advances, the computational effort is still considerably increased compared to the non-relativistic ansatz due to the diagonalization of the one-electron Dirac matrix and the applicability of the corresponding calculations is restricted to molecules with typically less than 40 atoms and one or two heavy elements only. Therefore, one aim of this work is to introduce robust local approximations to reduce the computational costs without significant loss of accuracy. For this purpose, the diagonal local approximation to the unitary decoupling transformation^[104,105] (DLU) will be applied to NMR shifts and NMR indirect spin–spin coupling constants. Thus, the analytical derivatives of the DLU-X2C Hamiltonian derived by the author^[106,107] will be generalized to magnetic properties.

Obviously, electron correlation and the two-electron interaction needs to be treated as well. The most sophisticated ansatz, currently used together with the discussed relativistic Hamiltonians, is coupled-cluster (CC) theory.^[101,108–112] It was shown that CC theory is highly accurate for NMR properties^[113–116] but comes with high computational costs. Namely, the “gold standard” of quantum chemistry coupled-cluster singles, doubles, and perturbative triples [CCSD(T)] formally scales as $\mathcal{O}(N^7)$ with system size, N . Therefore, the calculations are often restricted to small molecules and benchmark studies. In contrast, density functional theory (DFT) is applicable to large molecules thanks to its low-order scaling of $\mathcal{O}(N)$ to $\mathcal{O}(N^2)$ ^[117–120] and offers a good cost-accuracy ratio for both main-group and transition-metal compounds.^[121–125] However, the exact exchange-correlation functional is not known and therefore approximations are introduced. In this work, functionals up to the fourth rung of Jacob’s ladder^[126] will be considered, that is hybrid density

functionals, which combine DFT with the non-local exchange contribution of Hartree–Fock (HF) theory. Functionals incorporating a static amount of HF exchange, i.e. the same amount of exchange at every point in space, are termed global hybrid density functionals.^[127] The most prominent example of this class is undoubtedly B3LYP using 20% HF exchange.^[128–130] Varying the amount of HF exchange to reduce the self-interaction error gives another class of functionals, called range-separated functionals.^[131] This class is able to describe charge-transfer interactions^[132] as e.g. in the CAM-B3LYP functional.^[133] Range separation allows for tuning the amount of exchange in the long-range region. Alternatively, the molecule may be fully divided into “normal” regions, where common semilocal density functional approximations perform well, and into “abnormal” regions, where semilocal approximations fail.^[134] For example, a simple one-electron system is poorly described with semilocal approximations. This forms the basis of local hybrid functionals (LHFs) like LH-BLYP,^[135] allowing for a varying amount of HF exchange based on a local mixing function (LMF). Here, the admixture of exchange is, for instance, controlled by the iso-orbital indicator.^[136] Various other parameters for the LMF were suggested and are reviewed in Ref. 137. With such indicators, a LMF is able to increase the amount of HF exchange to 100% and therefore cancels self-electron interaction in regions, where the density behaves similar to a one-electron system. The developed functionals are usually assessed for rather small molecules and thermochemical properties^[138–142] often lacking a comparison to other classes of LMFs and LHFs presented by other groups. Thus, another aim of this work is to assess the accuracy of various local hybrid density functional approximations for NMR properties and compare it to conventional semilocal functionals.

Lastly, the finite basis set for the expansion of the quantum chemical operators is of major importance for quantum chemistry. Almost all quantum chemical methods rely on a suitable basis set.^[143–148] The basis set expansion allows to make use of linear algebra operations, which are efficiently carried out on contemporary central processing units (CPUs) and graphics processing units (GPUs). For this basis set expansions, Gaussian-type functions or orbitals (GTOs) are usually chosen to make use of efficient integral evaluation schemes.^[149–160] The physically straightforward choice of Slater-type functions and orbitals (STOs) results in more complicated integrals but describes the correct functional form of the atomic orbitals. A linear combination of GTOs with the same angular momentum number is formed to approximate the correct functional form of the atomic orbitals. Here, a fixed number of so-called primitive GTOs is combined with fixed contraction coefficients, allowing for two different contraction schemes. On the one hand, the same primitive GTOs may be combined with different contraction coefficients for the different atomic orbitals. This general contraction scheme is used in the correlation consistent basis sets^[46,161–177] and the atomic natural orbital (ANO) basis sets.^[178–185] Dyall and co-workers developed general-contracted four-component relativistic all-electron basis sets.^[186–193] These feature different contraction coefficients for the large and the small component and are therefore employed in an uncontracted fashion in quasirelativistic approaches. On the other hand, the contraction may be performed based on segments and spatial regions. Here, the first contracted s -type GTO describes the $1s$ shell and the inner region of the other shells with the same angular momentum number, e.g., the $2s$ and the $3s$ shells. Segmented-contracted basis sets are advantageous for the integral evaluation in many program suites. In contrast to general-contracted basis sets, the contractions do not correspond to atomic orbitals. The segmented-contraction scheme is utilized for the optimization of the Karlsruhe “def” bases^[194–197] and the error-balanced “def2” basis sets.^[198–200] These basis sets were developed for non-relativistic and scalar-relativistic ECP calculations. The self-consistent DFT treatment of spin–orbit coupling requires extensions of the p and d functions to describe the energetic splitting.^[201] This was realized in the “dhf” basis sets.^[202] Later, the Karlsruhe basis set library was extended by all-electron relativistic basis sets optimized with the X2C Hamiltonian.^[203,204] Other segmented-contracted relativistic all-electron basis sets were developed by Jorge *et al.*^[205–215] or Noro, Sekiya, and Koga at Sapporo^[216–218] with the low-order DKH Hamiltonian. All basis sets mentioned so far are optimized in energy calculations based on the variational principle. Consequently, only functions with an impact on the energy are optimized

and added. As the NMR shielding constants depend on the electron density close to the nuclei, an accurate treatment necessitates tight basis functions, i.e. GTOs with a large exponent.^[219,220] However, tight functions do not considerably affect the energy and such functions have to be added *a posteriori*. Therefore, the development of tailored basis sets for NMR shielding constants and shifts will be discussed and evaluated in this work.

To put it in a nutshell, the central aim of this thesis is to consider all three parameters of quantum chemical NMR calculations for heavy elements, that is

1. derive and implement the DLU-X2C Hamiltonian for NMR shifts and coupling constants
2. assess the quality of the first four rungs of Jacob's ladder in DFT for NMR properties
3. develop optimized Gaussian-type basis sets for relativistic all-electron calculations of NMR shifts

to arrive at a robust and efficient approach for NMR shifts and coupling constants throughout the periodic table of elements. Therefore, X2C becomes an efficient tool for NMR spectroscopy of large molecules. The respective implementation in TURBOMOLE^[221–224] will be applied to chemical problems in organometallic chemistry and heavy-element clusters. An efficient relativistic framework further allows to study all-metal aromaticity based on ring currents.

This work is structured as follows. In chapters 2 and 3 the fundamentals of relativistic quantum chemistry and density functional theory in quantum chemistry will be discussed. In chapters 4 and 5, the derivatives of the DLU-X2C Hamiltonian for NMR shifts and coupling constants will be derived. Chapters 6 and 7, discuss the solution of the generalized coupled-perturbed Kohn–Sham equations to calculate the two-electron parts in a density functional framework. The development of NMR-tailored basis sets is described in chapter 8 together with a comparison to other frequently employed relativistic all-electron basis sets. Chapters 9 and 10 assess the accuracy of the DLU-X2C Hamiltonian and the different density functional approximations used herein. Applications of the developed computational methodology to phosphinidenide complexes and all-metal aromaticity are presented in chapters 11 and 12, respectively. Finally, the work is summarized and concluded in chapter 13.

2 Fundamentals of Exact Two-Component Theory

In this chapter, the derivation of the one-electron (local) exact two-component Hamiltonian is reviewed. The derivation starts with the Dirac–Hamilton operator and introduces the matrix representation based on the kinetic balance condition. An exact two-component Hamiltonian is then obtained using a block-diagonalization of the one-electron Dirac matrix. The introduced error and formal consequences by neglecting the many-electron potential is discussed. The diagonal local approximation to the unitary decoupling transformation is presented. This chapter concludes with the reduction of the two-component or quasirelativistic Hamiltonian to a one-component or scalar-relativistic Hamiltonian.

2.1 Notation

A notation similar to Ref. 28 is adopted for operators and the respective matrix representations in a (finite) basis of one-electron functions. Scalar operators are denoted as \hat{O} and vector operators are denoted as $\hat{\vec{O}}$. Matrix representations using four-component basis functions are indicated as \mathbb{M} whereas \mathbf{M} denotes a matrix in a two-component basis. The two-component basis functions, $\{\phi_\mu\}$, are chosen as a direct product of spin-free basis functions, $\{\lambda_\mu\}$, and the spin functions, $\{\alpha, \beta\}$, according to $\{\lambda_\mu\} \otimes \{\alpha, \beta\}$. The matrix representation of the scalar functions, $\{\lambda_\mu\}$, is indicated by \mathbf{M} . We will employ atom-centered basis functions and make use of Dirac’s *bra-ket* notation for quantum mechanics.^[225] The split notation using large (L) and small (S) component is employed for the four-component basis functions and wave functions. The wave function is denoted as Ψ . The two-component complex spinor orbitals are indicated as $\{\varphi_i\}$ whereas $\{\psi_i\}$ refer to one-component real molecular orbitals (MOs). Therefore, Greek indices denote the basis function and Latin indices denote the MO or spinor orbitals. Gaussian-based atomic units are used unless explicitly stated differently. The position space is considered and all matrix elements are formed in this space.

2.2 Dirac–Hamilton Operator

The physical framework for an electron moving at a speed close to the speed of light is relativistic quantum mechanics. Here, the theory of special relativity is connected with quantum mechanics. The two fundamental postulates of Einstein’s theory of special relativity^[24] are:

1. The physical laws are identical in all inertial frames of reference.
2. The speed of light, c , in vacuum is identical in all inertial frames of reference.

From a mathematical point of view, this means that the physical laws and equations must be invariant with respect to a Lorentz transformation in the four-dimensional space consisting of the time, t , and the three

spatial components (x, y, z) .^[226] Such a transformation may consequently mix the space and the time coordinates. The Schrödinger equation^[20–23] forms the basis of quantum mechanics and reads

$$i \frac{\partial}{\partial t} \Psi = \frac{\hat{p}^2}{2} \Psi. \quad (2.1)$$

Here, a single free electron is considered. Ψ denotes the wave function, which describes the state, and \hat{p} is the momentum operator, which is defined as

$$\hat{p} = -i\vec{\nabla} = -i \left(\frac{\partial}{\partial x} \quad \frac{\partial}{\partial y} \quad \frac{\partial}{\partial z} \right)^T \quad (2.2)$$

with the Cartesian directions x , y , and z . However, the Schrödinger equation does not obey the laws of special relativity. The fact that the Schrödinger equation is not Lorentz invariant can be easily rationalized by the orders of the space and time derivatives. The left-hand side of Eq. 2.1 consists of the first-order derivative with respect to the time, whereas the right-hand side consists of the second-order derivatives of the space components. An equation connecting special relativity and quantum mechanics was derived by Dirac in 1928^[25] and reads

$$\left[\beta c^2 + c\vec{\alpha} \cdot \hat{p} \right] \Psi = i \frac{\partial}{\partial t} \Psi \quad \text{with} \quad \Psi = \begin{pmatrix} \Psi^L \\ \Psi^S \end{pmatrix}. \quad (2.3)$$

The first term of the left-hand side is the rest energy and the second term is the kinetic energy. The trace-less quantities $\vec{\alpha}$ and β are defined as

$$\alpha_i = \begin{pmatrix} 0_2 & \sigma_i \\ \sigma_i & 0_2 \end{pmatrix}, \quad \beta = \begin{pmatrix} \sigma_0 & 0_2 \\ 0_2 & -\sigma_0 \end{pmatrix}, \quad (2.4)$$

employing the Pauli spin matrices, $\vec{\sigma} = (\sigma_x, \sigma_y, \sigma_z)$, and the (2×2) identity matrix, σ_0 ,

$$\sigma_x = \begin{pmatrix} 0 & 1 \\ 1 & 0 \end{pmatrix}, \quad \sigma_y = \begin{pmatrix} 0 & -i \\ i & 0 \end{pmatrix}, \quad \sigma_z = \begin{pmatrix} 1 & 0 \\ 0 & -1 \end{pmatrix}. \quad (2.5)$$

Consequently, the complex (4×4) Dirac equation intrinsically includes the electron spin by construction. In contrast, the electron spin has to be introduced into the non-relativistic Schrödinger equation in an *ad hoc* fashion. The (4×4) dimension of the Dirac equation is a consequence of the electron spin and the fact that the Dirac equation not only describes states with a positive energy but also states with a negative energy.^[227] This phenomenon was later assigned to the existence of the electron's antiparticle, the positron. The spin and both mentioned particles increase the dimension by a factor of four compared to the non-relativistic Schrödinger equation. Thus, the wave function Ψ is termed the four-component spinor consisting of the two component large and small wave functions, Ψ^L and Ψ^S . The names are derived from the absolute value of the components for positive energy solutions where the large component is larger by a mean factor of c as shown in the next section. The free-particle Dirac equation will be generalized to a molecular chemical system, i.e. bound particles in an external potential, in two steps. First, a single electron in the presence of N nuclei is treated. Second, the many-electron case is discussed.

To consider an electron in the field of the nuclei, the electron-nucleus potential, \hat{V} , and the Born–Oppenheimer approximation^[228] are introduced. This yields the Dirac equation of an electron in the field of the clamped nuclei^[31]

$$\hat{h}_D \begin{pmatrix} \Psi^L \\ \Psi^S \end{pmatrix} = E \begin{pmatrix} \Psi^L \\ \Psi^S \end{pmatrix} \quad (2.6)$$

with the one-electron Dirac–Hamilton operator

$$\hat{h}_D = (\beta - I_4) c^2 + c\vec{\alpha} \cdot \hat{\vec{p}} + \hat{V} = \begin{pmatrix} \hat{V} & c\vec{\sigma} \cdot \hat{\vec{p}} \\ c\vec{\sigma} \cdot \hat{\vec{p}} & \hat{V} - 2c^2 \end{pmatrix}. \quad (2.7)$$

I_4 is the (4×4) identity matrix. Here, the relativistic energy scale was shifted by using $(\beta - I_4)$. This ensures that the relativistic and the non-relativistic energy scale are aligned. Approximating the nuclei, N , as point charges yields the charge density

$$\rho_{PC}(\vec{R}) = Z\delta(\vec{R} - \vec{R}_N). \quad (2.8)$$

Here, the nuclear charge density is defined via Dirac’s delta distribution. This results in the potential

$$\hat{V}_{PC} = - \sum_N \frac{Z_N}{|\vec{r} - \vec{R}_N|}, \quad (2.9)$$

where Z_N refers to the charge of the corresponding nucleus. \vec{r} and \vec{R}_N denote the position vectors of the electron and the nucleus, respectively. The use of the point-charge model results in a singularity at the origin. To remove this singularity, the finite nucleus model is introduced.^[229,230] In this model, the potential is commonly approximated by a Gaussian charge density

$$\rho_G(\vec{R}) = Z \left(\frac{\zeta}{\pi} \right)^{3/2} \exp\left(-\zeta(\vec{R} - \vec{R}_N)^2\right) \quad (2.10)$$

with the exponent ζ . The exponent ζ is defined with the root-mean-square (RMS) radius of the nucleus^[231] based on the isotope or atomic mass number, M ,

$$\sqrt{\langle R_N^2 \rangle} = \left(0.836M^{1/3} + 0.570 \right) \text{ fm} \quad (2.11)$$

according to^[232]

$$\zeta = \frac{3}{2 \langle R_N^2 \rangle}. \quad (2.12)$$

For instance, the RMS radius of the ^1H and ^{232}Th nuclei is about 1.40822 fm and 5.70721 fm, respectively.^[204,232] The potential in this finite nucleus model reads^[233]

$$\hat{V}_G = - \frac{Z}{|\vec{r} - \vec{R}_N|} \operatorname{erf}\left(\sqrt{\zeta}|\vec{r} - \vec{R}_N|\right), \quad (2.13)$$

where the error function, $\operatorname{erf}(x)$, is defined as

$$\operatorname{erf}(x) = \frac{2}{\sqrt{\pi}} \int_0^x \exp(-t^2) dt. \quad (2.14)$$

This comparably simple analytical form is the main reason to approximate the extended structure of the nuclei with a Gaussian charge distribution.^[232] The integral evaluation is described in detail in Sec. A.1.

For many electron systems, the Dirac–Hamilton operator in Eq. 2.7 is commonly combined with the two-particle Coulomb operator, $\hat{g}_C(i, j)$, for the electron-electron interaction. This results in the Dirac–Coulomb–Hamilton operator

$$\hat{H}_{\text{DC}} = \sum_i \hat{h}_{\text{D}}(i) + \sum_{i < j} \hat{g}_C(i, j) = \sum_i \left[(\beta - I_4) c^2 + c\vec{\alpha} \cdot \hat{\vec{p}} + \hat{V} \right] + \sum_{i < j} \frac{1}{|\vec{r}_i - \vec{r}_j|}. \quad (2.15)$$

The resulting molecular Dirac–Coulomb equation

$$\hat{H}_{\text{DC}}\Psi = E\Psi \quad (2.16)$$

is not strictly invariant with respect to a Lorentz transformation but serves as a good approximation.^[27,28,31] Note that further corrections such as the Gaunt^[234] and Breit^[235] term, which consider magnetic and current interactions, are still not strictly Lorentz invariant. Furthermore, the Dirac–Coulomb Hamiltonian is not bound from below.^[236] Expanding the wave function Ψ as a Slater determinant of one-particle states gives rise to bound states only. However, there will also be an indefinite number of degenerate Slater determinants with one-particle states of the negative-energy continuum. This problem is termed Brown–Ravenhall disease or continuum dissolution.^[236–238] This drawback can be removed via the no-pair approximation, i.e. all Slater determinants with negative-energy states are removed with projection operators.^[239–241] Formally, all negative-energy states will be excluded from the summation of the Dirac–Coulomb–Hamilton operator in a second quantization form.^[31] These four-component or often called “fully” relativistic approaches result in considerable computational demands and their applicability is therefore limited compared to the non-relativistic analogs of the Schrödinger equation.^[29,242] Furthermore, the states of the negative-energy subspace may lead to conceptual problems in chemical calculations. Thus, it is desirable to decouple the negative-energy and the positive-energy states in order to obtain an *electrons-only* approach.^[70,243] Note that the energy scale in Eq. 2.7 is shifted by the term $(\beta - I_4)$ to be aligned with energy scale of the Schrödinger equation. Consequently, the so-called positive energy states lead to a negative energy for bound molecular orbitals or spinors. In the following, we will consider the one-electron Dirac equation only.

2.3 Pauli Equation and Non-Relativistic Limit

To demonstrate the reduction of the four-component Dirac equation to a two-component equation at the operator level, the Pauli equation^[244] as the simplest approximation is briefly discussed. This also illustrates the different relativistic effects described by the one-electron Dirac Hamiltonian. A thorough derivation of the Pauli equation is presented in Refs. 27, 28, and 245. To begin with, Eq. 2.6 can be reformulated as two equations

$$\hat{V}\Psi^L + c(\vec{\sigma} \cdot \hat{\vec{p}})\Psi^S = E\Psi^L, \quad (2.17)$$

$$c(\vec{\sigma} \cdot \hat{\vec{p}})\Psi^L + (\hat{V} - 2c^2)\Psi^S = E\Psi^S. \quad (2.18)$$

Then, the small component is eliminated to find an equation for the large component only. Rearranging the above equations results in a relation of the large and small component

$$\Psi^S = \left(1 + \frac{E - \hat{V}}{2c^2} \right)^{-1} \frac{\vec{\sigma} \cdot \hat{\vec{p}}}{2c} \Psi^L = \hat{Y} \frac{\vec{\sigma} \cdot \hat{\vec{p}}}{2c} \Psi^L \quad (2.19)$$

with the energy-dependent operator \hat{Y} . Note that $\langle \hat{V} \rangle = -E - 2mc^2$ is non-zero for the electronic solutions in a finite nucleus model.^[27,31] The energy-dependent form of \hat{Y} can be simplified by a Taylor expansion using the speed of light, c ,

$$\hat{Y} = \left(1 + \frac{E - \hat{V}}{2c^2} \right)^{-1} \approx 1 - \frac{E - \hat{V}}{2c^2} + \dots \quad (2.20)$$

In the non-relativistic limit, the speed of light approaches infinity, $c \rightarrow \infty$. Thus, the expansion can be terminated after the first term, $\hat{Y} = 1$, and the two-component form of the Schrödinger equation is obtained

$$\left(\frac{\hat{p}^2}{2} + \hat{V} \right) \Psi_L = E \Psi_L. \quad (2.21)$$

Note that the electron spin is still included in Ψ_L . The first-order relativistic corrections are derived by considering the second term in Eq. 2.20. After rearrangements, this yields the form of the Pauli equation including first-order relativistic corrections

$$\left[\frac{\hat{p}^2}{2} + \hat{V} - \frac{\hat{p}^4}{2} + \frac{\vec{\nabla}^2 \hat{V}}{8c^2} + \frac{1}{4c^2} \vec{\sigma} \cdot \left(\vec{\nabla} \hat{V} \times \hat{p} \right) \right] \Psi_L = E \Psi_L. \quad (2.22)$$

The additional terms are known as the mass-velocity term, the Darwin term, and the spin-orbit interaction. The mass-velocity term considers the dependence of the electron mass on the velocity according to Einstein's equivalence of mass and energy.^[42] The Darwin term describes the *Zitterbewegung* of the electron, i.e. the electron shows oscillations around its mean position and therefore changes the electron-nucleus potential. Note that both the mass-velocity term and the Darwin term do not depend on the Pauli matrices. Therefore, they describe the scalar-relativistic corrections. In contrast, the spin-orbit interaction, $\vec{\sigma} \cdot \left(\vec{\nabla} \hat{V} \times \hat{p} \right)$, couples the momentum and the spin. In the point-charge model, the term can be simplified and cast into its more familiar form

$$\hat{h}_{SO} = \frac{1}{4c^2} \vec{\sigma} \cdot \left(\vec{\nabla} \hat{V} \times \hat{p} \right) = \sum_N \frac{Z_N}{2c^2 |\vec{r} - \vec{R}_N|^3} \hat{s} \cdot \hat{l}_N. \quad (2.23)$$

The spin operator, \hat{s} , and the angular momentum operator, \hat{l} , are defined as

$$\hat{s} = \frac{1}{2} \vec{\sigma}, \quad (2.24)$$

$$\hat{l}_N = \left(\vec{r} - \vec{R}_N \right) \times \hat{p}. \quad (2.25)$$

The spin-orbit interaction introduces the energy splitting for orbitals with a non-vanishing angular momentum quantum number. The Pauli Hamiltonian cannot be used in variational calculations since it is not bound from below. So, the individual terms are only used as perturbation operators. However, perturbation theory is only sufficient for light elements.^[33] Moreover, the expansion by order of c is problematic for Coulomb potentials.^[76] An expansion in the potential results in the variationally stable regular approximation.^[75,76] Truncation of the latter after the first term leads to the zeroth-order regular approximation (ZORA).^[75-78]

$$\hat{h}_{ZORA} = \frac{1}{2} \left(\vec{\sigma} \cdot \hat{p} \right) \hat{\mathcal{K}} \left(\vec{\sigma} \cdot \hat{p} \right) + \hat{V}, \quad (2.26)$$

$$\hat{\mathcal{K}} = \frac{2c^2}{2c^2 - \hat{V}}, \quad (2.27)$$

where the operator $\hat{\mathcal{K}}$ leads to an effective kinetic energy term.

2.4 Restricted Kinetic Balance Condition and Basis Set Expansion

The Pauli Hamiltonian and ZORA reduce the one-electron Dirac–Hamilton operator to a two-component form at an operator level by a Taylor expansion. In quantum chemistry, a finite basis set is introduced according to the linear combination of atomic orbitals (LCAO) ansatz.^[245–247] For the Hamiltonians discussed so far, the basis set expansion is introduced *after* the positive-energy and negative-energy subspaces have been decoupled by approximations. All equations are fully derived in an operator form. Alternatively, the basis set expansion can be introduced *right at the beginning* by realizing that the decoupled relativistic operator itself is not needed but only its matrix representation. However, the basis set expansion of the large and the small component needs to consider the relation between these components to avoid a variational collapse and to ensure the correct non-relativistic limit.^[248] In the non-relativistic limit, the relation between Ψ^L and Ψ^S according to Eq. 2.19 becomes

$$\Psi^S = \frac{\vec{\sigma} \cdot \hat{p}}{2c} \Psi^L. \quad (2.28)$$

This recovers the kinetic energy and the quadratic terms in \hat{p} of the Schrödinger equation. Eq. 2.28 forms the foundation of the restricted kinetic balance condition (RKB) and the (finite) basis set expansion of the wave functions Ψ_i^L and Ψ_i^S for the state i in a set of one-electron spinor functions, ϕ_μ , reads^[248–250]

$$|\psi_i^L\rangle = \sum_{\mu} c_{\mu i}^L |\phi_{\mu}\rangle, \quad (2.29)$$

$$|\psi_i^S\rangle = \sum_{\mu} c_{\mu i}^S \frac{\vec{\sigma} \cdot \hat{p}}{2c} |\phi_{\mu}\rangle. \quad (2.30)$$

Expanding the one-electron Dirac equation of Eq. 2.6 in such a basis results in the matrix form^[249,251]

$$\begin{pmatrix} \mathbf{V} & \mathbf{T} \\ \mathbf{T} & \frac{1}{4c^2} \mathbf{W} - \mathbf{T} \end{pmatrix} \begin{pmatrix} \mathbf{C}_+^L & \mathbf{C}_-^L \\ \mathbf{C}_+^S & \mathbf{C}_-^S \end{pmatrix} = \begin{pmatrix} \mathbf{S} & \mathbf{0}_2 \\ \mathbf{0}_2 & \frac{1}{2c^2} \mathbf{T} \end{pmatrix} \begin{pmatrix} \mathbf{C}_+^L & \mathbf{C}_-^L \\ \mathbf{C}_+^S & \mathbf{C}_-^S \end{pmatrix} \begin{pmatrix} \epsilon_+ & \mathbf{0}_2 \\ \mathbf{0}_2 & \epsilon_- \end{pmatrix}, \quad (2.31)$$

where indices of ϵ indicate the respective energy subspace. This equation can be written in a compact form as

$$\mathbb{D}\mathbf{C} = \mathbb{M}\mathbf{C}\mathbf{E} \quad (2.32)$$

which defines the Dirac matrix, \mathbb{D} , and the relativistic metric, \mathbb{M} , as

$$\mathbb{D} = \begin{pmatrix} \mathbf{V} & \mathbf{T} \\ \mathbf{T} & \frac{1}{4c^2} \mathbf{W} - \mathbf{T} \end{pmatrix}, \quad (2.33)$$

$$\mathbb{M} = \begin{pmatrix} \mathbf{S} & \mathbf{0}_2 \\ \mathbf{0}_2 & \frac{1}{2c^2} \mathbf{T} \end{pmatrix}. \quad (2.34)$$

Note that in this form the Dirac equation is structurally similar to the Roothaan–Hall equations,^[252,253] which will be discussed in Sec. 3.2.

The matrix representation of the overlap integrals, \mathbf{S} , the kinetic energy, \mathbf{T} , and the potential, \mathbf{V} , are block-diagonal in the two-component space.

$$\mathbf{S} = \begin{pmatrix} \mathbf{S} & \mathbf{0} \\ \mathbf{0} & \mathbf{S} \end{pmatrix}, \quad \mathbf{S}_{\mu\nu} = \langle \lambda_\mu | \lambda_\nu \rangle \quad (2.35)$$

$$\mathbf{T} = \begin{pmatrix} \mathbf{T} & \mathbf{0} \\ \mathbf{0} & \mathbf{T} \end{pmatrix}, \quad \mathbf{T}_{\mu\nu} = \langle \lambda_\mu | \frac{1}{2} \hat{p}^2 | \lambda_\nu \rangle \quad (2.36)$$

$$\mathbf{V} = \begin{pmatrix} \mathbf{V} & \mathbf{0} \\ \mathbf{0} & \mathbf{V} \end{pmatrix}, \quad \mathbf{V}_{\mu\nu} = \langle \lambda_\mu | \hat{V} | \lambda_\nu \rangle \quad (2.37)$$

The one-component Hermitian matrices \mathbf{S} , \mathbf{T} , and \mathbf{V} are the same as the corresponding matrix representations of the non-relativistic Schrödinger equation.^[252,253] The relativistically modified potential matrix, \mathbf{W} , is Hermitian but not block-diagonal and complex in the two-component space^[251]

$$\mathbf{W}_{\mu\nu} = \langle \phi_\mu | (\vec{\sigma} \cdot \hat{p}) \hat{V} (\vec{\sigma} \cdot \hat{p}) | \phi_\nu \rangle. \quad (2.38)$$

However, \mathbf{W} can be rearranged to consist of four real one-component matrices by applying Dirac's vector identity^[25]

$$(\vec{\sigma} \cdot \vec{A}) (\vec{\sigma} \cdot \vec{B}) = \sigma_0 \vec{A} \cdot \vec{B} + i \vec{\sigma} \cdot (\vec{A} \times \vec{B}). \quad (2.39)$$

This separates the spin-free and the spin-dependent terms of the relativistically modified potential and leads to

$$\mathbf{W} = \begin{pmatrix} \mathbf{W}^0 + i\mathbf{W}^z & \mathbf{W}^y + i\mathbf{W}^x \\ -\mathbf{W}^y + i\mathbf{W}^x & \mathbf{W}^0 - i\mathbf{W}^z \end{pmatrix} \quad (2.40)$$

with the symmetric matrix \mathbf{W}^0 and the antisymmetric matrices \mathbf{W}^x , \mathbf{W}^y , and \mathbf{W}^z

$$\mathbf{W}_{\mu\nu}^0 = \langle \lambda_\mu | \hat{p}_x \hat{V} \hat{p}_x + \hat{p}_y \hat{V} \hat{p}_y + \hat{p}_z \hat{V} \hat{p}_z | \lambda_\nu \rangle, \quad (2.41)$$

$$\mathbf{W}_{\mu\nu}^x = \langle \lambda_\mu | \hat{p}_y \hat{V} \hat{p}_z - \hat{p}_z \hat{V} \hat{p}_y | \lambda_\nu \rangle, \quad (2.42)$$

$$\mathbf{W}_{\mu\nu}^y = \langle \lambda_\mu | \hat{p}_z \hat{V} \hat{p}_x - \hat{p}_x \hat{V} \hat{p}_z | \lambda_\nu \rangle, \quad (2.43)$$

$$\mathbf{W}_{\mu\nu}^z = \langle \lambda_\mu | \hat{p}_x \hat{V} \hat{p}_y - \hat{p}_y \hat{V} \hat{p}_x | \lambda_\nu \rangle. \quad (2.44)$$

The structure of these matrices is a consequence of the cross-product in Eq. 2.39 and the hermiticity of the Dirac matrix. The spin-free contribution \mathbf{W}^0 describes scalar-relativistic effects whereas the matrices \mathbf{W}^x , \mathbf{W}^y , and \mathbf{W}^z making up the spin-dependent part describe spin-orbit coupling. Besides the incompleteness of the basis set in practical calculations, no approximations were introduced into the one-electron Dirac equation of Eq. 2.6 so far.

2.5 Exact Decoupling of the Dirac Hamiltonian in a Matrix Representation

The Dirac equation in its matrix form still describes the positive-energy and the negative-energy subspaces. The latter can be removed by a block-diagonalization of the Dirac matrix, \mathbb{D} , based on a unitary transformation as suggested by Foldy and Wouthuysen^[65]

$$\mathbb{U}^\dagger \mathbb{D} \mathbb{U} = \begin{pmatrix} \mathbf{h}^+ & \mathbf{0}_2 \\ \mathbf{0}_2 & \mathbf{h}^- \end{pmatrix} \quad \text{with} \quad \mathbb{U}^\dagger \mathbb{U} = \mathbb{U} \mathbb{U}^\dagger = \mathbb{I}_4. \quad (2.45)$$

Such a unitary transformation leads to the electrons-only or quasirelativistic two-component equation

$$\mathbf{h}^+ \mathbf{C} = \mathbf{E}^+ \mathbf{S} \mathbf{C}. \quad (2.46)$$

An explicit expression of the unitary transformation was derived by Heully *et al.*^[66] at an operator level

$$\hat{U} = \begin{pmatrix} \hat{U}^{LL} & \hat{U}^{LS} \\ \hat{U}^{SL} & \hat{U}^{SS} \end{pmatrix} = \begin{pmatrix} \frac{1}{\sqrt{1+\hat{X}^\dagger \hat{X}}} & \frac{-\hat{X}^\dagger}{\sqrt{1+\hat{X} \hat{X}^\dagger}} \\ \frac{\hat{X}}{\sqrt{1+\hat{X}^\dagger \hat{X}}} & \frac{1}{\sqrt{1+\hat{X} \hat{X}^\dagger}} \end{pmatrix} = \begin{pmatrix} 1 & -\hat{X}^\dagger \\ \hat{X} & 1 \end{pmatrix} \begin{pmatrix} \hat{R} & 0 \\ 0 & \hat{R}' \end{pmatrix}. \quad (2.47)$$

Here the operator \hat{X} carries out the decoupling itself whereas the operators \hat{R} and \hat{R}' perform the renormalization for the positive-energy and the negative-energy states. The decoupling operator, \hat{X} , is defined via the relation of the large and the small component

$$\Psi^S = \hat{X} \Psi^L. \quad (2.48)$$

Note that \hat{X} is related to the operator \hat{Y} of Eq. 2.19 via $\hat{X} = \hat{Y} \vec{\sigma} \cdot \hat{\mathbf{p}} / 2c$. However, there is no simple energy-independent form of the decoupling operator but a non-linear operator identity^[66]

$$\hat{X} = \frac{1}{2c^2} \left(c \left(\vec{\sigma} \cdot \hat{\mathbf{p}} \right) - \left[\hat{X}, \hat{V} \right] - \hat{X} c \left(\vec{\sigma} \cdot \hat{\mathbf{p}} \right) \hat{X} \right), \quad (2.49)$$

which involves the commutator of the decoupling and the potential operator, $[\hat{X}, \hat{V}] = \hat{X} \hat{V} - \hat{V} \hat{X}$. This formalism is impractical in actual calculations. The computational effort to solve this non-linear equation is no improvement compared to employing four-component approaches directly.^[28] However, one does not need the decoupling operator itself. Eq. 2.48 can be solved in a matrix representation,^[85–88,90] which then becomes

$$\mathbf{C}_+^S = \mathbf{X} \mathbf{C}_+^L \quad \Leftrightarrow \quad \mathbf{X} = \mathbf{C}_+^S (\mathbf{C}_+^L)^{-1}. \quad (2.50)$$

The eigenvectors of the positive-energy states are obtained in one step by a diagonalization of the Dirac equation in its matrix representation according to Eqs. 2.31 and Eq. 2.32. Therefore, an exact two-component (X2C) theory is derived for the matrix representation of the decoupled electrons-only Dirac–Hamilton operator. We note in passing that Eq. 2.31 can be transformed using the one-component momentum eigenbasis.^[90,105] This results in a unit metric and allows to use a standard diagonalization. However, such an approach is detrimental for analytical derivatives as it requires to calculate the derivative of the transformation, and the diagonalization of the Dirac equation is not the time-determining step for analytical derivatives.^[107] Therefore, a non-orthogonal basis is employed in this work.

The renormalization matrix, R , is defined by Eq. 2.47 and the known decoupling matrix, X ,^[91]

$$RR = \tilde{S}^{-1}S \quad \text{with} \quad \tilde{S} = S + \frac{1}{2c^2}X^\dagger TX \quad (2.51)$$

The choice in practical computations is

$$R = S^{-1/2} \left(S^{-1/2} \tilde{S} S^{-1/2} \right)^{-1/2} S^{1/2}. \quad (2.52)$$

The renormalization ensures the proper transformation from the Dirac picture to the Schrödinger picture, i.e. the coefficients of the large component are transformed to coefficients of the two-component wave function and the relativistic metric is transformed to the non-relativistic metric. This allows to incorporate the one-electron X2C scheme into the non-relativistic machinery of a quantum chemical program suite. Note that the renormalization matrix is not Hermitian but positive definite.^[254]

The unitary transformation matrix is now fully defined and the X2C Hamiltonian reads

$$h^+ = \begin{pmatrix} U^{LL,\dagger} & U^{SL,\dagger} \\ T & \frac{1}{4c^2}W - T \end{pmatrix} \begin{pmatrix} U^{LL} \\ U^{SL} \end{pmatrix} = R^\dagger L^{\text{NESC}} R. \quad (2.53)$$

Here, L^{NESC} denotes the matrix representation of Dyall's operator in the normalized elimination of the small component approach.^[93-96] The NESC matrix reads

$$L^{\text{NESC}} = V + X^\dagger T + T X + X^\dagger \left(\frac{1}{4c^2}W - T \right) X. \quad (2.54)$$

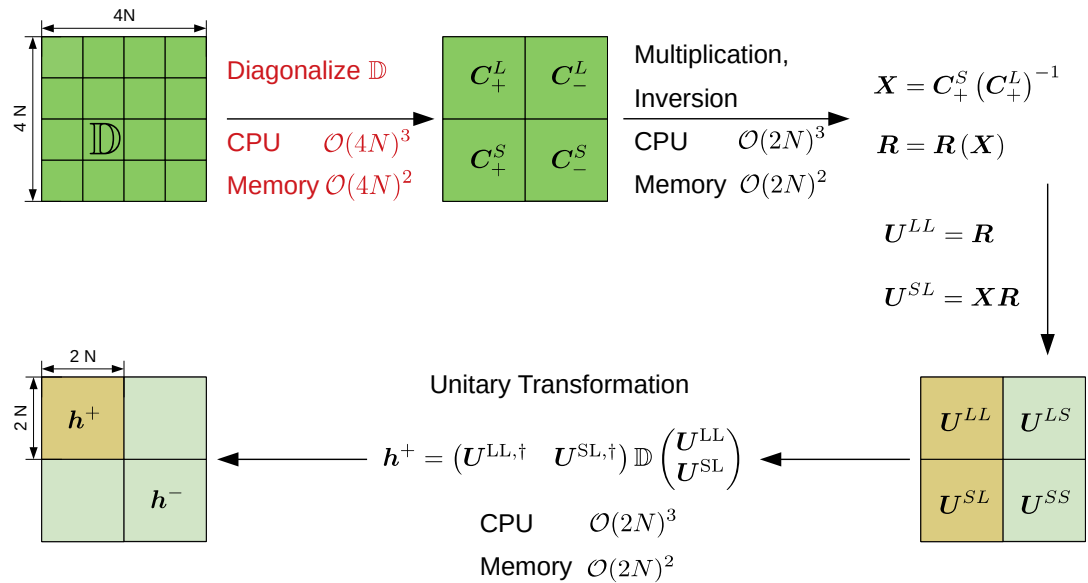


Figure 2.1: Workflow of the X2C transformation. N denotes the number of basis functions. The scaling of the CPU time and the memory demands are reported for the individual steps. The most demanding step is denoted by red color.

The workflow of the X2C transformation is illustrated in Fig. 2.1 and consists of four main steps.

1. Set up the Dirac matrix.
2. Diagonalization of the Dirac matrix to obtain its eigenvectors.
3. Matrix multiplications and inversion to construct the decoupling and renormalization matrix.
4. Perform unitary transformation to calculate the electrons-only Hamiltonian.

The relativistic decoupling of the Dirac Hamiltonian is carried out in the uncontracted basis set as the contraction coefficients of the large and small component differ significantly, see for instance Ref. 186. Thus, the X2C Hamiltonian is transformed to the contracted basis after the decoupling.^[242] In this way, the computational effort for the remaining steps of the quantum chemical calculation is reduced.

2.6 Consequences of the Relativistic One-Electron Ansatz for Many-Electron Systems

In the last sections, the one-electron Dirac equation was considered. For many-electron systems and molecules, using the one-electron X2C Hamiltonian in combination with the uncorrected many-electron Coulomb contribution results in an approximation of the four-component approaches. The X2C transformation is also applicable to the many-electron Dirac–Coulomb Hamiltonian by including the electron–electron potential operator in Eqs. 2.37 and 2.38. This still decouples the negative-energy and the positive-energy subspaces but does not result in a computationally more efficient approach as it requires the diagonalization of the many-electron Dirac matrix just like the parent four-component approach. Alternatively, the unitary transformation matrix of the one-electron part can be applied to the four-component Coulomb matrix.^[92] Formally, the X2C transformation of the one-electron Hamiltonian and the corresponding wave function requires such a so-called picture-change transformation of the two-electron operators. The uncorrected or non-relativistic Coulomb integrals are identical to the large-large block of the four-component Coulomb matrix but not the positive-energy block. Therefore, the unitary transformation should be applied to all two-electron operators and the property operators for expectation values. On the one hand, this picture-change correction reduces the deviation from the full Dirac–Coulomb Hamiltonian. On the other hand, such a scheme considerably increases the computational costs as it requires to set up the four-component two-electron contribution and calculate all necessary integrals. Therefore, a common choice is to combine the one-electron X2C Hamiltonian with the untransformed two-electron contributions.^[31,242] However, this choice leads to an overestimation of the spin-orbit splitting of the spinors. Approximate corrections for the two-electron part are introduced by an effective one-electron potential^[255–260] or by a mean-field ansatz.^[261,262] In this work, an effective one-electron potential according to Boettger^[255] is considered. Here, the screening of the full nuclear charge by the electron density is modeled and the correction is thus termed screened nuclear spin–orbit (SNSO) approximation. Originally, Boettger suggested to rescale the spin-orbit (SO) part of the one-electron Hamiltonian in second-order Douglas–Kroll–Hess theory

$$\mathbf{h}_{\mu\nu}^{\text{SNSO}} = \mathbf{h}_{\mu\nu}^{\text{SO}} - \sqrt{\frac{Q(l_\mu)}{Z_\mu}} \mathbf{h}_{\mu\nu}^{\text{SO}} \sqrt{\frac{Q(l_\nu)}{Z_\nu}}, \quad (2.55)$$

where Z_μ refers to the charge of the atom-center of the basis function ϕ_μ . $Q(l)$ is a screening factor, which depends on the orbit angular momentum of the basis function.

$$Q(l) = 0, 2, 10, 28, \dots \quad \text{for} \quad l = 0, 1, 2, 3, \dots \quad (2.56)$$

For higher angular momentum numbers, this scheme can be generalized and the screening factor is calculated by^[263]

$$Q(l \geq 4) = l(l+1)(2l+1)/3. \quad (2.57)$$

Van Wüllen and Michauk later suggested to directly apply the screening factors to the spin-dependent contributions of the relativistically modified potential, i.e. the matrices \mathbf{W}^x , \mathbf{W}^y , and \mathbf{W}^z ,^[258]

$$\mathbf{W}_{\mu\nu}^{\text{SNSO}} = \mathbf{W}_{\mu\nu}^{\text{SO}} - \sqrt{\frac{Q(l_\mu)}{Z_\mu}} \mathbf{W}_{\mu\nu}^{\text{SO}} \sqrt{\frac{Q(l_\nu)}{Z_\nu}}. \quad (2.58)$$

In this form, the screening factors are applied in the integral evaluation, which facilitates the computation of the SNSO approximated Hamiltonian. The difference in the orbital energies and the SO splittings between these two approaches is negligible.^[260] The SNSO approximation efficiently corrects the energies of the occupied spinors but the results deteriorate for the virtual spinors. Therefore, a modified SNSO (mSNSO) approximation was introduced by Filatov and co-workers.^[259] Here, the screening factor, $Q'(l)$, is defined by

$$Q'(l) = \begin{cases} Q(l) & \text{if } Z > Q(l) \\ Q(l') & \text{if } Z \leq Q(l) \end{cases}, \quad (2.59)$$

where l' is the maximal orbital angular momentum number, l , so that $Z > Q(l')$. Additionally, the parameters $Q(l)$ were reoptimized at the X2C level to match the four-component SO splittings of the xenon and the radon atom yielding

$$Q(1) = 2.34 \operatorname{erf}(34500/\zeta_p), \quad (2.60)$$

$$Q(2) = 11.0, \quad (2.61)$$

$$Q(3) = 28.84, \quad (2.62)$$

where ζ_p is the exponent of the p -type function.

Furthermore, an important conceptual difference between the molecular four-component approach and the one-electron X2C scheme for many-electron systems is that the derivatives of the eigenvectors of the Dirac matrix are needed in the latter. Therefore, the derivative of the decoupling and the renormalization matrix are required.^[97,98] In the four-component approaches, the Hellmann-Feynman theorem^[264,265] may be used directly and the derivatives of the spinor vectors can be avoided for first-order derivatives, see for instance Ref. 266. However, the derivatives of the renormalization and the decoupling matrix are of crucial importance for an exact decoupling in the presence of an external perturbation. Therefore, the complete analytical energy derivative for a many-electron system necessitates the derivative of \mathbf{R} and \mathbf{X} .^[109,267] A simple picture-change correction of the integrals as done for the property operators of expectation values in Sec. A.2 is generally not sufficient.

2.7 Local Approximations of the X2C Hamiltonian

The computational effort for diagonalization of the Dirac equation in a matrix form scales as $\mathcal{O}[(4N)^3]$, where N is the number of uncontracted basis functions. The one-electron part of the non-relativistic Schrödinger equation consists only of the integral evaluation of the overlap matrix (Eq. 2.35), the kinetic energy matrix (Eq. 2.36), and the electron-nucleus potential (Eq. 2.37). This formally scales as $\mathcal{O}(N^2)$ and is reduced by integral screening techniques. Efficient molecular implementations of density functional theory scale between $\mathcal{O}(N)$ and $\mathcal{O}(N^2)$.^[117-120] Consequently, the X2C step may become the bottleneck in density

functional calculations of large molecules. Relativistic effects are local effects as illustrated by the success of relativistic effective core potentials for many molecular properties.^[43–45] Therefore, local approximations of the unitary decoupling transformation were already considered in Dyall’s pioneering work on the NESC approach. Here, the decoupling operator was approximated as a direct sum of the respective contributions of the atomic Dirac equations.^[95,96] This approximation was also introduced to the X2C Hamiltonian and corresponds to the idea “from atoms to molecule”.^[87–89] Such an approximation reduces the dimension of the Dirac matrix for the diagonalization to obtain the eigenvectors. Yet, the full renormalization matrix is used in this approximation and the reduction of the total computational effort is limited. Thus, Peng and Reiher suggested to approximate the unitary transformation matrix as a diagonal local approximation of the atomic blocks according to^[104]

$$\mathbf{U}^{LL} = \bigoplus_A \mathbf{U}_{AA}^{LL} = \bigoplus_A \mathbf{R}_{AA}, \quad (2.63)$$

$$\mathbf{U}^{SL} = \bigoplus_A \mathbf{U}_{AA}^{SL} = \bigoplus_A \mathbf{X}_{AA} \mathbf{R}_{AA}. \quad (2.64)$$

Here, the complete electron-nuclei potential is used to treat the molecular environment. The atomic blocks are formed based on the atom center of the basis functions. An element of the Dirac matrix in Eq. 2.33 with the same atom center, A , in the the *bra* and the *ket* belongs to the corresponding atomic diagonal block, AA , whereas matrix elements with different atom centers in the *bra* (A) and the *ket* (B) belongs to the atomic off-diagonal block, AB . This approximation is termed diagonal local approximation to the unitary decoupling transformation (DLU). The atomic diagonal blocks of the X2C Hamiltonian are calculated as^[104,105]

$$\mathbf{h}_{AA}^+ = \begin{pmatrix} \mathbf{U}_{AA}^{LL,\dagger} & \mathbf{U}_{AA}^{SL,\dagger} \end{pmatrix} \mathbb{D}_{AA} \begin{pmatrix} \mathbf{U}_{AA}^{LL} \\ \mathbf{U}_{AA}^{SL} \end{pmatrix}. \quad (2.65)$$

The DLU scheme also considers the atomic off-diagonal blocks of the Hamiltonian

$$\mathbf{h}_{AB}^+ = \begin{pmatrix} \mathbf{U}_{AA}^{LL,\dagger} & \mathbf{U}_{AA}^{SL,\dagger} \end{pmatrix} \mathbb{D}_{AB} \begin{pmatrix} \mathbf{U}_{BB}^{LL} \\ \mathbf{U}_{BB}^{SL} \end{pmatrix}. \quad (2.66)$$

Therefore, the diagonalization is only performed for the atomic diagonal blocks and the atomic off-diagonal blocks are calculated based on matrix multiplications. The latter are of crucial importance to retain the information about the molecular environment. Similar approximations were suggested previously but did not consider the relativistic corrections to the atomic off-diagonal blocks.^[257,268] Instead, the off-diagonal blocks were approximated by the non-relativistic limit

$$\mathbf{h}_{AB}^+ = \mathbf{T}_{AB} + \mathbf{V}_{AB}. \quad (2.67)$$

However, such an approximation is not sufficient for an accurate description of the Hamiltonian.^[269] Using the atomic diagonal blocks only results in considerable errors for the potential energy surface and does not allow for an accurate structure optimization.^[104] Within the basis set representation herein, the explicit expressions for Eqs. 2.65 and 2.66 are given as^[107]

$$\mathbf{h}_{AA}^+ = \mathbf{R}_{AA}^\dagger \left(\mathbf{V}_{AA} + \mathbf{T}_{AA} \mathbf{X}_{AA} + \mathbf{X}_{AA}^\dagger \mathbf{T}_{AA} + \mathbf{X}_{AA}^\dagger \left[\frac{1}{4c^2} \mathbf{W}_{AA} - \mathbf{T}_{AA} \right] \mathbf{X}_{AA} \right) \mathbf{R}_{AA}, \quad (2.68)$$

$$\mathbf{h}_{AB}^+ = \mathbf{R}_{AA}^\dagger \left(\mathbf{V}_{AB} + \mathbf{T}_{AB} \mathbf{X}_{BB} + \mathbf{X}_{AA}^\dagger \mathbf{T}_{AB} + \mathbf{X}_{AA}^\dagger \left[\frac{1}{4c^2} \mathbf{W}_{AB} - \mathbf{T}_{AB} \right] \mathbf{X}_{BB} \right) \mathbf{R}_{BB}. \quad (2.69)$$

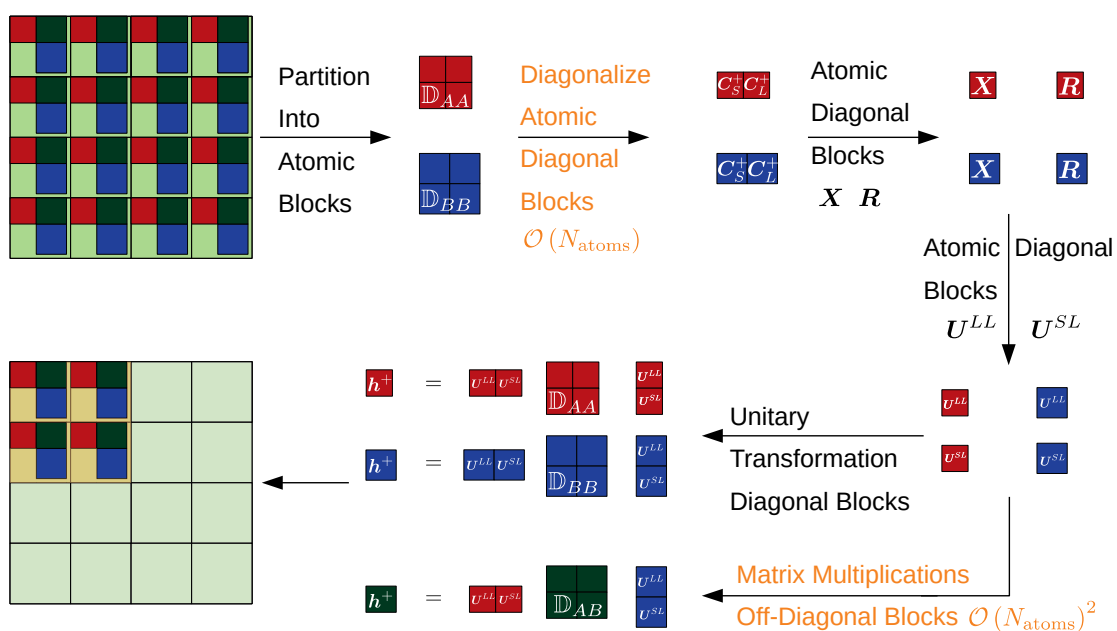


Figure 2.2: Workflow of the DLU-X2C transformation. A molecule consisting of different atoms is assumed. N_{atoms} denotes the number of atoms. The scaling of the CPU time is reported for most time-consuming steps. The most demanding steps are denoted by orange color.

Thus, both the dimension for the diagonalization of the Dirac matrix and also for the matrix multiplications to construct the renormalization matrix are reduced to the atomic dimensions in the DLU scheme. Still, it is necessary to evaluate all blocks of the one-electron integrals.

The DLU scheme is illustrated in Fig. 2.2. The main steps are as follows.

1. Set up the atomic diagonal blocks and perform the X2C decoupling for all atomic blocks, i.e. obtain the atomic diagonal blocks of the decoupling matrix and the renormalization matrix.
2. Perform the unitary decoupling transformation for the atomic diagonal blocks of the Hamiltonian.
3. Perform the matrix multiplications with the atomic diagonal blocks of the unitary transformation matrix and the atomic off-diagonal blocks of the one-electron integrals to calculate the atomic off-diagonal blocks of the Hamiltonian.

The computational effort of the atomic diagonal blocks scales as $\mathcal{O}(N_{\text{atoms}})$, where N_{atoms} denotes the number of atoms. The atomic off-diagonal blocks scale as $\mathcal{O}(N_{\text{atoms}}^2)$ due to the number of the unique atom pairs. Therefore, the DLU-X2C Hamiltonian can be applied to large molecular systems and clusters with thousands of basis functions.^[105,107,270]

2.8 Reduction to a Scalar-Relativistic One-Component Hamiltonian

The DLU-X2C Hamiltonian significantly reduces the computational costs but still describes scalar-relativistic effects and spin-orbit coupling in a complex matrix form. The quasirelativistic X2C and DLU-X2C Hamiltonian can be reduced to a one-component scalar-relativistic form. A scalar-relativistic approximation is desirable for properties or molecular groups, where the impact of spin-orbit coupling is minuscule. Dirac's

vector identity in Eq. 2.39 can be used to separate the underlying operator products into its spin-free (SF) and the spin-dependent (SD) contribution as shown for the matrix \mathbf{W} in Eqs. 2.38 and 2.40, where

$$\left(\vec{\sigma} \cdot \hat{p}\right) \hat{V} \left(\vec{\sigma} \cdot \hat{p}\right) = \sigma_0 \hat{p} \cdot \hat{V} \hat{p} + i\vec{\sigma} \cdot \left(\hat{p} \times \hat{V} \hat{p}\right) \quad (2.70)$$

was used. Consequently, the matrix \mathbf{W} in Eq. 2.40 may also be written as

$$\mathbf{W} = \begin{pmatrix} \mathbf{W}^0 & \mathbf{0} \\ \mathbf{0} & \mathbf{W}^0 \end{pmatrix} + \begin{pmatrix} i\mathbf{W}^z & \mathbf{W}^y + i\mathbf{W}^x \\ -\mathbf{W}^y + i\mathbf{W}^x & -i\mathbf{W}^z \end{pmatrix} = \mathbf{W}^{\text{SF}} + \mathbf{W}^{\text{SD}}. \quad (2.71)$$

Neglecting the spin-dependent terms of \mathbf{W} , i.e. neglecting the terms depending on the Pauli matrices σ_x , σ_y , and σ_z , in the Dirac matrix results in the spin-free four-component Dirac matrix^[251]

$$\mathbb{D}^{\text{SF}} = \begin{pmatrix} \mathbf{V} & \mathbf{T} \\ \mathbf{T} & \frac{1}{4c^2} \mathbf{W}^{\text{SF}} - \mathbf{T} \end{pmatrix} = \begin{pmatrix} \mathbf{V} & \mathbf{0} & \mathbf{T} & \mathbf{0} \\ \mathbf{0} & \mathbf{V} & \mathbf{0} & \mathbf{T} \\ \mathbf{T} & \mathbf{0} & \frac{1}{4c^2} \mathbf{W}^0 - \mathbf{T} & \mathbf{0} \\ \mathbf{0} & \mathbf{T} & \mathbf{0} & \frac{1}{4c^2} \mathbf{W}^0 - \mathbf{T} \end{pmatrix}. \quad (2.72)$$

As all (2×2) super blocks are block-diagonal, the dimension can be reduced according to

$$\mathbb{D}^{\text{SF}} = \begin{pmatrix} \mathbf{V} & \mathbf{T} \\ \mathbf{T} & \frac{1}{4c^2} \mathbf{W}^0 - \mathbf{T} \end{pmatrix} \otimes \mathbf{1}_2. \quad (2.73)$$

Note that the metric in Eq. 2.34, \mathbb{M} , does not include any spin-dependent terms and is thus already block-diagonal. Therefore, the spin-free Dirac equation can be cast into a two-component form employing real matrices only. Application of the X2C decoupling scheme to the two-component spin-free Dirac equation yields an one-component spin-free or scalar-relativistic X2C Hamiltonian

$$\mathbf{h}^+ = \mathbf{R}^\dagger \left(\mathbf{V} + \mathbf{X}^\dagger \mathbf{T} + \mathbf{T} \mathbf{X} + \mathbf{X}^\dagger \left[\frac{1}{4c^2} \mathbf{W}^0 - \mathbf{T} \right] \mathbf{X} \right) \mathbf{R}. \quad (2.74)$$

Since the scalar-relativistic X2C Hamiltonian matrix is real and symmetric, all symmetry properties and dimensions are identical to the non-relativistic Hamiltonian.

3 Fundamentals of Two-Component Hartree–Fock and Density Functional Theory

In this chapter, Gaussian basis sets are described and the necessary fundamentals of two-component Hartree–Fock and density functional theory are reviewed. Density functional approximations within the Kohn–Sham framework are discussed up to the fourth rung of Jacob’s ladder.

3.1 Gaussian Atom-Centered Basis Sets

In quantum chemistry, the many-electron wave function is approximated with a single or multiple Slater determinants.^[271,272] So, the N -electron wave function is written as an antisymmetric tensor product of one-electron wave functions, $\{\varphi\}$, the molecular orbitals (MOs) or spinors.

$$|\Psi_{SD}(1, 2, \dots, N)\rangle = \frac{1}{\sqrt{N!}} \det \left[\begin{array}{c} (|\varphi_1^\alpha\rangle) \\ (|\varphi_1^\beta\rangle) \end{array} \otimes \begin{array}{c} (|\varphi_2^\alpha\rangle) \\ (|\varphi_2^\beta\rangle) \end{array} \otimes \dots \otimes \begin{array}{c} (|\varphi_N^\alpha\rangle) \\ (|\varphi_N^\beta\rangle) \end{array} \right] \quad (3.1)$$

The antisymmetry considers the Pauli exclusion principle for fermions.^[273] The complex spinor functions are expanded in a set of real spin-free one-electron basis functions, λ_μ , as a linear combination of atomic orbitals (LCAO)

$$|\varphi_i\rangle = \begin{pmatrix} |\varphi_i^\alpha\rangle \\ |\varphi_i^\beta\rangle \end{pmatrix} = C_{\mu i} |\phi_\mu\rangle = \begin{pmatrix} C_{\mu i}^\alpha \\ C_{\mu i}^\beta \end{pmatrix} |\lambda_\mu\rangle. \quad (3.2)$$

Here, the expansion coefficients, $C_{\mu i}^\sigma$ ($\sigma = \alpha, \beta$), are complex. Employing real and spin-free basis functions allows for an efficient integral evaluation as the complex integrals can be constructed based on the non-relativistic integrals.^[274,275] Note that uppercase letters are used for the LCAO expansion coefficients, $C_{\mu i}^\sigma$, whereas lowercase letters are used for the expansion of the 4c spinors for the X2C approach, $c_{\mu i}^L$ and $c_{\mu i}^S$.

Almost all quantum chemistry program suites employ Gaussian-type orbitals (GTOs) for the LCAO ansatz.^[143–148] Here, a molecular orbital or a spinor is expanded in the basis of atom-centered Gaussian functions. A Cartesian GTO or Cartesian atomic orbital (CAO) reads

$$\lambda_\mu(x, y, z) = N_\mu (x - X_\mu)^{\mu_x} (y - Y_\mu)^{\mu_y} (z - Z_\mu)^{\mu_z} \exp \left[-\zeta_\mu \left(\vec{r} - \vec{R}_\mu \right)^2 \right], \quad (3.3)$$

where the lower case letters refer to the electronic coordinates and upper case letters to the nuclear coordinates. The atom center is denoted as \vec{R}_μ and N_μ is a normalization constant. Based on the analytical solution of the hydrogen atom,^[20] Slater functions or Slater-type orbitals (STOs) would be a more reasonable choice. A Cartesian STO reads

$$\lambda_\mu(x, y, z) = N_\mu (x - X_\mu)^{\mu_x} (y - Y_\mu)^{\mu_y} (z - Z_\mu)^{\mu_z} \exp \left[-\zeta_\mu |\vec{r} - \vec{R}_\mu| \right]. \quad (3.4)$$

These STOs are, for instance, used in the Amsterdam density functional (ADF) program suite,^[276] which is commonly used for ZORA calculations. However, STOs lead to more complicated integrals in molecular calculations and are not necessarily superior. In contrast, the Gaussian product theorem allows for an efficient integral evaluation as the product of two Gaussian functions is again a Gaussian function according to^[151]

$$\exp\left[-\zeta_\mu\left(\vec{r}-\vec{R}_\mu\right)^2\right]\exp\left[-\zeta_\nu\left(\vec{r}-\vec{R}_\nu\right)^2\right]=A_{\mu\nu}\exp\left[-p\left(\vec{r}-\vec{R}_P\right)^2\right] \quad (3.5)$$

with the sum of the two exponents, p , the new center of the product Gaussian, P , and a constant $A_{\mu\nu}$

$$p = \zeta_\mu + \zeta_\nu, \quad (3.6)$$

$$P = \frac{\zeta_\mu\vec{R}_\mu + \zeta_\nu\vec{R}_\nu}{p}, \quad (3.7)$$

$$A_{\mu\nu} = \exp\left[-\frac{\zeta_\mu\zeta_\nu}{\zeta_\mu + \zeta_\nu}\left(\vec{R}_\mu - \vec{R}_\nu\right)^2\right]. \quad (3.8)$$

Moreover, GTOs allow for more efficient screening procedures as the functional value rapidly decreases with increasing distance from the atom center.^[272] The functional form of the Slater-type orbitals is modeled by a linear combination or contraction of Gaussian functions. Multiple primitive GTOs are combined with fixed coefficients to form a single contracted GTO. The contraction is performed either based on atomic orbitals directly in general-contracted basis sets or by dividing the atomic orbitals into segments based on the nodes in segmented-contracted basis sets. General-contracted basis sets use the same Gaussian functions of a given angular momentum, l , for all contracted functions. So, the contracted GTO directly corresponds to an atomic orbital. In contrast, segmented-contracted basis sets use a contracted GTO of a given angular momentum number to model the spatial region of all orbitals with that angular momentum number. For instance, the contracted GTO of the $1s$ orbital is used to describe the spatial region up to the (radial) node of the $2s$ orbital. Therefore, the contracted GTOs do not correspond to atomic orbitals directly. The general-contracted scheme leads to larger basis sets in terms of primitive functions and more involved integral algorithms are required to avoid calculating the same integrals multiple times.^[277]

Describing each atomic orbital or segment with a single contracted GTO is not sufficient for an accurate treatment. So, multiple contracted GTOs are employed and the cardinal number states the number of contracted GTOs for each orbital or segment. For instance, DZ, TZ, and QZ refers to double- ζ , triple- ζ , and quadruple- ζ meaning that two, three, or four contracted (or uncontracted) GTOs are employed. Chemical bonds and many properties are driven by the valence region. Thus, it is computationally advantageous to use multiple contracted functions only in the valence region. This is denoted by a V in the basis set name, for instance, VTZ or TZV denote a valence triple- ζ basis set. Such bases can be optimized in atomic calculations based on the variational principle,^[194,195] which ensures that the minimum of the energy with the chosen number of basis functions is reached. According to the variational principle the exact energy with the true wave function, Ψ , is always lower than or identical to the energy with a trial function, $\tilde{\Psi}$,

$$E_{\text{exact}} = \frac{\langle\Psi|\hat{H}|\Psi\rangle}{\langle\Psi|\Psi\rangle} \leq \frac{\langle\tilde{\Psi}|\hat{H}|\tilde{\Psi}\rangle}{\langle\tilde{\Psi}|\tilde{\Psi}\rangle}. \quad (3.9)$$

The charge density in molecules may be non-symmetric or anisotropic due to polarization. Therefore, functions with a higher l quantum number, describing the unoccupied shells, are needed.^[278] Such functions are called polarization functions and are denoted by a p or P in the basis set name, e.g., pVTZ or TZVP.

3.2 Two-Component Hartree–Fock Theory

Hartree–Fock (HF) theory approximates the many-electron wave function by a single Slater determinant and minimizes the energy, i.e. the expectation value of the Hamiltonian, based on the variational principle.^[279,280] The orthonormality of the MOs or spinors imposes a constraint. Mathematically, this is realized by a constrained minimization with the method of Lagrange multipliers. The detailed derivation can be found in many textbooks.^[245,272,281,282] The canonical generalized HF (GHF) equations are^[47]

$$\hat{F}_i |\varphi\rangle_i = \epsilon_i |\varphi_i\rangle \quad (3.10)$$

and the Fock operator is defined as

$$\hat{F}_i = \hat{h}_i + \sum_j (\hat{J}_j - \hat{K}_j) \quad (3.11)$$

with the Coulomb and the exchange operators

$$\langle \varphi_i | \hat{J}_j | \varphi_i \rangle = \langle ij | ij \rangle = \iint \varphi_i^*(\vec{r}_1) \varphi_j^*(\vec{r}_2) \frac{1}{|\vec{r}_1 - \vec{r}_2|} \varphi_i(\vec{r}_1) \varphi_j(\vec{r}_2) d\vec{r}_1 d\vec{r}_2, \quad (3.12)$$

$$\langle \varphi_i | \hat{K}_j | \varphi_i \rangle = \langle ij | ji \rangle = \iint \varphi_i^*(\vec{r}_1) \varphi_j^*(\vec{r}_2) \frac{1}{|\vec{r}_1 - \vec{r}_2|} \varphi_j(\vec{r}_1) \varphi_i(\vec{r}_2) d\vec{r}_1 d\vec{r}_2. \quad (3.13)$$

The integrals may also be written in Mulliken notation

$$\langle \varphi_i | \hat{J}_j | \varphi_i \rangle = (ii | jj) = \iint \varphi_i^*(\vec{r}_1) \varphi_i(\vec{r}_1) \frac{1}{|\vec{r}_1 - \vec{r}_2|} \varphi_j^*(\vec{r}_2) \varphi_j(\vec{r}_2) d\vec{r}_1 d\vec{r}_2, \quad (3.14)$$

$$\langle \varphi_i | \hat{K}_j | \varphi_i \rangle = (ij | ji) = \iint \varphi_i^*(\vec{r}_1) \varphi_j(\vec{r}_1) \frac{1}{|\vec{r}_1 - \vec{r}_2|} \varphi_j^*(\vec{r}_2) \varphi_i(\vec{r}_2) d\vec{r}_1 d\vec{r}_2. \quad (3.15)$$

The Coulomb operator describes the electrostatic interaction whereas the exchange operator results from the Pauli exclusion principle and cancels the self-interaction. The eigenvalues, ϵ_i , or orbital energies can be used to calculate the ionization energies.^[283] For a closed-shell system in non-relativistic quantum chemistry or without magnetic induction, the orbitals are real and do not depend on the electron spin. If all orbitals are either doubly occupied or unoccupied, GHF reduces to restricted Hartree–Fock (RHF) theory. Expansion of the one-particle states into a basis set leads to the Roothaan–Hall equations.^[252,253] In a two-component GHF formalism, the Roothaan–Hall equations read

$$\mathbf{FC} = \mathbf{SC}\epsilon \quad (3.16)$$

with the overlap matrix, \mathbf{S} , the coefficients, \mathbf{C} , and the eigenvalue matrix ϵ . The Fock matrix reads^[27,28,275,284]

$$\mathbf{F} = \begin{pmatrix} \mathbf{h}^0 + i\mathbf{h}_{\text{SO}}^z & \mathbf{h}_{\text{SO}}^x - i\mathbf{h}_{\text{SO}}^y \\ \mathbf{h}_{\text{SO}}^x + i\mathbf{h}_{\text{SO}}^y & \mathbf{h}^0 - i\mathbf{h}_{\text{SO}}^z \end{pmatrix} + \begin{pmatrix} \mathbf{J} - \mathbf{K}^{\alpha\alpha} & -\mathbf{K}^{\alpha\beta} \\ -\mathbf{K}^{\beta\alpha} & \mathbf{J} - \mathbf{K}^{\beta\beta} \end{pmatrix}, \quad (3.17)$$

where the scalar-relativistic contribution is denoted by \mathbf{h}^0 and the spin–orbit contributions by $\mathbf{h}_{\text{SO}}^{x,y,z}$. The first is symmetric whereas the latter are antisymmetric. So, the full one-electron Hamiltonian matrix and the Fock matrix are complex and Hermitian. The Coulomb, \mathbf{J} , and the exchange matrix, \mathbf{K} , are given as

$$\mathbf{J}_{\mu\nu} = \sum_i n_i \langle \mu\kappa | \nu\eta \rangle \left(\text{Re}(C_{\kappa i}^\sigma) \text{Re}(C_{\eta i}^\sigma) + \text{Im}(C_{\kappa i}^\sigma) \text{Im}(C_{\eta i}^\sigma) \right), \quad (3.18)$$

$$\mathbf{K}_{\mu\nu}^{\sigma_1\sigma_2} = \sum_i n_i \langle \mu\kappa | \eta\nu \rangle (C_{\kappa i}^{\sigma_1})^* C_{\eta i}^{\sigma_2}. \quad (3.19)$$

Here, n_i denotes the occupation of the spinor $|\varphi_i\rangle$. As in the 1c case, the Roothaan–Hall equations can be formulated in terms of a one-particle density matrix,

$$\mathbf{D} = \sum_i n_i |\varphi_i\rangle \langle \varphi_i| = \begin{pmatrix} \mathbf{D}^{\alpha\alpha} & \mathbf{D}^{\alpha\beta} \\ \mathbf{D}^{\beta\alpha} & \mathbf{D}^{\beta\beta} \end{pmatrix}. \quad (3.20)$$

The density matrix is commonly partitioned into four real and imaginary complex blocks. In terms of complex expansion coefficients of the LCAO approach, $C_{\mu i}^\sigma$, these blocks become

$$\operatorname{Re}(D_{\nu\mu}^{\sigma_1\sigma_2}) = \sum_i n_i [\operatorname{Re}(C_{\nu i}^{\sigma_1}) \operatorname{Re}(C_{\mu i}^{\sigma_2}) + \operatorname{Im}(C_{\nu i}^{\sigma_1}) \operatorname{Im}(C_{\mu i}^{\sigma_2})], \quad (3.21)$$

$$\operatorname{Im}(D_{\nu\mu}^{\sigma_1\sigma_2}) = \sum_i n_i [-\operatorname{Re}(C_{\nu i}^{\sigma_1}) \operatorname{Im}(C_{\mu i}^{\sigma_2}) + \operatorname{Im}(C_{\nu i}^{\sigma_1}) \operatorname{Re}(C_{\mu i}^{\sigma_2})]. \quad (3.22)$$

Only the $\alpha\alpha$ and the $\beta\beta$ block of the density matrix are Hermitian, while the two remaining blocks $\alpha\beta$ and $\beta\alpha$ are general matrices. Therefore, symmetric and antisymmetric linear combinations of the blocks are formed as the Hamiltonian, the Fock matrix, and the complete density matrix are still Hermitian. The symmetric combinations are given as $\operatorname{Re}(\mathbf{D}^{\alpha\alpha}) \pm \operatorname{Re}(\mathbf{D}^{\beta\beta})$, $\operatorname{Re}(\mathbf{D}^{\alpha\beta}) + \operatorname{Re}(\mathbf{D}^{\beta\alpha})$, and $\operatorname{Im}(\mathbf{D}^{\alpha\beta}) - \operatorname{Im}(\mathbf{D}^{\beta\alpha})$, whereas the four antisymmetric linear combinations are $\operatorname{Im}(\mathbf{D}^{\alpha\alpha}) \pm \operatorname{Im}(\mathbf{D}^{\beta\beta})$, $\operatorname{Re}(\mathbf{D}^{\alpha\beta}) - \operatorname{Re}(\mathbf{D}^{\beta\alpha})$, and $\operatorname{Im}(\mathbf{D}^{\alpha\beta}) + \operatorname{Im}(\mathbf{D}^{\beta\alpha})$. The Coulomb matrix only requires the symmetric combination $\operatorname{Re}(\mathbf{D}^{\alpha\alpha}) + \operatorname{Re}(\mathbf{D}^{\beta\beta})$, which forms the real total particle density matrix, \mathbf{D}^0 . Therefore, the Coulomb integrals become

$$\mathbf{J}_{\mu\nu} = \langle \mu\kappa | \nu\eta \rangle [\operatorname{Re}(\mathbf{D}^{\alpha\alpha}) + \operatorname{Re}(\mathbf{D}^{\beta\beta})]_{\mu\nu} = \langle \mu\kappa | \nu\eta \rangle \mathbf{D}_{\mu\nu}^0 = (\mu\nu | \kappa\eta) \mathbf{D}_{\mu\nu}^0. \quad (3.23)$$

In contrast, the exchange integrals are obtained with all eight linear combinations.^[275,284] Using additional symmetry restrictions, this may be reduced to six linear combinations.^[275] The total energy is obtained as the trace of the density and the Fock matrix, where the Coulomb and the exchange matrix are rescaled by a factor of one half,

$$E_{\text{total}} = \operatorname{tr} \left(\mathbf{D} \left[\mathbf{h} + \frac{1}{2} (\mathbf{J} - \mathbf{K}) \right] \right). \quad (3.24)$$

Thus, the total energy is not the sum of the spinor or MO energies. As the Coulomb and the exchange integrals depend on the density matrix, an iterative procedure is required to solve the HF and the Roothaan–Hall equations. Here, the equations are solved with a self-consistent field (SCF) approach. That is, the density matrix is varied until the energy change within two iterations falls below a given threshold. More sophisticated approaches consider the orbital energies and the root mean square of the density matrix to indicate the convergence of the SCF procedure. The initial guess for the SCF procedure is commonly obtained from the extended Hückel theory^[285–288] or a core Hamiltonian guess.

In Hartree–Fock theory, an electron is embedded in the mean field of the other electrons. Therefore, the electrons are uncorrelated *per definitionem*^[289] as the correlation energy is defined as the difference of the exact energy and the HF energy. Therefore, the results of Hartree–Fock theory are rarely used nowadays but form a basis for many accurate post-Hartree–Fock methods. In such methods, the electron correlation can be considered via perturbation theory as outlined by Møller and Plesset^[290] or by using a linear combination of Slater determinants as ansatz for the wave function (configuration interaction).^[291] The correlation energy may also be calculated with the coupled-cluster method,^[292,293] which uses HF as its reference as well. Alternatively, the correlation energy can be expressed as a functional of the density and not in a wave function context. This is done in density functional theory but its practical implementation for molecular systems is fairly similar and commonly based on implementations of HF theory.^[294]

3.3 Approximations of the Two-Electron Integrals

The evaluation of the Coulomb and exchange integrals scales as $\mathcal{O}(N_{\text{bf}}^4)$, where N_{bf} denotes the basis functions. Approximations are introduced to reduce the computational effort. Herein, we use the resolution of the identity approximation for the Coulomb integrals^[295–298] (RI- J) and the seminumerical exchange approximation (semiK).^[299–311] In the RI- J approximation, the Coulomb integrals are formally approximated by inserting a resolution of the identity and introducing auxiliary basis functions according to

$$\mathbf{J}_{\mu\nu} = (\mu\nu|\kappa\eta) \mathbf{D}_{\mu\nu}^0 \approx \sum_{P,Q} (\mu\nu|P) (P|Q)^{-1} (Q|\kappa\eta) \mathbf{D}_{\mu\nu}^0. \quad (3.25)$$

Here, the products of two basis functions are approximated by an auxiliary basis set with N_{aux} functions,

$$\lambda_\mu(\vec{r})\lambda_\nu(\vec{r}) \approx \sum_P C_{\mu\nu}^P P(\vec{r}). \quad (3.26)$$

This reduces the computational effort by one power to $\mathcal{O}(2N_{\text{bf}}^2 N_{\text{aux}} + N_{\text{aux}}^3)$. The $\mathcal{O}(N_{\text{aux}}^3)$ scaling is caused by the inversion of the matrix consisting of the integral $(P|Q)$. The auxiliary basis functions are optimized to fit the electron total density.^[312] As the Coulomb integrals only depend on this quantity, the RI- J approximation is identical in the one and two-component formalism.^[275]

The seminumerical exchange approximation was originally developed in the context of pseudospectral methods for HF theory^[299–303] and later adapted by Neese and co-workers.^[304] Here, the integration for the one-component exchange integrals

$$\mathbf{K}_{\mu\nu} = \sum_{\kappa\eta} (\mu\kappa|\nu\eta) D_{\kappa\eta} \quad (3.27)$$

is split into two separate steps. First, one integration is carried out analytically. Second, the other integration step is performed numerically on a grid in real space. This yields

$$\mathbf{K}_{\mu\nu} = \sum_g w_g X_\mu^g \sum_\eta A_{\nu\eta}^g F_\eta^g, \quad (3.28)$$

$$X_\mu^g = \lambda_\mu(\vec{r}_g), \quad (3.29)$$

$$F_\eta^g = \sum_\kappa D_{\kappa\eta} X_\kappa^g, \quad (3.30)$$

$$A_{\nu\eta}^g = \int \frac{1}{|\vec{r}_g - \vec{r}_2|} \lambda_\nu(\vec{r}_2) \lambda_\eta(\vec{r}_2) d\vec{r}_2. \quad (3.31)$$

Here, \vec{r}_g are the coordinates of the grid points and w_g are the integration weights. In the two-component formalism, the exchange integrals are split into the symmetric and the antisymmetric contributions^[311]

$$\mathbf{K}_{\mu\nu}^{\text{sym}} = \sum_g w_g \sum_{\kappa\eta} [X_\mu^g X_\kappa^g A_{\nu\eta}^g + A_{\nu\kappa}^g X_\mu^g X_\eta^g] D_{\kappa\eta}^{\text{sym}}, \quad (3.32)$$

$$\mathbf{K}_{\mu\nu}^{\text{anti}} = \sum_g w_g \sum_{\kappa\eta} [X_\mu^g X_\kappa^g A_{\nu\eta}^g - A_{\nu\kappa}^g X_\mu^g X_\eta^g] D_{\kappa\eta}^{\text{anti}}. \quad (3.33)$$

The two-component semiK approximation was originally implemented by Plessow and Weigend.^[305] This implementation was later reworked by Holzer with an efficient screening procedure based on the Schwarz inequality^[313,314] and a suitable dealiasing scheme resulting in a scaling between $\mathcal{O}(N^1)$ and $\mathcal{O}(N^2)$.^[311] The numerical integration routines are taken from the density functional code and are described in detail in Ref. 315.

3.4 Two-Component Density Functional Theory and Kohn–Sham Equations

Instead of calculating the many-electron wave function, $\Psi(\vec{r}_1, \vec{r}_2, \dots, \vec{r}_N)$, and the energy as an expectation value of the Hamiltonian, the density, $\rho(\vec{r})$, can be chosen as the basic variable. The density is given by

$$\rho(\vec{r}) = N \int \dots \int \Psi^*(\vec{r}_1, \vec{r}_2, \dots, \vec{r}_N) \Psi(\vec{r}_1, \vec{r}_2, \dots, \vec{r}_N) d\vec{r}_2 \dots d\vec{r}_N \quad (3.34)$$

with the number of electrons N . This is the central idea of density functional theory (DFT) and reduces the dimension from $3N$ to 3.^[316–318] In contrast to the wave function, the density is also accessible in X-ray experiments. This section will first discuss the non-relativistic DFT formalism. The generalization to a relativistic two-component framework is considered afterwards. The first attempts of DFT were made by Thomas^[319] and Fermi^[320] for the kinetic energy of the uniform electron gas. Here, the kinetic energy can be expressed as a functional of the density according to

$$T_{\text{TF}}[\rho(\vec{r})] = \frac{3}{10} \left(\frac{3}{8\pi} \right)^{2/3} \int \rho^{5/3}(\vec{r}) d\vec{r}. \quad (3.35)$$

The Thomas–Fermi model was generalized to account for the exchange interaction by Dirac, who derived an exchange energy functional for the homogeneous electron gas^[321]

$$E_X[\rho(\vec{r})] = -\frac{3}{4} \left(\frac{3}{\pi} \right)^{1/3} \int \rho(\vec{r})^{4/3} d\vec{r}, \quad (3.36)$$

which can be rewritten with the exchange energy density, $\epsilon_X[\rho(\vec{r})]$,

$$E_X[\rho(\vec{r})] = \int \rho(\vec{r}) \epsilon_X[\rho(\vec{r})] d\vec{r}, \quad (3.37)$$

$$\epsilon_X[\rho(\vec{r})] = -\frac{3}{4} \left(\frac{3}{\pi} \right)^{1/3} \rho(\vec{r})^{1/3}. \quad (3.38)$$

The Thomas–Fermi–Dirac model is not sufficient for molecules due to the kinetic energy expression.^[322] Nevertheless, it suggests that the wave function can be replaced by the electron density as the basic variable. This was formally proven with the Hohenberg–Kohn theorems.^[323] The Hohenberg–Kohn theorems state:

1. The external potential, $\hat{V}(\vec{r})$, is up to a constant a unique functional of the electron density, $\rho(\vec{r})$. The external potential contains the information of the considered system in the Hamiltonian and thus the ground-state is a unique functional of the electron density, $\rho(\vec{r})$.
2. A variational principle holds for the electron density, $\rho(\vec{r})$, as the basic variable.

We note in passing that the original proof of Hohenberg and Kohn is mathematically incomplete and a rigorous formulation was presented by Levy^[324,325] and Lieb.^[326] Despite formally justifying the Thomas–Fermi–Dirac model, the insufficient description of the kinetic energy persists. Kohn and Sham reintroduced a wave function and the Slater determinant into DFT,^[327] making use of the respective kinetic energy. The Kohn–Sham model considers a non-interacting system with the same density as the real system of interest, i.e. a molecule. This allows to write the ground-state energy as

$$E = \int \hat{V}(\vec{r}) \rho(\vec{r}) d\vec{r} + \frac{1}{2} \iint \frac{\rho(\vec{r}_1) \rho(\vec{r}_2)}{|\vec{r}_1 - \vec{r}_2|} d\vec{r}_1 d\vec{r}_2 + T_s[\rho(\vec{r})] + E_{XC}[\rho(\vec{r})] \quad (3.39)$$

with the kinetic energy of the non-interacting system, T_s , and the exchange-correlation energy, E_{XC} . The exact wave function of a non-interacting system is a Slater determinant. Minimizing the energy leads to the Kohn–Sham equations

$$\hat{F}_{KS} |\psi_i\rangle = \epsilon_i |\psi_i\rangle. \quad (3.40)$$

Here, the Kohn–Sham–Fock operator is defined as

$$\hat{F}_{KS} = \hat{T} + \hat{V} + \hat{J} + \hat{V}_{XC} \quad (3.41)$$

with the exchange-correlation (XC) potential

$$\hat{V}_{XC}[\rho(\vec{r})] = \frac{\delta E_{XC}[\rho(\vec{r})]}{\delta \rho(\vec{r})}. \quad (3.42)$$

The kinetic energy and the Coulomb interaction are evaluated like in HF theory with the one-component Kohn–Sham orbitals, $\{|\psi_i\rangle\}$. The electron density is obtained as

$$\rho(\vec{r}) = \sum_i |\psi_i(\vec{r})|^2. \quad (3.43)$$

In quantum chemical calculations, the Kohn–Sham equations are expanded in a finite basis like the HF equations and solved with the SCF procedure.^[328] The exact exchange-correlation potential is not known and therefore approximations are introduced. These are discussed in the next section. The exchange-correlation terms are calculated on a grid to perform the integration numerically.^[315,328,329]

So far, we considered a closed-shell system in the restricted Kohn–Sham (RKS) theory. For open-shell-systems, not only the total density, ρ , but additionally the spin density, ρ_z , is required, resulting in the so-called unrestricted Kohn–Sham (UKS) approach. The latter quantities are calculated based on the electron density of each spin

$$\rho = \rho^\alpha + \rho^\beta, \quad (3.44)$$

$$\rho_z = \rho^\alpha - \rho^\beta. \quad (3.45)$$

Therefore, the exchange-correlation functional becomes spin-dependent

$$\hat{V}_{XC}^\sigma[\rho(\vec{r})] = \frac{\delta E_{XC}[\rho^\alpha(\vec{r}), \rho^\beta(\vec{r})]}{\delta \rho^\sigma(\vec{r})} \quad \text{with } \sigma = \alpha, \beta \quad (3.46)$$

resulting in an energy difference of singlet and triplet states. In a two-component formalism, the spin vector density and the corresponding matrices are introduced.^[275,330,331] Here, these matrices are introduced in an *ad hoc* fashion. A rigorous formulations requires to generalize the constrained-search formalism^[324–326] to a (relativistic) two-component or four-component framework and to proof the existence of E_{XC} . The total density matrix, \mathbf{M}_0 , and the spin vector density matrices, \mathbf{M}_i ($i = x, y, z$), are defined as

$$\mathbf{M}_0 = \text{Re}(\mathbf{D}^{\alpha\alpha}) + \text{Re}(\mathbf{D}^{\beta\beta}), \quad (3.47)$$

$$\mathbf{M}_x = \text{Re}(\mathbf{D}^{\alpha\beta}) + \text{Re}(\mathbf{D}^{\beta\alpha}), \quad (3.48)$$

$$\mathbf{M}_y = \text{Im}(\mathbf{D}^{\alpha\beta}) - \text{Im}(\mathbf{D}^{\beta\alpha}), \quad (3.49)$$

$$\mathbf{M}_z = \text{Re}(\mathbf{D}^{\alpha\alpha}) - \text{Re}(\mathbf{D}^{\beta\beta}). \quad (3.50)$$

The spin vector density or spin magnetization vector becomes

$$m_i(\vec{r}) = \sum_{\mu\nu} \lambda_\mu(\vec{r}) [\mathbf{M}_i]_{\mu,\nu} \lambda_\nu(\vec{r}), \quad (3.51)$$

where λ_μ denotes a real basis function. The spin density can be defined by the components of the spin magnetization vector or the length of the spin magnetization vector, $s = |m(\vec{r})|$. The first ansatz is termed collinear approach as a fixed quantization axis is chosen to define the spin density. This does not require major modifications of the existing non-relativistic infrastructure when an unrestricted Kohn–Sham formalism is available.^[332] However, the spin density is not invariant with respect to rotations in spin space. Using the length of the spin magnetization vector to define the spin density restores rotational invariance in spin space.^[275,331] The XC potential in a non-collinear generalized Kohn–Sham (GKS) ansatz reads

$$\begin{aligned} \mathbf{V}_{XC}[M_0(\mathbf{r}), M_i(\mathbf{r})] &= \frac{\delta E_{XC}[M_0(\vec{r}), \rho_i(\vec{r})]}{\delta M_0(\mathbf{r})} + \vec{\sigma}_i \frac{\delta E_{XC}[M_0(\vec{r}), M_i(\vec{r})]}{\delta M_i(\vec{r})} \\ &= \begin{pmatrix} \mathbf{V}_{XC}^0 + i\mathbf{V}_{XC}^z & \mathbf{V}_{XC}^x - i\mathbf{V}_{XC}^y \\ \mathbf{V}_{XC}^x + i\mathbf{V}_{XC}^y & \mathbf{V}_{XC}^0 - i\mathbf{V}_{XC}^z \end{pmatrix} = \begin{pmatrix} \mathbf{V}_{XC}^{\alpha\alpha} & \mathbf{V}_{XC}^{\alpha\beta} \\ \mathbf{V}_{XC}^{\beta\alpha} & \mathbf{V}_{XC}^{\beta\beta} \end{pmatrix}. \end{aligned} \quad (3.52)$$

Here, the numerical integration requires the four density matrices \mathbf{M}_0 and \mathbf{M}_i . The extension is carried out based on an UKS implementation as discussed in detail in Ref. 274. The Kohn–Sham–Fock matrix becomes

$$F_{KS} = \begin{pmatrix} \mathbf{h}^0 + i\mathbf{h}_{SO}^z & \mathbf{h}_{SO}^x - i\mathbf{h}_{SO}^y \\ \mathbf{h}_{SO}^x + i\mathbf{h}_{SO}^y & \mathbf{h}^0 - i\mathbf{h}_{SO}^z \end{pmatrix} + \begin{pmatrix} \mathbf{J} + \mathbf{V}_{XC}^{\alpha\alpha} & \mathbf{V}_{XC}^{\alpha\beta} \\ \mathbf{V}_{XC}^{\beta\alpha} & \mathbf{J} + \mathbf{V}_{XC}^{\beta\beta} \end{pmatrix}. \quad (3.53)$$

3.5 Density Functional Approximations

As the exact analytical form of the exchange–correlation potential is not known, approximations are introduced. These are classified according to Jacob’s ladder, which forms the path from Hartree theory or the “Hartree hell” with neither exchange nor correlation to chemical accuracy, where energy predictions are in the range of ± 1 kJ/mol with respect to the exact result.^[126] Currently, the first five rungs are defined as:^[124,125]

1. Local spin-density approximation (LSDA)
2. Generalized gradient approximation (GGA)
3. Meta-generalized gradient approximation (meta-GGA)
4. Hybrid functionals
5. Double hybrid functionals

The first three rungs represent the “pure” density functional approximations, where the exchange correlation functional depends on the density and its derivatives only. Hybrid functionals incorporate exact Hartree–Fock exchange. This can be done with either a fixed amount of HF exchange in the global hybrid functionals^[127] or based on range-separation with a larger amount of exchange for the long-range region in the so-called range-separated hybrid (RSH) functionals.^[131,133] Alternatively, a fully local amount of HF exchange can be used with functionals dubbed local hybrid functionals (LHFs).^[135] Double hybrid functionals^[333] include the unoccupied orbitals in the functional approximation by introducing terms of second-order Møller–Plesset perturbation (MP2) theory^[334] or the random phase approximation (RPA).^[335] Double hybrid functionals

show a formal scaling of $\mathcal{O}(N^5)$ and their self-consistent implementation is significantly more involved compared to hybrid functionals.^[336] Therefore, double hybrid functionals will not be considered herein. In the following, the first four rungs will be briefly described. For simplicity, we will focus on the exchange contribution and consider the UKS formalism. The GKS expressions are obtained by replacing the one-component Kohn–Sham MOs, $\{\psi_i\}$, with the two-component spinors, $\{\varphi_i\}$, and using the total density and the spin vector density of Eq. 3.51.

3.5.1 Local Spin-Density Approximation

The local spin-density approximation is based on the considerations of the Thomas–Fermi–Dirac model. It is assumed that the exchange–correlation potential and the energy solely depend on the density. The exchange contribution is given by Dirac’s expression

$$E_X^{\text{LSDA}}[\rho_\sigma(\vec{r})] = \sum_\sigma \int \epsilon_{X,\sigma}^{\text{LSDA}} d\vec{r} = \sum_\sigma -\frac{3}{4} \left(\frac{3}{\pi}\right)^{1/3} \int \rho_\sigma(\vec{r})^{4/3} d\vec{r} \quad (3.54)$$

and the correlation part is obtained by Monte–Carlo simulations of the homogeneous electron gas as shown by Vosko, Wilk, and Nusair.^[337] The combination of these two terms forms the S-VWN functional.

3.5.2 Generalized Gradient Approximation

The LSDA shows large errors for chemical systems and is therefore inappropriate in their description. To arrive at an improvement, the inhomogeneities in the density need to be addressed. This is most easily done by a Taylor expansion based on the density and the first correction is obtained with the density gradient, $\vec{\nabla}\rho_\sigma$. However, a simple expansion with the reduced spin density gradient, $s_\sigma = \frac{|\vec{\nabla}\rho_\sigma|}{\rho_\sigma^{4/3}}$, leads to issues for the asymptotic limit. Becke suggested to calculate the GGA exchange energy with the inhomogeneity correction factor^[338]

$$g_{X,\sigma}^{\text{GGA}} = 1 + c_X u_\sigma = 1 + c_X \frac{\gamma s_\sigma^2}{1 + \gamma s_\sigma^2}, \quad (3.55)$$

where γ and c_X are optimized parameters. Therefore, the GGA exchange energy may be generally written as^[339]

$$E_X^{\text{GGA}} = \sum_\sigma \int \epsilon_{X,\sigma}^{\text{LSDA}} g_{X,\sigma}^{\text{GGA}} d\vec{r}, \quad (3.56)$$

$$g_{X,\sigma}^{\text{GGA}} = \sum_j c_{X,j} u_\sigma^j. \quad (3.57)$$

Here $g_{X,\sigma}^{\text{GGA}}$ is given as a polynomial series. Popular functionals of this class are BP86,^[128,340] PBE,^[341] BLYP,^[128,129] and the NMR-optimized KT3 functional.^[342]

3.5.3 Meta-Generalized Gradient Approximation

The expansion can be carried out further to consider the Laplacian, $\vec{\nabla}^2\rho_\sigma$, or the kinetic energy density, τ_σ ,^[343] which is formally related to the Laplacian by^[344]

$$\tau_\sigma = \frac{\vec{\nabla}^2\rho_\sigma}{2} = \frac{1}{2} \sum_j |\hat{p} \psi_{j,\sigma}|^2. \quad (3.58)$$

Note that the inclusion of the kinetic energy density requires additional care for the calculation of magnetic properties as discussed in chapter 7. The functional form of the meta-GGA functionals are commonly written with the dimensionless variables^[345]

$$t_\sigma = \frac{5}{6} (6\pi^2)^{2/3} \frac{\rho_\sigma^{5/3}}{\tau_\sigma} \quad \text{and} \quad w_\sigma = \frac{t_\sigma - 1}{t_\sigma + 1}. \quad (3.59)$$

Similar to the GGAs, the general form of a meta-GGAs (mGGAs) can be cast into an expression with a polynomial series^[125]

$$E_X^{\text{mGGA}} = \sum_\sigma \int \epsilon_{X,\sigma}^{\text{LSDA}} g_{X,\sigma}^{\text{mGGA}} d\vec{r}, \quad (3.60)$$

$$g_{X,\sigma}^{\text{mGGA}} = \sum_{i,j} c_{X,ij} w_\sigma^i u_\sigma^j. \quad (3.61)$$

Popular functionals of this rung are TPSS,^[346] SCAN,^[347] and the Minnesota functionals.^[348]

3.5.4 Global and Range-Separated Hybrid Density Functionals

The GGA and meta-GGA functionals provide a significant improvement upon LSDA functionals. Yet, “pure” density functionals show a self-interaction error. While in HF theory the Coulomb and exchange integrals in Eqs. 3.11–3.15 cancel each other for $i = j$, this is not necessarily the case when replacing \mathbf{K} by one of the previously discussed expressions for E_X . Moreover, GGA functionals slightly overestimate the atomization energies whereas HF dramatically underestimates the atomization energies. Thus, Becke suggested to combine HF and DFT in global hybrid density functionals^[349,350]

$$E_{XC}^{\text{GH}} = c_X E_X^{\text{HF}} + (1 - c_X) E_X^{\text{DFT}} + c_{\text{opp}} E_C^{\text{DFT,opp}}(\vec{r}) + c_{\text{par}} E_C^{\text{DFT,par}}(\vec{r}). \quad (3.62)$$

c_X is a fixed parameter while the coefficients c_{opp} and c_{par} consider the correlation of electrons with opposite and parallel spin orientation. The sum of the two correlation contributions results in the total correlation energy, E_C^{DFT} . Global hybrid functionals are formally motivated with the adiabatic connection.^[351–354] Popular functionals of this rung are the BH&HLYP (50 % HF exchange),^[128,129,350] B3LYP (20 % HF exchange),^[128–130] PBE0 (25 % HF exchange),^[355] and the TPSSh functional (10 % HF exchange).^[356] However, the amount of HF exchange in these functionals is too small to completely cancel the self-interaction error—especially in the long range region. Therefore, range-separation is introduced.^[357,358] Here the Coulomb operator is divided into a short range (sr) and a long range (lr) region according to

$$\frac{1}{|\vec{r}_1 - \vec{r}_2|} = \frac{1 - \text{erf}(\omega|\vec{r}_1 - \vec{r}_2|)}{|\vec{r}_1 - \vec{r}_2|} + \frac{\text{erf}(\omega|\vec{r}_1 - \vec{r}_2|)}{|\vec{r}_1 - \vec{r}_2|} \quad (3.63)$$

with the range-separation parameter ω . This is also called Coulomb attenuating method (CAM) as the Coulomb operator of the short-range part is attenuated by the complementary error function and the long-range part is attenuated by the error function itself.^[357] The general functional form reads^[125]

$$E_{XC}^{\text{RSH}} = c_{X,\text{sr}} E_{X,\text{sr}}^{\text{HF}} + c_{X,\text{lr}} E_{X,\text{lr}}^{\text{HF}} + (1 - c_{X,\text{sr}}) E_{X,\text{sr}}^{\text{DFT}} + (1 - c_{X,\text{lr}}) E_{X,\text{lr}}^{\text{DFT}} + E_C^{\text{DFT}}. \quad (3.64)$$

Setting $c_{X,\text{lr}} = 1$ removes the self-interaction error of the exchange part. Frequently used RSH functionals are LC- ω PBE,^[359] ω B97X-D,^[360] CAM-B3LYP,^[133] CAM-QTP-00,^[361] and CAM-QTP-02.^[362]

3.5.5 Local Hybrid Density Functionals

Local hybrid functionals constitute a more general hybrid density functional approximation with a position-dependent admixture of HF exchange based on a local mixing function (LMF), $a(\vec{r})$, according to^[135]

$$E_{\text{XC}} = \sum_{\sigma} \int \rho_{\sigma}(\vec{r}) [(1 - a_{\sigma}(\vec{r})) e_{\text{X},\sigma}^{\text{DFT}}(\vec{r}) + a_{\sigma}(\vec{r}) e_{\text{X},\sigma}^{\text{HF}}(\vec{r})] d\vec{r} + E_{\text{C}}^{\text{DFT}}. \quad (3.65)$$

Here, a spin-dependent LMF was assumed. Note that spin-independent as well as spin-dependent LMFs were suggested. The impact of a spin-independent LMF on Eq. 3.65 will be discussed below for the t-LMF based local hybrid functionals. Yet, the ansatz of a spin-independent LMF is not restricted to this local mixing function.

The HF exchange expression is obtained as

$$E_{\text{X}}^{\text{HF}} = \int e_{\text{X}}^{\text{HF}}(\vec{r}) \rho(\vec{r}) d\vec{r}. \quad (3.66)$$

Perdew *et al.* motivated LHF by observing that semilocal density functionals work well in some regions but fail or perform poorly in others. Therefore, the molecule is divided into a “normal” and an “abnormal” region.^[134] In contrast to range-separated functionals, the LHF feature a smoother variation of the incorporation of HF exchange. However, the integration for the LHF is significantly more involved than for global and range-separated hybrid functions. The HF exchange integrals are typically evaluated analytically in quantum chemistry codes whereas the integration for the XC parts is done numerically. Therefore, Plessow and Weigend suggested to apply the seminumerical exchange approximation of Sec. 3.3 to LHF.^[305] With this approximation, all contributions of Eq. 3.65 are calculated numerically on a grid. This allows for a simultaneous evaluation of the exchange and the correlation parts. In the semiK approximation, the term

$$e_{\text{X},\sigma}^{\text{HF}}(\vec{r}_1) \rho_{\sigma}(\vec{r}_1) = -\frac{1}{2} \sum_{pqrs} D_{pq}^{\sigma} D_{rs}^{\sigma} \int \frac{\lambda_{\mu}^*(\vec{r}_1) \lambda_{\kappa}(\vec{r}_1) \lambda_{\nu}^*(\vec{r}_2) \lambda_{\eta}(\vec{r}_2)}{|\vec{r}_1 - \vec{r}_2|} d\vec{r}_2 \quad (3.67)$$

is calculated analytically. The remaining integration is carried out numerically on a grid

$$E_{\text{X, HF}}^{\text{LHF}} = \sum_{\sigma} \sum_g w_g a(\vec{r}_g) e_{\text{X},\sigma}^{\text{HF}}(\vec{r}_g) \rho_{\sigma}(\vec{r}_g). \quad (3.68)$$

In the original implementation of Plessow and Weigend,^[305] the energy was not calculated in a self-consistent way but based on the HF orbitals. This implementation was later extended to allow for self-consistent calculations^[363] and applied to geometry gradients^[364] based on the existing seminumerical energy derivatives.^[284,305] Jaramillo and co-workers suggested a local mixing function based on the iso-orbital indicator^[135] and subsequently various LMFs were proposed, see Refs. 132 and 137 for an overview. In the following, we will consider LMFs based on the iso-orbital indicator (t-LMF), the correlation length (z-LMF), and the second-order Görling–Levy perturbation limit (PSTS-LMF). This comparison is based on Ref. 365.

LMF Based on the Iso-Orbital Indicator

The most frequently used ansatz for the local mixing function $a(\vec{r})$ is based on the iso-orbital indicator of the original LH-BLYP functional.^[135] In an UKS formalism, the t-LMF reads

$$\text{t-LMF: } a_{\sigma}(\vec{r}) = c_t \frac{\tau_{\sigma}^{\text{vW}}}{\tau_{\sigma}} = c_t \frac{|\vec{\nabla}\rho_{\sigma}|^2}{8\rho_{\sigma}\tau_{\sigma}}, \quad (3.69)$$

where τ^{vW} is the von Weizsäcker approximation to the kinetic energy density,^[366] and τ is the kinetic energy density used for meta-GGAs. The fixed factor c_t controls the maximum amount of Hartree–Fock exchange. In one-electron regions, the von Weizsäcker approximation will be equal to the kinetic energy density, $\tau^{\text{vW}} = \tau$. Thus, 100 % HF exchange can be incorporated to fully cancel the self-interaction error. Note that many LMFs of the Kaupp group do not use 100 % HF exchange in the one-electron regions to improve the thermochemical properties. For instance, the LH07t-SVWN^[138] and LH12ct-SsirPW92 functional^[139] use $c_t = 0.48$ and $c_t = 0.646$, respectively. LH12ct-SsirPW92 and LH20t feature a spin-independent or so-called “common” LMF. In a common LMF, all spin quantities are replaced by the total quantities. For most quantities, this means that simply the sum is formed, however, this is not true for the von Weizsäcker approximation to the kinetic energy density as due to the denominator the total quantity is not generally the sum of the two spin-resolved contributions, $\tau_{\alpha}^{\text{vW}}$ and τ_{β}^{vW} . Unlike for the correlation energy, which is the sum of the opposite and parallel spin channels, Eq. 3.65 neglects the α - β cross terms due to the index σ and the respective summation for the exchange energy. The common LMF consists of the α and β spin variables and therefore introduces the coupling terms in a simple manner. The total energy of a common LMF reads

$$E_{\text{XC}} = \int d\vec{r} \sum_{\sigma=\alpha,\beta} \rho_{\sigma}(\vec{r}) [(1 - a(\vec{r})) e_{\text{X},\sigma}^{\text{DFT}}(\vec{r}) + a(\vec{r}) e_{\text{X},\sigma}^{\text{HF}}(\vec{r})] + E_{\text{C}}^{\text{DFT}}(\vec{r}) \quad (3.70)$$

with the common t-LMF

$$a(\vec{r}) = c_t \frac{\tau^{\text{vW}}}{\tau} = c_t \frac{|\vec{\nabla}\rho|^2}{8\rho\tau} = c_t \frac{|\vec{\nabla}\rho_{\alpha}|^2 + 2\vec{\nabla}\rho_{\alpha} \cdot \vec{\nabla}\rho_{\beta} + |\vec{\nabla}\rho_{\beta}|^2}{8(\rho_{\alpha} + \rho_{\beta})(\tau_{\alpha} + \tau_{\beta})}. \quad (3.71)$$

The idea of a common LMF is not restricted to the t-LMF. We note in passing that the spin cross terms may be also considered with a LMF depending on the spin polarization^[367] in the spirit of Becke’s B05 functional,^[368,369] however, this ansatz has stirred less interest than the common LMF. Popular functionals of this class are the original local hybrid functional LH-BLYP and the LH07t-SVWN,^[138] LH12ct-SsirPW92,^[139] LH14ct-calPBE,^[140] and LH20t^[370] functionals of the Kaupp group. Among these, the LH12ct-SsirPW92 and LH20t functional employ a common t-LMF.

LMFs Based on the Correlation Length

Another suitable indicator for the LMF is the correlation length as shown by Johnson.^[141] Here, the exchange energy is expressed with the exchange potential, U_{X} , as

$$E_{\text{X}}^{\text{DFT}} = \sum_{\sigma} \int \rho_{\sigma} U_{\text{X},\sigma} d\vec{r}. \quad (3.72)$$

The exchange potential is defined with the exchange hole, h_{X} ,

$$U_{\text{X},\sigma} = \int \frac{1}{s} |h_{\text{X},\sigma}(\vec{r}, s)| ds. \quad (3.73)$$

The correlation length is obtained with the inverse of the exchange potential^[371]

$$z_{\sigma\sigma'} = c_{\sigma\sigma'} (|U_{X,\sigma}|^{-1} + |U_{X,\sigma'}|^{-1}) \quad (3.74)$$

with $c_{\alpha\beta} = 0.63$ and $c_{\sigma\sigma} = 0.88$.^[371] For the HF exchange contribution of LHF, only the parallel spin orientation was considered. This means that the α - β cross terms in Eq. 3.70 are neglected. The respective z-LMF is constructed with the error function of the correlation length to obtain a smoothly varying function between 0 and 1. Note that the correlation length itself may yield values outside this range. The respective z-LMF is defined as

$$a_{\sigma}(\vec{r}) = \text{erf}(c_z z_{\sigma\sigma}). \quad (3.75)$$

Similar to c_t , the parameter c_z controls the maximum amount of HF exchange. The only functional optimized with this z-LMF is Johnson's local hybrid functional^[141] based on the B88 exchange^[128] and correlation.^[371] Herein, we will refer to this functional as LHJ14. The empirical parameter c_z was optimized with the G3 test set^[372] consisting of 222 atomization energies. This yields $c_z = 0.10$ and the optimized parameters for the dynamic correlation are $c_{\text{opp}} = 1.156$ and $c_{\text{par}} = 1.472$.

PSTS Local Hybrid Functional

A considerably more involved LMF was suggested by Perdew, Staroverov, Tao, and Scuseria (PSTS) based on the TPSS functional.^[134] For the PSTS functional, the local mixing function consists of two contributions according to

$$a(\vec{r}) = 1 - [1 - a_1(\vec{r})][1 - a_2(\vec{r})] \quad (3.76)$$

The first LMF a_1 considers regions where exchange should dominate and the second LMF a_2 is optimized for regions where the hole density does not integrate to -1 . The first LMF, $a_1(\vec{r})$, is defined as

$$a_1(\vec{r}) = \frac{1}{1 + A \ln(1 + Bu)}; \quad u = \frac{e_{\text{C}}^{\text{GL2-TPSS}}}{e_{\text{X}}^{\text{LSDA}}}, \quad (3.77)$$

where $e_{\text{C}}^{\text{GL2-TPSS}}$ is the second order Görling–Levy perturbation (GL2) limit^[373] of the TPSS correlation.^[346] A and B are thermochemically optimized constants described below. The LMF a_1 is able to detect the one-electron regions in a molecule and increases the amount of exchange to cancel the self-interaction error.

The second LMF a_2 incorporates spin polarization based on the ratio of HF exchange and TPSS exchange according to

$$a_2(\vec{r}) = g\left(\frac{\zeta^2}{r_s}\right) f(v); \quad v = \frac{e_{\text{X}}^{\text{HF}}}{e_{\text{X}}^{\text{TPSS}}}. \quad (3.78)$$

Note that the inclusion of the spin polarization in the PSTS LMF conceptually differs from inclusion of the spin polarization as an additional variable to consider the α - β spin cross terms.^[367] In Eq. 3.78, ζ denotes the relative spin polarization

$$\zeta = \frac{\rho_{\alpha} - \rho_{\beta}}{\rho_{\alpha} + \rho_{\beta}} \quad (3.79)$$

and the uniform gas is considered, i.e. $\rho = 3/4\pi r_s^3$ was assumed to calculate r_s . The function $g(x)$ is defined as

$$g(x) = \frac{Dx}{1 + Ex} \quad (3.80)$$

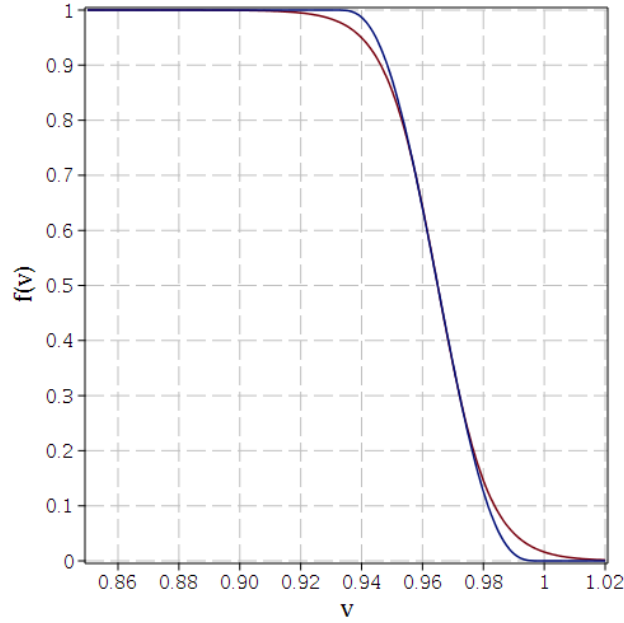


Figure 3.1: Comparison of choices for $f(v)$ in Eq. 3.83 (red) and Eq. 3.81 (blue). The latter was originally used in Ref. 134 (blue). Taken from Ref. 365.

with the empirical parameters D and E . The function $f(v)$ was chosen to be

$$f(v) = \begin{cases} 1 & \text{if } v \leq C \\ \frac{1}{1 + \exp[1/(1-v)^F - 1/(v-C)^F]} & \text{if } C < v < 1 \\ 0 & \text{if } v \geq 1 \end{cases} \quad (3.81)$$

with the empirical parameter C and

$$F = -\frac{3}{2 \ln[(1-C)/2]} > 0. \quad (3.82)$$

Note that very few implementations of the Perdew-Staroverov-Tao-Scuseria (PSTS) LHF besides the original not self-consistent implementation have been reported.^[374,375] This may be due to the significantly more complicated functional form but also due to the choice of the function f , which may result in numerical instabilities for derivatives. Therefore, Holzer suggested to approximate $f(v)$ as

$$f(v) = 0.5 - 0.5 \tanh\left(\frac{v - 0.5(1+C)}{0.017}\right) \quad (3.83)$$

resulting in the modified PSTS (mPSTS) functional.^[365] Fig. 3.1 shows that the two choices for $f(v)$ are very similar. Note that the LMF a_2 vanishes everywhere for closed-shell systems and therefore mPSTS and PSTS become identical.

The parameters A , B , C , D , and E are optimized with the 148 standard enthalpies of formation of the G2/97 test set^[376] and the 53 reaction barrier heights of the BH2/03 test set.^[377] This yields the parameters $A = 3.14$, $B = 146$, $C = 0.930$, $D = 5.17$, and $E = 9.49$.^[134]

Gauge Transformation of Local Hybrid Functionals

Tao *et al.* pointed out that the energy density $\rho(\vec{r})\epsilon_{xc}(\vec{r})$ is not unique.^[378] The exact-exchange energy density can be modified by a gauge transformation term, $G(\vec{r})$,

$$e_X^{\text{HF,DFT}}(\vec{r}) = e_X^{\text{HF}}(\vec{r}) + G(\vec{r}). \quad (3.84)$$

To ensure that the total energy is unchanged by the gauge transformation, $G(\vec{r})$ must satisfy the condition

$$\int G(\vec{r})\rho(\vec{r}) d\vec{r} = 0. \quad (3.85)$$

Tao *et al.* suggested that $G(\vec{r})$ should be chosen so that $e_X^{\text{HF,DFT}}(\vec{r})$ is as close as possible to the semilocal exchange-energy density in atoms.^[378] Yet, most local hybrid functionals do not consider the gauge transformation term. The LH14ct-calPBE^[140] and LH20t^[370] local hybrid functionals introduce a gauge transformation term or calibration function. Here, the exchange-correlation energy is generalized to

$$E_{\text{XC}} = \sum_{\sigma} \int \rho_{\sigma}(\vec{r}) [(1 - a_{\sigma}(\vec{r})) \{e_{X,\sigma}^{\text{DFT}}(\vec{r}) + G_{\sigma}(\vec{r})\} + a_{\sigma}(\vec{r})e_{X,\sigma}^{\text{HF}}(\vec{r})] d\vec{r} + E_C^{\text{DFT}}(\vec{r}). \quad (3.86)$$

However, the calibration functions proposed by the Kaupp group are numerically demanding and often worsen the SCF convergence behavior.^[370] Self-consistent implementations of the LH-BLYP, LH07t-SVWN, LH12ct-SsirPW92, PSTS, mPSTS, and LHJ14 functionals use the conventional gauge instead and neglect the calibration function. Note that for PSTS a gauge transformed formulation was used in the not self-consistent calculations based on TPSS orbitals.^[134] The respective optimized parameters are $A = 2.7$, $B = 132$, $C = 0.940$, $D = 6.13$, and $E = 8.02$.

4 NMR Shieldings and Shifts in Scalar-Relativistic X2C Theory

NMR shifts with the scalar-relativistic X2C Hamiltonian were first presented by Cheng *et al.*^[101] and later the ansatz was generalized to account for spin-orbit coupling.^[102,103] The presented approaches utilize HF or CC theory and are restricted to rather small molecules due to the associated computational costs of both the one and two-electron terms. Furthermore, they do not account for the finite nuclear size of the vector potential and the scalar potential. Herein, efficiency is ensured by the DLU scheme in a DFT framework and the finite nucleus model is used throughout all integrals. NMR shifts are implemented in a scalar-relativistic approximation.^[379] The scalar-relativistic approximation is sufficient for molecules, where the bonding is dominated by p orbitals^[380–382] such as in organometallic alkynyl compounds^[383] and xenon fluorides.^[101] Moreover, it is sufficient for transition-metal oxo molecules and many halogen-free tin compounds.^[12,384] If the bonding contains considerable contribution of s orbitals, the Fermi-contact interaction dominates and a spin-orbit approach is required for an accurate prediction of NMR shieldings and shifts. The impact of a heavy atom on the NMR shifts of neighboring light atoms is described in more detail in Ref. 385.

The chapter is structured as follows. After an introduction to the basic concepts of relativistic NMR shielding calculations in Sec. 4.1 and 4.2, the DLU-X2C is fully derived in the following sections. This includes a complete derivation of the underlying X2C ansatz for the atomic diagonal blocks. The scalar-relativistic one-electron part is connected to the DFT framework using the coupled-perturbed Kohn–Sham equations in Sec. 4.7. Furthermore, the implementation can be used to calculate the magnetically induced current density as shown in Sec. 4.8.

4.1 NMR Shielding Tensor, Vector Potential, and Gauge-Including Atomic Orbitals

Magnetic fields are introduced into the Dirac equation by the generalized momentum operator according to the principle of minimal coupling^[386]

$$\hat{p} \longrightarrow \hat{\pi} = \hat{p} + \frac{1}{c} \hat{A}. \quad (4.1)$$

Therefore, the linear momentum operator, \hat{p} , is replaced with its generalization, $\hat{\pi}$. In magnetostatics, the vector potential is generally defined as^[387,388]

$$\vec{A}(\vec{r}) = \int \frac{\vec{j}(\vec{r}')}{|\vec{r} - \vec{r}'|} d\vec{r}' \quad (4.2)$$

with the current density \vec{j} . The corresponding magnetic field is obtained as

$$\vec{B}(\vec{r}) = \text{rot}(\vec{A}) = \vec{\nabla} \times \vec{A}. \quad (4.3)$$

For a static and homogeneous external magnetic field, the vector potential becomes

$$\vec{A}_O^B(\vec{r}) = \frac{1}{2} \vec{B} \times \vec{r}_O \quad \text{with} \quad \vec{r}_O = \vec{r} - \vec{R}_O, \quad (4.4)$$

where O denotes the gauge origin, which will be discussed in more detail below. The magnetic field is uniquely defined by the vector potential but the opposite is not true. The vector potential may be changed by a gauge transformation, that is a term $\vec{\nabla}g$ can be added to the vector potential without changing the magnetic field as the rotation of this term is zero, where g is an arbitrary scalar function. Quantum chemistry commonly employs the Coulomb gauge^[6–10]

$$\text{div}(\vec{A}) = \vec{\nabla} \cdot \vec{A} = 0. \quad (4.5)$$

Therefore, the linear momentum operator and the vector potential commute. We note in passing that the Coulomb gauge is not strictly Lorentz invariant. For molecules, the nuclei need to be further considered. The vector potential associated with the nuclear magnetic moments, \vec{m}_I , is given as^[389]

$$\vec{A}_I^m(\vec{r}) = -\vec{m}_I \times \vec{\nabla} G_I(\vec{r}) \quad \text{with} \quad G_I(\vec{r}) = \int \frac{w_I(\vec{R}_I)}{|\vec{r} - \vec{R}_I|} d\vec{R}, \quad (4.6)$$

where a finite charge distribution is assumed. Here, w_I is a weight function describing the finite nuclear size and the shape of the nucleus. Note that $\vec{\nabla}$ refers to the electronic coordinates. The weight function is required to be normalized. Choosing a Gaussian charge distribution as outlined in Sec. 2.2 leads to

$$w_I(\vec{R}_I) = \left(\frac{\eta}{\pi}\right)^{3/2} \exp\left(-\zeta(\vec{R} - \vec{R}_I)^2\right). \quad (4.7)$$

Hennum *et al.*^[390] showed that this expression may be simplified using the lower incomplete gamma function, $P(\frac{1}{2}, \zeta r_I^2)$, to facilitate the integral evaluation according to

$$\vec{A}_I^m(\vec{r}) = \vec{m}_I \times \vec{\nabla}_I \mathcal{G}_I = \vec{m}_I \times \vec{\nabla}_I \left(\frac{P(\frac{1}{2}, \zeta \vec{r}_I^2)}{|\vec{r}_I|} \right), \quad (4.8)$$

where $\vec{\nabla}_I$ acts upon the nuclear coordinates. The lower incomplete gamma function is defined as

$$P(a, x) = \frac{1}{\Gamma(a)} \int_0^x t^{a-1} e^{-t} dt \quad \text{with} \quad \Gamma(a) = \int_0^\infty t^{a-1} e^{-t} dt. \quad (4.9)$$

The point-charge model is obtained for $\zeta \rightarrow \infty$, which is equal to $\mathcal{G}_I = 1/|r_I|$. The vector potential then reduces to the well known form

$$\vec{A}_I^m(\vec{r}) = \frac{\vec{m}_I \times \vec{r}_I}{|\vec{r}_I|^3}. \quad (4.10)$$

The total vector potential is simply the sum of the contribution of the magnetic field and the nuclear magnetic moments

$$\vec{A} = \vec{A}^B + \vec{A}^m = \vec{A}^B + \sum_I^N \vec{A}_I^m. \quad (4.11)$$

Consequently, the total energy depends on the external magnetic field and the nuclear magnetic moments. The energy may be written with a Taylor expansion

$$\begin{aligned}
 E(\vec{B}, \vec{m}_I) = & E(0) + \sum_u \frac{\partial E}{\partial B_u} \Big|_{\vec{B}=0} B_u + \sum_N \sum_u \frac{\partial E}{\partial m_u^N} \Big|_{\vec{m}^N=0} m_u^N \\
 & + \frac{1}{2} \sum_{u,v} \frac{\partial^2 E}{\partial B_u \partial B_v} \Big|_{\vec{B}=0} B_u B_v + \sum_N \sum_{u,v} \frac{\partial^2 E}{\partial B_u \partial m_v^N} \Big|_{\vec{B}, \vec{m}^N=0} B_u m_v^N \\
 & + \frac{1}{2} \sum_{N,N'} \sum_{u,v} \frac{\partial^2 E}{\partial m_u^N \partial m_v^{N'}} \Big|_{\vec{m}^N=0} m_u^N m_v^{N'}.
 \end{aligned} \tag{4.12}$$

Here, the first-order terms are the Zeeman and the hyperfine coupling interaction, respectively. The second-order terms are the magnetizability tensor, the NMR shielding tensor, and the NMR indirect spin–spin coupling tensor. In this chapter, we only consider the NMR shielding tensor whereas the next chapter deals with the NMR coupling tensor. The Schwarz theorem holds for the second-order terms thus the NMR shielding tensor may be defined as

$$\sigma_{vu}^I = \frac{\partial^2 E}{\partial B_u \partial m_{I,v}} \Big|_{\vec{B}, \vec{m}^N=0} \quad \text{with } u, v \in \{x, y, z\}. \tag{4.13}$$

Forming the trace of the shielding tensor results in the isotropic shielding constant

$$\sigma^I = \frac{1}{3} \left(\sigma_{xx}^I + \sigma_{yy}^I + \sigma_{zz}^I \right). \tag{4.14}$$

The anisotropy of the shielding tensor is defined as

$$\Delta\sigma^I = \sqrt{\frac{3}{2} \left(\frac{1}{4} \sum_{u,v} (\sigma_{uv}^I + \sigma_{vu}^I)^2 - 3(\sigma^I)^2 \right)}. \tag{4.15}$$

A straightforward calculation of the NMR shielding tensor will depend on the gauge origin due to the vector potential of the external magnetic field. However, the results are required to be independent of the gauge origin as it contains no physical meaning. Therefore, the dependence will vanish in the limit of a complete basis set. However, calculations with the complete basis set limit are impractical and the gauge origin is removed by including a phase factor in the one-electron basis functions

$$\lambda_\mu(\vec{B}, \vec{r}) = \exp(-i\Lambda_{\mu O}) \lambda_\mu(\vec{r}). \tag{4.16}$$

This was first suggested by London^[391] and later applied to quantum chemistry by Ditchfield.^[392–394] The complex phase factor is defined as

$$\Lambda_{\mu O}(\vec{B}, \vec{r}) = \frac{1}{2c} (\vec{R}_{\mu O} \times \vec{r}) \cdot \vec{B} \tag{4.17}$$

where $\vec{R}_{\mu O} = \vec{R}_\mu - \vec{R}_O$. As these basis functions explicitly include the gauge origin, they are called gauge-including atomic orbitals (GIAOs). Matrix elements with these basis functions do not depend on the gauge origin as shown exemplarily for the overlap matrix

$$\begin{aligned} \mathbf{S}_{\mu\nu}(\vec{B}, \vec{r}) &= \langle \lambda_\mu(\vec{B}, \vec{r}) | \lambda_\nu(\vec{B}, \vec{r}) \rangle \\ &= \langle \lambda_\mu | e^{i\Lambda_{\mu\nu}} | \lambda_\nu \rangle = \int \exp\left[\frac{i}{2c}(\vec{R}_{\mu\nu} \times \vec{r})\right] \lambda_\mu^*(\vec{r}) \lambda_\nu(\vec{r}) d\vec{r}. \end{aligned} \quad (4.18)$$

Throughout this work, GIAOs will be denoted by explicitly field-dependent basis functions, $\lambda_\nu(\vec{B}, \vec{r})$. Compared to the field-free basis functions, the GIAOs necessitate additional integral derivatives to calculate the NMR shielding tensor of Eq. 4.13 as the one-electron and the two-electron integrals depend on the magnetic field. The NMR shielding tensor with GIAOs in a one-component ansatz reads

$$\sigma_{vu}^I = \left(\frac{\partial^2 E}{\partial B_u \partial m_{I,v}} \right)_0 = \text{tr} \left(\mathbf{D} \frac{\partial^2 \mathbf{h}}{\partial B_u \partial m_{I,v}} \right)_0 + \text{tr} \left(\frac{\partial \mathbf{D}}{\partial B_u} \frac{\partial \mathbf{h}}{\partial m_{I,v}} \right)_0, \quad (4.19)$$

where all derivatives are formed in the limit of a vanishing perturbation as indicated by $(\dots)_0$. First taking the derivative with respect to the nuclear magnetic moments and then forming the derivative with respect to the magnetic field reduces the computational effort as only three perturbed density matrices, $\partial \mathbf{D} / \partial B_u$, have to be calculated. To arrive at a (scalar-relativistic) gauge-invariant X2C formalism for NMR shieldings, the following steps are necessary.

1. Set up the Dirac matrix in the presence of a magnetic field and the nuclear magnetic moments with GIAOs.
2. Form the one-electron integral derivatives and separate the terms into the spin-free and the spin-dependent contributions.
3. Calculate the derivatives of the decoupling and the renormalization matrix.

This allows to evaluate the three one-electron Hamiltonian derivatives, i.e. $\partial \mathbf{h} / \partial B_u$, $\partial \mathbf{h} / \partial m_v$, and $\partial^2 \mathbf{h} / \partial B_u \partial m_{I,v}$. The derivative of the X2C Hamiltonian with respect to the magnetic field is required to calculate the perturbed density matrix as shown in Sec. 4.7.

4.2 Restricted Magnetic Balance Condition and Diamagnetic Contribution

Accounting for magnetic perturbations with the generalized momentum operator leads to the one-electron Dirac operator

$$\hat{h}_D = c\vec{\alpha} \cdot \hat{\vec{\pi}} + (\beta - I_4)c^2 + \hat{V}. \quad (4.20)$$

Next, the Dirac operator has to be expanded in a basis set. This expansion must ensure the correct non-relativistic limit as discussed in Sec. 2.4. Note that the Schrödinger equation contains the generalized momentum in a quadratic or bilinear form and thus describes diamagnetic interactions. The Schrödinger Hamiltonian reads in analogy to Eq. 2.1

$$\hat{h}_S = \frac{1}{2}\hat{\vec{\pi}}^2 + \hat{V} = \frac{1}{2}\hat{p}^2 + \frac{1}{2c}\hat{A} \cdot \hat{p} + \frac{1}{2c}\hat{p} \cdot \hat{A} + \frac{1}{2c^2}\hat{A}^2 + \hat{V}. \quad (4.21)$$

Simply expanding the Dirac Hamiltonian in a restricted kinetically balanced basis set will consequently not ensure the exact non-relativistic limit with finite basis sets. Therefore, the linear momentum operator is generalized in the balance condition.^[49,395] This results in the restricted magnetic balance (RMB) condition^[57]

$$|\phi_\mu^S\rangle = \frac{1}{2c} \left(\vec{\sigma} \cdot \hat{p} + \frac{1}{c} \vec{\sigma} \cdot \hat{A}^B + \frac{1}{c} \vec{\sigma} \cdot \hat{A}^m \right) |\phi_\mu^L\rangle. \quad (4.22)$$

The RMB ensures the variational stability to $\mathcal{O}(c^{-4})$. For NMR shieldings and shifts, it is sufficient to consider the vector potential of the magnetic field only^[101-103] and the basis set expansion is

$$|\psi_i^L\rangle = \sum_\mu c_{\mu i}^L e^{-i\Lambda_{\mu O}} |\phi_\mu\rangle, \quad (4.23)$$

$$|\psi_i^S\rangle = \sum_\mu c_{\mu i}^S e^{-i\Lambda_{\mu O}} \frac{\vec{\sigma} \cdot \left(\hat{p} + \frac{1}{c} \hat{A}_\mu^B \right)}{2c} |\phi_\mu\rangle, \quad (4.24)$$

where we used the identity^[58]

$$\left(\hat{p} + \frac{1}{c} \hat{A}_O^B \right) e^{-i\Lambda_{\mu O}} = e^{-i\Lambda_{\mu O}} \left(\hat{p} + \frac{1}{c} \hat{A}_\mu^B \right). \quad (4.25)$$

The one-electron Dirac equation in the presence of a magnetic perturbation follows as

$$\begin{pmatrix} \mathbf{V} & \mathbf{\Pi}^\dagger \\ \mathbf{\Pi} & \frac{1}{4c^2} \mathbf{W} - \mathbf{T} \end{pmatrix} \begin{pmatrix} \mathbf{C}_-^L & \mathbf{C}_+^L \\ \mathbf{C}_-^S & \mathbf{C}_+^S \end{pmatrix} = \begin{pmatrix} \mathbf{S} & \mathbf{0}_2 \\ \mathbf{0}_2 & \frac{1}{2c^2} \mathbf{T} \end{pmatrix} \begin{pmatrix} \mathbf{C}_-^L & \mathbf{C}_+^L \\ \mathbf{C}_-^S & \mathbf{C}_+^S \end{pmatrix} \begin{pmatrix} \epsilon_- & \mathbf{0}_2 \\ \mathbf{0}_2 & \epsilon_+ \end{pmatrix}, \quad (4.26)$$

where the notation of Cremer *et al.*^[98] is employed for convenience. This order of $-$ and $+$ is consistent with the sorting of the LAPACK routines.^[396] The overlap and potential matrix are still block-diagonal in the two-component space

$$\mathbf{S} = \begin{pmatrix} \mathbf{S} & 0 \\ 0 & \mathbf{S} \end{pmatrix} \quad \text{with} \quad \mathbf{S}_{\mu\nu} = \langle \lambda_\mu | e^{i\Lambda_{\mu\nu}} | \lambda_\nu \rangle, \quad (4.27)$$

$$\mathbf{V} = \begin{pmatrix} \mathbf{V} & 0 \\ 0 & \mathbf{V} \end{pmatrix} \quad \text{with} \quad \mathbf{V}_{\mu\nu} = \langle \lambda_\mu | e^{i\Lambda_{\mu\nu}} \hat{V} | \lambda_\nu \rangle. \quad (4.28)$$

These matrices differ from their parents in Eqs. 2.35 and 2.37 by the use of field-dependent basis functions. The other matrices in Eq. 4.26 depend on the Pauli matrices as they are obtained with the small component basis functions. Thus, the kinetic energy matrix, \mathbf{T} , the generalized momentum matrix, $\mathbf{\Pi}$, and the relativistically modified potential, \mathbf{W} , are not block-diagonal according to

$$\mathbf{T}_{\mu\nu} = \frac{1}{2} \langle \phi_\mu | e^{i\Lambda_{\mu\nu}} [\vec{\sigma} \cdot \left(\hat{p} + \frac{1}{c} \hat{A}_\nu^B \right)] [\vec{\sigma} \cdot \left(\hat{p} + \frac{1}{c} \hat{A}_\nu^B \right)] | \phi_\nu \rangle, \quad (4.29)$$

$$\mathbf{\Pi}_{\mu\nu}^\dagger = \frac{1}{2} \langle \phi_\mu | e^{i\Lambda_{\mu\nu}} [\vec{\sigma} \cdot \left(\hat{p} + \frac{1}{c} \hat{A}_\nu^B + \frac{1}{c} \hat{A}_T^m \right)] [\vec{\sigma} \cdot \left(\hat{p} + \frac{1}{c} \hat{A}_\nu^B \right)] | \phi_\nu \rangle, \quad (4.30)$$

$$\mathbf{\Pi}_{\mu\nu} = \frac{1}{2} \langle \phi_\mu | e^{i\Lambda_{\mu\nu}} [\vec{\sigma} \cdot \left(\hat{p} + \frac{1}{c} \hat{A}_\nu^B \right)] [\vec{\sigma} \cdot \left(\hat{p} + \frac{1}{c} \hat{A}_\nu^B + \frac{1}{c} \hat{A}_T^m \right)] | \phi_\nu \rangle, \quad (4.31)$$

$$\mathbf{W}_{\mu\nu} = \langle \phi_\mu | e^{i\Lambda_{\mu\nu}} [\vec{\sigma} \cdot \left(\hat{p} + \frac{1}{c} \hat{A}_\nu^B \right)] \hat{V} [\vec{\sigma} \cdot \left(\hat{p} + \frac{1}{c} \hat{A}_\nu^B \right)] | \phi_\nu \rangle. \quad (4.32)$$

Note that the Dirac matrix is Hermitian but the large-small, $\mathbf{\Pi}^\dagger$, and the small-large block, $\mathbf{\Pi}$, are not. The quadratic terms in the vector potential solely arise due to the RMB condition and ensure the correct non-relativistic limit of the unperturbed density contribution in Eq. 4.13. This part is often the largest absolute contribution to the NMR shielding tensor. Hence, a proper relativistic and non-relativistic description is of uttermost importance. The use of GIAOs throughout ensures gauge-origin invariance with small basis sets.

4.3 Derivatives of the X2C Hamiltonian and Scalar-Relativistic Approximation

The calculations of the NMR shielding tensors requires the derivative of the Hamiltonian with respect to the magnetic field, the magnetic moments, and the mixed derivative. To begin with, the X2C Hamiltonian in the presence of magnetic fields based on Eqs. 2.53 and 4.26 is considered to identify the terms, which have to be differentiated. The magnetic-field dependent X2C Hamiltonian reads

$$\mathbf{h}^+ \left(\vec{R}, \vec{m}_I \right) = \mathbf{R}^\dagger \left(\vec{R}, \vec{m}_I \right) \mathbf{L}^{\text{NESC}} \mathbf{R} \left(\vec{R}, \vec{m}_I \right), \quad (4.33)$$

where all matrices are evaluated in the limit of a vanishing perturbation. Inserting the explicit expression for the NESC matrix (see also Eq. 2.54) yields

$$\begin{aligned} \mathbf{h}^+ \left(\vec{R}, \vec{m}_I \right) = & \mathbf{R}^\dagger \left(\vec{R}, \vec{m}_I \right) \mathbf{V} \left(\vec{B} \right) \mathbf{R} \left(\vec{R}, \vec{m}_I \right) \\ & + \mathbf{R}^\dagger \left(\vec{R}, \vec{m}_I \right) \left[\mathbf{X}^\dagger \left(\vec{R}, \vec{m}_I \right) \mathbf{\Pi} \left(\vec{R}, \vec{m}_I \right) + \mathbf{\Pi}^\dagger \left(\vec{R}, \vec{m}_I \right) \mathbf{X} \left(\vec{R}, \vec{m}_I \right) \right] \mathbf{R} \left(\vec{R}, \vec{m}_I \right) \\ & + \mathbf{R}^\dagger \left(\vec{R}, \vec{m}_I \right) \left[\mathbf{X}^\dagger \left(\vec{R}, \vec{m}_I \right) \left(\frac{1}{4c^2} \mathbf{W} \left(\vec{B} \right) - \mathbf{T} \left(\vec{B} \right) \right) \mathbf{X} \left(\vec{R}, \vec{m}_I \right) \right] \mathbf{R} \left(\vec{R}, \vec{m}_I \right), \end{aligned} \quad (4.34)$$

where all matrices depend on the magnetic field due to the expansion with GIAOs. According to Eq. 4.34, the derivative of the X2C Hamiltonian depends on the integral derivatives and the derivatives of the decoupling and the renormalization matrix. The derivatives of the latter are required to ensure an exact decoupling in the presence of a perturbation and to obtain the full analytical derivative of the energy with respect to \vec{m}_I and \vec{B} . Note that the derivatives are evaluated in the limit of a vanishing perturbation. For clarity, the derivatives of the Hamiltonian and the one-electron integrals are considered separately in the next subsections and the derivatives of the decoupling and the renormalization matrix are described in Sec. 4.4 and 4.5, respectively. The general derivative of the X2C Hamiltonian with respect to the perturbation λ is given as

$$\mathbf{h}^{+,\lambda} = \mathbf{R}^{\dagger,\lambda} \mathbf{L} \mathbf{R} + \mathbf{R}^\dagger \mathbf{L}^\lambda \mathbf{R} + \mathbf{R}^\dagger \mathbf{L} \mathbf{R}^\lambda, \quad (4.35)$$

where the derivative of the NESC matrix contains the derivative of the decoupling matrix and the one-electron integrals according to the product rule. The superscript of the NESC matrix, \mathbf{L} , is omitted for brevity.

4.3.1 Magnetic Field Derivatives

All one-electron integrals depend on the magnetic field. Therefore, the derivatives of all matrices are required. The potential matrix and the overlap matrix are block-diagonal in the two-component space. Accordingly, the respective scalar-relativistic integral derivatives are

$$\left(\frac{\partial \mathbf{V}_{\mu\nu}}{\partial B_u}\right)_0 = \frac{i}{2c} \langle \lambda_\mu | (\vec{R}_{\mu\nu} \times \hat{r})_u \hat{V} | \lambda_\nu \rangle, \quad (4.36)$$

$$\left(\frac{\partial \mathbf{S}_{\mu\nu}}{\partial B_u}\right)_0 = \frac{i}{2c} \langle \lambda_\mu | (\vec{R}_{\mu\nu} \times \hat{r})_u | \lambda_\nu \rangle. \quad (4.37)$$

The derivatives are purely imaginary and antisymmetric. The other matrices contain a spin-dependent and a spin-independent contribution, which are separated by applying the Dirac identity. The spin-independent contribution of the kinetic energy matrix reads

$$\left(\frac{\partial \mathbf{T}_{\mu\nu}}{\partial B_u}\right)_0 = \frac{i}{4c} \langle \lambda_\mu | (\vec{R}_{\mu\nu} \times \hat{r})_u \hat{p}^2 | \lambda_\nu \rangle + \frac{1}{2c} \langle \lambda_\mu | (\hat{r} \times \hat{p})_u | \lambda_\nu \rangle \quad (4.38)$$

and the spin-dependent or spin-orbit part is not block-diagonal in the two-component space according to

$$\left(\frac{\partial \mathbf{T}_{\mu\nu}^{\text{SO}}}{\partial B_u}\right)_0 = \sigma_u \langle \lambda_\mu | \lambda_\nu \rangle. \quad (4.39)$$

The spin-orbit part may be evaluated with the overlap integrals and sorting onto the respective blocks in the two-component space. However, all spin-orbit contributions are neglected in a scalar-relativistic approximation.

The spin-independent integral and spin-dependent derivatives of the generalized momentum matrix are given as

$$\left(\frac{\partial \mathbf{\Pi}_{\mu\nu}^\dagger}{\partial B_u}\right)_0 = \frac{i}{4c} \langle \lambda_\mu | (\vec{R}_{\mu\nu} \times \hat{r})_u \hat{p}^2 | \lambda_\nu \rangle + \frac{1}{2c} \langle \lambda_\mu | (\hat{r} \times \hat{p})_u | \lambda_\nu \rangle = \left(\frac{\partial \mathbf{T}_{\mu\nu}}{\partial B_u}\right)_0, \quad (4.40)$$

$$\left(\frac{\partial \mathbf{\Pi}_{\mu\nu}^{\dagger, \text{SO}}}{\partial B_u}\right)_0 = \sigma_u \langle \lambda_\mu | \lambda_\nu \rangle = \left(\frac{\partial \mathbf{T}_{\mu\nu}^{\text{SO}}}{\partial B_u}\right)_0. \quad (4.41)$$

The corresponding derivatives of the relativistically modified potential are

$$\begin{aligned} \left(\frac{\partial \mathbf{W}_{\mu\nu}^0}{\partial B_u}\right)_0 &= \frac{i}{2c} \langle \lambda_\mu | (\vec{R}_{\mu\nu} \times \hat{r})_u \hat{p} \cdot \hat{V} \hat{p} | \lambda_\nu \rangle \\ &+ \frac{1}{2c} \langle \lambda_\mu | (\hat{r}_\nu \times \hat{p})_u \hat{V} + \hat{V} (\hat{r}_\nu \times \hat{p})_u | \lambda_\nu \rangle, \end{aligned} \quad (4.42)$$

$$\begin{aligned} \left(\frac{\partial \mathbf{W}_{\mu\nu}^{\text{SO}}}{\partial B_u}\right)_0 &= \langle \lambda_\mu | (\vec{R}_{\mu\nu} \times \hat{r})_u i\vec{\sigma} \cdot (\hat{p} \times \hat{V} \hat{p}) | \lambda_\nu \rangle + \sigma_u \langle \lambda_\mu | \hat{V} | \lambda_\nu \rangle \\ &+ \langle \lambda_\mu | \frac{i}{2c} \sigma_u (\hat{p} \hat{V}) \cdot \hat{r}_\nu - \frac{i}{2c} (\hat{p} \hat{V})_u (\vec{\sigma} \cdot \hat{r}_\nu) | \lambda_\nu \rangle. \end{aligned} \quad (4.43)$$

The notation $(\hat{p} \hat{V})$ indicates that the momentum operator only acts on the potential operator and not on the further terms on the right-hand side. All scalar-relativistic integral derivatives are purely imaginary and antisymmetric. Thus, all matrices are Hermitian and complex algebra can be avoided by simply changing

the sign for the adjoint matrix and adding a factor of -1 for the multiplication of two purely imaginary matrices. The derivative of the NESC matrix becomes

$$\begin{aligned} \mathbf{L}_u^B = & \mathbf{V}_u^B + \mathbf{\Pi}_u^{\dagger,B} \mathbf{X} + \mathbf{\Pi}^{\dagger} \mathbf{X}_u^B + \mathbf{X}_u^{\dagger,B} \mathbf{\Pi} + \mathbf{X}^{\dagger} \mathbf{\Pi}_u^B \\ & + \mathbf{X}_u^{\dagger,B} \left(\frac{1}{4c^2} \mathbf{W}^0 - \mathbf{T} \right) \mathbf{X} + \mathbf{X}^{\dagger} \left(\frac{1}{4c^2} \mathbf{W}_u^{0,B} - \mathbf{T}^{\lambda} \right) \mathbf{X} + \mathbf{X}^{\dagger} \left(\frac{1}{4c^2} \mathbf{W}^0 - \mathbf{T} \right) \mathbf{X}_u^B, \end{aligned} \quad (4.44)$$

where a short-hand notation $\mathbf{V}_u^B = (\partial \mathbf{V} / \partial B_u)_0$ is applied. Therefore, the derivative of the X2C Hamiltonian reads

$$\mathbf{h}_u^{+,B} = \mathbf{R}^{\dagger} \mathbf{L}_u^B \mathbf{R} + \mathbf{R}_u^{\dagger,B} \mathbf{L} \mathbf{R} + \mathbf{R}^{\dagger} \mathbf{L} \mathbf{R}_u^B. \quad (4.45)$$

The integral derivatives of the kinetic energy, the generalized momentum, and the overlap matrix are already available in a non-relativistic implementation.^[397,398] The relativistically modified potential only arises in relativistic all-electron approaches and the finite nucleus model of the potential matrix is also commonly employed in relativistic calculations only. These integrals are evaluated with a combination of Gauss–Rys^[155–158] and Gauss–Hermite integration as shown in the appendix A.1. Here, the integration over the variable of the Laplace transformation is carried out with the Gauss–Rys method and the spatial integration is done with Gauss–Hermite quadrature. Based on the nuclear potential integral, the other required integrals are obtained as linear combinations. Consider a Cartesian atomic orbital and the spatial vector \vec{r} . As the three coordinates are independent of each other, the scalar x changes the integral according to

$$\langle x | \hat{x} | \lambda_{\mu} \rangle = (x - X_{\mu} + X_{\mu}) \langle x | \lambda_{\mu} \rangle = \langle x | \lambda_{\mu} + 1_x \rangle + X_{\mu} \langle x | \lambda_{\mu} \rangle, \quad (4.46)$$

where the short-hand notation

$$\langle x | \lambda_{\mu} + 1_x \rangle = (x - X_{\mu})^{\mu_x + 1} (y - Y_{\mu})^{\mu_y} (z - Z_{\mu})^{\mu_z} \exp \left[-\zeta_{\mu} \left(\vec{r} - \vec{R}_{\mu} \right)^2 \right] \quad (4.47)$$

was used. The other Cartesian directions are obtained by trivial substitutions. Therefore, the derivative of the potential with respect to the magnetic field in x direction, B_x , is evaluated as

$$\begin{aligned} \left(\frac{\partial \mathbf{V}_{\mu\nu}}{B_u} \right)_0 &= \frac{i}{2c} \langle \lambda_{\mu} | (\vec{R}_{\mu\nu} \times \hat{r})_x \hat{V} | \lambda_{\nu} \rangle \\ &= \frac{i}{2c} Y_{\mu\nu} \left(\langle \lambda_{\mu} | \hat{V} | \lambda_{\nu} + 1_z \rangle + Z_{\nu} \langle \lambda_{\mu} | \hat{V} | \lambda_{\nu} \rangle \right) \\ &\quad - \frac{i}{2c} Z_{\mu\nu} \left(\langle \lambda_{\mu} | \hat{V} | \lambda_{\nu} + 1_y \rangle + Y_{\nu} \langle \lambda_{\mu} | \hat{V} | \lambda_{\nu} \rangle \right) \end{aligned} \quad (4.48)$$

since the spatial vector and the potential operator commute. The spatial vector may also act on the *bra* by making use of its hermiticity. For the relativistically modified potential, the effect of the momentum operator is required

$$\langle x | \hat{p}_x | \lambda_{\mu} \rangle = -i \mu_x \langle x | \lambda_{\mu} - 1_x \rangle + 2i \zeta_{\mu} \langle x | \lambda_{\mu} + 1_x \rangle. \quad (4.49)$$

In consequence, all required integrals of the relativistically modified potential can be constructed by the application of the momentum operator and the spatial vector onto the *bra* and the *ket* basis functions. For instance, the term with $\hat{V} (\hat{r} \times \hat{p})_u$ in Eq. 4.42 is evaluated as

$$\begin{aligned} \langle \lambda_{\mu} | \hat{V} (\hat{r}_{\nu} \times \hat{p})_x | \lambda_{\nu} \rangle = & 2i \zeta_{\nu} \langle \lambda_{\mu} | \hat{V} | \lambda_{\nu} + 1_y + 1_z \rangle - i \mu_z \langle \lambda_{\mu} | \hat{V} | \lambda_{\nu} + 1_y - 1_z \rangle \\ & - 2i \zeta_{\nu} \langle \lambda_{\mu} | \hat{V} | \lambda_{\nu} + 1_y + 1_z \rangle - i \mu_y \langle \lambda_{\mu} | \hat{V} | \lambda_{\nu} - 1_y + 1_z \rangle \end{aligned} \quad (4.50)$$

and the term with $(\hat{r}_\nu \times \hat{p})_u \hat{V}$ is evaluated in similar fashion by applying the operator onto the *bra* basis function and making use of $\vec{r}_\nu = \vec{r}_\mu + \vec{R}_{\mu\nu}$. The remaining term $(\vec{R}_{\mu\nu} \times \hat{r})_u \hat{p} \cdot \hat{V} \hat{p}$ is obtained as follows. First, we consider the three parts of the $\hat{p}_v \hat{V} \hat{p}_v$ with $v \in \{x, y, z\}$ separately as they are independent of each other. The matrix element is rearranged using the adjoint of $(\vec{R}_{\mu\nu} \times \hat{r})_u \hat{p}_v$.

First, consider the trivial case $u = v$,

$$\begin{aligned}
 \langle \hat{p}_x (\vec{R}_{\mu\nu} \times \hat{r})_x \lambda_\mu | \hat{V} \hat{p}_x | \lambda_\nu \rangle = & \mu_x \nu_x Y_{\mu\nu} \langle \lambda_\mu - 1_x | \hat{V} | \lambda_\nu - 1_x + 1_z \rangle \\
 & + \mu_x \nu_x Y_{\mu\nu} Z_\nu \langle \lambda_\mu - 1_x | \hat{V} | \lambda_\nu - 1_x \rangle \\
 & - 2\zeta_\mu \nu_x Y_{\mu\nu} \langle \lambda_\mu + 1_x | \hat{V} | \lambda_\nu - 1_x + 1_z \rangle \\
 & - 2\zeta_\mu \nu_x Y_{\mu\nu} Z_\nu \langle \lambda_\mu + 1_x | \hat{V} | \lambda_\nu - 1_x \rangle \\
 & - 2\zeta_\nu \mu_x Y_{\mu\nu} \langle \lambda_\mu - 1_x | \hat{V} | \lambda_\nu + 1_x + 1_z \rangle \\
 & - 2\zeta_\nu \mu_x Y_{\mu\nu} Z_\nu \langle \lambda_\mu - 1_x | \hat{V} | \lambda_\nu + 1_x \rangle \\
 & + 4\zeta_\mu \zeta_\nu Y_{\mu\nu} \langle \lambda_\mu + 1_x | \hat{V} | \lambda_\nu + 1_x + 1_z \rangle \\
 & + 4\zeta_\mu \zeta_\nu Y_{\mu\nu} Z_\nu \langle \lambda_\mu + 1_x | \hat{V} | \lambda_\nu + 1_x \rangle \\
 & - \mu_x \nu_x Z_{\mu\nu} \langle \lambda_\mu - 1_x | \hat{V} | \lambda_\nu - 1_x + 1_y \rangle \\
 & - \mu_x \nu_x Z_{\mu\nu} Y_\nu \langle \lambda_\mu - 1_x | \hat{V} | \lambda_\nu - 1_x \rangle \\
 & + 2\zeta_\mu \nu_x Z_{\mu\nu} \langle \lambda_\mu + 1_x | \hat{V} | \lambda_\nu - 1_x + 1_y \rangle \\
 & + 2\zeta_\mu \nu_x Z_{\mu\nu} Y_\nu \langle \lambda_\mu + 1_x | \hat{V} | \lambda_\nu - 1_x \rangle \\
 & + 2\zeta_\nu \mu_x Z_{\mu\nu} \langle \lambda_\mu - 1_x | \hat{V} | \lambda_\nu + 1_x + 1_y \rangle \\
 & + 2\zeta_\nu \mu_x Z_{\mu\nu} Y_\nu \langle \lambda_\mu - 1_x | \hat{V} | \lambda_\nu + 1_x \rangle \\
 & - 4\zeta_\mu \zeta_\nu Z_{\mu\nu} \langle \lambda_\mu + 1_x | \hat{V} | \lambda_\nu + 1_x + 1_y \rangle \\
 & - 4\zeta_\mu \zeta_\nu Z_{\mu\nu} Y_\nu \langle \lambda_\mu + 1_x | \hat{V} | \lambda_\nu + 1_x \rangle.
 \end{aligned} \tag{4.51}$$

Here, the momentum operator and the position operator act onto different Cartesian directions and therefore they commute, which results in many terms and requires some bookkeeping but the integral evaluation itself is similar to the unperturbed integrals.^[106] For the other cases, the crossproduct term yields a scalar x and thus the momentum operator will act onto x and the *bra* basis function. Adding zero to x leads to

$$\langle \hat{p}_x \hat{x} \lambda_\mu | \hat{V} \hat{p}_x | \lambda_\nu \rangle = \langle \hat{p}_x (\hat{x} - X_\mu) \lambda_\mu | \hat{V} \hat{p}_x | \lambda_\nu \rangle + X_\mu \langle \hat{p}_x \lambda_\mu | \hat{V} \hat{p}_x | \lambda_\nu \rangle. \tag{4.52}$$

The first term is calculated as

$$\begin{aligned}
 \langle \hat{p}_x (\hat{x} - X_\mu) \lambda_\mu | \hat{V} \hat{p}_x | \lambda_\nu \rangle = & 4\zeta_\mu \zeta_\nu \langle \lambda_\mu + 2_x | \hat{V} | \lambda_\nu + 1_x \rangle \\
 & - 2\zeta_\nu (\mu_x + 1) \langle \lambda_\mu | \hat{V} | \lambda_\nu + 1_x \rangle \\
 & - 2\zeta_\mu \nu_x \langle \lambda_\mu + 2_x | \hat{V} | \lambda_\nu - 1_x \rangle \\
 & + (\mu_x + 1) \nu_x \langle \lambda_\mu | \hat{V} | \lambda_\nu - 1_x \rangle
 \end{aligned} \tag{4.53}$$

and the second term becomes

$$\begin{aligned}
 X_\mu \langle \hat{p}_x \lambda_\mu | \hat{V} \hat{p}_x | \lambda_\nu \rangle = & \mu_x \nu_x X_\mu \langle \lambda_\mu - 1_x | \hat{V} | \lambda_\nu - 1_x \rangle \\
 & - 2\zeta_\mu \nu_x X_\mu \langle \lambda_\mu + 1_x | \hat{V} | \lambda_\nu - 1_x \rangle \\
 & - 2\zeta_\nu \mu_x X_\mu \langle \lambda_\mu - 1_x | \hat{V} | \lambda_\nu + 1_x \rangle \\
 & + 4\zeta_\mu \zeta_\nu X_\mu \langle \lambda_\mu + 1_x | \hat{V} | \lambda_\nu + 1_x \rangle.
 \end{aligned} \tag{4.54}$$

The remaining terms for the derivative of \mathbf{W}^0 are obtained by interchanging the Cartesian directions and indices.

4.3.2 Magnetic Moment Derivatives

Solely the generalized momentum matrix gives non-vanishing derivatives with respect to the magnetic moments as the other matrices do not depend on the magnetic moments. The spin-free integrals read

$$\left(\frac{\partial \mathbf{\Pi}_{\mu\nu}^\dagger}{\partial m_{I,u}} \right)_0 = \frac{1}{2c} \langle \lambda_\mu | (\vec{\nabla}_I \hat{\mathcal{G}}_I \times \hat{p})_u | \lambda_\nu \rangle \quad (4.55)$$

while the spin-dependent integrals are given as

$$\left(\frac{\partial \mathbf{\Pi}_{\mu\nu}^{\dagger, \text{SO}}}{\partial m_{I,u}} \right)_0 = \frac{i}{2c} \langle \lambda_\mu | \left([\vec{\sigma} \cdot \vec{\nabla}_I \hat{\mathcal{G}}_I] \hat{p}_u - \sigma_u [\vec{\nabla}_I \hat{\mathcal{G}}_I \cdot \hat{p}] \right) | \lambda_\nu \rangle. \quad (4.56)$$

In the point charge model, the spin-dependent integrals reduce to

$$\left(\frac{\partial \mathbf{\Pi}_{\mu\nu}^\dagger}{\partial m_{I,u}} \right)_0 = \frac{1}{2c} \langle \lambda_\mu | \hat{r}_I^{-3} (\hat{r}_I \times \hat{p})_u | \lambda_\nu \rangle. \quad (4.57)$$

The spin-free integrals are imaginary and antisymmetric. The integrals are evaluated in similar fashion to the previous subsection by exploiting the effect of p_x onto the *ket* basis function. The term involving $\vec{\nabla} \mathcal{G}$ is calculated using translation invariance based on the considerations of Hennum and co-workers.^[390] The integrals involving \mathcal{G} and $\vec{\nabla}$ onto the *ket* basis functions are evaluated similar to the nuclear potential integrals as

$$\mathcal{G}(\vec{r}) = \int \frac{w_I(\vec{R}_I)}{|\vec{r} - \vec{R}_I|} d\vec{R}_I = -\frac{1}{Z} V(\vec{r}). \quad (4.58)$$

The derivative of the X2C Hamiltonian follows as

$$\mathbf{h}_u^{+, m_I} = \mathbf{R}_u^{\dagger, m_I} \mathbf{L} \mathbf{R} + \mathbf{R}^\dagger \mathbf{L}_u^{m_I} \mathbf{R} + \mathbf{R}^\dagger \mathbf{L} \mathbf{R}_u^{m_I} \quad (4.59)$$

with the derivative of the NESC matrix

$$\begin{aligned} \mathbf{L}_u^{m_I} = & \mathbf{X}_u^{\dagger, m_I} \mathbf{\Pi} + \mathbf{X}^\dagger \mathbf{\Pi}_u^{m_I} + \mathbf{\Pi}_u^{\dagger, m_I} \mathbf{X} + \mathbf{\Pi}^\dagger \mathbf{X}_u^{m_I} \\ & + \mathbf{X}_u^{\dagger, m_I} \left(\frac{1}{4c^2} \mathbf{W} - \mathbf{T} \right) \mathbf{X} + \mathbf{X}^\dagger \left(\frac{1}{4c^2} \mathbf{W} - \mathbf{T} \right) \mathbf{X}_u^{m_I}. \end{aligned} \quad (4.60)$$

4.3.3 Mixed Derivatives

According to the last subsection, the generalized momentum matrix is also the only matrix with non-zero mixed derivatives. The scalar-relativistic contribution is given as

$$\begin{aligned} \left(\frac{\partial^2 \mathbf{\Pi}_{\mu\nu}^\dagger}{\partial B_u m_{I,v}} \right)_0 = & \frac{1}{4c^2} \langle \lambda_\mu | \delta_{uv} \left((\vec{\nabla}_I \hat{\mathcal{G}}_I) \cdot \hat{r}_\nu \right) - (\vec{\nabla}_I \hat{\mathcal{G}}_I)_u (\hat{r}_\nu)_v | \lambda_\nu \rangle \\ & + \frac{i}{4c^2} \langle \lambda_\mu | (\vec{R}_{I,\mu\nu} \times \hat{r})_u \left((\vec{\nabla}_I \hat{\mathcal{G}}_I) \times \hat{p} \right)_v | \lambda_\nu \rangle \end{aligned} \quad (4.61)$$

and the spin-orbit contribution reads

$$\begin{aligned} \left(\frac{\partial^2 \mathbf{\Pi}_{\mu\nu}^{\dagger, \text{SO}}}{\partial B_u m_{I,v}} \right)_0 &= -\frac{1}{2c^2} \langle \lambda_\mu | \left(\vec{R}_{\mu\nu} \times \hat{r} \right)_u \left[\vec{\sigma} \cdot \vec{\nabla}_I \hat{G}_I \hat{p}_v - \sigma_v \vec{\nabla}_I \hat{G}_I \cdot \hat{p} \right] | \lambda_\nu \rangle \\ &\quad - \frac{i}{4c^2} \langle \lambda_\mu | \epsilon_{vuw} \vec{\sigma} \cdot \vec{\nabla}_I \hat{G}_I (\hat{r}_\nu)_w - \sigma_v \left(\hat{r}_\nu \times \vec{\nabla}_I \hat{G}_I \right)_u | \lambda_\nu \rangle \end{aligned} \quad (4.62)$$

with the Levi–Civita tensor ϵ_{vuw} . The scalar-relativistic integrals are real and symmetric. In non-relativistic calculations, the first term of these integrals is referred to as the diamagnetic integrals and the second term gives rise to the paramagnetic unperturbed density contribution.

Differentiating the X2C-Hamiltonian in Eq. 4.34 yields

$$\begin{aligned} \mathbf{h}_{u,v}^{B,m_I} &= \left(\mathbf{R}_{u,v}^{\dagger, B, m_I} \mathbf{L} \mathbf{R} + \mathbf{R}^\dagger \mathbf{L}^{\text{NESC}} \mathbf{R}_{u,v}^{B, m_I} \right) + \left(\mathbf{R}_{u,v}^{\dagger, B_u} \mathbf{L} \mathbf{R}_v^{m_I} + \mathbf{R}_v^{\dagger, m_I} \mathbf{L} \mathbf{R}_u^B \right) \\ &\quad + \left(\mathbf{R}_u^{\dagger, B} \mathbf{L}_v^{m_I} \mathbf{R} + \mathbf{R}^\dagger \mathbf{L}_v^{m_I} \mathbf{R}_u^B \right) + \left(\mathbf{R}_v^{\dagger, m_I} \mathbf{L}_u^B \mathbf{R} + \mathbf{R}^\dagger \mathbf{L}_u^B \mathbf{R}_v^{m_I} \right) \\ &\quad + \left(\mathbf{R}^\dagger \mathbf{L}_{u,v}^{B, m_I} \mathbf{R} \right). \end{aligned} \quad (4.63)$$

The second derivative of the NESC matrix reads

$$\begin{aligned} \mathbf{L}_{u,v}^{B, m_I} &= \mathbf{\Pi}_{u,v}^{\dagger, B, m_I} \mathbf{X} + \mathbf{\Pi}_u^{\dagger, B} \mathbf{X}_v^{m_I} + \mathbf{\Pi}_v^{\dagger, m_I} \mathbf{X}_u^B + \mathbf{\Pi}^\dagger \mathbf{X}_{u,v}^{B, m_I} \\ &\quad + \mathbf{X}_{u,v}^{\dagger, B, m_I} \mathbf{\Pi} + \mathbf{X}_u^{\dagger, B} \mathbf{\Pi}_v^{m_I} + \mathbf{X}_v^{\dagger, m_I} \mathbf{\Pi}_u^B + \mathbf{X}^\dagger \mathbf{\Pi}_{u,v}^{B, m_I} \\ &\quad + \mathbf{X}_{u,v}^{\dagger, B, m_I} (\mathbf{W} - \mathbf{T}) \mathbf{X} + \mathbf{X}_v^{\dagger, m_I} (\mathbf{W}_u^B - \mathbf{T}_u^B) \mathbf{X} \\ &\quad + \mathbf{X}_u^{\dagger, B} (\mathbf{W} - \mathbf{T}) \mathbf{X}_v^{m_I} + \mathbf{X}_v^{\dagger, m_I} (\mathbf{W} - \mathbf{T}) \mathbf{X}_u^B \\ &\quad + \mathbf{X}^\dagger (\mathbf{W}_u^B - \mathbf{T}_u^B) \mathbf{X}_v^{m_I} + \mathbf{X}^\dagger (\mathbf{W} - \mathbf{T}) \mathbf{X}_{u,v}^{B, m_I}. \end{aligned} \quad (4.64)$$

Note that the second derivative of the NESC matrix involves all one-electron integral derivatives discussed previously. So, a strict separation into diamagnetic and paramagnetic contributions like in non-relativistic quantum chemistry is problematic. Thus, the NMR shielding tensor is only partitioned into the perturbed and the unperturbed density contribution in X2C calculations. The matrix multiplications for all Hamiltonian derivatives are efficiently carried out with the basic linear algebra subroutine^[399,400] (BLAS) DGEMM.

4.4 Response Equations for the Derivatives of the Decoupling Matrix

This section compares different ansätze^[108,109,254,267,379] for the calculation of the derivative of the decoupling matrix. It is shown that these lead to the same result and the choice of the ansatz is made according to the efficiency. The general two-component response equations are derived and the simplification as well as the explicit expressions for the scalar-relativistic shielding tensor are given at the end of each subsection.

4.4.1 First Derivatives

A straightforward differentiation of Eq. 2.50 yields^[108]

$$\mathbf{X}^\lambda = \left(\mathbf{C}_+^{S, \lambda} - \mathbf{X} \mathbf{C}_+^{L, \lambda} \right) \left(\mathbf{C}_+^L \right)^{-1}. \quad (4.65)$$

The evaluation of this equation necessitates the perturbed coefficients, which are available with response theory. As discussed in Sec. 2.4, the one-electron Dirac equation in a matrix representation is of the same

structural form as the Roothaan–Hall equations.^[252,253] Therefore, the application of response theory to the perturbed decoupling matrix is similar to the perturbed density matrix. The one-electron Dirac equations and the normalization condition read

$$\mathbb{D}\mathbf{C} = \mathbf{M}\mathbf{C}\mathbf{E}, \quad (4.66)$$

$$\mathbf{C}^\dagger\mathbf{M}\mathbf{C} = \mathbb{I}, \quad (4.67)$$

where \mathbb{E} is a diagonal matrix containing the energy eigenvalues and \mathbb{I} is the (4×4) identity matrix. The perturbed coefficients, \mathbf{C}^λ , are assumed as a linear combination of the unperturbed coefficients, \mathbf{C} , according to

$$\begin{pmatrix} \mathbf{C}_-^{L,\lambda} & \mathbf{C}_+^{L,\lambda} \\ \mathbf{C}_-^{S,\lambda} & \mathbf{C}_+^{S,\lambda} \end{pmatrix} = \begin{pmatrix} \mathbf{C}_-^L & \mathbf{C}_+^L \\ \mathbf{C}_-^S & \mathbf{C}_+^S \end{pmatrix} \mathbb{U}^\lambda. \quad (4.68)$$

The orbital rotation matrix \mathbb{U}^λ mixes the coefficients of the positive energy and the negative energy subspace. A Taylor expansion is carried out to arrive at an explicit expression for the orbital rotation matrix

$$\mathbb{D}^\lambda\mathbf{C} + \mathbb{D}\mathbf{C}^\lambda = \mathbf{M}^\lambda\mathbf{C}\mathbf{E} + \mathbf{M}\mathbf{C}^\lambda\mathbf{E} + \mathbf{M}\mathbf{C}\mathbf{E}^\lambda. \quad (4.69)$$

Collecting all first-order terms is most easily done in the basis of the unperturbed solutions, which is obtained by multiplication with \mathbf{C}^\dagger from the left. The Dirac matrix and the metric in this basis read

$$\tilde{\mathbb{D}} = \mathbf{C}^\dagger\mathbb{D}\mathbf{C} = \mathbf{E}, \quad (4.70)$$

$$\tilde{\mathbb{M}} = \mathbf{C}^\dagger\mathbf{M}\mathbf{C} = \mathbb{I}. \quad (4.71)$$

The first-order response equation follows as

$$\tilde{\mathbb{D}}^\lambda - \tilde{\mathbb{M}}^\lambda\mathbf{E} = \tilde{\mathbb{E}}^\lambda + \mathbb{U}^\lambda\mathbf{E} - \mathbf{E}\mathbb{U}^\lambda, \quad (4.72)$$

which may be rearranged using the commutator to the simplified form^[102]

$$[\mathbb{U}^\lambda, \mathbf{E}] = \left(\tilde{\mathbb{D}}^\lambda - \tilde{\mathbb{M}}^\lambda\mathbf{E} \right) - \mathbf{E}^\lambda. \quad (4.73)$$

In principle, this equation allows to calculate all matrix elements of \mathbb{U}^λ . However, the expression will become unstable for near-degenerate or degenerate states. Therefore, these matrix elements utilize the normalization condition in Eq. 4.67. The respective first-order equation reads

$$\mathbb{U}^{\dagger,\lambda} + \tilde{\mathbb{M}}^\lambda + \mathbb{U}^\lambda = 0. \quad (4.74)$$

Further assuming canonicity, i.e. the matrix \mathbb{E}^λ is diagonal, results in the working equations

$$\mathbb{U}_{pq}^\lambda = \frac{\tilde{\mathbb{D}}_{pq}^\lambda - \tilde{\mathbb{M}}_{pq}^\lambda\mathbf{E}_{qq}}{\mathbf{E}_{qq} - \mathbf{E}_{pp}} \quad \forall p \neq q, \quad (4.75)$$

$$\mathbb{U}_{pp}^\lambda = -\frac{1}{2}\tilde{\mathbb{M}}_{pp}^\lambda. \quad (4.76)$$

Eq. 4.75 is used for elements with a larger energy difference and Eq. 4.76 is used for the near-degenerate and degenerate states. The indices p and q run over all states, i.e. over both the negative and positive energy subspace. The accuracy and the numerical stability of this ansatz consequently relies on the identification of near-degenerate states. Cheng and Gauss suggested to use a threshold of 10^{-4} a.u.^[401] and this threshold was also used in the preceding implementation of geometry gradients in TURBOMOLE.^[106,107] For geometry

gradients, the threshold is validated or optimized by comparison to numerical energy gradients of highly symmetric systems like Ag_{13} in O_h and I_h symmetry. However, numerical gradients for the magnetic field derivative of the NMR tensor requires major extensions of the implementation to support finite fields^[402] and using the same threshold of 10^{-4} a.u. for the NMR derivatives is a straightforward choice. Note that this ansatz is similar to the semi-canonical coupled-perturbed Hartree–Fock (CPHF) and Kohn–Sham (CPKS) equations.^[403,404] However, the response equations are solved directly in one step. The drawback of this ansatz is that the full orbital rotation matrix is required. Rewriting the response equations for the decoupling matrix based on the non-canonical CPHF and CPKS equations^[405] is thus desirable to avoid the calculation of the full matrix \mathbb{U}^λ and to avoid the optimization of the threshold for near-degenerate states to ensure the numerical stability.^[254]

In the non-canonical CPHF approach, the orbital rotation matrix is partitioned into the occupied-occupied, occupied-virtual, virtual-occupied, and virtual-virtual blocks. In X2C response theory, the orbital rotation matrix is therefore partitioned based on the energy subspaces according to

$$\mathbb{U}^\lambda = \begin{pmatrix} \mathbf{U}_{--}^\lambda & \mathbf{U}_{-+}^\lambda \\ \mathbf{U}_{+-}^\lambda & \mathbf{U}_{++}^\lambda \end{pmatrix}, \quad (4.77)$$

where the signs indicate the energy subspaces. This expression is now inserted into Eq. 4.68 to compute the perturbed coefficients of the positive energy subspace as

$$\mathbf{C}_+^{L,\lambda} = \mathbf{C}_-^L \mathbf{U}_{-+}^\lambda + \mathbf{C}_+^L \mathbf{U}_{++}^\lambda, \quad (4.78)$$

$$\mathbf{C}_+^{S,\lambda} = \mathbf{C}_-^S \mathbf{U}_{-+}^\lambda + \mathbf{C}_+^S \mathbf{U}_{++}^\lambda. \quad (4.79)$$

Note that the orbital rotation matrix still mixes the positive and the negative energy subspace coefficients. The derivative of the decoupling matrix becomes

$$\mathbf{X}^\lambda = [\mathbf{C}_-^S \mathbf{U}_{-+}^\lambda + \mathbf{C}_+^S \mathbf{U}_{++}^\lambda - \mathbf{X} (\mathbf{C}_-^L \mathbf{U}_{-+}^\lambda + \mathbf{C}_+^L \mathbf{U}_{++}^\lambda)] (\mathbf{C}_+^L)^{-1}. \quad (4.80)$$

So, only two of the four blocks of \mathbb{U}^λ are needed. The positive-positive block is further eliminated by using the normalization condition of the large component^[96]

$$\mathbf{C}_{L+}^\dagger \tilde{\mathbf{S}} \mathbf{C}_{L+} = \mathbf{I}. \quad (4.81)$$

The perturbed decoupling matrix is thus obtained as

$$\mathbf{X}^\lambda = (\mathbf{C}_-^S - \mathbf{X} \mathbf{C}_-^L) \mathbf{U}_{-+}^\lambda \mathbf{C}_+^{L,\dagger} \tilde{\mathbf{S}}. \quad (4.82)$$

Therefore, only one block of the orbital rotation matrix is required and only matrices in the two-component space are needed. Assuming $\mathbf{E}_{-+}^\lambda = \mathbf{0}_2$, the negative-positive or positronic-electronic subblock of the orbital rotation matrix is given as

$$(\mathbf{U}_{-+}^\lambda)_{kl} = \frac{(\tilde{\mathbf{D}}_{-+}^\lambda)_{kl} - (\tilde{\mathbf{M}}_{-+}^\lambda)_{kl} (\mathbf{E}_{++})_{ll}}{(\mathbf{E}_{++})_{ll} - (\mathbf{E}_{--})_{kk}}, \quad (4.83)$$

where the indices k and l only run over the respective subblock. The negative and positive energy subspace are separated by a gap of $2c^2$ and therefore the denominator will always be numerically stable. The corresponding derivative of the Dirac matrix and the metric read

$$\tilde{\mathbf{D}}_{-+}^{\lambda} = \mathbf{C}_{-}^{L,\dagger} \mathbf{V}^{\lambda} \mathbf{C}_{+}^{L} + \mathbf{C}_{-}^{L,\dagger} \mathbf{\Pi}^{\dagger,\lambda} \mathbf{C}_{+}^{S} + \mathbf{C}_{-}^{S,\dagger} \mathbf{\Pi}^{\lambda} \mathbf{C}_{+}^{L} + \mathbf{C}_{-}^{S,\dagger} \left(\frac{1}{4c^2} \mathbf{W}^{\lambda} - \mathbf{T}^{\lambda} \right) \mathbf{C}_{+}^{S}, \quad (4.84)$$

$$\tilde{\mathbf{M}}_{-+}^{\lambda} = \mathbf{C}_{-}^{L,\dagger} \mathbf{S}^{\lambda} \mathbf{C}_{+}^{L} + \frac{1}{2c^2} \mathbf{C}_{-}^{S,\dagger} \mathbf{T}^{\lambda} \mathbf{C}_{+}^{S}. \quad (4.85)$$

Both ansätze are implemented for geometry gradients and identical results are obtained. However, the non-canonical solver is faster by a factor of about 2 and the memory demands are decreased. Therefore, only the non-canonical ansatz is pursued for second derivatives below.

The explicit expression for the magnetic field derivative of \mathbf{X} is given as

$$\mathbf{X}_u^B = (\mathbf{C}_{-}^S - \mathbf{X} \mathbf{C}_{-}^L) (\mathbf{U}_u^B)_{-+} \mathbf{C}_{+}^{L,\dagger} \tilde{\mathbf{S}} \quad (4.86)$$

with the orbital rotation matrix

$$(\mathbf{U}_{u,-+}^B)_{kl} = \frac{(\tilde{\mathbf{D}}_{u,-+}^B)_{kl} - (\tilde{\mathbf{M}}_{u,-+}^B)_{kl} (\mathbf{E}_{++})_{ll}}{(\mathbf{E}_{++})_{ll} - (\mathbf{E}_{--})_{kk}}. \quad (4.87)$$

The derivative of the Dirac matrix and the metric is obtained according to

$$\tilde{\mathbf{D}}_{u,-+}^B = \mathbf{C}_{-}^{L,\dagger} \mathbf{V}_u^B \mathbf{C}_{+}^{L} + \mathbf{C}_{-}^{L,\dagger} \mathbf{\Pi}_u^{\dagger,B} \mathbf{C}_{+}^{S} + \mathbf{C}_{-}^{S,\dagger} \mathbf{\Pi}_u^B \mathbf{C}_{+}^{L} + \mathbf{C}_{-}^{S,\dagger} \left(\frac{1}{4c^2} \mathbf{W}_u^B - \mathbf{T}_u^B \right) \mathbf{C}_{+}^{S}, \quad (4.88)$$

$$\tilde{\mathbf{M}}_{u,-+}^B = \mathbf{C}_{-}^{L,\dagger} \mathbf{S}_u^B \mathbf{C}_{+}^{L} + \frac{1}{2c^2} \mathbf{C}_{-}^{S,\dagger} \mathbf{T}_u^B \mathbf{C}_{+}^{S}. \quad (4.89)$$

For the derivative of the magnetic moments, the corresponding derivatives of the decoupling matrix are computed as

$$\mathbf{X}_u^{m_I} = (\mathbf{C}_{-}^S - \mathbf{X} \mathbf{C}_{-}^L) (\mathbf{U}_u^{m_I})_{-+} \mathbf{C}_{+}^{L,\dagger} \tilde{\mathbf{S}}, \quad (4.90)$$

$$(\mathbf{U}_{u,-+}^{m_I})_{kl} = \frac{(\tilde{\mathbf{D}}_{u,-+}^{m_I})_{kl}}{(\mathbf{E}_{++})_{ll} - (\mathbf{E}_{--})_{kk}}, \quad (4.91)$$

$$\tilde{\mathbf{D}}_{u,-+}^{m_I} = \mathbf{C}_{-}^{L,\dagger} \mathbf{\Pi}_u^{\dagger,m_I} \mathbf{C}_{+}^{S} + \mathbf{C}_{-}^{S,\dagger} \mathbf{\Pi}_u^{m_I} \mathbf{C}_{+}^{L}, \quad (4.92)$$

since the derivative of the metric vanishes. All matrix multiplications are carried out with DGEMM and the Dirac matrix is diagonalized with the metric using the LAPACK routine^[396] DSYGV. The inverse of the decoupling matrix is formed with DGETRF and DGETRI.^[399,400] DGETRF computes the lower-upper factorization of a matrix and DGETRI subsequently computes the inverse of the matrix.

4.4.2 Second Derivatives

For the second-order perturbed coefficients, we introduce the ansatz for the linear combinations as

$$\mathbb{C}^{\kappa\lambda} = \mathbb{C} [\mathbb{U}^{\kappa,\lambda} + \mathbb{U}^\kappa \mathbb{U}^\lambda] = \mathbb{C} \tilde{\mathbb{U}}^{\kappa,\lambda}. \quad (4.93)$$

For the non-canonical solver, the second-order orbital rotation matrix, $\tilde{\mathbb{U}}^{\kappa\lambda}$, is partitioned into the four subblocks like for the first-order matrix in Eq. 4.77. Differentiating Eq. 4.82 and using the normalization condition of the large component results in

$$\begin{aligned} \mathbf{X}^{\kappa,\lambda} = (\mathbf{C}_{S-} - \mathbf{X} \mathbf{C}_{L-}) [& \tilde{\mathbf{U}}_{-+}^{\kappa,\lambda} - \mathbf{U}_{-+}^\kappa \mathbf{U}_{++}^\lambda - \mathbf{U}_{-+}^\lambda \mathbf{U}_{++}^\kappa \\ & - \mathbf{U}_{-+}^\kappa \mathbf{C}_{L+}^\dagger \tilde{\mathbf{S}} \mathbf{C}_{L-} \mathbf{U}_{-+}^\lambda \\ & - \mathbf{U}_{-+}^\lambda \mathbf{C}_{L+}^\dagger \tilde{\mathbf{S}} \mathbf{C}_{L-} \mathbf{U}_{-+}^\kappa] \mathbf{C}_{L+}^\dagger \tilde{\mathbf{S}}. \end{aligned} \quad (4.94)$$

Therefore, only the positronic-electronic block of the second-order orbital rotation matrix is needed whereas also the electronic-electronic block of the first-order orbital rotation matrix is required. Differentiating Eq. (4.73) the second-order orbital rotation matrix is given as^[102,254]

$$\begin{aligned} [\tilde{\mathbb{U}}^{\kappa,\lambda}, \mathbb{E}] = & \tilde{\mathbb{D}}^{\kappa,\lambda} - \tilde{\mathbb{M}}^{\kappa,\lambda} \mathbb{E} - \mathbb{E}^{\kappa,\lambda} \\ & + \mathbb{U}^\kappa [\mathbb{U}^\lambda, \mathbb{E}] + \mathbb{U}^\lambda [\mathbb{U}^\kappa, \mathbb{E}] \\ & + \mathbb{U}^{\dagger,\kappa} (\tilde{\mathbb{D}}^\lambda - \tilde{\mathbb{M}}^\lambda \mathbb{E}) + (\tilde{\mathbb{D}}^\lambda - \tilde{\mathbb{M}}^\lambda \mathbb{E}) \mathbb{U}^\kappa \\ & + \mathbb{U}^{\dagger,\lambda} (\tilde{\mathbb{D}}^\kappa - \tilde{\mathbb{M}}^\kappa \mathbb{E}) + (\tilde{\mathbb{D}}^\kappa - \tilde{\mathbb{M}}^\kappa \mathbb{E}) \mathbb{U}^\lambda. \end{aligned} \quad (4.95)$$

Note that the matrix products in this equation requires all four blocks of the first-order orbital rotation matrix—even for the positronic-electronic block of $\tilde{\mathbb{U}}^{\kappa\lambda}$ only. In Ref. 102, Yoshizawa and co-workers further separated the electronic-electronic block of $\tilde{\mathbb{U}}^\lambda$ and $\tilde{\mathbb{U}}^\kappa$ with the virtual and occupied spinors. However, this is only applicable to molecular calculations with uncontracted basis sets and will not be considered herein. In line with the non-canonical CPHF solver,^[405] we assume

$$\mathbf{E}_{-+}^\lambda = \mathbf{0}_2, \quad (4.96)$$

$$\mathbf{U}_{--}^{\dagger,\lambda} = \mathbf{U}_{--}^\lambda, \quad (4.97)$$

$$\mathbf{U}_{++}^{\dagger,\lambda} = \mathbf{U}_{++}^\lambda. \quad (4.98)$$

This allows to calculate the positronic-positronic and electronic-electronic block of the orbital rotation matrix based on the normalization condition and ensures the numerical stability. The corresponding blocks are computed as

$$\mathbf{U}_{--}^\lambda = -\frac{1}{2} \tilde{\mathbf{M}}_{--}^\lambda, \quad (4.99)$$

$$\mathbf{U}_{++}^\lambda = -\frac{1}{2} \tilde{\mathbf{M}}_{++}^\lambda. \quad (4.100)$$

The expression for the perturbation κ are obtained by interchanging λ and κ . Inserting this into Eq. 4.95 and subsequent simplification, yields the positronic-electronic block of the second-order orbital rotation matrix

$$\begin{aligned}
(\tilde{\mathbf{U}}_{-+}^{\kappa,\lambda})_{kl} = & \frac{1}{(\mathbf{E}_{++})_{ll} - (\mathbf{E}_{--})_{kk}} \left\{ (\tilde{\mathbf{D}}_{-+}^{\kappa,\lambda})_{kl} - (\tilde{\mathbf{M}}_{-+}^{\kappa,\lambda})_{kl} (\mathbf{E}_{++})_{ll} \right. \\
& + (\mathbf{U}_{--}^{\kappa} \mathbf{U}_{-+}^{\lambda} + \mathbf{U}_{-+}^{\kappa} \mathbf{U}_{++}^{\lambda} + \mathbf{U}_{--}^{\lambda} \mathbf{U}_{-+}^{\kappa} + \mathbf{U}_{-+}^{\lambda} \mathbf{U}_{++}^{\kappa})_{kl} (\mathbf{E}_{++})_{ll} \\
& - (\mathbf{U}_{--}^{\kappa} \mathbf{E}_{--} \mathbf{U}_{-+}^{\lambda} + \mathbf{U}_{-+}^{\kappa} \mathbf{E}_{++} \mathbf{U}_{++}^{\lambda} + \mathbf{U}_{--}^{\lambda} \mathbf{E}_{--} \mathbf{U}_{-+}^{\kappa} + \mathbf{U}_{-+}^{\lambda} \mathbf{E}_{++} \mathbf{U}_{++}^{\kappa})_{kl} \\
& + \left[\mathbf{U}_{--}^{\dagger,\kappa} \left((\tilde{\mathbf{D}}_{-+}^{\lambda}) - (\tilde{\mathbf{M}}_{-+}^{\lambda})(\mathbf{E}_{++}) \right) + \mathbf{U}_{-+}^{\dagger,\kappa} \left((\tilde{\mathbf{D}}_{++}^{\lambda}) - (\tilde{\mathbf{M}}_{++}^{\lambda})(\mathbf{E}_{++}) \right) \right]_{kl} \\
& + \left[\left(\tilde{\mathbf{D}}_{--}^{\lambda} - \tilde{\mathbf{M}}_{--}^{\lambda} \mathbf{E}_{--} \right) \mathbf{U}_{-+}^{\kappa} + \left(\tilde{\mathbf{D}}_{-+}^{\lambda} - \tilde{\mathbf{M}}_{-+}^{\lambda} \mathbf{E}_{++} \right) \mathbf{U}_{++}^{\kappa} \right]_{kl} \\
& + \left[\mathbf{U}_{--}^{\dagger,\lambda} \left((\tilde{\mathbf{D}}_{-+}^{\kappa}) - (\tilde{\mathbf{M}}_{-+}^{\kappa})(\mathbf{E}_{++}) \right) + \mathbf{U}_{-+}^{\dagger,\lambda} \left((\tilde{\mathbf{D}}_{++}^{\kappa}) - (\tilde{\mathbf{M}}_{++}^{\kappa})(\mathbf{E}_{++}) \right) \right]_{kl} \\
& \left. + \left[\left(\tilde{\mathbf{D}}_{--}^{\kappa} - \tilde{\mathbf{M}}_{--}^{\kappa} \mathbf{E}_{--} \right) \mathbf{U}_{-+}^{\lambda} + \left(\tilde{\mathbf{D}}_{-+}^{\kappa} - \tilde{\mathbf{M}}_{-+}^{\kappa} \mathbf{E}_{++} \right) \mathbf{U}_{++}^{\lambda} \right]_{kl} \right\}. \quad (4.101)
\end{aligned}$$

The three other blocks of the Dirac matrix and the metric are obtained with the corresponding coefficients similar to Eqs. 4.84 and 4.85.

For the explicit expressions to calculate the second-order orbital rotation matrix, the four blocks of \mathbb{U}_u^B are computed as

$$(\mathbf{U}_{u,--}^B)_{kl} = -\frac{1}{2}(\tilde{\mathbf{M}}_{u,--}^B)_{kl}, \quad (4.102)$$

$$(\mathbf{U}_{u,-+}^B)_{kl} = \frac{(\tilde{\mathbf{D}}_{u,-+}^B)_{kl} - (\tilde{\mathbf{M}}_{u,-+}^B)_{kl} (\mathbf{E}_{++})_{ll}}{(\mathbf{E}_{++})_{ll} - (\mathbf{E}_{--})_{kk}}, \quad (4.103)$$

$$(\mathbf{U}_{u,+-}^B)_{kl} = \frac{(\tilde{\mathbf{D}}_{u,+-}^B)_{kl} - (\tilde{\mathbf{M}}_{u,+-}^B)_{kl} (\mathbf{E}_{--})_{ll}}{(\mathbf{E}_{--})_{ll} - (\mathbf{E}_{++})_{kk}}, \quad (4.104)$$

$$(\mathbf{U}_{u,++}^B)_{kl} = -\frac{1}{2}(\tilde{\mathbf{M}}_{u,++}^B)_{kl}. \quad (4.105)$$

Similarly, the magnetic moment derivatives read

$$(\mathbf{U}_{u,--}^{m_I})_{kl} = \mathbf{0}_2, \quad (4.106)$$

$$(\mathbf{U}_{u,-+}^{m_I})_{kl} = \frac{(\tilde{\mathbf{D}}_{u,-+}^{m_I})_{kl}}{(\mathbf{E}_{++})_{ll} - (\mathbf{E}_{--})_{kk}}, \quad (4.107)$$

$$(\mathbf{U}_{u,+-}^{m_I})_{kl} = \frac{(\tilde{\mathbf{D}}_{u,+-}^{m_I})_{kl}}{(\mathbf{E}_{--})_{ll} - (\mathbf{E}_{++})_{kk}}, \quad (4.108)$$

$$(\mathbf{U}_{u,++}^{m_I})_{kl} = \mathbf{0}_2. \quad (4.109)$$

Therefore, the positronic-electron block of the second-order orbital rotation matrix is calculated according to

$$\begin{aligned}
(\tilde{\mathbf{U}}_{u,v,-+}^{B,m_I})_{kl} = & \frac{1}{(\mathbf{E}_{++})_{ll} - (\mathbf{E}_{--})_{kk}} \left\{ (\tilde{\mathbf{D}}_{u,v,-+}^{B,m_I})_{kl} \right. \\
& + (\mathbf{U}_{v,-+}^{m_I} \mathbf{U}_{u,++}^B + \mathbf{U}_{u,--}^B \mathbf{U}_{v,-+}^{m_I})_{kl} (\mathbf{E}_{++})_{ll} - (\mathbf{U}_{v,-+}^{m_I} \mathbf{E}_{++} \mathbf{U}_{u,++}^B + \mathbf{U}_{u,--}^B \mathbf{E}_{--} \mathbf{U}_{v,-+}^{m_I})_{kl} \\
& + \left[\mathbf{U}_{v,-+}^{\dagger,m_I} \left((\tilde{\mathbf{D}}_{u,++}^B) - (\tilde{\mathbf{M}}_{u,++}^B)(\mathbf{E}_{++}) \right) \right]_{kl} + \left[\left(\tilde{\mathbf{D}}_{u,--}^B - \tilde{\mathbf{M}}_{u,--}^B \mathbf{E}_{--} \right) \mathbf{U}_{v,-+}^{m_I} \right]_{kl} \\
& \left. + \left[\mathbf{U}_{u,--}^{\dagger,B} (\tilde{\mathbf{D}}_{v,-+}^{m_I}) \right]_{kl} + \left[\tilde{\mathbf{D}}_{v,-+}^{m_I} \mathbf{U}_{u,++}^B \right]_{kl} \right\}. \quad (4.110)
\end{aligned}$$

The respective derivative of the decoupling matrix follows as

$$\begin{aligned} X_{u,v}^{B,m_I} = (C_{S-} - X C_{L-}) [& \tilde{U}_{uv,-+}^{B,m_I} - U_{v,-+}^{m_I} U_{u,++}^B \\ & - U_{u,-+}^B C_{L+}^\dagger \tilde{S} C_{L-} U_{v,-+}^{m_I} \\ & - U_{v,-+}^{m_I} C_{L+}^\dagger \tilde{S} C_{L-} U_{u,-+}^B] C_{L+}^\dagger \tilde{S}. \end{aligned} \quad (4.111)$$

Again, all matrix multiplications are computed with DGEMM and the multiplications with the diagonal matrices \mathbf{E}_{--} and \mathbf{E}_{++} are calculated with DAXPY.^[399,400]

4.5 Sylvester Matrix Equations for the Derivatives of the Renormalization Matrix

The derivatives of the renormalization matrix are obtained by solving Sylvester matrix equations. Cheng and Gauss used the product rule for Eq. 2.52 and calculated the respective derivatives of $S^{1/2}$ and $(S^{-1/2} \tilde{S} S^{-1/2})^{-1/2}$ with Sylvester equations.^[108,109] Note that the individual matrices are Hermitian but the renormalization matrix is non-Hermitian. Therefore, this ansatz avoids complex algebra in a scalar-relativistic implementation. However, the number of Sylvester equations to be solved increases considerably for second derivatives. Therefore, the ansatz of Zou *et al.*^[254] is used herein. Here, the positive definiteness and the mathematical structure of the renormalization matrix is exploited to avoid complex algebra in scalar-relativistic calculations. Like in the previous subsection, the general two-component equations are derived and then simplified for the scalar-relativistic NMR shielding tensor. The quadratic form of the renormalization matrix^[96]

$$RR = \tilde{S}^{-1} S \quad (4.112)$$

is used to set up the Sylvester matrix equation as differentiating this equations results in

$$RR^\lambda + R^\lambda R = Q^\lambda \quad (4.113)$$

with the right-hand side

$$Q^\lambda = \tilde{S}^{-1} (S^\lambda - \tilde{S}^\lambda RR). \quad (4.114)$$

Differentiating Eq. 4.112 twice yields the Sylvester matrix equation for second derivatives

$$RR^{\kappa\lambda} + R^{\kappa\lambda} R = Q^{\kappa\lambda} \quad (4.115)$$

with the right-hand side

$$\begin{aligned} Q^{\kappa\lambda} = & \tilde{S}^{-1} \left[S^{\kappa\lambda} - \tilde{S}^{\kappa\lambda} RR + \tilde{S}^\lambda \tilde{S}^{-1} (\tilde{S}^\kappa RR - S^\kappa) + \tilde{S}^\kappa \tilde{S}^{-1} (\tilde{S}^\lambda RR - S^\lambda) \right] \\ & - R^\lambda R^\kappa - R^\kappa R^\lambda. \end{aligned} \quad (4.116)$$

Note that this approach requires to solve only one Sylvester equation for first and second derivatives.

The Sylvester matrix equation can be solved using an eigenvalue decomposition method. Here, the renormalization matrix is diagonalized. For a non-Hermitian matrix, this is done by multiplication with the eigenvectors, V_R . These eigenvectors are obtained by a diagonalization of

$$K = (S^{-1/2} \tilde{S} S^{-1/2})^{-1/2} \quad (4.117)$$

and making use of the transformation in Eq. 2.52,

$$\mathbf{V}_R = \mathbf{S}^{-1/2} \mathbf{V}_K. \quad (4.118)$$

Note that \mathbf{K} is Hermitian and therefore the diagonalization is performed with the standard diagonalization routines DSYEV and ZHEEV.^[396] The eigenvalues of the renormalization matrix are then obtained as

$$\mathbf{r} = \mathbf{V}_R^\dagger \mathbf{R} \mathbf{V}_R, \quad (4.119)$$

where the generalized inverse^[406] of \mathbf{V}_R is defined according to

$$\mathbf{V}_R^\dagger = \left(\mathbf{V}_R^\dagger \mathbf{V}_R \right)^{-1} \mathbf{V}_R^\dagger = \mathbf{V}_R^\dagger \left(\mathbf{V}_R \mathbf{V}_R^\dagger \right)^{-1}. \quad (4.120)$$

Subsequently, the Sylvester matrix is transformed with the eigenbasis of the renormalization matrix to simplify the left-hand side

$$\mathbf{r} \mathbf{R}^\lambda + \mathbf{R}^\lambda \mathbf{r} = \mathbf{V}_R^\dagger \mathbf{Q}^\lambda \mathbf{V}_R. \quad (4.121)$$

This equation is rearranged as the matrix of the eigenvalues \mathbf{r} is diagonal and the Sylvester matrix is solved as

$$(\mathbf{R})_{\mu\nu}^\lambda = \sum_{a,b} \frac{1}{r_a + r_b} (\mathbf{V}_R)_{\mu a} \left[\mathbf{V}_R^\dagger \mathbf{Q}^\lambda \mathbf{V}_R \right]_{ab} \left(\mathbf{V}_R^\dagger \right)_{b\nu}. \quad (4.122)$$

The result is then transformed back to the original basis using \mathbf{V}_R^\dagger and \mathbf{V}_R . The Sylvester matrix for second derivatives is solved in the same manner by replacing \mathbf{Q}^λ with $\mathbf{Q}^{\kappa\lambda}$ and \mathbf{R}^λ with $\mathbf{R}^{\kappa\lambda}$.

The magnetic field derivative of the scalar-relativistic matrix \mathbf{R} is obtained with

$$\mathbf{Q}_u^B = \tilde{\mathbf{S}}^{-1} \left(\mathbf{S}_u^B - \tilde{\mathbf{S}}_u^B \mathbf{R} \mathbf{R} \right) \quad (4.123)$$

and all two-component matrices, \mathbf{M} , above are replaced by the one-component analogues, \mathbf{M} . The derivative with respect to the magnetic moments simplifies to

$$\mathbf{Q}_u^{m_I} = -\tilde{\mathbf{S}}^{-1} \tilde{\mathbf{S}}_u^{m_I} \mathbf{R} \mathbf{R}. \quad (4.124)$$

Here, the perturbed overlap matrix vanishes whereas $\tilde{\mathbf{S}}$ depends on \mathbf{X} and $\mathbf{X}_u^{m_I}$. The mixed second derivative is calculated with the right-hand side

$$\begin{aligned} \mathbf{Q}_{u,v}^{Bm_I} = & \tilde{\mathbf{S}}^{-1} \left[-\tilde{\mathbf{S}}_{u,v}^{B,m_I} \mathbf{R} \mathbf{R} + \tilde{\mathbf{S}}_u^B \tilde{\mathbf{S}}^{-1} \tilde{\mathbf{S}}_v^{m_I} \mathbf{R} \mathbf{R} + \tilde{\mathbf{S}}_v^{m_I} \tilde{\mathbf{S}}^{-1} \left(\tilde{\mathbf{S}}_u^B \mathbf{R} \mathbf{R} - \mathbf{S}_u^B \right) \right] \\ & - \mathbf{R}_u^B \mathbf{R}_v^{m_I} - \mathbf{R}_v^{m_I} \mathbf{R}_u^B. \end{aligned} \quad (4.125)$$

Again, the mixed derivative of the overlap matrix is zero and only the mixed derivative of $\tilde{\mathbf{S}}$ is needed. No complex algebra is employed as both the eigenvalues and eigenvectors of \mathbf{R} are real.^[254] The implementation was checked against the eigenvalue method of Cheng and Gauss^[108,109] and using the LAPACK routine^[396] DTRSYL, which solves the general real Sylvester matrix equation with the canonical Schur form using the LAPACK routine DHSEQR.

4.6 DLU-X2C for NMR Shifts

Applying the DLU scheme to the scalar-relativistic approximation of the X2C Hamiltonian in Eq. 4.34 results in the following equation for the atomic diagonal blocks

$$\begin{aligned} \mathbf{h}_{AA}^+ &= \mathbf{R}_{AA}^\dagger \mathbf{L}_{AA} \mathbf{R}_{AA} \\ &= \mathbf{R}_{AA}^\dagger \left(\mathbf{V}_{AA} + \mathbf{\Pi}_{AA}^\dagger \mathbf{X}_{AA} + \mathbf{X}_{AA}^\dagger \mathbf{\Pi}_{AA} \right) \mathbf{R}_{AA} \\ &\quad + \mathbf{R}_{AA}^\dagger \left[\mathbf{X}_{AA}^\dagger \left(\frac{1}{4c^2} \mathbf{W}_{AA} - \mathbf{T}_{AA} \right) \mathbf{X}_{AA} \right] \mathbf{R}_{AA}. \end{aligned} \quad (4.126)$$

The atomic off-diagonal blocks read

$$\begin{aligned} \mathbf{h}_{AB}^+ &= \mathbf{R}_{AA}^\dagger \mathbf{L}_{AB} \mathbf{R}_{BB} \\ &= \mathbf{R}_{AA}^\dagger \left(\mathbf{V}_{AB} + \mathbf{\Pi}_{AB}^\dagger \mathbf{X}_{BB} + \mathbf{X}_{AA}^\dagger \mathbf{\Pi}_{AB} \right) \mathbf{R}_{BB} \\ &\quad + \mathbf{R}_{AA}^\dagger \left[\mathbf{X}_{AA}^\dagger \left(\frac{1}{4c^2} \mathbf{W}_{AB} - \mathbf{T}_{AB} \right) \mathbf{X}_{BB} \right] \mathbf{R}_{BB}. \end{aligned} \quad (4.127)$$

All matrices are spin-independent and only the atomic diagonal block of the decoupling and the renormalization matrix are required. Note that all blocks of the one-electron integrals are needed and consequently it is necessary to compute all blocks of the integral derivatives for the perturbed DLU-X2C Hamiltonian. Differentiating the atomic diagonal block with respect to the magnetic field results in

$$\mathbf{h}_{u,AA}^B = \mathbf{R}_{u,AA}^{\dagger,B} \mathbf{L}_{AA} \mathbf{R}_{AA} + \mathbf{R}_{AA}^\dagger \mathbf{L}_{u,AA}^B \mathbf{R}_{AA} + \mathbf{R}_{AA}^\dagger \mathbf{L}_{AA} \mathbf{R}_{u,AA}^B \quad (4.128)$$

and the atomic off-diagonal blocks are given as

$$\mathbf{h}_{u,AB}^B = \mathbf{R}_{u,AA}^{\dagger,B} \mathbf{L}_{AB} \mathbf{R}_{BB} + \mathbf{R}_{AA}^\dagger \mathbf{L}_{u,AB}^B \mathbf{R}_{BB} + \mathbf{R}_{AA}^\dagger \mathbf{L}_{AB} \mathbf{R}_{u,AB}^B, \quad (4.129)$$

with the derivative of the respective block of the NESC matrix

$$\begin{aligned} \mathbf{L}_{u,AB}^B &= \mathbf{V}_{u,AB}^B + \mathbf{\Pi}_{u,AB}^{\dagger,B} \mathbf{X}_{BB} + \mathbf{\Pi}_{AB}^\dagger \mathbf{X}_{u,BB}^B + \mathbf{X}_{u,AA}^{\dagger,B} \mathbf{\Pi}_{AB} + \mathbf{X}_{AA}^\dagger \mathbf{\Pi}_{u,AB}^B + \\ &\quad + \mathbf{X}_{u,AA}^{\dagger,B} \left(\frac{1}{4c^2} \mathbf{W}_{AB} - \mathbf{T}_{AB} \right) \mathbf{X}_{BB} + \mathbf{X}_{AA}^\dagger \left(\frac{1}{4c^2} \mathbf{W}_{u,AB}^B - \mathbf{T}_{u,AB}^B \right) \mathbf{X}_{BB} \\ &\quad + \mathbf{X}_{AA}^\dagger \left(\frac{1}{4c^2} \mathbf{W}_{AB} - \mathbf{T}_{AB} \right) \mathbf{X}_{u,BB}^B. \end{aligned} \quad (4.130)$$

The derivatives of atomic diagonal blocks are calculated identically to the full X2C derivatives. Accordingly, employing the DLU-X2C Hamiltonian requires solving the response equations for the perturbed decoupling matrix and the Sylvester matrix equations for the renormalization matrix for the atomic diagonal blocks only. This significantly reduces computational costs as the dimensions of the involved matrices are reduced to the atomic dimensions. Therefore, the computation of these blocks scales as $\mathcal{O}(N)$ with the size of the system, N . The derivative of the atomic off-diagonal blocks are subsequently calculated by ordinary matrix multiplications, which are carried out with DGEMM. The computation of the atomic off-diagonal blocks scales as $\mathcal{O}(N^2)$. Therefore, the calculations of the magnetic-field derivatives comes at nearly the same computational costs as energy calculations. Only the memory requirements are increased as not only the integrals but also the integral derivatives and the atomic diagonal blocks of perturbed decoupling and renormalization matrix are needed.

The derivatives with respect to the magnetic moment are computed similarly. the corresponding derivatives of the DLU-X2C Hamiltonian are

$$\mathbf{h}_{u,AA}^{m_I} = \mathbf{R}_{u,AA}^{\dagger,m_I} \mathbf{L}_{AA} \mathbf{R}_{AA} + \mathbf{R}_{AA}^{\dagger} \mathbf{L}_{u,AA}^{m_I} \mathbf{R}_{AA} + \mathbf{R}_{AA}^{\dagger} \mathbf{L}_{AA} \mathbf{R}_{u,AA}^{m_I} \quad (4.131)$$

and the atomic off-diagonal blocks are given as

$$\mathbf{h}_{u,AB}^{m_I} = \mathbf{R}_{u,AA}^{\dagger,m_I} \mathbf{L}_{AB} \mathbf{R}_{BB} + \mathbf{R}_{AA}^{\dagger} \mathbf{L}_{u,AB}^{m_I} \mathbf{R}_{BB} + \mathbf{R}_{AA}^{\dagger} \mathbf{L}_{AB} \mathbf{R}_{u,BB}^{m_I}, \quad (4.132)$$

with the derivative of the NESC matrix

$$\begin{aligned} \mathbf{L}_{u,AB}^{m_I} = & \mathbf{\Pi}_{u,AB}^{\dagger,m_I} \mathbf{X}_{BB} + \mathbf{\Pi}_{AB}^{\dagger} \mathbf{X}_{u,BB}^{m_I} + \mathbf{X}_{u,AA}^{\dagger,m_I} \mathbf{\Pi}_{AB} + \mathbf{X}_{AA}^{\dagger} \mathbf{\Pi}_{u,AB}^{m_I} + \\ & + \mathbf{X}_{u,AA}^{\dagger,m_I} \left(\frac{1}{4^2} \mathbf{W}_{AB} - \mathbf{T}_{AB} \right) \mathbf{X}_{BB} + \mathbf{X}_{AA}^{\dagger} \left(\frac{1}{4c^2} \mathbf{W}_{AB} - \mathbf{T}_{AB} \right) \mathbf{X}_{u,BB}^{m_I}. \end{aligned} \quad (4.133)$$

For a molecule consisting of N nuclei, the computation time for the atomic diagonal blocks scales as $\mathcal{O}(N^2)$ and $\mathcal{O}(N^3)$ for the off-diagonal blocks. Compared to the magnetic-field derivatives, many integral derivatives are zero, which reduces the computational demands for the calculations of a single derivative. The derivatives with respect to different magnetic moments are independent and are thus computed separately to reduce the memory demands.

Further differentiation of the above equations yields the mixed derivatives. The mixed derivatives of the atomic diagonal block for the unperturbed density contribution read

$$\begin{aligned} \mathbf{h}_{u,v,AA}^{B,m_I} = & \mathbf{R}_{u,v,AA}^{\dagger,B,m_I} \mathbf{L}_{AA} \mathbf{R}_{AA} + \mathbf{R}_{u,AA}^{\dagger,B} \mathbf{L}_{v,AA}^{m_I} \mathbf{R}_{AA} + \mathbf{R}_{u,AA}^{\dagger,B} \mathbf{L}_{AA} \mathbf{R}_{v,AA}^{m_I} \\ & + \mathbf{R}_{v,AA}^{\dagger,m_I} \mathbf{L}_{u,AA}^B \mathbf{R}_{AA} + \mathbf{R}_{AA}^{\dagger} \mathbf{L}_{u,v,AA}^{B,m_I} \mathbf{R}_{AA} + \mathbf{R}_{AA}^{\dagger} \mathbf{L}_{u,AA}^B \mathbf{R}_{v,AA}^{m_I} \\ & + \mathbf{R}_{v,AA}^{\dagger,m_I} \mathbf{L}_{AA} \mathbf{R}_{u,AA}^B + \mathbf{R}_{AA}^{\dagger} \mathbf{L}_{v,AA}^{m_I} \mathbf{R}_{u,AA}^B + \mathbf{R}_{AA}^{\dagger} \mathbf{L}_{AA} \mathbf{R}_{u,v,AA}^{B,m_I} \end{aligned} \quad (4.134)$$

and the off-diagonal blocks are given as

$$\begin{aligned} \mathbf{h}_{u,v,AB}^{B,m_I} = & \mathbf{R}_{u,v,AA}^{\dagger,B,m_I} \mathbf{L}_{AB} \mathbf{R}_{BB} + \mathbf{R}_{u,AA}^{\dagger,B} \mathbf{L}_{v,AB}^{m_I} \mathbf{R}_{BB} + \mathbf{R}_{u,AA}^{\dagger,B} \mathbf{L}_{AB} \mathbf{R}_{v,BB}^{m_I} \\ & + \mathbf{R}_{v,AA}^{\dagger,m_I} \mathbf{L}_{u,AB}^B \mathbf{R}_{BB} + \mathbf{R}_{AA}^{\dagger} \mathbf{L}_{u,v,AB}^{B,m_I} \mathbf{R}_{BB} + \mathbf{R}_{AA}^{\dagger} \mathbf{L}_{u,AB}^B \mathbf{R}_{v,BB}^{m_I} \\ & + \mathbf{R}_{v,AA}^{\dagger,m_I} \mathbf{L}_{AB} \mathbf{R}_{u,BB}^B + \mathbf{R}_{AA}^{\dagger} \mathbf{L}_{v,AB}^{m_I} \mathbf{R}_{u,BB}^B + \mathbf{R}_{AA}^{\dagger} \mathbf{L}_{AB} \mathbf{R}_{u,v,BB}^{B,m_I}. \end{aligned} \quad (4.135)$$

The second derivatives of the NESC matrix read

$$\begin{aligned} \mathbf{L}_{u,v,AB}^{B,m_I} = & \mathbf{\Pi}_{u,v,AB}^{\dagger,B,m_I} \mathbf{X}_{BB} + \mathbf{\Pi}_{u,AB}^{\dagger,B} \mathbf{X}_{v,BB}^{m_I} + \mathbf{\Pi}_{v,AB}^{\dagger,m_I} \mathbf{X}_{u,BB}^B + \mathbf{\Pi}_{AB}^{\dagger} \mathbf{X}_{u,v,BB}^{B,m_I} \\ & + \mathbf{X}_{u,v,AA}^{\dagger,B,m_I} \mathbf{\Pi}_{AB} + \mathbf{X}_{u,AA}^{\dagger,B} \mathbf{\Pi}_{v,AB}^{m_I} + \mathbf{X}_{v,AA}^{\dagger,m_I} \mathbf{\Pi}_{u,AB}^B + \mathbf{X}_{AA}^{\dagger} \mathbf{\Pi}_{u,v,AB}^{B,m_I} \\ & + \mathbf{X}_{u,v,AA}^{\dagger,B,m_I} \left(\frac{1}{4c^2} \mathbf{W}_{AB} - \mathbf{T}_{AB} \right) \mathbf{X}_{BB} + \mathbf{X}_{v,AA}^{\dagger,m_I} \left(\frac{1}{4c^2} \mathbf{W}_{u,AB}^B - \mathbf{T}_{u,AB}^B \right) \mathbf{X}_{BB} \\ & + \mathbf{X}_{u,AA}^{\dagger,B} \left(\frac{1}{4c^2} \mathbf{W}_{AB} - \mathbf{T}_{AB} \right) \mathbf{X}_{v,BB}^{m_I} + \mathbf{X}_{v,AA}^{\dagger,m_I} \left(\frac{1}{4c^2} \mathbf{W}_{AB} - \mathbf{T}_{AB} \right) \mathbf{X}_{u,BB}^B \\ & + \mathbf{X}_{AA}^{\dagger} \left(\frac{1}{4c^2} \mathbf{W}_{u,AB}^B - \mathbf{T}_{u,AB}^B \right) \mathbf{X}_{v,BB}^{m_I} + \mathbf{X}_{AA}^{\dagger} \left(\frac{1}{4c^2} \mathbf{W}_{AB} - \mathbf{T}_{AB} \right) \mathbf{X}_{u,v,BB}^{B,m_I}. \end{aligned} \quad (4.136)$$

Therefore, the three first and second-order derivatives of all atomic blocks are needed to compute the atomic off-diagonal blocks. Additionally, all first and second integral derivatives are required. The computational algorithms for the DLU-X2C approach to NMR shieldings are based on the geometry gradients.^[106,107] A nuclear selection scheme is available for the derivatives with respect to the nuclear magnetic moments.^[407,408]

The algorithm is presented in Fig. 4.1 for the unperturbed density contribution. The following steps are performed for every nucleus of interest as it improves the readability of the code and allows for an easier maintenance. The computation time of the initialization steps and all steps of the unperturbed quantities is negligible for analytical derivatives.^[106,107] First, the necessary initialization steps are performed. The modules process contracted basis sets and therefore the information of the uncontracted basis sets needs to be gathered in a first step together with the setup of the matrix for the transformation from Cartesian to spherical basis functions (CAO-AO transformation). Next, unperturbed integrals are calculated in the CAO basis and the integral batches are transformed into the AO basis on the fly. Heavy elements necessitate basis functions with a large angular momentum and consequently storing the matrices in the AO basis significantly reduces the memory demands. The integral evaluation supports the OpenMP scheme for a shared memory parallelization. In the uncontracted basis space, every field of the integral array is calculated in one shot without the need to sum up the contributions of different primitive basis functions. Therefore, no OMP ATOMIC and OMP CRITICAL directives are required to avoid race conditions. These directives avoid that multiple thread simultaneously change the value of an array. Then, the atomic information for the DLU scheme is supplied, i.e. the center of every basis function and the mapping of the indices is generated.

After these initialization steps, the program loops over the atomic diagonal blocks and performs the X2C decoupling. The loop is parallelized with OpenMP. In this loop, the near-linear dependencies are removed by a diagonalization of the overlap matrix with the LAPACK routine^[396] DSPEV and subsequently removing all eigenvectors referring to an eigenvalue smaller than $5 \cdot 10^{-14}$. This value was optimized with general-contracted basis sets and ensures the numerical stability of the inverse of C_+^L . The relativistic decoupling of the atomic diagonal blocks is performed in the linear-independent AO (IAO) basis using the LAPACK routine^[396] DSYGV. All quantities for the DLU-X2C Hamiltonian derivatives are accumulated on a vector. In principle, the integrals may be also calculated within the loop, however, this would result in a decreased efficiency of the parallelization of the integrals as the number of basis functions is significantly larger than the number of atoms.

For the perturbed quantities, all integral derivatives are first calculated in an OpenMP framework similar to the unperturbed integrals. Then, the derivatives of the atomic diagonal blocks of the Hamiltonian are computed. Again, the loop over atoms is parallelized with OpenMP. The derivative of the Hamiltonian and all other X2C response quantities are obtained in the IAO basis and then transformed to the AO basis. The derivatives of the decoupling and the renormalization matrix are collected on a second vector for the atomic off-diagonal blocks. The atomic off-diagonal block of the Hamiltonian derivative is computed with matrix multiplications in the AO basis. Note that due to the hermiticity of the perturbed Hamiltonian, the loop over the atomic off-diagonal blocks exploits the permutation symmetry and the adjoint of the perturbed Hamiltonian of a pair AB is obtained based on the antisymmetry of the perturbed Hamiltonian. This loop also supports the OpenMP architecture. After computing all atomic diagonal and off-diagonal blocks, the perturbed Hamiltonian is transformed to the CAO basis as the density is stored in this basis. The perturbed Hamiltonian is then contracted and the trace with the density is formed simultaneously. This step is parallelized with OpenMP using the OMP REDUCTION clause for the NMR shielding tensor to avoid race conditions. Therefore, each thread uses its own array and the contributions are added after the complete parallel calculation. The respective increase of the memory demands is absolutely negligible due to the dimension of the shielding tensor.

Calculate unperturbed density contribution of the NMR shielding tensor:

$$\text{tr} \left(\mathbf{D} \frac{\partial^2 \mathbf{h}}{\partial B_u \partial m_{I,v}} \right)_0 \quad \text{with } u, v \in \{x, y, z\}$$

Initialization

1. Initialization of transformations and uncontracted basis set
2. Calculate all unperturbed integrals: $\mathbf{S}, \mathbf{T}, \mathbf{V}, \mathbf{W}^0$ in CAO basis and transformation to spherical AO basis on the fly
3. Initialize atomic information for DLU scheme

Unperturbed quantities

4. **Loop** over atomic diagonal blocks
 - a) Get atomic diagonal blocks of $\mathbf{S}, \mathbf{T}, \mathbf{V}, \mathbf{W}^0$
 - b) Diagonalize overlap matrix and remove linear dependencies
 - c) Transformation to linear-independent AO (IAO) basis
 - d) Perform X2C decoupling step and obtain the matrices $\mathbf{X}, \mathbf{R}, \tilde{\mathbf{S}}, \mathbf{V}_R, \mathbf{r}, \mathbf{L}$ etc.
 - e) Collect the atomic diagonal blocks of $\mathbf{X}, \mathbf{R}, \mathbf{L}, \tilde{\mathbf{S}}, \tilde{\mathbf{S}}^{-1}, \mathbf{V}_R, \mathbf{V}_R^\dagger, \mathbf{C}_-^L, \mathbf{C}_+^L, \mathbf{C}_-^S, \mathbf{C}_+^S, \mathbf{E}_{--}, \mathbf{E}_{++}$, and the AO-IAO transformation matrix on a vector
5. **End loop** over atomic diagonal blocks

Perturbed quantities

6. Compute all integral derivatives: $\mathbf{S}^B, \mathbf{\Pi}^B, \mathbf{V}^B, \mathbf{W}^{0,B}, \mathbf{\Pi}^m, \mathbf{\Pi}^{B,m}$ in CAO and transformation to spherical AO on the fly
7. **Loop** over Cartesian directions u
 - a) **Loop** over Cartesian directions v
 - i. **Loop** over atomic diagonal blocks
 - A. Read atomic diagonal quantities on vector
 - B. Get atomic diagonal blocks of integral derivatives
 - C. Transformation to IAO basis
 - D. Compute mixed derivative of Hamiltonian and back-transformation to AO basis
 - E. Collect quantities for atomic off-diagonal blocks on another vector: $\mathbf{X}^B, \mathbf{R}^B, \mathbf{X}^m, \mathbf{R}^m, \mathbf{X}^{B,m}, \mathbf{R}^{B,m}$
 - ii. **End Loop** over atomic diagonal blocks
 - iii. **Loop** over atomic off-diagonal blocks
 - A. Read atomic diagonal quantities on vectors
 - B. Get atomic off-diagonal blocks of integral derivatives
 - C. Perform matrix multiplications for off-diagonal block of DLU-X2C Hamiltonian
 - D. Form conjugate transpose of atomic off-diagonal block
 - iv. **End Loop** over atomic off-diagonal blocks
 - v. Transform derivative of Hamiltonian to CAO basis
 - vi. Perform contraction of Hamiltonian derivative
 - vii. Form trace with unperturbed density
 - b) **End Loop** over Cartesian direction v
8. **End Loop** over Cartesian direction u

Figure 4.1: Algorithm for the calculation of the unperturbed density contribution of the NMR shielding tensor with the DLU-X2C Hamiltonian. The sorting steps for the DLU-X2C Hamiltonian are omitted for clarity.

4.7 Coupled-Perturbed Hartree–Fock and Kohn–Sham Equations

This section reviews the CPHF and CPKS equations for NMR shielding tensors.^[397,398,403–405,409–412] The one-electron X2C scheme presented in the previous sections is integrated into the non-relativistic machinery by replacing the non-relativistic integral derivatives with the scalar-relativistic X2C or DLU-X2C Hamiltonian derivatives. Therefore, the existing program code regarding the two-electron integrals and the CPHF/CPKS solver^[14,398,407,413–416] are unaffected by the changes. As all first derivatives are purely imaginary and antisymmetric, the imaginary unit may be explicitly written to employ real matrices.^[14] However, it is more convenient to use the imaginary matrices and complex LCAO coefficients for the next chapters. This allows for a straightforward generalization of the CPHF and CPKS equations to a two-component framework. In a closed-shell restricted Hartree–Fock formalism, the density matrix of Eq. 3.20 becomes

$$D_{\mu\nu}^{\lambda} = 2 \sum_i^{N/2} C_{\mu i}^* C_{\nu i} \quad (4.137)$$

as all orbitals are either doubly occupied or unoccupied. The perturbed density matrix is obtained by a straightforward differentiation of Eq. 4.137

$$D_{\mu\nu}^{\lambda} = 2 \sum_i^{N/2} (C_{\mu i}^{\lambda*} C_{\nu i} + C_{\mu i}^* C_{\nu i}^{\lambda}) \quad (4.138)$$

with the short-hand notation $\lambda = B_u$. Similar to Sec. 4.4, the perturbed coefficients are assumed as a linear combination of the unperturbed coefficients

$$C_{\mu i}^{\lambda} = \sum_p C_{\mu p} O_{pi}^{\lambda} = \sum_j C_{\mu j} O_{ji}^{\lambda} + \sum_a C_{\mu a} O_{ai}^{\lambda}, \quad (4.139)$$

where i, j, \dots refer to occupied orbitals, a, b, \dots to virtual orbitals, and p, q, \dots to arbitrary orbitals. O_{pi}^{λ} denotes the unitary orbital rotation matrix and is partitioned into an occupied-occupied tensor space and a virtual-occupied tensor space. The virtual-virtual tensor space of the orbital rotation matrix does not contribute. Differentiating the Roothaan–Hall equations for Hartree–Fock followed by multiplication with $C_{\mu p}^*$ from the left results in

$$\begin{aligned} \sum_{\mu,\nu} C_{\mu p}^* (F_{\mu\nu}^{\lambda} - \epsilon_i S_{\mu\nu}^{\lambda} C_{\nu i}) &= \sum_p \sum_{\mu,\nu} C_{\mu q}^* (\epsilon_i S_{\mu\nu} C_{\nu p} O_{pi}^{\lambda} - \epsilon_p S_{\mu\nu} C_{\nu p} O_{pi}^{\lambda}) \\ &= \sum_p (\epsilon_i - \epsilon_p) \delta_{pq} O_{pi}^{\lambda} \\ &= (\epsilon_i - \epsilon_q) O_{qi}^{\lambda}. \end{aligned} \quad (4.140)$$

Similarly, differentiating the normalization condition yields

$$\begin{aligned} - \sum_{\mu,\nu} C_{\mu i}^* S_{\mu\nu}^{\lambda} C_{\nu j} &= \sum_p \sum_{\mu,\nu} C_{\mu p}^* O_{pi}^{*\lambda} S_{\mu\nu} C_{\nu j} + C_{\mu i}^* S_{\mu\nu} C_{\nu p} O_{pj}^{\lambda} \\ &= \sum_p (O_{pi}^{*\lambda} \delta_{pj} + O_{pj}^{\lambda} \delta_{pi}) \\ &= (O_{ji}^{*\lambda} + O_{ij}^{\lambda}). \end{aligned} \quad (4.141)$$

These equations are called coupled-perturbed Hartree–Fock equations and form an under-constrained linear system of equations. Therefore, additional assumptions are necessary. Assuming $O_{ji}^{*\lambda} = O_{ij}^{\lambda}$ [405] allows to compute the occupied-occupied block according to

$$O_{ij}^{\lambda} = -\frac{1}{2} \sum_{\mu,\nu} C_{\mu i}^{*} S_{\mu\nu}^{\lambda} C_{\nu j} = -\frac{1}{2} S_{ij}^{\lambda}. \quad (4.142)$$

Therefore, an explicit and numerically stable expression for the occupied-occupied block of the orbital rotation matrix is found. The elements of the virtual-occupied block read

$$O_{ai}^{\lambda} = \frac{F_{ai}^{\lambda} - \epsilon_i S_{ai}^{\lambda}}{\epsilon_i - \epsilon_a}. \quad (4.143)$$

The gap between the occupied and the virtual orbitals is usually large enough to avoid numerical inaccuracies for closed-shell systems. Note that the perturbed Fock matrix depends on the perturbed density and thus on the orbital rotation matrix according to

$$F_{\mu\nu}^{\lambda} = h_{\mu\nu}^{\lambda} + \sum_{\kappa,\omega} (D_{\kappa\omega}^{\lambda} G_{\mu\nu\kappa\omega} + D_{\kappa\omega} G_{\mu\nu\kappa\omega}^{\lambda}), \quad (4.144)$$

$$G_{\mu\nu\kappa\omega} = \sum_{\kappa,\omega} (\mu\nu|\kappa\omega) - \frac{1}{2} (\mu\omega|\kappa\nu), \quad (4.145)$$

where $G_{\mu\nu\kappa\omega}$ indicates the two-electron integrals, i.e. the Coulomb and exchange integrals in HF. Therefore, an iterative approach is required to solve the CPHF equations. The occupied-occupied response of the density is already explicitly defined with the perturbed overlap matrix. Thus, Eq. 4.143 may be partitioned into a left-hand side (LHS), which depends on the occupied-virtual block of the orbital rotation matrix, and a right-hand side (RHS), which is independent of O_{ai}^{λ} , [417]

$$(\epsilon_i - \epsilon_a) O_{ai}^{\lambda} - G_{ai}[O_{bj}^{\lambda}] = \text{RHS}_{ai}^{\lambda} \quad (4.146)$$

with the right-hand side

$$\text{RHS}_{ai}^{\lambda} = F_{ai}^{\lambda}[D] - \epsilon_i S_{ai}^{\lambda} + G_{ai}[O_{jk}^{\lambda}]. \quad (4.147)$$

Here, $F_{ai}^{\lambda}[D]$ denotes the integral derivatives of the Fock matrix with the unperturbed density matrix. $G_{ai}[O_{bj}^{\lambda}]$ and $G_{ai}[O_{ij}^{\lambda}]$ indicate that the two-electron integrals are obtained using the occupied-virtual and the occupied-occupied orbital rotation matrix to calculate the perturbed density matrix, $D_{\mu\nu}^{\lambda}$. The Coulomb integrals for the terms $G_{ai}[O_{bj}^{\lambda}]$ and $G_{ai}[O_{ij}^{\lambda}]$ vanish as the perturbed density matrix is imaginary and antisymmetric whereas the Coulomb integrals are real and symmetric. The RHS contribution $G_{\mu\nu}[O_{jk}^{\lambda}]$ reads

$$\begin{aligned} G_{\mu\nu}[O_{jk}^{\lambda}] &= -\frac{1}{2} \sum_{\kappa,\lambda} \sum_{j,k} 2 \left[C_{\kappa k}^{*} O_{kj}^{*\lambda} C_{\omega j} + C_{\kappa j}^{*} C_{\omega k} O_{kj}^{\lambda} \right] (\mu\omega|\kappa\nu) \\ &= \frac{1}{2} \sum_{\kappa,\lambda} \sum_{j,k} \left[C_{\kappa k}^{*} S_{kj}^{*\lambda} C_{\omega j} + C_{\kappa j}^{*} C_{\omega k} S_{kj}^{\lambda} \right] (\mu\omega|\kappa\nu) \end{aligned} \quad (4.148)$$

and $G_{ai}[O_{jk}^{\lambda}]$ is obtained by a transformation to the MO space. Similarly, $G_{\mu\nu}[O_{bj}^{\lambda}]$ is given as

$$G_{\mu\nu}[O_{bj}^{\lambda}] = -\frac{1}{2} \sum_{\kappa,\lambda} \sum_{a,j} 2 \left[C_{\kappa a}^{*} O_{aj}^{*\lambda} C_{\omega i} + C_{\kappa j}^{*} C_{\omega a} O_{aj}^{\lambda} \right] (\mu\omega|\kappa\nu) \quad (4.149)$$

and $G_{ai}[O_{bj}^{\lambda}]$ is again obtained by transformation to the MO space.

For the CPKS equations, the exchange-correlation potential is considered in the Fock matrix

$$G_{\mu\nu\kappa\omega} = \sum_{\kappa,\omega} [(\mu\nu|\kappa\omega) D_{\kappa\omega}] + V_{XC,\mu\nu}. \quad (4.150)$$

The terms $G_{ai}[O_{bj}^\lambda]$ and $G_{ai}[O_{ij}^\lambda]$ include the matrix representation of the exchange-correlation kernel instead of the exchange integrals. The XC kernel is defined as

$$f^{XC} = \frac{\partial^2 E_{XC}}{\partial \rho(\vec{r}) \partial \rho(\vec{r}')}. \quad (4.151)$$

In the uncoupled approximation^[418,419] the exchange-correlation energy depends on the density and its derivatives but not on the current density. Therefore, the XC kernel term vanishes as the perturbed density matrix is purely imaginary and antisymmetric whereas the XC kernel is symmetric. The CPKS equations of “pure” density functional approximations are consequently solved in a single step as $G_{ai}[O_{bj}^\lambda]$ is zero.

The latter equations can be cast into a matrix form to show the connection to time-dependent density functional theory^[420–422] (TD-DFT)

$$\begin{pmatrix} \mathbf{A} & \mathbf{B} \\ \mathbf{B}^* & \mathbf{A}^* \end{pmatrix} \begin{pmatrix} \mathbf{X} \\ \mathbf{Y} \end{pmatrix} = \begin{pmatrix} \mathbf{P}^\nu \\ \mathbf{P}^{\nu*} \end{pmatrix} \quad (4.152)$$

with the matrices

$$A_{ia,jb} = (\epsilon_a - \epsilon_i) \delta_{ij} \delta_{ab} + C_{ia,jb}, \quad (4.153)$$

$$B_{ia,jb} = C_{ia,bj}. \quad (4.154)$$

In a non-relativistic and scalar-relativistic formalism, these matrices are Hermitian. Note that (ia) and (jb) are the combined indices. The coupling matrix $C_{pq,rs}$ is defined as

$$C_{pq,rs} = \begin{cases} (pq|f^H|sr) - (pr|f^H|sq) & \text{for HF} \\ (pq|f^H|sr) + (pq|f^{XC}|sr) & \text{for DFT} \end{cases} \quad (4.155)$$

with the Hartree and the XC kernel. Here, the Hartree kernel is defined as

$$f^H = \frac{1}{|\vec{r}_1 - \vec{r}_2|} \quad (4.156)$$

and the exchange-correlation kernel is defined in Eq. 4.151. \mathbf{P} collects the elements of the RHS.

4.8 Magnetically Induced Current Densities

As shown in the last section, the magnetic perturbation induces a response of density matrix and thus the electron density of the molecule. In compounds with a cyclic delocalized π -system, this creates a ring current in analogy to Ampère’s circuital law of classical mechanics. In the following, the gauge-including magnetically induced current (GIMIC) method^[19,423,424] to calculate the ring current of a quantum chemical system is briefly derived.

In the presence of a homogeneous external magnetic field, \vec{B} , and the nuclear magnetic moments, \vec{m}_I , the wave function can be generally expanded as^[425]

$$\Psi = \Psi^{(0)} + \sum_{u=x,y,z} \Psi^{B_u} B_u + \sum_I \sum_{u=x,y,z} \Psi^{m_{I,u}} m_{I,u} + \dots \quad (4.157)$$

with the field free wave function $\Psi^{(0)}$. The current density may be expanded in a similar manner as the wave function. Considering the magnetic field only yields

$$j_u = j_u^{(0)} + j_u^{B_v} B_v + \dots, \quad (4.158)$$

where $j_u^{B_v}$ is the current density susceptibility—usually denoted magnetically induced current density for simplicity. The current density response with respect to the magnetic moments can be written in a similar form^[16,425]

$$j_v = j_v^{(0)} + j_v^{m_{I,v}} m_{I,v} + \dots \quad (4.159)$$

In analogy to classical electrodynamics,^[387,388] the second-order interaction energy can be expressed with the first-order induced current densities as^[16,425,426]

$$E^{B,B} = \frac{1}{2} \int \vec{A}^B(\vec{r}) \cdot \vec{j}^B(\vec{r}) d\vec{r}, \quad (4.160)$$

$$E^{m_I,B} = - \int \vec{A}_I^m(\vec{r}) \cdot \vec{j}^B(\vec{r}) d\vec{r} = - \int \vec{A}_B(\vec{r}) \cdot \vec{j}^{m_I}(\vec{r}) d\vec{r}, \quad (4.161)$$

$$E^{m_P,m_Q} = - \int \vec{A}_P^m(\vec{r}) \cdot \vec{j}^{m_Q}(\vec{r}) d\vec{r} = - \int \vec{A}_Q^m(\vec{r}) \cdot \vec{j}^{m_P}(\vec{r}) d\vec{r}, \quad (4.162)$$

where Schwarz's theorem was used. Therefore, the nuclear magnetic shielding tensor can be evaluated with a Biot–Savart-like expression as

$$\sigma_{uv}^I = \frac{\partial^2 E^{m_I,B}}{\partial m_{I,u} \partial B_v} = -\epsilon_{uwt} \int \frac{(r_w - R_{I,w})}{|\vec{r} - \vec{R}_I|^3} \frac{\partial j_t(\vec{r})}{\partial B_v} d\vec{r} \quad (4.163)$$

with the Levi–Civita tensor ϵ_{uwt} and the point-charge model. Assuming the Biot–Savart-like expression and the quantum chemical expression yield the same results, Eqs. 4.19 and 4.163 allow to calculate the magnetically induced current density by rearranging the equations. In non-relativistic quantum chemistry, the magnetically induced current density is obtained as^[423]

$$\begin{aligned} \frac{\partial j_u(\vec{r})}{\partial B_v} &= \sum_{\mu\nu} D_{\mu\nu} \frac{\partial \lambda_\mu^*(\vec{B}, \vec{r})}{\partial B_v} \frac{\partial \tilde{h}(\vec{r})}{\partial m_{I,u}} \lambda_\nu(\vec{B}, \vec{r}) \\ &+ \sum_{\mu\nu} D_{\mu\nu} \lambda_\mu^*(\vec{B}, \vec{r}) \frac{\partial \tilde{h}(\vec{r})}{\partial m_{I,u}} \frac{\partial \lambda_\nu(\vec{B}, \vec{r})}{\partial B_v} \\ &+ \sum_{\mu\nu} \frac{\partial D_{\mu\nu}}{\partial B_v} \lambda_\mu^*(\vec{B}, \vec{r}) \frac{\partial \tilde{h}(\vec{r})}{\partial m_{I,u}} \lambda_\nu(\vec{B}, \vec{r}) \\ &- \epsilon_{uwt} \left[\sum_{\mu\nu} D_{\mu\nu} \lambda_\mu^*(\vec{B}, \vec{r}) \frac{\partial^2 \tilde{h}(\vec{r})}{\partial m_{I,u} \partial B_t} \lambda_\nu(\vec{B}, \vec{r}) \right] \end{aligned} \quad (4.164)$$

with the non-singular Hamiltonian operator derivatives

$$\frac{\partial \tilde{h}(\vec{r})}{\partial m_{I,u}} = (\vec{r} - \vec{R}_I) \times \hat{p}, \quad (4.165)$$

$$\frac{\partial^2 \tilde{h}(\vec{r})}{\partial m_{I,u} \partial B_v} = \frac{1}{2} \left((\vec{r} - \vec{R}_O) \cdot (\vec{r} - \vec{R}_I) \delta_{uv} - (\vec{r} - \vec{R}_O)_u \cdot (\vec{r} - \vec{R}_N)_v \right). \quad (4.166)$$

The gauge-origin dependence is removed with GIAOs as the derivative of the GIAOs also result in a gauge-origin dependence and the individual dependencies cancel each other. Eq. 4.164 only contains the density matrix and the perturbed density matrix as well as the values of basis function (derivatives) and the Hamiltonian derivatives at a certain point in space. Thus, the magnetically induced current density is calculated on a grid. The current strength is then obtained by numerical integration along a plane. The density matrix and the perturbed density matrix are available from NMR shift calculations with a quantum chemistry program suite as described in Sec. 4.7. Following, the magnetically induced current density is computed on a grid with the GIMIC code,^[427] which also calculates the basis function (derivatives) and the Hamiltonian derivatives. A fully consistent X2C treatment of the magnetically induced current density would require to replace the derivatives of the Hamiltonian operator in Eq. 4.164. However, the X2C Hamiltonian is only accessible in matrix form. Thus, a fully consistent X2C approach requires major modifications of the GIMIC program. Moreover, the most important ingredient for the magnetic response of the current density is the perturbed density matrix of a NMR shielding calculation. Herein, we evaluate Eq. 4.164 without the complete X2C picture-change correction.

5 Quasirelativistic NMR Indirect Spin–Spin Coupling Constants

The NMR indirect spin–spin coupling constant (SSCC) describes the splitting of the NMR shifts based on the molecular environment. The theoretical framework was developed by Ramsey in a non-relativistic theory.^[428] The NMR coupling constants consists of four contributions, namely the paramagnetic spin–orbit (PSO) term, the Fermi-contact (FC) interactions, the spin-dipole (SD) term, and the diamagnetic spin–orbit integrals. The FC and SD term are spin-dependent^[429] and therefore only arise in a quasirelativistic X2C framework. Recently, Yoshizawa presented an X2C implementation of NMR coupling constants at the HF and MP2 level of theory.^[430] However, results were only presented for diatomic molecules and the finite nuclear size effects of the vector potential were neglected. Therefore, an efficient implementation in a DFT framework with the finite nucleus model for both the scalar and the vector potential is presented in this work. The implementation was carried out in collaboration with Fabian Mack,^[431] who interfaced the relativistic routines to the existing infrastructure for NMR coupling constants.^[432]

The chapter is structured as follows. After a formal definition of the NMR coupling constant and a discussion of the balance condition in Sec. 5.1, the derivatives of the X2C Hamiltonian are derived in Sec. 5.2 and the DLU scheme is introduced in Sec. 5.3. The relativistic integrals are compared to the non-relativistic theory in Sec. 5.4.

5.1 Definition and Balance Condition

In the Taylor expansion of the electronic energy E in Eq. 4.12, the NMR indirect nuclear spin–spin coupling tensor is given as the second derivative with respect to the magnetic moments of the nuclei M and N in the limit of a vanishing perturbation ($m_{M,u} = m_{N,v} = 0$). This defines the reduced NMR coupling tensor

$$(\mathbf{K}_{M,N})_{uv} = \left(\frac{\partial^2 E}{\partial m_{M,u} \partial m_{N,v}} \right)_0 = \text{Tr} (\mathbf{D} \mathbf{h}_{u,v}^{M,N}) + \text{Tr} (\mathbf{D}_u^M \mathbf{h}_v^N) \quad (5.1)$$

introducing the short-hand notation

$$\mathbf{h}_{u,v}^{M,N} = \left(\frac{\partial^2 \mathbf{h}}{\partial m_{M,u} \partial m_{N,v}} \right)_{m_{M,u}=m_{N,v}=0} \quad (5.2)$$

and the (isotropic) reduced coupling constant, K_{MN} , is defined as the average of the diagonal elements of the (3×3) matrix $\mathbf{K}_{M,N}$. The reduced coupling constant is commonly given in units of 10^{19} T J^{-2} . The equation for the coupling constant is of the same structural form as for the NMR shielding constant. One of the two terms depends on the density matrix and the second derivative of the Hamiltonian, whereas the other term includes the response of the density matrix. The calculation of the perturbed density matrix is described in detail in the next chapter based on the generalized CPHF and CPKS equations.

In experimental measurements, the coupling constant J_{MN} in Hz is the quantity of interest and the corresponding coupling tensor is defined as

$$(\mathbf{J}_{M,N})_{uv} = h \frac{\gamma_M}{2\pi} \frac{\gamma_N}{2\pi} (\mathbf{K}_{M,N})_{uv} \quad (5.3)$$

with the gyromagnetic ratio γ_M of a given nucleus M .^[432–434] The isotropic coupling constant, J_{MN} , is given as

$$J_{MN} = \frac{1}{3} \left((\mathbf{J}_{M,N})_{xx} + (\mathbf{J}_{M,N})_{yy} + (\mathbf{J}_{M,N})_{zz} \right), \quad (5.4)$$

whereas the anisotropic contribution reads

$$\Delta J_{MN} = \sqrt{\frac{3}{2} \left(\frac{1}{4} \sum_{u,v} ((\mathbf{J}_{MN})_{uv} + (\mathbf{J}_{MN})_{vu})^2 - 3J_{MN}^2 \right)}. \quad (5.5)$$

The nuclear magnetic moments, i.e. the magnetic perturbation, is introduced in the Dirac Hamiltonian with the principle of minimal coupling^[386]

$$\hat{p} \longrightarrow \hat{\pi} = \hat{p} + \frac{1}{c} \hat{A} = \hat{p} + \frac{1}{c} \sum_M \hat{A}_M, \quad (5.6)$$

where the vector potential, \vec{A}_M , of the nucleus M is defined as in Eq. 4.6,

$$\vec{A}_M(\vec{r}) = -\vec{m}_M \times \vec{\nabla} \mathcal{G}_M(\vec{r}) \quad \text{with} \quad \mathcal{G}_M(\vec{r}) = \int \frac{w_M(\vec{R}_M)}{|\vec{r} - \vec{R}|} d\vec{R}, \quad (5.7)$$

where \vec{R}_M denotes the position of the nucleus M .

To ensure the exact non-relativistic limit, the RKB condition is generalized to the RMB condition including the nuclear magnetic moments similar to NMR shifts as discussed in Sec. 4.2. The basis set expansion in a restricted magnetically balanced basis set reads^[60]

$$|\psi_i^L\rangle = \sum_{\mu} c_{\mu i}^L |\phi_{\mu}\rangle, \quad (5.8)$$

$$|\psi_i^S\rangle = \sum_{\mu} c_{\mu i}^S \frac{1}{2c} \vec{\sigma} \cdot \left(\hat{p} + \frac{1}{c} \hat{A} \right) |\phi_{\mu}\rangle. \quad (5.9)$$

This leads to the four-component Dirac equation in a RMB basis,

$$\begin{pmatrix} \mathbf{V} & \mathbf{H}^{\dagger} \\ \mathbf{H} & \frac{1}{4c^2} \mathbf{W} - \mathbf{T} \end{pmatrix} \begin{pmatrix} \mathbf{C}_{-}^L & \mathbf{C}_{+}^L \\ \mathbf{C}_{-}^S & \mathbf{C}_{+}^S \end{pmatrix} = \begin{pmatrix} \mathbf{S} & \mathbf{0}_2 \\ \mathbf{0}_2 & \frac{1}{2c^2} \mathbf{T} \end{pmatrix} \begin{pmatrix} \mathbf{C}_{-}^L & \mathbf{C}_{+}^L \\ \mathbf{C}_{-}^S & \mathbf{C}_{+}^S \end{pmatrix} \begin{pmatrix} \epsilon_{-} & \mathbf{0}_2 \\ \mathbf{0}_2 & \epsilon_{+} \end{pmatrix}, \quad (5.10)$$

where the notation of Cremer *et al.*^[98] is used. The structure is identical to Eq. 4.26, yet the matrices differ. The overlap matrix, \mathbf{S} and the potential matrix, \mathbf{V} , are again block-diagonal in the space of the two-component spinor functions

$$\mathbf{S} = \begin{pmatrix} \mathbf{S} & \mathbf{0} \\ \mathbf{0} & \mathbf{S} \end{pmatrix}, \quad \text{with} \quad \mathbf{S}_{\mu\nu} = \langle \lambda_{\mu} | \lambda_{\nu} \rangle, \quad (5.11)$$

$$\mathbf{V} = \begin{pmatrix} \mathbf{V} & \mathbf{0} \\ \mathbf{0} & \mathbf{V} \end{pmatrix}, \quad \text{with} \quad \mathbf{V}_{\mu\nu} = \langle \lambda_{\mu} | \hat{V} | \lambda_{\nu} \rangle. \quad (5.12)$$

These matrices are identical to the ones in Eq. 2.31 as no field-dependent basis functions are employed for SSCCs. The other matrices depend on the balance condition and the vector potential. These matrices are not block-diagonal and describe both scalar-relativistic and spin-orbit effects

$$\mathbf{T}_{\mu\nu} = \frac{1}{2} \langle \phi_\mu | [\vec{\sigma} \cdot (\hat{\vec{p}} + \frac{1}{c} \hat{\vec{A}})] [\vec{\sigma} \cdot (\hat{\vec{p}} + \frac{1}{c} \hat{\vec{A}})] | \phi_\nu \rangle, \quad (5.13)$$

$$\mathbf{II}_{\mu\nu}^\dagger = \frac{1}{2} \langle \phi_\mu | [\vec{\sigma} \cdot (\hat{\vec{p}} + \frac{1}{c} \hat{\vec{A}})] [\vec{\sigma} \cdot (\hat{\vec{p}} + \frac{1}{c} \hat{\vec{A}})] | \phi_\nu \rangle, \quad (5.14)$$

$$\mathbf{II}_{\mu\nu} = \frac{1}{2} \langle \phi_\mu | [\vec{\sigma} \cdot (\hat{\vec{p}} + \frac{1}{c} \hat{\vec{A}})] [\vec{\sigma} \cdot (\hat{\vec{p}} + \frac{1}{c} \hat{\vec{A}})] | \phi_\nu \rangle, \quad (5.15)$$

$$\mathbf{W}_{\mu\nu} = \langle \phi_\mu | [\vec{\sigma} \cdot (\hat{\vec{p}} + \frac{1}{c} \hat{\vec{A}})] \hat{V} [\vec{\sigma} \cdot (\hat{\vec{p}} + \frac{1}{c} \hat{\vec{A}})] | \phi_\nu \rangle. \quad (5.16)$$

Eq. 4.26 for NMR shifts considers the vector potential of the external magnetic field in the balance condition, whereas the vector potential of the magnetic moments is used in the equations of this chapter. In contrast to Eq. 4.26, \mathbf{II} is Hermitian as the complete vector potential is used in the generalized momentum for the Dirac-Hamilton operator and the balance condition. Note that the RMB condition will result in quadratic terms of the vector potential and diamagnetic interactions are described.^[49,395] However, the derivatives of the relativistically modified potential with respect to the magnetic moments are problematic^[430] as they contain divergent contributions in quasirelativistic ansätze^[435,436] and even yield large values in the finite nucleus model.^[437] Yoshizawa computed these integrals with partial integration and the finite nucleus model for the scalar potential but judges that he “failed in the accurate calculation of the integrals”^[430] as the results show an unreasonably large deviation from the experimental findings at the MP2 level. Neglecting the derivative of \mathbf{W} in an RMB ansatz results in an imbalanced approach.^[430] Therefore, we may ask the question whether the RMB is needed for SSCCs from a pragmatic point of view, i.e. to obtain accurate results. One the one hand, the RMB ensures variational stability and the exact non-relativistic limit regardless of the size of the finite basis set. The deviation of the orbital energies is of $\mathcal{O}(c^{-4})$.^[57] On the other hand, NMR SSCCs are calculated in the limit of vanishing magnetic moments. Considering the above equations this means that the quadratic term of \vec{A} results in non-vanishing second-order integral derivatives of \mathbf{T} , \mathbf{II} , and \mathbf{W} . However, this diamagnetic contribution is usually small or negligible for NMR SSCCs.^[82,83,116] Consequently, the RKB results in a good approximation of the non-relativistic limit^[50-53] and is also commonly used for the related hyperfine coupling constant in X2C and DKH.^[438-440] Note that including the response of the decoupling and renormalization matrix as outlined in Sec. 4.4 and 4.5 yields a non-zero second derivative. Therefore, using the RKB condition instead of the RMB condition is expected to yield minor “errors” for SSCCs. This approximation is not valid for NMR shielding constants as the absolute value of the diamagnetic term is often the largest contribution.

Expanding the Dirac-Hamilton operator with the generalized momentum in a restricted kinetically balanced basis set^[248]

$$|\psi_i^L\rangle = \sum_{\mu} c_{\mu i}^L |\phi_{\mu}\rangle, \quad (5.17)$$

$$|\psi_i^S\rangle = \sum_{\mu} c_{\mu i}^S \frac{\vec{\sigma} \cdot \hat{\vec{p}}}{2c} |\phi_{\mu}\rangle, \quad (5.18)$$

leads to the four-component Dirac equation in a RKB basis, which is of the same structure as Eq. 5.10. However, the matrices \mathbf{T} and \mathbf{W} are independent of the vector potential. Note that the metric of the small component, \mathbf{T} , becomes identical to the kinetic energy matrix in Eq. 2.31 and is therefore block-diagonal.

For the sake of completeness, \mathbf{T} reads

$$\mathbf{T} = \begin{pmatrix} \mathbf{T} & \mathbf{0} \\ \mathbf{0} & \mathbf{T} \end{pmatrix}, \quad \text{with} \quad \mathbf{T}_{\mu\nu} = \langle \lambda_\mu | \frac{1}{2} \hat{p}^2 | \lambda_\nu \rangle. \quad (5.19)$$

\mathbf{W} corresponds to the relativistically modified potential in Eq. 2.40

$$\mathbf{W}_{\mu\nu} = \langle \phi_\mu | (\vec{\sigma} \cdot \hat{p}) \hat{V} (\vec{\sigma} \cdot \hat{p}) | \phi_\nu \rangle \quad (5.20)$$

and may be partitioned into the one-component matrices \mathbf{W}^0 , \mathbf{W}^x , \mathbf{W}^y , and \mathbf{W}^z . Only the generalized momentum matrix, $\mathbf{\Pi}$, depends on the vector potential. The generalized momentum matrix reads

$$\mathbf{\Pi}_{\mu\nu}^\dagger = \frac{1}{2} \langle \phi_\mu | \vec{\sigma} \cdot \left(\hat{p} + \frac{1}{c} \hat{A} \right) | (\vec{\sigma} \cdot \hat{p}) \phi_\nu \rangle. \quad (5.21)$$

The matrix $\mathbf{\Pi}^\dagger$ is not Hermitian with the RKB condition yet the full Dirac matrix is still Hermitian. The X2C Hamiltonian with the nuclear magnetic moments in a RKB basis set follows as

$$\mathbf{h}^+ (\vec{m}_N) = \mathbf{R}^\dagger (\vec{m}_N) \mathbf{L} (\vec{m}_N) \mathbf{R} (\vec{m}_N) \quad (5.22)$$

with the NESC matrix

$$\mathbf{L} (\vec{m}_N) = \mathbf{V} + \mathbf{X}^\dagger (\vec{m}_N) \mathbf{\Pi} (\vec{m}_N) + \mathbf{\Pi}^\dagger (\vec{m}_N) \mathbf{X} (\vec{m}_N) + \mathbf{X}^\dagger (\vec{m}_N) \left(\frac{1}{4c^2} \mathbf{W} - \mathbf{T} \right) \mathbf{X} (\vec{m}_N). \quad (5.23)$$

Note that the decoupling and the renormalization matrix still depend on the nuclear magnetic moments in an RKB basis.

5.2 Derivatives of the X2C Hamiltonian

5.2.1 First Derivatives of the X2C Hamiltonian

The first derivative of the X2C Hamiltonian with respect to the magnetic moments was already discussed in Sec. 4.3.2 for scalar-relativistic NMR shifts. For SSCCs, a two-component framework is employed, which requires a complex matrix framework and consequently more general equations are obtained. Differentiating Eq. 5.22 with respect to the nuclear magnetic moment \vec{m}_M results in

$$\mathbf{h}_u^{+,M} = \mathbf{R}_u^{\dagger,M} \mathbf{L} \mathbf{R} + \mathbf{R}^\dagger \mathbf{L}_u^M \mathbf{R} + \mathbf{R}^\dagger \mathbf{L} \mathbf{R}_u^M \quad (5.24)$$

with the first-order derivative of the NESC matrix

$$\begin{aligned} \mathbf{L}_u^M = & \mathbf{X}_u^{\dagger,M} \mathbf{\Pi} + \mathbf{X}^\dagger \mathbf{\Pi}_u^M + \mathbf{\Pi}_u^{\dagger,M} \mathbf{X} + \mathbf{\Pi}^\dagger \mathbf{X}_u^M \\ & + \mathbf{X}_u^{\dagger,M} \left(\frac{1}{4c^2} \mathbf{W} - \mathbf{T} \right) \mathbf{X} + \mathbf{X}^\dagger \left(\frac{1}{4c^2} \mathbf{W} - \mathbf{T} \right) \mathbf{X}_u^M. \end{aligned} \quad (5.25)$$

Only \mathbf{R} , \mathbf{X} , and $\mathbf{\Pi}$ depend on the nuclear magnetic moments and will yield non-zero derivatives. Compared to the magnetic-field derivative of NMR shifts, the number of integral derivatives is significantly reduced due to the RKB condition and field-independent basis functions.

The derivative of the generalized momentum matrix is given as

$$\left(\mathbf{H}_{\mu\nu}^\dagger\right)_u^M = \frac{1}{2c} \left\langle \phi_\mu \left| \left(\vec{\nabla}_M \hat{G}_M \times \vec{\sigma} \right)_u \right| \left(\vec{\sigma} \cdot \hat{p} \right) \phi_\nu \right\rangle. \quad (5.26)$$

For an efficient implementation, it is advantageous to separate the integral derivative into the spin-independent and the spin-dependent contributions using the Dirac identity, resulting in

$$\begin{aligned} \left(\mathbf{H}_{\mu\nu}^\dagger\right)_u^M &= \frac{\partial}{\partial m_u^M} \left[\frac{1}{2} \langle \lambda_\mu | \hat{\pi} \cdot \hat{p} | \lambda_\nu \rangle \sigma_0 + \frac{1}{2} \langle \lambda_\mu | i\vec{\sigma} \cdot \left(\hat{\pi} \times \hat{p} \right) | \lambda_\nu \rangle \right] \\ &= \frac{1}{2c} \langle \lambda_\mu | \left(\vec{\nabla}_M \hat{G}_M \times \hat{p} \right)_u | \lambda_\nu \rangle \sigma_0 \\ &\quad + \frac{i}{2c} \langle \lambda_\mu | \left(\left[\vec{\sigma} \cdot \vec{\nabla}_M \hat{G}_M \right] \hat{p}_u - \sigma_u \left[\vec{\nabla}_M \hat{G}_M \cdot \hat{p} \right] \right) | \lambda_\nu \rangle. \end{aligned} \quad (5.27)$$

This allows to construct the two-component matrix with the one-component integral derivative matrices by sorting onto the respective spin blocks. The integrals are the same as for the NMR shielding constants discussed in Sec. 4.3.2. In the point-charge limit, $\left(\mathbf{H}_{\mu\nu}^\dagger\right)_u^M$ reduces to

$$\left(\mathbf{H}_{\mu\nu}^\dagger\right)_u^M = \frac{1}{2c} \langle \lambda_\mu | \hat{r}_M^{-3} \left(\vec{r}_M \times \hat{p} \right)_u | \lambda_\nu \rangle \sigma_0 + \frac{i}{2c} \langle \lambda_\mu | \hat{r}_M^{-3} \left(\vec{\sigma} \cdot \vec{r}_M \hat{p}_u - \sigma_u \vec{r}_M \cdot \hat{p} \right) | \lambda_\nu \rangle. \quad (5.28)$$

The scalar-relativistic or spin-independent contribution is the PSO term. These integrals are imaginary and antisymmetric. As shown in Sec. 5.4, the spin-dependent part corresponds to the Fermi-contact and the spin-dipole term. The spin-dependent contribution is non-symmetric. Thus, the matrix is partitioned into the symmetric and antisymmetric part according to

$$\mathbf{M}_{\mu\nu}^\pm = \frac{1}{2} (\mathbf{M}_{\mu\nu} \pm \mathbf{M}_{\nu\mu}), \quad (5.29)$$

where \mathbf{M}^+ indicates the symmetric contribution and \mathbf{M}^- denotes the antisymmetric contribution. For efficiency, the matrices are calculated in the CAO basis and are partitioned into the two contributions during the transformation to the spherical AO basis set, thereby avoiding additional loops. The integral derivatives are evaluated in the same way as outlined in Sec. 4.3.2.

The derivative of the decoupling matrix is obtained by solving response equations as shown for the general two-component formalism in Sec. 4.4.1. For the magnetic moments, this results in

$$\mathbf{X}^\lambda = (\mathbf{C}_{S-} - \mathbf{X}\mathbf{C}_{L-}) \mathbf{U}_{-+}^\lambda \mathbf{C}_{L+}^\dagger \tilde{\mathbf{S}} \quad (5.30)$$

and the negative-positive block of the orbital rotation matrix is computed according to

$$\left(\mathbf{U}_{-+}^\lambda\right)_{kl} = \frac{\left(\tilde{\mathbf{D}}_{-+}^\lambda\right)_{kl}}{\left(\mathbf{E}_{++}\right)_{ll} - \left(\mathbf{E}_{--}\right)_{kk}}. \quad (5.31)$$

This only requires to transform the integral derivatives of the generalized momentum matrix to the basis of the unperturbed solutions according to

$$\tilde{\mathbf{D}}_{-+}^\lambda = \mathbf{C}_{-}^{L,\dagger} \mathbf{\Pi}^{\dagger,\lambda} \mathbf{C}_{+}^S + \mathbf{C}_{-}^{S,\dagger} \mathbf{\Pi}^\lambda \mathbf{C}_{+}^L. \quad (5.32)$$

The matrix multiplications are performed with the BLAS routine ZGEMM3M.^[399,400] The inverse of the coefficients \mathbf{C}_{+}^L for the decoupling matrix is obtained with the routines ZGETRI and ZGETRF.^[399,400]

According to Sec. 4.5, the perturbed renormalization matrix is calculated by solving the Sylvester matrix equation

$$\mathbf{R}\mathbf{R}_u^M + \mathbf{R}_u^M\mathbf{R} = \tilde{\mathbf{S}}^{-1}\tilde{\mathbf{S}}_u^M\mathbf{R}\mathbf{R} \quad (5.33)$$

using the eigenvalue decomposition method. The complex matrix \mathbf{K} in Eq. 4.117 is diagonalized with the LAPACK routine^[396] ZHEEV. The matrix multiplications for the generalized inverse of the eigenvectors of the renormalization and the transformations are again performed with ZGEMM3M. The matrix multiplications scale as $\mathcal{O}(N^3)$, where N measures the system size. Compared to the scalar-relativistic formalism, the computation time formally increases by a factor of 32 due to the doubled dimension and the complex numbers ($4 \cdot 2^3$).^[105]

5.2.2 Second Derivatives of the X2C Hamiltonian

The Dirac matrix possesses no bilinear terms regarding \vec{A} in an RKB basis. So, the second derivative of the X2C Hamiltonian becomes

$$\begin{aligned} h_{u,v}^{+,M,N} = & \mathbf{R}_{u,v}^{\dagger,M,N}\mathbf{L}\mathbf{R} + \mathbf{R}_u^{\dagger,M}\mathbf{L}_v^N\mathbf{R} + \mathbf{R}_u^{\dagger,M}\mathbf{L}\mathbf{R}_v^N \\ & + \mathbf{R}_v^{\dagger,N}\mathbf{L}_u^M\mathbf{R} + \mathbf{R}^{\dagger}\mathbf{L}_{u,v}^{M,N}\mathbf{R} + \mathbf{R}^{\dagger}\mathbf{L}_u^M\mathbf{R}_v^N \\ & + \mathbf{R}_v^{\dagger,N}\mathbf{L}\mathbf{R}_u^M + \mathbf{R}^{\dagger}\mathbf{L}_v^N\mathbf{R}_u^M + \mathbf{R}^{\dagger}\mathbf{L}\mathbf{R}_{u,v}^{M,N} \end{aligned} \quad (5.34)$$

with the derivative of the NESC matrix

$$\begin{aligned} \mathbf{L}_{u,v}^{M,N} = & \mathbf{X}_{u,v}^{\dagger,M,N}\mathbf{\Pi} + \mathbf{X}_u^{\dagger,M}\mathbf{\Pi}_v^N + \mathbf{X}_v^{\dagger,N}\mathbf{\Pi}_u^M \\ & + \mathbf{\Pi}_u^{\dagger,M}\mathbf{X}_v^N + \mathbf{\Pi}^{\dagger}\mathbf{X}_{u,v}^{M,N} + \mathbf{\Pi}_v^{\dagger,N}\mathbf{X}_u^M \\ & + \mathbf{X}_{u,v}^{\dagger,M,N}\left(\frac{1}{4c^2}\mathbf{W} - \mathbf{T}\right)\mathbf{X} + \mathbf{X}_u^{\dagger,M}\left(\frac{1}{4c^2}\mathbf{W} - \mathbf{T}\right)\mathbf{X}_v^N \\ & + \mathbf{X}^{\dagger}\left(\frac{1}{4c^2}\mathbf{W} - \mathbf{T}\right)\mathbf{X}_{u,v}^{M,N} + \mathbf{X}_v^{\dagger,N}\left(\frac{1}{4c^2}\mathbf{W} - \mathbf{T}\right)\mathbf{X}_u^M. \end{aligned} \quad (5.35)$$

Note that the derivative of the X2C Hamiltonian only arises due to the response of the decoupling and the renormalization matrix. Neglecting these derivatives as commonly done for the hyperfine coupling constant^[438–440] or the g tensor^[439] in electron paramagnetic resonance (EPR) spectroscopy will yield zero for the second derivative and not result in the full analytical derivative of the energy. Here, the second-order derivative of the decoupling matrix is given as

$$\begin{aligned} \mathbf{X}^{\kappa\lambda} = & (\mathbf{C}_{S-} - \mathbf{X}\mathbf{C}_{L-}) \left[\tilde{\mathbf{U}}_{-+}^{\kappa\lambda} - \mathbf{U}_{-+}^{\kappa} \mathbf{C}_{L+}^{\dagger} \tilde{\mathbf{S}} \mathbf{C}_{L-} \mathbf{U}_{-+}^{\lambda} \right. \\ & \left. - \mathbf{U}_{-+}^{\lambda} \mathbf{C}_{L+}^{\dagger} \tilde{\mathbf{S}} \mathbf{C}_{L-} \mathbf{U}_{-+}^{\kappa} \right] \mathbf{C}_{L+}^{\dagger} \tilde{\mathbf{S}} \end{aligned} \quad (5.36)$$

with the second-order orbital rotation matrix

$$\begin{aligned} (\tilde{\mathbf{U}}_{-+}^{\kappa\lambda})_{kl} = & \frac{1}{(\mathbf{E}_{++})_{ll} - (\mathbf{E}_{--})_{kk}} \left\{ \left[\mathbf{U}_{+-}^{\dagger,\kappa} \tilde{\mathbf{D}}_{++}^{\lambda} \right]_{kl} + \left[\tilde{\mathbf{D}}_{--}^{\lambda} \mathbf{U}_{-+}^{\kappa} \right]_{kl} \right. \\ & \left. + \left[\mathbf{U}_{+-}^{\dagger,\lambda} \tilde{\mathbf{D}}_{++}^{\kappa} \right]_{kl} + \left[\tilde{\mathbf{D}}_{--}^{\kappa} \mathbf{U}_{-+}^{\lambda} \right]_{kl} \right\}. \end{aligned} \quad (5.37)$$

This is a simplified form of Eq. 4.101 as the metric vanishes in a RKB basis set and consequently the negative-negative and the positive-positive block of the first-order orbital rotation matrix, $\mathbf{U}_{--}^{\lambda}$ and $\mathbf{U}_{++}^{\lambda}$, vanish.

The negative-positive block is given in Eq. 5.31 and the positive-negative block reads

$$(\mathbf{U}_{+-}^\lambda)_{kl} = \frac{(\tilde{\mathbf{D}}_{+-}^\lambda)_{kl}}{(\mathbf{E}_{--})_{ll} - (\mathbf{E}_{++})_{kk}}. \quad (5.38)$$

The remaining blocks of the perturbed Dirac matrix in the basis of the unperturbed solutions are obtained according to

$$\tilde{\mathbf{D}}_{--}^\lambda = \mathbf{C}_-^{L,\dagger} \mathbf{\Pi}^{\dagger,\lambda} \mathbf{C}_-^S + \mathbf{C}_-^{S,\dagger} \mathbf{\Pi}^\lambda \mathbf{C}_-^L, \quad (5.39)$$

$$\tilde{\mathbf{D}}_{+-}^\lambda = \mathbf{C}_+^{L,\dagger} \mathbf{\Pi}^{\dagger,\lambda} \mathbf{C}_-^S + \mathbf{C}_+^{S,\dagger} \mathbf{\Pi}^\lambda \mathbf{C}_-^L, \quad (5.40)$$

$$\tilde{\mathbf{D}}_{++}^\lambda = \mathbf{C}_+^{L,\dagger} \mathbf{\Pi}^{\dagger,\lambda} \mathbf{C}_+^S + \mathbf{C}_+^{S,\dagger} \mathbf{\Pi}^\lambda \mathbf{C}_+^L. \quad (5.41)$$

Finally, the derivative of the renormalization matrix is calculated by solving the Sylvester matrix equation

$$\mathbf{R}\mathbf{R}_{u,v}^{M,N} + \mathbf{R}_{u,v}^{M,N}\mathbf{R} = \mathbf{Q} \quad (5.42)$$

with the right-hand side

$$\mathbf{Q} = -\tilde{\mathbf{S}}^{-1} \left[\tilde{\mathbf{S}}_{u,v}^{M,N} \mathbf{R}\mathbf{R} + \tilde{\mathbf{S}}_u^M \tilde{\mathbf{S}}^{-1} \tilde{\mathbf{S}}_v^N \mathbf{R}\mathbf{R} + \tilde{\mathbf{S}}_v^N \tilde{\mathbf{S}}^{-1} \tilde{\mathbf{S}}_u^M \mathbf{R}\mathbf{R} - \mathbf{R}_u^M \mathbf{R}_v^N - \mathbf{R}_v^N \mathbf{R}_u^M \right] \quad (5.43)$$

using an eigenvalue decomposition method as above. Compared to the first-order derivatives, the working equations of the second-order derivatives include significantly more terms and are more demanding, however, the implementation is very similar as all matrix multiplications can still be performed with ZGEMM3M. The number of matrix multiplications is reduced compared to NMR shifts in the last chapter as the integral derivatives of all matrices except for $\mathbf{\Pi}$ and $\mathbf{\Pi}^\dagger$ vanish.

5.3 Local Approximation of the X2C Hamiltonian

The second derivative or the DSO term in X2C is the most demanding contribution in terms of computational effort as it requires to calculate a considerable number of matrix multiplications. However, the absolute contribution of these terms is often small or even negligible compared to the first derivatives. Therefore, reducing the computational costs is highly desirable. Applying the diagonal local approximation to the unitary decoupling transformation to the Hamiltonian in Eq. 5.22 gives the atomic diagonal blocks

$$\mathbf{h}_{AA}^+ = \mathbf{R}_{AA}^\dagger \left(\mathbf{V}_{AA} + \mathbf{\Pi}_{AA}^\dagger \mathbf{X}_{AA} + \mathbf{X}_{AA}^\dagger \mathbf{\Pi}_{AA} + \mathbf{X}_{AA}^\dagger \left[\frac{1}{4c^2} \mathbf{W}_{AA} - \mathbf{T}_{AA} \right] \mathbf{X}_{AA} \right) \mathbf{R}_{AA} \quad (5.44)$$

and the atomic off-diagonal blocks

$$\mathbf{h}_{AB}^+ = \mathbf{R}_{AA}^\dagger \left(\mathbf{V}_{AB} + \mathbf{\Pi}_{AB}^\dagger \mathbf{X}_{BB} + \mathbf{X}_{AA}^\dagger \mathbf{\Pi}_{AB} + \mathbf{X}_{AA}^\dagger \left[\frac{1}{4c^2} \mathbf{W}_{AB} - \mathbf{T}_{AB} \right] \mathbf{X}_{BB} \right) \mathbf{R}_{BB}. \quad (5.45)$$

These equations are structurally identical to Eqs. 4.126 and 4.127, however, the matrices are formulated in the two-component space. Differentiating these equations results in the perturbed spin-orbit DLU-X2C Hamiltonian in analogy to Eqs. 4.131 and 4.132. As for NMR shifts, the atomic diagonal block is simply obtained by considering the atomic dimensions in the response equations for the decoupling and the renormalization matrix. The off-diagonal blocks are constructed by matrix multiplications with the obtained atomic diagonal matrices and the atomic off-diagonal blocks of the integrals and the integral derivatives.

For completeness, the atomic diagonal blocks read

$$\begin{aligned}
\mathbf{h}_{AA,u}^{+,M} = & \mathbf{R}_{AA,u}^{\dagger,M} \left(\mathbf{V}_{AA} + \mathbf{\Pi}_{AA}^{\dagger} \mathbf{X}_{AA} + \mathbf{X}_{AA}^{\dagger} \mathbf{\Pi}_{AA} + \mathbf{X}_{AA}^{\dagger} \left[\frac{1}{4c^2} \mathbf{W}_{AA} - \mathbf{T}_{AA} \right] \mathbf{X}_{AA} \right) \mathbf{R}_{AA} \\
& + \mathbf{R}_{AA}^{\dagger} \left(\mathbf{V}_{AA} + \mathbf{\Pi}_{AA}^{\dagger} \mathbf{X}_{AA} + \mathbf{X}_{AA}^{\dagger} \mathbf{\Pi}_{AA} + \mathbf{X}_{AA}^{\dagger} \left[\frac{1}{4c^2} \mathbf{W}_{AA} - \mathbf{T}_{AA} \right] \mathbf{X}_{AA} \right) \mathbf{R}_{AA,u}^M \\
& + \mathbf{R}_{AA}^{\dagger} \left(\mathbf{\Pi}_{AA,u}^{\dagger,M} \mathbf{X}_{AA} + \mathbf{\Pi}_{AA}^{\dagger} \mathbf{X}_{AA,u}^M + \mathbf{X}_{AA,u}^{\dagger,M} \mathbf{\Pi}_{AA} + \mathbf{X}_{AA}^{\dagger} \mathbf{\Pi}_{AA,u}^M \right) \mathbf{R}_{AA} \\
& + \mathbf{R}_{AA}^{\dagger} \left(\mathbf{X}_{AA,u}^{\dagger,M} \left[\frac{1}{4c^2} \mathbf{W}_{AA} - \mathbf{T}_{AA} \right] \mathbf{X}_{AA} + \mathbf{X}_{AA}^{\dagger} \left[\frac{1}{4c^2} \mathbf{W}_{AA} - \mathbf{T}_{AA} \right] \mathbf{X}_{AA,u}^M \right) \mathbf{R}_{AA}
\end{aligned} \tag{5.46}$$

and the off-diagonal blocks follow as

$$\begin{aligned}
\mathbf{h}_{AB,u}^{+,M} = & \mathbf{R}_{AA,u}^{\dagger,M} \left(\mathbf{V}_{AB} + \mathbf{\Pi}_{AB}^{\dagger} \mathbf{X}_{BB} + \mathbf{X}_{AA}^{\dagger} \mathbf{\Pi}_{AB} + \mathbf{X}_{AA}^{\dagger} \left[\frac{1}{4c^2} \mathbf{W}_{AB} - \mathbf{T}_{AB} \right] \mathbf{X}_{BB} \right) \mathbf{R}_{BB} \\
& + \mathbf{R}_{AA}^{\dagger} \left(\mathbf{V}_{AB} + \mathbf{\Pi}_{AB}^{\dagger} \mathbf{X}_{BB} + \mathbf{X}_{AA}^{\dagger} \mathbf{\Pi}_{AB} + \mathbf{X}_{AA}^{\dagger} \left[\frac{1}{4c^2} \mathbf{W}_{AB} - \mathbf{T}_{AB} \right] \mathbf{X}_{BB} \right) \mathbf{R}_{BB,u}^M \\
& + \mathbf{R}_{AA}^{\dagger} \left(\mathbf{\Pi}_{AB,u}^{\dagger,M} \mathbf{X}_{BB} + \mathbf{\Pi}_{AB}^{\dagger} \mathbf{X}_{BB,u}^M + \mathbf{X}_{AA,u}^{\dagger,M} \mathbf{\Pi}_{AB} + \mathbf{X}_{AA}^{\dagger} \mathbf{\Pi}_{AB,u}^M \right) \mathbf{R}_{BB} \\
& + \mathbf{R}_{AA}^{\dagger} \left(\mathbf{X}_{AA,u}^{\dagger,M} \left[\frac{1}{4c^2} \mathbf{W}_{AB} - \mathbf{T}_{AB} \right] \mathbf{X}_{BB} + \mathbf{X}_{AA}^{\dagger} \left[\frac{1}{4c^2} \mathbf{W}_{AB} - \mathbf{T}_{AB} \right] \mathbf{X}_{BB,u}^M \right) \mathbf{R}_{BB}.
\end{aligned} \tag{5.47}$$

The implementation is described Fig. 5.1. The initialization steps are essentially the same as for the implementation of NMR shieldings except that the spin–orbit matrices \mathbf{W}^x , \mathbf{W}^y , \mathbf{W}^z are computed. The (m)SNSO approach is available for these matrices. First, the atomic diagonal blocks of the unperturbed X2C quantities are calculated by removing the linear dependencies and transforming the one-component matrices from the spherical AO basis to the linear-independent AO (IAO) basis. Secondly, the two-component matrices are constructed in the IAO basis and the X2C decoupling step is carried out using the LAPACK routine^[396] ZHEGV for the diagonalization of the complex Dirac matrix. The obtained matrices are stored on a vector in the IAO basis for the evaluation of Eq. 5.46 and 5.47.

The integral derivatives are evaluated in the one-component space and the two-component matrices are constructed when needed using the Pauli matrices to sort the one-component matrix elements onto the corresponding spin blocks. The atomic diagonal blocks of the perturbed Hamiltonian are obtained by first gathering all required quantities in the IAO basis and then solving the first-order response equations for the decoupling matrix and the Sylvester matrix equation for the renormalization matrix. The matrix multiplications are generally performed with ZGEMM3M. The routine ZAXPY^[399,400] is used for the multiplication of a general matrix with a diagonal matrix. The derivatives of the decoupling and the renormalization matrix are transformed to the AO basis, collected in a second vector, and used to compute all matrix multiplications in Eq. 5.47 for the atomic off-diagonal block. After the computation of all atomic diagonal and off-diagonal blocks, the resulting DLU-X2C Hamiltonian derivative is transformed to the CAO basis and the contraction of the basis set is applied. Then, the perturbed Hamiltonian is transformed to the AO basis and the spinor space. The result is stored on disk for the solver of the CPHF or CPKS equations. All integral evaluations, the loops over the atomic diagonal and off-diagonal blocks, as well as the transformation and contraction at the end of the algorithm are parallelized with OpenMP.

Calculate the first derivatives of the DLU-X2C Hamiltonian for SSCCs:

$$\left(\frac{\partial \mathbf{h}}{\partial m_{N,v}} \right)_0 \quad \text{with } u \in \{x, y, z\}$$

Initialization

1. Initialization of transformations and uncontracted basis set
2. Calculate all unperturbed integrals: \mathbf{S} , \mathbf{T} , \mathbf{V} , \mathbf{W}^0 , \mathbf{W}^x , \mathbf{W}^y , \mathbf{W}^z in CAO basis and transformation to spherical AO basis on the fly
3. Initialize atomic information for DLU scheme

Unperturbed quantities

4. **Loop** over atomic diagonal blocks
 - a) Get atomic diagonal blocks of \mathbf{S} , \mathbf{T} , \mathbf{V} , \mathbf{W}^0 , \mathbf{W}^x , \mathbf{W}^y , \mathbf{W}^z
 - b) Diagonalize overlap matrix and remove linear dependencies
 - c) Transformation to linear-independent AO (IAO) basis
 - d) Perform X2C decoupling step and obtain the matrices \mathbf{X} , \mathbf{R} , $\tilde{\mathbf{S}}$, \mathbf{V}_R , \mathbf{r} , \mathbf{L} etc.
 - e) Collect the atomic diagonal blocks of \mathbf{X} , \mathbf{R} , \mathbf{L} , $\tilde{\mathbf{S}}$, $\tilde{\mathbf{S}}^{-1}$, \mathbf{V}_R , \mathbf{V}_R^{-1} , \mathbf{C}_-^L , \mathbf{C}_+^L , \mathbf{C}_-^S , \mathbf{C}_+^S , \mathbf{E}_{--} , \mathbf{E}_{++} , and the AO-IAO transformation matrix on a vector
5. **End loop** over atomic diagonal blocks

Perturbed quantities

6. Compute all integral derivatives: spin blocks for $\mathbf{\Pi}^M$ in CAO and transformation to spherical AO on the fly
7. **Loop** over Cartesian directions u
 - a) **Loop** over atomic diagonal blocks
 - i. Read atomic diagonal quantities on vector
 - ii. Get atomic diagonal blocks of integral derivatives
 - iii. Transformation to IAO basis
 - iv. Compute mixed derivative of Hamiltonian and back-transformation to AO basis
 - v. Collect quantities for atomic off-diagonal blocks on another vector: \mathbf{X}^M , \mathbf{R}^M
 - b) **End Loop** over atomic diagonal blocks
 - c) **Loop** over atomic off-diagonal blocks
 - i. Read atomic diagonal quantities on vectors
 - ii. Get atomic off-diagonal blocks of integral derivatives
 - iii. Perform matrix multiplications for off-diagonal block of DLU-X2C Hamiltonian
 - iv. Form conjugate transpose of atomic off-diagonal block
 - d) **End Loop** over atomic off-diagonal blocks
 - e) Transform derivative of Hamiltonian to CAO basis
 - f) Perform contraction of Hamiltonian derivative and transformation to spherical AO basis
8. **End Loop** over Cartesian direction u

Connection to CPHF or CPKS solver

9. Transformation to spinor space for CPHF or CPKS equations

Figure 5.1: Algorithm for the calculation of the first derivatives of the DLU-X2C Hamiltonian. The sorting steps for the DLU-X2C Hamiltonian are omitted for clarity.

Further differentiating Eq. 5.46 and 5.47 gives the Hamiltonian contribution to the DSO term. The atomic diagonal blocks become

$$\begin{aligned} \mathbf{h}_{u,v,AA}^{M,N} = & \mathbf{R}_{u,v,AA}^{M,N} \mathbf{L}_{AA} \mathbf{R}_{AA} + \mathbf{R}_{u,AA}^{\dagger,M} \mathbf{L}_{v,AA}^N \mathbf{R}_{AA} + \mathbf{R}_{u,AA}^{\dagger,M} \mathbf{L}_{AA} \mathbf{R}_{v,AA}^N \\ & + \mathbf{R}_{v,AA}^{\dagger,N} \mathbf{L}_{u,AA}^M \mathbf{R}_{AA} + \mathbf{R}_{AA}^{\dagger} \mathbf{L}_{u,v,AA}^{M,N} \mathbf{R}_{AA} + \mathbf{R}_{AA}^{\dagger} \mathbf{L}_{u,AA}^M \mathbf{R}_{v,AA}^N \\ & + \mathbf{R}_{v,AA}^{\dagger,N} \mathbf{L}_{AA} \mathbf{R}_{u,AA}^M + \mathbf{R}_{AA}^{\dagger} \mathbf{L}_{v,AA}^N \mathbf{R}_{u,AA}^M + \mathbf{R}_{AA}^{\dagger} \mathbf{L}_{AA} \mathbf{R}_{u,v,AA}^{M,N} \end{aligned} \quad (5.48)$$

and the off-diagonal blocks follow as

$$\begin{aligned} \mathbf{h}_{u,v,AB}^{M,N} = & \mathbf{R}_{u,v,AA}^{\dagger,M,N} \mathbf{L}_{AB} \mathbf{R}_{BB} + \mathbf{R}_{u,AA}^{\dagger,M} \mathbf{L}_{v,AB}^N \mathbf{R}_{BB} + \mathbf{R}_{u,AA}^{\dagger,M} \mathbf{L}_{AB} \mathbf{R}_{v,BB}^N \\ & + \mathbf{R}_{v,AA}^{\dagger,N} \mathbf{L}_{u,AB}^M \mathbf{R}_{BB} + \mathbf{R}_{AA}^{\dagger} \mathbf{L}_{u,v,AB}^{M,N} \mathbf{R}_{BB} + \mathbf{R}_{AA}^{\dagger} \mathbf{L}_{u,AB}^M \mathbf{R}_{v,BB}^N \\ & + \mathbf{R}_{v,AA}^{\dagger,N} \mathbf{L}_{AB} \mathbf{R}_{u,BB}^M + \mathbf{R}_{AA}^{\dagger} \mathbf{L}_{v,AB}^N \mathbf{R}_{u,BB}^M + \mathbf{R}_{AA}^{\dagger} \mathbf{L}_{AB} \mathbf{R}_{u,v,BB}^{M,N}. \end{aligned} \quad (5.49)$$

The second derivatives of the NESC matrix read

$$\begin{aligned} \mathbf{L}_{u,v,AB}^{M,N} = & \mathbf{\Pi}_{u,AB}^{\dagger,M} \mathbf{X}_{v,BB}^N + \mathbf{\Pi}_{v,AB}^{\dagger,N} \mathbf{X}_{u,BB}^M + \mathbf{\Pi}_{AB}^{\dagger} \mathbf{X}_{u,v,BB}^{M,N} \\ & + \mathbf{X}_{u,v,AA}^{\dagger,M,N} \mathbf{\Pi}_{AB} + \mathbf{X}_{u,AA}^{\dagger,M} \mathbf{\Pi}_{v,AB}^N + \mathbf{X}_{v,AA}^{\dagger,N} \mathbf{\Pi}_{u,AB}^M \\ & + \mathbf{X}_{u,v,AA}^{\dagger,M,N} \left(\frac{1}{4c^2} \mathbf{W}_{AB} - \mathbf{T}_{AB} \right) \mathbf{X}_{BB} + \mathbf{X}_{u,AA}^{\dagger,M} \left(\frac{1}{4c^2} \mathbf{W}_{AB} - \mathbf{T}_{AB} \right) \mathbf{X}_{v,BB}^N \\ & + \mathbf{X}_{v,AA}^{\dagger,N} \left(\frac{1}{4c^2} \mathbf{W}_{AB} - \mathbf{T}_{AB} \right) \mathbf{X}_{u,BB}^M + \mathbf{X}_{AA}^{\dagger} \left(\frac{1}{4c^2} \mathbf{W}_{AB} - \mathbf{T}_{AB} \right) \mathbf{X}_{u,v,BB}^{M,N}. \end{aligned} \quad (5.50)$$

The second derivative of the DLU-X2C is contracted with the unperturbed density matrix. Therefore, the algorithm has a similar structure as in Fig. 4.1, however, it works in the two-component space for the relativistic decoupling and the response steps for the derivatives. Therefore, the spin–orbit matrices \mathbf{W}^x , \mathbf{W}^y , \mathbf{W}^z are considered and the complex BLAS or LAPACK routines are used: DGEMM is replaced by ZGEMM3M, DSYGV by ZHEGV, DAXPY by ZAXPY, and so on.

5.4 Comparison to the Non-Relativistic Integral Derivatives

To consider the impact of the RKB condition on the non-relativistic limit, the integral derivatives of the previous sections are compared to Ramsey’s theory.^[428] The four contributions of the Hamilton operator to the NMR SSCC are given by

$$\hat{h}_N^{\text{FC}} = \frac{8\pi}{3c} \sum_i \delta(\vec{r} - \vec{r}_{iN}) \hat{\vec{s}}_i, \quad (5.51)$$

$$\hat{h}_N^{\text{SD}} = \frac{1}{c} \sum_i \frac{3\vec{r}_{iN}^T \hat{\vec{s}}_i \vec{r}_{iN} - r_{iN}^2 \hat{\vec{s}}_i}{|\vec{r}_{iN}|^5}, \quad (5.52)$$

$$\hat{h}_N^{\text{PSO}} = -\frac{i}{c} \sum_i \frac{\vec{r}_{iN} \times \nabla_i}{|\vec{r}_{iN}|^3}, \quad (5.53)$$

$$\hat{h}_{N,M}^{\text{DSO}} = \frac{1}{c^2} \sum_i \frac{3\vec{r}_{iN}^T \vec{r}_i \mathbf{L}_3 - \vec{r}_{iN} \vec{r}_{iN}^T}{|\vec{r}_{iN}|^3 |\vec{r}_{iM}|^3}, \quad (5.54)$$

with \vec{s}_i denoting the spin of the electron i . Note that Ramsey employs the point charge model for the vector potential and the scalar potential. The FC, SD, and the PSO term require the first-order response of the density matrix, which is obtained similar to time-dependent density functional calculations^[412,416,420,422,441]

and the terms are considered separately for a closed-shell system with a total spin of zero.^[6] The PSO term is contracted with the density response of an imaginary singlet transition and the FC or SD term are contracted with the density response of a real triplet transition. Due to spin-orbit coupling, the electron spin is no longer a good quantum number, i.e. the wave function is no longer an eigenfunction of the electron spin. So, the three terms have to be considered together in a relativistic framework.

In the non-relativistic limit, the speed of light, c , approaches infinity for all terms except the magnetic perturbation, i.e. the generalized momentum. The needed blocks of the unitary transformation matrix, \mathbf{U}^{LL} and \mathbf{U}^{SL} , become unit matrices^[104] and the derivatives vanish. Accordingly, \mathbf{X} and \mathbf{R} are unit matrices in this limit. The non-relativistic (NR) limit of the X2C Hamiltonian derivative follows as

$$\lim_{\text{NR}} \mathbf{h}_u^{+,M} = \mathbf{\Pi}_u^{\dagger,M} + \mathbf{\Pi}_u^M. \quad (5.55)$$

So, the derivatives of $\mathbf{\Pi}^\dagger$ and $\mathbf{\Pi}$ can simply be added. Note that the sum of these two matrices is Hermitian. Consequently, the hermiticity of the non-relativistic Hamiltonian is recovered. The PSO term directly corresponds to the spin-independent contribution of the sum and requires no further simplification. The remaining spin-dependent integral reads

$$\sum_v \sigma_v \int \frac{r_{M,v}}{r_M^3} \nabla_u (\lambda_\mu \lambda_\nu) d\vec{r} - \frac{1}{2c} \sigma_u \int \frac{\vec{r}_M \cdot \vec{\nabla}}{r_M^3} (\lambda_\mu \lambda_\nu) d\vec{r}. \quad (5.56)$$

As shown by Kutzelnigg,^[429] the derivative can be moved to the operator using integration by parts. Here, the integral is simplified following the formulation of Feng and co-workers for the hyperfine coupling constant.^[440] Therefore, the second integral becomes

$$\begin{aligned} -\frac{1}{2c} \sigma_u \int \frac{\vec{r}_M \cdot \vec{\nabla}}{r_M^3} (\lambda_\mu \lambda_\nu) d\vec{r} &= \frac{1}{2c} \sigma_u \int \frac{\vec{\nabla} \cdot \vec{r}_M}{r_M^3} (\lambda_\mu \lambda_\nu) d\vec{r} \\ &= \frac{4\pi}{2c} \sigma_u \int \delta(\vec{r} - \vec{r}_M) (\lambda_\mu \lambda_\nu) d\vec{r}. \end{aligned} \quad (5.57)$$

The last rearrangement was made using the Green's function for the electrostatic potential

$$\vec{\nabla}^2 \frac{1}{|\vec{r}_M|} = -4\pi \delta(\vec{r} - \vec{r}_M) \quad (5.58)$$

and

$$\vec{\nabla} \frac{1}{|\vec{r}_M|} = -\frac{\vec{r}_M}{r_M^3}. \quad (5.59)$$

Using integration by parts for the other term in Eq. 5.56 yields the same result for $u = v$ with a prefactor of $-1/3$.^[440] Considering that the spin vector operator is defined as $\hat{\vec{s}} = \frac{1}{2} \vec{\sigma}$. The non-relativistic Fermi-contact term is recovered. The other parts of the sum with $v \neq u$ yield the SD term similar to Ref. 442. Therefore, all first-order terms of Ramsey's theory are recovered in the non-relativistic limit in a RKB basis. The additional term with the derivative of \mathbf{W} , which only arises in a RMB basis, does not contribute to the non-relativistic limit due to the prefactor of $\frac{1}{4c^2}$.

As there are no bilinear terms in \vec{A} in $\mathbf{\Pi}^\dagger$ and $\mathbf{\Pi}$, the exact non-relativistic limit of the DSO term is not recovered. In a RKB basis, the DSO term solely arises due to the matrix multiplications like $\mathbf{\Pi}_u^{\dagger,M} \mathbf{X}_v^N$. Again, the absolute value of the DSO term is usually negligible and the resulting calculations with the X2C-RKB or the 4c-RKB Hamiltonian are in excellent agreement with the non-relativistic calculations for molecules consisting of light elements only.^[50-53] A similar behavior is observed for the hyperfine coupling constant.^[438-440]

6 Generalized Solver for Two-Component Response Equations

The calculation of the perturbed density matrix for the quasirelativistic treatment of NMR spin–spin coupling constants requires a generalized solver for the CPHF or CPKS equations. Such a solver was developed in collaboration with Max Kehry and Christof Holzer in the context of a two-component damped response formalism for the Bethe–Salpeter equation in the GW approximation (GW-BSE) and also used to obtain dynamic and static polarizabilities.^[443] Here, the solver will be applied to the NMR couplings in a HF and a DFT framework. Quasirelativistic static polarizabilities in an X2C framework are discussed in Appendix A.3. Dynamic polarizabilities are not discussed as the frequency-dependent extension was implemented by Max Kehry.

The perturbed density matrix is calculated by approximating the perturbed coefficients as a linear combination of the unperturbed coefficients. The orbital rotation matrix for the perturbation λ of the generalized CPHF and CPKS equations is obtained in the same manner as for the one-component approach outlined in Sec. 4.7 as^[79,444]

$$O_{ij}^\lambda = -\frac{1}{2}S_{ij}^\lambda, \quad (6.1)$$

$$O_{ai}^\lambda = \frac{F_{ai}^\lambda - S_{ai}^\lambda \epsilon_i}{\epsilon_i - \epsilon_a}, \quad (6.2)$$

where i, j, \dots and a, b, \dots indicate occupied and virtual spinor orbitals, respectively. p, q, \dots denote arbitrary spinor orbitals. S_{pq}^λ is the perturbed overlap matrix and F_{pq}^λ is the perturbed Fock matrix, which depends on the perturbed density matrix and the integral derivatives. ϵ denotes the spinor energies, i.e. the eigenvalues of the Hartree–Fock or Kohn–Sham equations. The first-order spinor coefficients are given as

$$(C_{\mu i}^\alpha)^\lambda = \sum_p C_{\mu p}^\alpha O_{pi}^\lambda, \quad (6.3)$$

$$(C_{\mu i}^\beta)^\lambda = \sum_p C_{\mu p}^\beta O_{pi}^\lambda. \quad (6.4)$$

Note that the orbital rotation matrix includes α - β spin rotations as the Fock matrix and the overlap matrix in the spinor space read

$$F_{ai}^\lambda = \sum_{\mu\nu} \left[C_{\mu a}^{\alpha*} (F_{\mu\nu}^{\alpha\alpha})^\lambda C_{\nu i}^\alpha + C_{\mu a}^{\alpha*} (F_{\mu\nu}^{\alpha\beta})^\lambda C_{\nu i}^\beta + C_{\mu a}^{\beta*} (F_{\mu\nu}^{\beta\alpha})^\lambda C_{\nu i}^\alpha + C_{\mu a}^{\beta*} (F_{\mu\nu}^{\beta\beta})^\lambda C_{\nu i}^\beta \right], \quad (6.5)$$

$$S_{ai}^\lambda = \sum_{\mu\nu} \left[C_{\mu a}^{\alpha*} (S_{\mu\nu}^{\alpha\alpha})^\lambda C_{\nu i}^\alpha + C_{\mu a}^{\alpha*} (S_{\mu\nu}^{\alpha\beta})^\lambda C_{\nu i}^\beta + C_{\mu a}^{\beta*} (S_{\mu\nu}^{\beta\alpha})^\lambda C_{\nu i}^\alpha + C_{\mu a}^{\beta*} (S_{\mu\nu}^{\beta\beta})^\lambda C_{\nu i}^\beta \right]. \quad (6.6)$$

The perturbed density matrix is obtained as the derivative of Eq. 3.20

$$D^\lambda = \begin{pmatrix} (\mathbf{D}^{\alpha\alpha})^\lambda & (\mathbf{D}^{\alpha\beta})^\lambda \\ (\mathbf{D}^{\beta\alpha})^\lambda & (\mathbf{D}^{\beta\beta})^\lambda \end{pmatrix}, \quad (6.7)$$

where the individual real and imaginary contributions are given as the derivatives of Eqs. 3.21 and 3.22

$$\begin{aligned} \operatorname{Re}(D_{\nu\mu}^{\sigma_1\sigma_2,\lambda}) &= \sum_i n_i \left[\operatorname{Re}(C_{\nu i}^{\sigma_1,\lambda}) \operatorname{Re}(C_{\mu i}^{\sigma_2}) + \operatorname{Im}(C_{\nu i}^{\sigma_1,\lambda}) \operatorname{Im}(C_{\mu i}^{\sigma_2}) \right] \\ &+ \sum_i n_i \left[\operatorname{Re}(C_{\nu i}^{\sigma_1}) \operatorname{Re}(C_{\mu i}^{\sigma_2,\lambda}) + \operatorname{Im}(C_{\nu i}^{\sigma_1}) \operatorname{Im}(C_{\mu i}^{\sigma_2,\lambda}) \right], \end{aligned} \quad (6.8)$$

$$\begin{aligned} \operatorname{Im}(D_{\nu\mu}^{\sigma_1\sigma_2,\lambda}) &= \sum_i n_i \left[-\operatorname{Re}(C_{\nu i}^{\sigma_1,\lambda}) \operatorname{Im}(C_{\mu i}^{\sigma_2}) + \operatorname{Im}(C_{\nu i}^{\sigma_1,\lambda}) \operatorname{Re}(C_{\mu i}^{\sigma_2}) \right] \\ &+ \sum_i n_i \left[-\operatorname{Re}(C_{\nu i}^{\sigma_1}) \operatorname{Im}(C_{\mu i}^{\sigma_2,\lambda}) + \operatorname{Im}(C_{\nu i}^{\sigma_1}) \operatorname{Re}(C_{\mu i}^{\sigma_2,\lambda}) \right]. \end{aligned} \quad (6.9)$$

σ_1 and σ_2 denote the spin. The occupied-occupied block is only non-zero for basis functions depending on the perturbation. Thus, only the occupied-virtual block of the orbital rotation matrix is required for NMR SSCs. The generalization of the static response equations discussed in Sec. 4.7 is given in the spinor space as

$$\begin{pmatrix} \mathbf{A} & \mathbf{B} \\ \mathbf{B}^* & \mathbf{A}^* \end{pmatrix} \begin{pmatrix} \mathbf{X} \\ \mathbf{Y} \end{pmatrix} = \begin{pmatrix} \mathbf{P}^\nu \\ \mathbf{P}^{\nu*} \end{pmatrix}, \quad (6.10)$$

where the first supermatrix on the left-hand side describes the electronic Hessian, \mathbf{H} . In a complex two-component formalism, \mathbf{A} is a Hermitian matrix and the matrix \mathbf{B} is complex symmetric. The electronic Hessian is a Hermitian and positive semidefinite matrix of full rank for the ground state. The vectors \mathbf{X} and \mathbf{Y} describe the occupied-virtual contribution of the perturbed density matrix. The matrices \mathbf{A} and \mathbf{B} depend on the electronic structure theory, i.e. Hartree–Fock or Kohn–Sham density functional theory in this work. The right-hand side contains the information on the perturbation and is specific to the desired molecular property. Thus, the calculation of NMR coupling constants and static polarizabilities essentially differs in the RHS. In a generalized Kohn–Sham DFT framework, the matrices \mathbf{A} and \mathbf{B} are given by

$$A_{ia,jb} = (\epsilon_a^{\text{KS}} - \epsilon_i^{\text{KS}}) \delta_{ij} \delta_{ab} + v_{ia,jb} + f_{ia,jb}^{\text{XC}}, \quad (6.11)$$

$$B_{ia,jb} = v_{ia,bj} + f_{ia,bj}^{\text{XC}}, \quad (6.12)$$

where ϵ_p^{KS} is the Kohn–Sham energy of the spinor p and $v_{ia,jb} = \langle aj|ib \rangle = (ai|jb) = (ia|bj)$ is a two-electron integral, which may be evaluated with the RI approximation. $f_{ia,jb}^{\text{XC}}$ is the non-collinear exchange-correlation kernel defined as

$$f^{\text{XC}} = \frac{\partial^2 E_{\text{XC}}}{\partial \rho(\vec{r}) \partial \rho(\vec{r}')} 1 \otimes 1 + \sum_{k=x,y,z} \frac{\partial^2 E_{\text{XC}}}{\partial s^2} \delta(\vec{r} - \vec{r}') \sigma_k \otimes \sigma_k \quad (6.13)$$

including the HF exchange contribution for global, local, and range-separated hybrid functionals according to the definition of the exchange-correlation energy in Sec. 3.5. The XC kernel is the first derivative of the exchange-correlation potential with respect to the density. Note that the XC kernel is evaluated in the space of the basis functions and subsequently transformed with the expansion coefficients of the spinors. In a two-component non-collinear Kohn–Sham formalism, the exchange-correlation kernel is a combination of the one-component XC kernels^[421] for singlet-singlet and singlet-triplet excitations.^[443,445] An expression for the exchange-correlation kernel is given in the the next chapter.

In generalized Hartree–Fock theory, the XC kernel and the Kohn–Sham spinor energies are replaced by the exchange integrals, K , and the HF spinor energies, ϵ^{HF} , leading to

$$A_{ia,jb} = (\epsilon_a^{\text{HF}} - \epsilon_i^{\text{HF}}) \delta_{ij} \delta_{ab} + v_{ia,jb} - K_{ia,jb}, \quad (6.14)$$

$$B_{ia,jb} = v_{ia,bj} - K_{ia,bj}, \quad (6.15)$$

where the exchange integrals, $K_{ia,jb} = \langle ib|ja \rangle = (ij|ba)$, may be calculated analytically or with the seminumerical exchange approximation discussed in Sec. 3.3. The efficient implementation of the two-electron integrals for the matrices \mathbf{A} and \mathbf{B} is described in detail in Refs. 446 and 447. Thanks to the structural similarities of the response equations for time-dependent DFT and the CPKS equations,^[420,422] all two-electron integrals are already available.^[311,416,441,445,448,449] The initial OpenMP implementation^[450,451] of the integrals, the XC kernel, and the matrix operations was reworked and extended with Christof Holzer to match the capabilities of the current computer infrastructure.^[450,452]

For NMR SSCCs, the RHS vector \mathbf{P}^ν contains the one-electron Hamiltonian derivatives with respect to the nuclear magnetic moments, \vec{m}_I , in the spinor space

$$\mathbf{P}_{pq}^\nu = (\mathbf{h}^{m_I})_{pq}^\nu = \sum_{\kappa\eta} C_{p\kappa}^* (\mathbf{h}^{m_I})_{\kappa\eta}^\nu C_{\eta q} \quad \text{with } \nu = x, y, z. \quad (6.16)$$

Note that the three derivatives for each nucleus are independent of each other and a nuclear selection scheme was implemented by Fabian Mack for the non-relativistic approach^[432] and carried over to the quasirelativistic two-component ansatz. The conductor-like screening model^[453,454] (COSMO) does neither result in additional terms for the RHS nor the LHS as COSMO does not depend on the magnetic moments and the contributions to the LHS vanish like for triplet transitions according to their symmetry.

The dimension of the matrices \mathbf{A} and \mathbf{B} is $(N_{\text{occ}} \cdot N_{\text{virt}})^2$, where N_{occ} and N_{virt} denote the occupied and virtual spinors. Thus, a straightforward solution of the response equation with a Cholesky decomposition is impractical for large molecules due to the effective scaling of $\mathcal{O}((N_{\text{occ}} \cdot N_{\text{virt}})^3) \approx \mathcal{O}(N^6)$. Therefore, Eq. 6.10 is not solved directly but with an iterative method. The solver outlined herein is based on the non-Hermitian eigenvalue solver of Ref. 455 developed for excitation energies in time-dependent density functional theory and the Bethe–Salpeter equation. This solver is described in more detail in Ref. 447. The following (block) conjugate gradient or generalized Davidson algorithm to find the M roots of a linear system of equations is proposed.

1. A set of M trial vectors is generated according to

$$\mathbf{v} = \begin{pmatrix} \mathbf{x}^\nu \\ \mathbf{y}^\nu \end{pmatrix} \quad (6.17)$$

with

$$x_{bj}^\nu = \frac{P_{bj}^\nu}{\epsilon_b - \epsilon_j}, \quad (6.18)$$

$$y_{bj}^\nu = \frac{P_{bj}^{\nu*}}{\epsilon_b - \epsilon_j}. \quad (6.19)$$

2. Set $n = M$.
3. Set $m = n$. Note that in the first iteration the subspace dimension is consequently $m = n = M$.
4. Loop for $n > 0$.
5. For $i = 1 \dots n$: Form the matrix-vector product $\mathbf{w}_{m-n+i} = \mathbf{H}\mathbf{v}_{m-n+i}$ and subsequently form the $(m \times m)$ LHS matrix \mathbf{Q} and the RHS vector \mathbf{q} of the subspace with

$$\mathbf{Q} = \mathbf{w}^\dagger \mathbf{V}, \quad (6.20)$$

$$\mathbf{q} = \mathbf{V}^\dagger \mathbf{p}, \quad (6.21)$$

where the trial vectors are collected column-wise in the matrix \mathbf{V} and \mathbf{p} is the supervector of the RHS, \mathbf{P}^ν and $\mathbf{P}^{\nu*}$.

6. The linear system of equations is solved in the subspace

$$\mathbf{Q}\mathbf{t} = \mathbf{q} \quad (6.22)$$

using a Gaussian elimination with partial pivoting. So, the solution vectors \mathbf{t} are obtained. This is done with the LAPACK routines^[396] ZPOTRF and ZPOTRS. Here, ZPOTRF computes the Cholesky factorization of the complex Hermitian and positive definite matrix \mathbf{Q} . ZPOTRS solves the linear system of equations. Note that the numerical stability of this method relies on fulfilling the requirements of the matrix properties for ZPOTRF. So, the conjugate gradient method will be aborted if the ground state is not obtained successfully in the preceding SCF calculation. For the non-Hermitian case like in dynamic polarizability calculations, ZGESV is used to solve the linear system of equations.

7. For $i = 1, \dots, n$: Form the residual vectors \mathbf{r} as

$$\mathbf{z} = \mathbf{V}\mathbf{t}, \quad (6.23)$$

$$\mathbf{r} = \mathbf{H}\mathbf{z} - \mathbf{p}. \quad (6.24)$$

8. For $i = 1, \dots, n$: The procedure is converged if $\|r_i\| < \text{tol}$ (default 10^{-6}). Update n as $n = n - 1$ for a converged trial vector.

9. For $i = 1, \dots, n$: Construct new trial vectors \mathbf{u} for all non-converged trial vectors from the residual vectors with a Jacobi–Davidson-like step

$$\mathbf{u} = \varepsilon \mathbf{M}^{-1} \mathbf{z} - \mathbf{M}^{-1} \mathbf{r}, \quad (6.25)$$

$$\mathbf{M} = \text{diag}(\mathbf{H}), \quad (6.26)$$

$$\varepsilon = \frac{\mathbf{z}^\dagger \mathbf{M}^{-1} \mathbf{r}}{\mathbf{z}^\dagger \mathbf{M}^{-1} \mathbf{z}}, \quad (6.27)$$

where the general Hermitian system of equations is preconditioned with the diagonal parts of the electronic Hessian.^[456] ε is a correction term.^[457]

10. For $i = 1, \dots, n$: Orthogonalization of \mathbf{u} with respect to the old trial vectors \mathbf{v} using the Gram–Schmidt procedure.
11. Increase the dimension of the trial space with $m = m + n$ and add the new trial vectors \mathbf{u} to the existing trial vectors \mathbf{v} and the matrix \mathbf{V} .
12. End loop if $n = 0$
13. Calculate the property by contracting the solution vectors \mathbf{X} and \mathbf{Y} with the RHS vectors.

7 Generalization of meta-GGA and Local Hybrid Functionals for Gauge Invariance

The generalization of the momentum operator, \hat{p} , to the generalized momentum, $\hat{\pi}$, for magnetic properties necessitates a generalization of the kinetic energy density, τ , for meta-GGAs and the τ -dependent hybrid functionals.^[458–462] Note that the respective implementation for NMR shifts and coupling constants was carried out in collaboration with Christof Holzer.^[365]

7.1 Gauge-Dependence of the Kinetic Energy Density

A fundamental requirement of electrodynamics is the invariance of all physical observables with respect to a gauge transformation of the vector potential^[387,388]

$$\vec{A}(\vec{r}) \longrightarrow \vec{A}'(\vec{r}) = \vec{A}(\vec{r}) + \vec{\nabla}\Lambda(\vec{r}), \quad (7.1)$$

where Λ is a real gauge function. The total energy and therefore the exchange-correlation energy as a function of the density, the density gradient, and the kinetic energy density

$$E_{XC} = \int f(\rho(\vec{r}), \vec{\nabla}\rho(\vec{r}), \tau(\vec{r})) d\vec{r} \quad (7.2)$$

is consequently required to be gauge invariant. This implies that either all terms of the XC energy are gauge-invariant or that the gauge-dependence of some terms cancel each other due to the explicit functional form. It can easily be shown that the kinetic energy density, τ , becomes gauge dependent and thus the XC energy is not gauge-invariant without further corrections.^[461,462] Consider the application of the gauge transformation in Eq. 7.1 to the Kohn–Sham orbitals

$$\psi_j(\vec{r}) \longrightarrow \psi'_j(\vec{r}) = \psi_j(\vec{r}) \exp\left(-\frac{i}{c}\Lambda(\vec{r})\right), \quad (7.3)$$

where a position dependent phase factor was introduced. Therefore, the kinetic energy density becomes

$$\tau(\vec{r}) \longrightarrow \tau'(\vec{r}) = \tau(\vec{r}) - \frac{1}{c}(\vec{\nabla}\Lambda(\vec{r})) \cdot \vec{j}_p(\vec{r}) + \frac{1}{2c^2}|\vec{\nabla}\Lambda(\vec{r})|^2\rho(\vec{r}) \quad (7.4)$$

with the paramagnetic current density \vec{j}_p ^[463]

$$\vec{j}_p(\vec{r}) = -\frac{i}{2} \sum_i \left(\psi_i^* \vec{\nabla} \psi_i - \psi_i \vec{\nabla} \psi_i^* \right) = \frac{i}{2} \sum_i \left(\psi_i \vec{\nabla} \psi_i^* - \psi_i^* \vec{\nabla} \psi_i \right) = \text{Re} \sum_i \psi_i^* \hat{p} \psi_i. \quad (7.5)$$

Here, the paramagnetic current density is the real part of the momentum density.^[464] The total current density in the presence of a vector potential is^[463]

$$\vec{j}(\vec{r}) = \text{Re} \left(\Psi^*(\vec{r}) \hat{\pi} \Psi(\vec{r}) \right) = \vec{j}_p(\vec{r}) + \frac{1}{c} \rho(\vec{r}) \vec{A}(\vec{r}). \quad (7.6)$$

In contrast to the physical or total current density, the paramagnetic current density does not depend on the vector potential. The transformed kinetic energy in Eq. 7.4 is a quadratic function of Λ and explicitly depends on the gauge. As no further corrections to cancel this gauge dependence were introduced so far, a simple meta-GGA exchange-correlation energy will be gauge dependent or gauge variant. Consequently, the iso-orbital constraint does not hold for $\tau'(\vec{r})$ as the gauge-transformed inhomogeneity parameter

$$z'(\vec{r}) = \frac{\tau^{vW}(\vec{r})}{\tau'(\vec{r})} \quad (7.7)$$

may take any value between zero and one depending on the gauge—even in one-electron regions.^[462]

7.2 Gauge-Invariant Formalism for NMR Shifts and Couplings

A first gauge-invariant generalization of the kinetic energy density was presented by Maximoff and Scuseria for NMR shielding constants and shifts.^[461] As discussed in Sec. 4.7, the CPKS equations are solved for the magnetic field derivatives and it is therefore sufficient to consider the gauge-invariant generalization of τ for the external magnetic field in the first place. Similar to the GIAOs, the external magnetic field may be included in the kinetic energy density according to^[461]

$$\tilde{\tau}_{\text{MS}}(\vec{r}) = \sum_i \left(\hat{p} + \frac{1}{c} \vec{A}_O^B \right) \psi_j^* \cdot \left(\hat{p} + \frac{1}{c} \vec{A}_O^B \right) \psi_j \quad (7.8)$$

with the gauge-origin-dependent vector potential of the external magnetic field

$$\vec{A}_O^B(\vec{r}) = \frac{1}{2} \vec{B} \times (\vec{r} - \vec{R}_O). \quad (7.9)$$

Here, $\tilde{\tau}_{\text{MS}}$ may be interpreted as the magnetic-field-generalized momentum density. Thus, the gauge-dependence is canceled for the generalized kinetic energy density and consequently for the exchange-correlation energy. In the limit of a zero-field, $\tilde{\tau} \rightarrow \tau$ holds. The tempting property of this choice is that it only affects the derivatives with respect to the magnetic field of the right-hand side in the CPKS equations to calculate the perturbed Fock matrix. The derivative of the XC contribution to the perturbed Fock matrix is obtained as

$$\frac{\partial F_{\mu\nu}^{XC}}{\partial B_u} = \frac{\partial}{\partial B_u} \frac{\partial E_{XC}}{\partial D_{\mu\nu}} = \frac{\partial}{\partial B_u} \left[\frac{\partial}{\partial D_{\mu\nu}} \int f(\rho(\vec{r}), \vec{\nabla}\rho(\vec{r}), \tilde{\tau}(\vec{r})) d\vec{r} \right], \quad (7.10)$$

where the derivative of f is calculated with the chain rule. The explicit expression for the derivative of the generalized kinetic energy density with respect to the density matrix in a GIAO basis does not depend on the density matrix. Consequently, no terms involving the perturbed density matrix arise for the XC contribution and the CPHF equations of meta-GGA functionals are solved directly in one step like for LSDA and GGA functionals. To show this, Eq. 7.8 is rearranged using τ according to

$$\tilde{\tau}_{\text{MS}}(\vec{r}) = \tau(\vec{r}) + \frac{1}{c} \vec{j}_p(\vec{r}) \cdot \vec{A}_O^B(\vec{r}) + \frac{1}{2c^2} |\vec{A}_O^B(\vec{r})|^2 \rho(\vec{r}). \quad (7.11)$$

Thus, the derivatives of ρ , τ , and \vec{j}_p with respect to the density matrix are needed to set up the Fock matrix. The derivatives of the individual terms read

$$\frac{\partial \rho}{\partial D_{\mu\nu}} = \lambda_\mu^* (\vec{B}, \vec{r}) \lambda_\nu (\vec{B}, \vec{r}), \quad (7.12)$$

$$\frac{\partial \tau}{\partial D_{\mu\nu}} = \frac{1}{2} \vec{\nabla} \lambda_{\mu}^* (\vec{B}, \vec{r}) \vec{\nabla} \lambda_{\nu} (\vec{B}, \vec{r}), \quad (7.13)$$

$$\frac{\partial \vec{j}_p}{\partial D_{\mu\nu}} = \frac{i}{2} \left[\lambda_{\nu} (\vec{B}, \vec{r}) \vec{\nabla} \lambda_{\mu}^* (\vec{B}, \vec{r}) - \lambda_{\mu}^* (\vec{B}, \vec{r}) \vec{\nabla} \lambda_{\nu} (\vec{B}, \vec{r}) \right]. \quad (7.14)$$

Here, the complex GIAOs are indicated by the explicit field dependence, $\lambda_{\mu} (\vec{B}, \vec{r})$. The field-free basis functions are denoted as $\lambda_{\mu} (\vec{r})$. The magnetic field dependence and the corresponding terms for the derivative with respect to the magnetic field arises due to the phase factor of the GIAOs. In linear response theory, the second-order term $|\vec{A}_O^B(\vec{r})|^2$ does not contribute to the first-order derivatives and the derivative of the term with $\tilde{\tau}_{\text{MS}}$ in Eq. 7.10 becomes

$$\begin{aligned} \frac{\partial}{\partial B_u} \frac{\partial \tilde{\tau}_{\text{MS}}}{\partial D_{\mu\nu}} &= \frac{\partial}{\partial B_u} \left[\frac{1}{2} \vec{\nabla} \lambda_{\mu}^* (\vec{B}, \vec{r}) \vec{\nabla} \lambda_{\nu} (\vec{B}, \vec{r}) \right] \\ &+ \frac{\partial}{\partial B_u} \left[\frac{i}{2c} \vec{A}_O^B \left\{ \lambda_{\nu} (\vec{B}, \vec{r}) \vec{\nabla} \lambda_{\mu}^* (\vec{B}, \vec{r}) - \lambda_{\mu}^* (\vec{B}, \vec{r}) \vec{\nabla} \lambda_{\nu} (\vec{B}, \vec{r}) \right\} \right]. \end{aligned} \quad (7.15)$$

So, this generalization preserves the symmetry of the derivatives of the XC energy of the left-hand side in the CPKS equations. Thus, the symmetry considerations of the uncoupled approximation^[418,419] still hold and no iterative procedure is required for meta-GGA functionals. This generalization is implemented in most quantum chemical program suites and was also implemented in TURBOMOLE.^[407] The implementation is described in detail in Ref. 414. However, the iso-orbital constraint is not satisfied. Moreover, the gauge correction depends on the vector potential and its application to time-dependent density functional theory or NMR coupling constants and related properties would require major modifications of the existing machinery and the calculation of specific DFT integrals for each property. The general form of this generalization is given as^[462]

$$\tilde{\tau}_{\text{MS}}(\vec{r}) = \tau(\vec{r}) + \frac{1}{c} \vec{j}_p(\vec{r}) \cdot \vec{A}(\vec{r}) + \frac{1}{2c^2} |\vec{A}(\vec{r})|^2 \rho(\vec{r}), \quad (7.16)$$

where \vec{A} is a general vector potential. Therefore, an application of this approach to NMR spin-spin coupling constants or hyperfine coupling tensors in electron paramagnetic resonance (EPR) spectroscopy is not desirable. Moreover, the loss of the iso-orbital constraint may be also problematic for local hybrid functionals based on the t-LMF.

Alternatively, Becke^[459] and Tao^[460] suggested to generalize the kinetic energy density with the paramagnetic current density in the spirit of current density functional theory (CDFT) to avoid the explicit dependence on the vector potential and the magnetic perturbation^[463,465]

$$\tilde{\tau}_{\text{BT}} = \tau - \frac{|\vec{j}_p|^2}{2\rho}. \quad (7.17)$$

The kinetic energy density is gauge invariant due to the gauge transformation of the paramagnetic current density

$$\vec{j}_p(\vec{r}) \longrightarrow \vec{j}'_p(\vec{r}) = \vec{j}_p(\vec{r}) - \frac{1}{c} \vec{\nabla} \Lambda(\vec{r}) \rho(\vec{r}). \quad (7.18)$$

The static meta-GGA ground-state properties and electric response properties like polarizabilities are not altered as $\tilde{\tau}_{\text{BT}}$ coincides with τ for these properties. It was shown^[462] that this choice ensures the iso-orbital constraint with a gauge-invariant inhomogeneity parameter and satisfies the von Weizsäcker inequality^[466]

$$\tau^{\text{vW}}(\vec{r}) \leq \tilde{\tau}(\vec{r}). \quad (7.19)$$

This ansatz was introduced into quantum chemistry program suites by Bates and Furche for time-dependent density functional theory and excited-state properties.^[462] A drawback of this ansatz is that for NMR shifts and related magnetic properties, $|\vec{j}_p|^2$ leads to a magnetic XC kernel in the left-hand side of the CPKS equations. Therefore, an iterative procedure is required even in non-hybrid DFT NMR calculations as noted by Bates and Furche.^[462] Essentially, the matrices of the XC kernel become non-symmetric and are thus partitioned into the respective symmetric and antisymmetric contributions. To demonstrate this, the basis set expansion of the magnetic-field derivatives of the paramagnetic current density is considered,^[467]

$$\begin{aligned} \frac{\partial}{\partial B_u} \frac{\partial \tilde{\tau}_{\text{BT}}}{\partial D_{\mu\nu}} &= \frac{\partial}{\partial B_u} \left[\frac{1}{2} \vec{\nabla} \lambda_\mu^* (\vec{B}, \vec{r}) \vec{\nabla} \lambda_\nu (\vec{B}, \vec{r}) \right] \\ &- \frac{\partial}{\partial B_u} \left[\frac{i}{2\rho} \vec{j}_p \left\{ \lambda_\nu (\vec{B}, \vec{r}) \vec{\nabla} \lambda_\mu^* (\vec{B}, \vec{r}) - \lambda_\mu^* (\vec{B}, \vec{r}) \vec{\nabla} \lambda_\nu (\vec{B}, \vec{r}) \right\} \right]. \end{aligned} \quad (7.20)$$

The derivative of \vec{j}_p with respect to the magnetic field reads

$$\begin{aligned} \frac{\partial \vec{j}_p}{\partial B_u} &= \frac{i}{2} \sum_{\mu\nu} \frac{\partial}{\partial B_u} \left[D_{\mu\nu} \left\{ \lambda_\nu (\vec{B}, \vec{r}) \vec{\nabla} \lambda_\mu^* (\vec{B}, \vec{r}) - \lambda_\mu^* (\vec{B}, \vec{r}) \vec{\nabla} \lambda_\nu (\vec{B}, \vec{r}) \right\} \right] \\ &= \frac{i}{2} \sum_{\mu\nu} \frac{\partial D_{\mu\nu}}{\partial B_u} \left\{ \lambda_\nu (\vec{B}, \vec{r}) \vec{\nabla} \lambda_\mu^* (\vec{B}, \vec{r}) - \lambda_\mu^* (\vec{B}, \vec{r}) \vec{\nabla} \lambda_\nu (\vec{B}, \vec{r}) \right\} \\ &- \frac{1}{4} \sum_{\mu\nu} D_{\mu\nu} \frac{\partial}{\partial B_u} \left\{ \vec{B} \times (\vec{R}_\mu - \vec{R}_O) + \vec{B} \times (\vec{R}_\nu - \vec{R}_O) \right\} \lambda_\mu^*(\vec{r}) \lambda_\nu(\vec{r}) \\ &- \frac{1}{2} \sum_{\mu\nu} D_{\mu\nu} (\vec{R}_{\mu\nu} \times \vec{r})_u \left(\lambda_\nu(\vec{r}) \vec{\nabla} \lambda_\mu^*(\vec{r}) - \lambda_\mu^*(\vec{r}) \vec{\nabla} \lambda_\nu(\vec{r}) \right). \end{aligned} \quad (7.21)$$

Here, the derivative of the paramagnetic current density depends on the perturbed density and the corresponding term in the left-hand side of the CPKS equations does not vanish as the term is purely imaginary and antisymmetric. The CPKS equations need to be solved in an iterative procedure for current-dependent meta-GGAs. Therefore, it has attracted less general interest for magnetic response properties. A pilot implementation of NMR shifts with the current-dependent generalization was just presented recently for meta-GGAs and t-LMF-based local hybrid functionals.^[467] This implementation was reworked in collaboration with Christof Holzer by interfacing the efficient routines developed in Ref. 462 for the left-hand side of the CPKS equations. This ensures that the resulting left-hand side contribution is numerically stable and strictly antisymmetric. Thus, a smooth convergence of the CPKS equations for large molecules is obtained. The implementation was verified by interfacing the non-relativistic one-component integrals to the general two-component non-Hermitian (block) conjugate gradient or Davidson solver, which simultaneously processes symmetric and antisymmetric contributions. Moreover, the implementation was extended to local hybrid functionals based on the z-LMF and the PSTS-LMF in conventional gauge.

NMR spin–spin coupling constants are commonly calculated with the gauge-variant kinetic energy density, τ .^[123,432,468] To the best of the author’s knowledge, no implementation with the generalized kinetic energy density was presented so far. However, the generalization of the kinetic energy density based on the paramagnetic current density can be applied straightforwardly to NMR coupling constants based on the time-dependent density functional implementation as shown below. In a non-relativistic approach, the response equations are solved separately for the paramagnetic spin–orbit, spin-dipole, and the Fermi-contact term.^[6] Here, the paramagnetic spin–orbit term is obtained directly for meta-GGAs with the gauge-variant kinetic energy density. This is no longer sufficient when considering the paramagnetic current density and $\tilde{\tau}_{\text{BT}}$ as the paramagnetic spin–orbit integrals are imaginary and antisymmetric. So, the symmetry is the same as for NMR shifts and consequently an iterative procedure is required for the current-dependent

meta-GGAs. Similar to static polarizabilities, the SD and the FC term are not altered by the generalization as the one-electron integrals for the right-hand side of the CPKS equations are real and the paramagnetic current density terms for the orbital rotation matrix of the left-hand side vanish. Therefore, the previously presented non-relativistic implementation of meta-GGAs and local hybrid functionals^[432] was extended to account for the paramagnetic current density in a gauge-invariant Kohn–Sham formalism by interfacing the routines of Ref. 462 for the PSO term. Compared to NMR shifts, the derivatives of $\tilde{\tau}_{BT}$ are simplified as the basis functions do not depend on the nuclear magnetic moments, \vec{m}_I ,

$$\frac{\partial}{\partial m_{I,u}} \frac{\partial \tilde{\tau}_{BT}}{\partial D_{\mu\nu}} = -\frac{\partial}{\partial m_{I,u}} \left[\frac{i}{2\rho} \vec{j}_p \left\{ \lambda_\nu(\vec{r}) \vec{\nabla} \lambda_\mu^*(\vec{r}) - \lambda_\mu^*(\vec{r}) \vec{\nabla} \lambda_\nu(\vec{r}) \right\} \right]. \quad (7.22)$$

Thus, only the paramagnetic current density and the density have to be evaluated, which are available from the time-dependent density functional theory implementation.^[416,462]

The extension to a Kramers-restricted^[469] (closed-shell) two-component framework, will be illustrated for local hybrid functionals as the most general τ -dependent functional class considered herein. The non-relativistic kernel of a local hybrid functional, f_{LH}^{XC} , was derived in Ref. 470 and the two-component XC kernel was later derived by Holzer^[443] in analogy to the GGA XC kernel.^[445,471,472] The non-collinear LHF XC kernel is defined as

$$\begin{aligned} f_{LH}^{XC,nc} &= \frac{\partial^2 E_{XC}}{\partial \rho(\vec{r}) \partial \rho(\vec{r}')} 1 \otimes 1 + \sum_{k=x,y,z} \frac{\partial^2 E_{XC}}{\partial s^2} \delta(\vec{r} - \vec{r}') \sigma_k \otimes \sigma_k \\ &= (C_{\mu a}^\alpha)^* C_{\nu i}^\alpha (\mu\nu | f_{LH}^{XC,s} | \kappa\eta) C_{\kappa b}^\alpha (C_{\eta j}^\alpha)^* + \sum_{k=x,y,z} \frac{\partial^2 E_{XC}}{\partial s^2} \delta(\vec{r} - \vec{r}') \sigma_k \otimes \sigma_k, \end{aligned} \quad (7.23)$$

where s denotes the norm of the non-collinear spin magnetization vector of Eq. 3.51. The second term can be simplified using the singlet and triplet kernels derived by Bauernschmitt and Ahlrichs,^[421] $f^{XC,s}$ and $f^{XC,t}$. Further making use of the complex-conjugate structure of the Kramers-symmetric reference state yields^[443]

$$\begin{aligned} (ai | f_{LH}^{XC,nc} | jb) &= \sum_{\mu\nu\kappa\eta} (C_{\mu a}^\alpha)^* C_{\nu i}^\alpha (\mu\nu | f_{LH}^{XC,s} | \kappa\eta) C_{\kappa b}^\alpha (C_{\eta j}^\alpha)^* + (C_{\mu a}^\alpha)^* C_{\nu i}^\alpha (\mu\nu | f_{LH}^{XC,t} | \kappa\eta) C_{\kappa n}^\beta (C_{\eta j}^\beta)^* \\ &\quad + (C_{\mu a}^\beta)^* C_{\nu i}^\beta (\mu\nu | f_{LH}^{XC,s} | \kappa\eta) C_{\kappa b}^\beta (C_{\eta j}^\beta)^* + (C_{\mu a}^\beta)^* C_{\nu i}^\beta (\mu\nu | f_{LH}^{XC,t} | \kappa\eta) C_{\kappa b}^\alpha (C_{\eta j}^\alpha)^* \\ &\quad + (C_{\mu a}^\beta)^* C_{\nu i}^\alpha (\mu\nu | f_{LH}^{XC,t} | \kappa\eta) C_{\kappa b}^\alpha (C_{\lambda j}^\beta)^* + (C_{\mu a}^\alpha)^* C_{\nu i}^\beta (\mu\nu | f_{LH}^{XC,t} | \kappa\eta) C_{\kappa b}^\beta (C_{\eta j}^\alpha)^*, \end{aligned} \quad (7.24)$$

where only 6 of 16 possible combinations are required to evaluate the XC kernel. All τ -dependent terms in the singlet and triplet kernel are replaced by the current-dependent generalization $\tilde{\tau}$ and the paramagnetic current density is calculated with the respective density matrices. The density matrices of the spin blocks ($\{\alpha\alpha\}$, $\{\alpha\beta\}$, $\{\beta\alpha\}$, $\{\beta\beta\}$) are split into the symmetric and the antisymmetric contribution to utilize the one-component routines. Note that the two-component meta-GGA and LHF XC kernels were implemented by Holzer^[452,455] and can be readily used for the two-component calculations of NMR SSCCs thanks to the general solver outlined in the previous chapter. However, the thresholds for the addition of the matrix elements to the kernel were tightened by five orders of magnitude in the two-component case to ensure a rapid convergence of the CPKS procedure. Note that in a quasirelativistic two-component formalism all three terms are evaluated simultaneously to set up the perturbed two-component Fock matrix. Thus, an iterative procedure is required for all “pure” density functional approximations.

8 Development of Tailored Basis Sets

The NMR shifts depend on the electron density in the vicinity of the nuclei. Therefore, optimized basis sets are required.^[219,220] The existing X2C orbital basis sets of double and triple- ζ quality^[203] are chosen as a starting point for the NMR-tailored basis sets of the same quality. These orbital basis sets were optimized in a variational procedure utilizing numerical gradients. Such an approach is impractical for larger basis sets. Therefore, analytical basis set gradients were derived and implemented in this work to develop the corresponding quadruple- ζ orbital basis sets.

8.1 Analytical Gradients and Symmetry Exploitation

In a variational procedure, the basis sets are optimized with a Newton–Raphson algorithm based on energy calculations, gradients, and a Hessian update for the relaxation step.^[194,195,473] The potential energy surface with respect to the basis set parameters is very complicated as the parameters are coupled. Therefore, the relaxation procedure requires to consider the exponents and the contraction coefficients simultaneously but freezing some parameters or resetting the Hessian update. To ensure a local minima is found, the Broyden–Fletcher–Goldfarb–Shanno algorithm^[474–477] is a common choice for the Hessian update. The optimization is performed for atoms in restricted-open-shell Hartree–Fock (ROHF) theory.^[478] This requires to exploit point group symmetry to prepare the atomic states.

To begin with, the analytical basis set gradients for the X2C Hamiltonian are derived. A contracted Cartesian Gaussian basis function centered at the nucleus A is defined as

$$\lambda_{\mu,A}(l_x, l_y, l_z) = \sum_i k_i g_{i,A}(l_x, l_y, l_z) \quad (8.1)$$

with the contraction coefficient k_i and the primitive Gaussian function $g_{i,A}$

$$g_{i,A}(l_x, l_y, l_z) = N_i (x - A_x)^{l_x} (y - A_y)^{l_y} (z - A_z)^{l_z} \exp \left[-\zeta_\mu \left(\vec{r}' - \vec{R}_A \right)^2 \right], \quad (8.2)$$

$$N_i = \left(\frac{2^{4L-1}}{\pi^3} \right)^{1/4} \left(\frac{1}{(2l_x - 1)!! (2l_y - 1)!! (2l_z - 1)!!} \right)^{1/2} \zeta_i^{(1/2)(L+1/2)}, \quad (8.3)$$

where the number L is defined as $L = l_x + l_y + l_z + 1$.^[194] !! indicates the double factorial. The derivative of the electronic energy^[410,479] with respect to the exponents ζ_μ reads

$$\frac{\partial E}{\partial \zeta_\mu} = \text{tr}(\mathbf{Dh}^{\zeta_\mu}) + \frac{1}{2} \text{tr}(\mathbf{\Gamma G}^{\zeta_\mu}) - \text{tr}(\mathbf{ZS}^{\zeta_\mu}) \quad (8.4)$$

with the one-electron density matrix \mathbf{D} , the two-electron integrals \mathbf{G} , the two-electron density matrix $\mathbf{\Gamma}$, and the energy-weighted density matrix \mathbf{Z} . The explicit expressions of these matrices depend on the chosen electronic structure theory.

In restricted HF theory, the LCAO coefficients are real and the matrices are defined as

$$\mathbf{D}_{\mu\nu} = 2 \sum_{i \in \text{occ}} C_{\mu i} C_{\nu i}, \quad (8.5)$$

$$\mathbf{Z}_{\mu\nu} = 2 \sum_{i \in \text{occ}} \epsilon_i C_{\mu i} C_{\nu i}, \quad (8.6)$$

$$(\mathbf{\Gamma G})_{\mu\nu} = \sum_{\kappa, \omega} \mathbf{D}_{\mu\nu} \mathbf{D}_{\kappa\omega} \left[(\mu\nu | \kappa\omega) - \frac{1}{2} (\mu\kappa | \nu\omega) \right]. \quad (8.7)$$

However, basis sets are optimized in ROHF to prepare the atomic states and therefore a brief review of ROHF is provided to derive the expressions. In ROHF, two sets of orbitals are considered. The first set, $\{\psi_k^c\}$, describes the doubly occupied closed-shell core. The second set, $\{\psi_r^o\}$, describes the partially occupied open shells. The two subsets are constructed with a Slater determinant and are orthonormal. The total energy is given as

$$E = 2 \sum_k h_k + \sum_{k,l} [2J_{kl} - K_{kl}] + f \left(2 \sum_r h_r + f \sum_{r,s} [2aJ_{rs} - bK_{rs}] + 2 \sum_{k,r} [2J_{kr} - K_{kr}] \right), \quad (8.8)$$

where h_k denotes the expectation value of the one-electron Hamiltonian with the doubly occupied orbital k and h_r the expectation value with the open-shell orbital r . The Coulomb and exchange matrix elements are defined accordingly. a , b , and f are parameters. a and b depend on the electronic state and f is the fractional occupation of the open shell. The individual contributions to the Coulomb operator can be described as

$$\hat{J}^c = \sum_k \hat{J}_k, \quad \hat{J}^o = f \sum_r \hat{J}_r, \quad \hat{J} = \hat{J}^c + \hat{J}^o \quad (8.9)$$

and the other operators may be partitioned in the same manner. Minimization of the energy with respect to the orbitals leads to the ROHF equations. This introduces coupling elements between the closed-shell and the partially open-shell orbitals. The Roothaan–Hall form of the ROHF equations reads

$$\mathbf{FC} = \epsilon \mathbf{SC}, \quad (8.10)$$

where the Fock matrix is defined as

$$\mathbf{F} = \mathbf{h} + \mathbf{P} - \mathbf{Q} + \mathbf{R}. \quad (8.11)$$

Here, \mathbf{P} is the total contribution of the two-electron integrals defined with the 4-index supermatrix of the Coulomb and the exchange operator

$$\mathbf{P} = (2\mathcal{J} - \mathcal{K}) \mathbf{D}, \quad (8.12)$$

where \mathbf{D} is the total density, $\mathbf{D} = \mathbf{D}^c + \mathbf{D}^o$. The matrix \mathbf{Q} describes the two-electron part of the open-shell contribution

$$\mathbf{Q} = (2a\mathcal{J} - b\mathcal{K}) \mathbf{D}^o \quad (8.13)$$

and the matrix \mathbf{R} is defined as

$$\mathbf{R} = \mathbf{SDQ} + \mathbf{QDS}. \quad (8.14)$$

For analytical derivatives in Eq. 8.4, the one-electron terms depend on the total density only and the two-electron terms are evaluated with the total contribution, \mathbf{P} , and the open-shell contribution, \mathbf{Q} , as well as the coupling terms, \mathbf{R} . The derivatives of the two-electron integrals \mathcal{J} and \mathcal{K} are used. In the scalar-relativistic

one-electron X2C ansatz, only the derivatives of the Hamiltonian $\mathbf{h}^{\zeta\mu}$ are different from the non-relativistic formalism.

The derivative of the X2C Hamiltonian with respect to the basis set exponent follows as

$$\mathbf{h}^{\zeta\mu} = \mathbf{R}^{\dagger, \zeta\mu} \mathbf{L} \mathbf{R} + \mathbf{R}^{\dagger} \mathbf{L}^{\zeta\mu} \mathbf{R} + \mathbf{R}^{\dagger} \mathbf{L} \mathbf{R}^{\zeta\mu} \quad (8.15)$$

with the derivative of the NESC matrix

$$\begin{aligned} \mathbf{L}^{\zeta\mu} = & \mathbf{V}^{\zeta\mu} + \mathbf{X}^{\dagger, \zeta\mu} \mathbf{T} + \mathbf{X}^{\dagger} \mathbf{T}^{\zeta\mu} + \mathbf{T}^{\zeta\mu} \mathbf{X} + \mathbf{T} \mathbf{X}^{\zeta\mu} \\ & + \mathbf{X}^{\dagger} \left(\frac{1}{4c^2} \mathbf{W}^{0, \zeta\mu} - \mathbf{T}^{\zeta\mu} \right) \mathbf{X} + \mathbf{X}^{\dagger, \zeta\mu} \left(\frac{1}{4c^2} \mathbf{W}^0 - \mathbf{T} \right) \mathbf{X} + \mathbf{X}^{\dagger} \left(\frac{1}{4c^2} \mathbf{W}^0 - \mathbf{T} \right) \mathbf{X}^{\zeta\mu}. \end{aligned} \quad (8.16)$$

The derivatives of the one-electron integrals are computed with the derivative of the basis functions

$$\begin{aligned} \frac{\partial \langle x | \lambda_{\mu, A}(l_x, l_y, l_z) \rangle}{\partial \zeta_{\mu}} = & \frac{\partial N_{\mu}}{\partial \eta_{\mu}} \frac{1}{N_{\mu}} \langle x | \lambda_{\mu}(l_x, l_y, l_z) \rangle \\ & - \langle x | \lambda_{\mu}(l_x + 2, l_y, l_z) \rangle - \langle x | \lambda_{\mu}(l_x, l_y + 2, l_z) \rangle - \langle x | \lambda_{\mu}(l_x, l_y, l_z + 2) \rangle. \end{aligned} \quad (8.17)$$

Therefore, all integrals are obtained by linear combinations. The derivative of the normalization constant results in a prefactor. For instance, the derivative of the potential matrix is given by

$$\mathbf{V}_{\mu\nu}^{\zeta\mu} = \frac{\partial N_{\mu}}{\partial \eta_{\mu}} \frac{1}{N_{\mu}} \langle \lambda_{\mu} | \hat{V} | \lambda_{\nu} \rangle + \langle \lambda_{\mu} + 2_x | \hat{V} | \lambda_{\nu} \rangle + \langle \lambda_{\mu} + 2_y | \hat{V} | \lambda_{\nu} \rangle + \langle \lambda_{\mu} + 2_z | \hat{V} | \lambda_{\nu} \rangle. \quad (8.18)$$

The other matrices are evaluated in the same manner. The derivatives of \mathbf{S} and \mathbf{T} are calculated with Gauss–Hermite integration and the derivatives of \mathbf{V} and \mathbf{W} by Gauss–Rys integration. The derivatives of the decoupling and the renormalization matrix are obtained by solving response equations and Sylvester matrix equations. The derivative of \mathbf{X} is computed according to

$$\mathbf{X}^{\zeta\mu} = (\mathbf{C}_{-}^S - \mathbf{X} \mathbf{C}_{-}^L) \mathbf{U}_{-+}^{\zeta\mu} + \mathbf{C}_{+}^{L, \dagger} \tilde{\mathbf{S}} \quad (8.19)$$

with the orbital rotation matrix

$$(\mathbf{U}_{-+}^{\zeta\mu})_{kl} = \frac{(\tilde{\mathbf{D}}^{\zeta\mu -+})_{kl} - (\tilde{\mathbf{M}}_{-+}^{\zeta\mu})_{kl} (\mathbf{E}_{++})_{ll}}{(\mathbf{E}_{++})_{ll} - (\mathbf{E}_{--})_{kk}}. \quad (8.20)$$

For the derivative of the renormalization matrix, the Sylvester equation

$$\mathbf{R} \mathbf{R}^{\zeta\mu} + \mathbf{R}^{\zeta\mu} \mathbf{R} = \tilde{\mathbf{S}}^{-1} (\mathbf{S}^{\zeta\mu} - \tilde{\mathbf{S}}^{\zeta\mu} \mathbf{R} \mathbf{R}) \quad (8.21)$$

is solved with an eigenvalue decomposition method. The algorithm for $\mathbf{h}^{\zeta\mu}$ is based on the geometry gradients.^[106,107] The derivative of the Hamiltonian with respect to the contraction coefficients, k_i , significantly differs from the derivatives discussed so far. The X2C Hamiltonian does not depend on the contraction coefficients and therefore no response or Sylvester matrix equations have to be solved. The X2C Hamiltonian is calculated like in energy calculations and the derivative is formed in the contraction step according to

$$\mathbf{h}^{k_i} = \mathbf{C}_{\text{cont}}^{\dagger, k_i} \mathbf{h}_{\text{X2C}} \mathbf{C}_{\text{cont}} + \mathbf{C}_{\text{cont}}^{\dagger} \mathbf{h}_{\text{X2C}} \mathbf{C}_{\text{cont}}^{k_i}. \quad (8.22)$$

The matrix \mathbf{C}_{cont} contains the contraction coefficients. Hence, the derivative of this matrix is trivial as the elements are either zero or one and the routine of the contraction only requires minor modifications to

calculate the respective derivative. As the basis sets are optimized in atomic calculations and then tested for a large set of small and mid-sized molecules, the DLU scheme is not implemented for basis set gradients.

The implementation exploits Abelian and non-Abelian point group symmetry based on the considerations of Ref. 105. Therefore, the integrals are still evaluated in C_1 symmetry but the algebraic steps support the point group symmetry to reduce the dimension of the involved matrices. After the integral evaluation and the on the fly transformation to the spherical atomic orbital basis, the matrices \mathbf{S} , \mathbf{T} , \mathbf{V} , and \mathbf{W}^0 are transformed to the symmetry-adapted (SAO) basis with the coefficients \mathbf{c}_{AS} as discussed in Ref. 480. In this basis, the matrices \mathbf{S}_{SS} , \mathbf{T}_{SS} , \mathbf{V}_{SS} , and \mathbf{W}_{SS}^0 are block-diagonal. Therefore, the relativistic decoupling is carried out separately for each block. The matrices \mathbf{X}_{SS} , \mathbf{R}_{SS} , $\tilde{\mathbf{S}}_{SS}$, $\tilde{\mathbf{S}}_{SS}^{-1}$, \mathbf{V}_{SS} , the eigenvectors, and the eigenvalues are obtained and kept in memory for the X2C response and Sylvester matrix equations. Similar to the unperturbed integrals, the integral derivatives are computed in C_1 symmetry in the spherical AO basis and subsequently transformed to the SAO basis. Also, the integral derivative matrices are block diagonal in this base and the response of \mathbf{X}_{SS} and \mathbf{R}_{SS} is obtained independently for every irreducible representation. This yields the perturbed Hamiltonian in the SAO basis, which needs to be transformed back to the AO basis with the inverse coefficients \mathbf{c}_{AS}^{-1} given as

$$\mathbf{c}_{AS}^{-1} = \mathbf{S}_{SS}^{-1} \mathbf{S}_{SA}. \quad (8.23)$$

\mathbf{S}_{SA} indicates that only one index is transformed from the AO to the SAO basis. The inverse of the overlap matrix \mathbf{S}_{SS}^{-1} is calculated independently for every irreducible representation. The perturbed Hamiltonian in the AO basis is further transformed to the CAO basis and contracted to form the trace with the density matrix.

With the described basis set gradients, the computation time is reduced to a few seconds compared to a few minutes with numerical gradients. The quadruple- ζ basis sets were then developed by Lucas Spiske, Patrik Pollak, and Florian Weigend. For balanced errors, the developed basis sets are tested with a large set of molecules featuring the oxidation states of nearly all elements up to radon.^[481] The errors are measured with respect to a large even-tempered basis set.^[203,482,483] The exponents are constructed by a factor of $\sqrt[4]{10}$ and functions are added until the energy is considered to be converged. The extensions for NMR shifts of the quadruple- ζ bases were then optimized by the author.^[483]

8.2 Optimized Basis Sets for NMR Shieldings and Shifts

The construction of the tailored basis sets is described in detail for the triple- ζ bases as these are the “default” choice for relativistic NMR shielding calculations. The double- ζ basis sets are obtained in the same manner and the description is shortened accordingly. The quadruple- ζ bases require different optimizations and considerations. During the development of the quadruple- ζ orbital basis sets it turned out that the previously constructed even-tempered basis set of Ref. 203 for the double and triple- ζ orbital and NMR-tailored basis sets is not sufficiently accurate for quadruple- ζ basis sets. Therefore, a larger even-tempered basis set was constructed in Ref. 483 and is used for the development of the NMR-tailored quadruple- ζ bases. The basis sets for NMR shieldings are optimized by analyzing the deficiencies of the underlying orbital basis sets and subsequent extensions to remove these shortcomings. Here, the central design principle is to keep the additions of further functions at a minimum to ensure that the other properties are not negatively affected by the extensions. Jensen previously showed that tight basis functions are needed for an accurate description of the density in the core region.^[219,220] Still, a detailed analysis of the deficits is necessary as Jensen studied light elements up to krypton in a non-relativistic approach and relativistic all-electron basis sets may require additional modifications.

8.2.1 Analysis of Deficits and Development of Optimized Basis Sets

To analyze the present deficits of the x2c-TZVPall basis set for NMR shieldings, a large molecular test set was chosen. The test set consists of 255 neutral closed-shell molecules^[484] with 555 shielding constants and is a subset of the previously collected test set for the development of the orbital basis sets.^[198,199,202,481,485,486] NMR shielding constants^[398,407,413] are calculated at the PBE^[341] level of theory with the scalar-relativistic Hamiltonian.^[105,107,379] The finite nucleus model is applied for both the scalar and the vector potential. Large grids are employed for the numerical integration of the exchange-correlation terms (grid 4a)^[482] and the SCF energies were converged with a threshold of $10^{-8} E_h$. The suffix “a” of the integration grid indicates an increased number of radial points. TURBOMOLE’s standard grids^[294,315] for heavy elements were developed for ECP calculations. The NMR calculations use a criterion of 10^{-7} a.u. for the norm of the residuum^[416] to ensure a well converged perturbed density matrix. Point group symmetry is not exploited to check for basis set incompleteness errors regarding symmetry-equivalent nuclei. However, only symmetry-inequivalent nuclei are considered in the statistical evaluation. The mean absolute error of the x2c-TZVPall basis, the x2c-TZVPPall bases with more polarization functions, and the x2c-TZVPall-2c bases with more p and d functions to describe the spin-orbit splitting are shown in Fig. 8.1. Errors are measured with respect to the even-tempered basis set of Ref. 203 and the shielding constants of the nuclei are sorted according to the group in the periodic table of elements. As expected, the error and the standard deviation increase for the heavy nuclei but also the range of the NMR shieldings increases. The x2c-TZVPPall basis set leads to essentially the same results as x2c-TZVPall for all groups. Therefore, additional polarization functions are not needed. In contrast, the two-component extensions lead to a significant improvement for the 6s, 5d, and 6p elements. Therefore, additional p and d functions are needed. Using the full two-component extensions is disadvantageous for triple- ζ basis sets as these may increase the size of the uncontracted basis set by up to 30%. The extensions for the p space are usually based on the first contracted p shell, those contraction coefficients were reoptimized to describe the splitting into the $P_{1/2}$ and $P_{3/2}$ states. This increases the flexibility of the basis set in the outer-core and the valence region. To reduce the number of functions to be added, the two-component extensions are modeled by a few uncontracted or primitive p and d functions. These functions were optimized by Robert Treß reducing the error with respect to the x2c-TZVPall-2c bases in several cycles with the complete test set. Functions with a large exponent are added for the heavy elements, e.g., an exponent between 280 and 330 for the 6p elements. This removes all shortcomings in the outer-core and the valence region. Note that adding these functions differs from the approach of Jensen^[219,220] but is necessary for heavy elements. For the 6p group, this reduces the mean absolute error from more than 450 ppm to less than 150 ppm. However, the impact of these functions is negligible up to the 5s group.

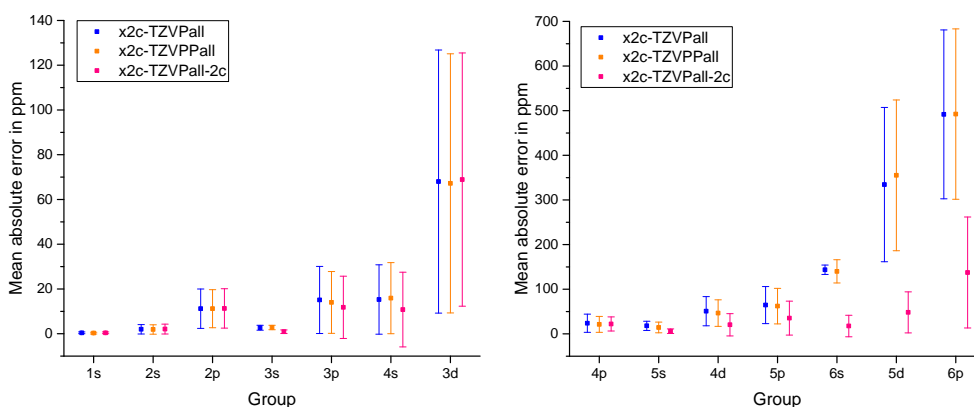


Figure 8.1: Mean absolute error in the shielding constants and standard deviation in ppm of all-electron relativistic triple- ζ bases with respect to the even-tempered basis set of Ref. 203.

Table 8.1: Exponents of the first segment for carbon. The exponents are shown in the left rows and the right rows contain the contraction coefficients. The first contracted GTO consists of four primitive functions.

x2c-TZVPall		x2c-TZVPall-s	
4p		4p	
34.707 038 490	0.005 368 429 499 9	225.595 750 19	0.000 294 631 690 00
7.955 898 785 1	0.035 952 788 969	34.707 038 490	0.005 174 918 299 8
2.379 171 553 6	0.142 320 109 89	7.955 898 785 1	0.036 091 895 998
0.814 393 594 87	0.342 778 420 56	2.379 171 553 6	0.141 975 700 01
		1p	
		0.814 393 594 87	1.000 000 000 0

For the core region, it is necessary to add tight functions—especially for the light elements. These are obtained as suggested by Jensen:^[219,220]

1. Add a single p function for every element by scaling the inner-most function (largest exponent) of the first segment with a factor of 6.5.
2. Exclude the outer-most primitive (smallest exponent) from the segment and use it as an additional augmentation function.
3. Reoptimize the contraction of the first segment to avoid a deterioration of other properties.

Note that the factor of 6.5 is at least to some extent arbitrary. Using a factor between 5 and 8 is a reasonable choice and essentially leads to the same results. We used 6.5 for consistency with the basis sets of Jensen. Step 3 is carried out with the analytical basis set gradients in atomic ROHF calculations for all elements except the lanthanides which utilize unrestricted HF theory to avoid convergence issues. The SCF calculations are considered to be converged based on an energy threshold of $10^{-10} E_h$ and a root mean square of the density of 10^{-10} . The same atomic states as for the underlying orbital basis set^[203] are prepared with the ROHF parameters and the symmetry constraints. All exponents differ at least by a factor of 1.5 to avoid linear dependencies and ensure a smooth SCF convergence. To illustrate the approach, consider the carbon atom. The largest exponent of the inner-most segment is 34.707038490 and therefore a function with an exponent of 225.59575019 is added. The p space is altered as shown in Tab. 8.1. The NMR-optimized basis sets are indicated by the suffix “-s”. Sulfur and chlorine required further changes in the contraction pattern for error-balanced shieldings. Here, the contraction pattern of aluminium, silicon, and phosphorous (51111) is changed to (42111). The x2c-TZVPall-s basis sets are obtained by simply adding the same polarization functions^[198] as for x2c-TZVPall. The x2c-SVPall-s basis set is constructed by using the same extensions for the outer-core and the valence-region as well as reoptimizing the first segment. Likewise, the contraction pattern for S and Cl is changed to (4211) compared to (5111) for Al, Si, and P.

The extensions of the quadruple- ζ bases are constructed similarly. The x2c-QZVPall basis set does not result in an improvement, whereas the two-component extensions lead to a significant improvement for heavy elements. These extensions are available for the heavy elements only and the extensions are small compared to the total size of the basis set. The number of basis functions throughout the test set is increased by about 7%. So, no minimal extensions were optimized and the two-component extensions are employed as is. Tests showed that only the 1s, 2s, 2p, and 3d groups require additional tight functions. Consequently, a single tight function is added as described above. For all other groups, the x2c-QZVPall bases already include large exponents. The contraction pattern of the x2c-SVPall-s, x2c-TZVPall-s, and the x2c-QZVPall-s basis sets are listed in Tab. 8.2. The bases are also available via the Basis Set Exchange library.^[487,488]

Table 8.2: Primitive and contracted basis functions of the x2c-SVPall-s, x2c-TZVPall-s, and x2c-QZVPall-s basis set. The exponents and contraction coefficients are given in Ref. 482 and 483.

Elements	x2c-SVPall-s			x2c-TZVPall-s			x2c-QZVPall-s		
	Primitive Space	Contracted Space	Primitive Space	Contracted Space	Primitive Space	Contracted Space	Primitive Space	Contracted Space	
H	(4s1p)	[2s1p]	(5p2p)	[3s2p]	(7s4p2d1f)	[4s4p2d1f]			
He	(4s1p)	[2s1p]	(5p2p)	[3s2p]	(8s4p2d1f)	[4s4p2d1f]			
Li	(7s4p)	[3s3p]	(11s4p)	[5s4p]	(15s6p3d1f)	[6s5p2d1f]			
Be	(7s5p)	[3s3p]	(11s5p1d)	[5s4p1d]	(15s7p3d1f)	[7s5p2d1f]			
B-O	(7s5p1d)	[3s3p1d]	(11s7p2d1f)	[5s4p2d1f]	(15s9p3d2f1g)	[7s5p3d2f1g]			
F	(8s5p1d)	[4s3p1d]	(12s7p2d1f)	[6s4p2d1f]	(15s9p3d2f1g)	[7s5p3d2f1g]			
Ne	(7s5p1d)	[3s3p1d]	(11s7p2d1f)	[5s4p2d1f]	(15s10p3d2f1g)	[7s5p3d2f1g]			
Na	(10s7p1d)	[4s3p1d]	(14s9p3d)	[5s5p3d]	(20s18p5d1f)	[9s7p4d1f]			
Mg	(10s7p1d)	[4s3p1d]	(14s9p3d)	[5s5p3d]	(20s18p4d1f)	[9s7p4d1f]			
Al-Ar	(10s8p1d)	[4s4p1d]	(14s10p3d1f)	[5s6p2d1f]	(20s20p4d2f1g)	[9s7p4d2f1g]			
K	(14s10p2d)	[5s4p2d]	(17s12p3d)	[6s5p3d]	(24s30p5d1f)	[11s9p4d1f]			
Ca	(14s10p4d)	[5s4p2d]	(17s13p4d)	[6s6p3d]	(24s30p6d2f)	[11s9p4d2f]			
Sc-Cr	(14s10p7d1f)	[5s4p4d1f]	(17s13p8d1f)	[6s6p5d1f]	(24s30p9d3f1g)	[11s9p5d3f1g]			
Mn-Cu	(14s10p7d1f)	[5s4p4d1f]	(17s13p8d1f)	[6s6p5d1f]	(24s30p10d4f1g)	[11s9p5d4f1g]			
Zn	(14s10p7d1f)	[5s4p4d1f]	(17s13p8d1f)	[6s6p5d1f]	(24s31p10d4f1g)	[11s10p6d4f1g]			
Ga	(14s12p6d)	[5s6p3d]	(17s14p8d1f)	[6s7p4d1f]	(24s32p10d2f1g)	[11s9p5d2f1g]			
Ge-Kr	(14s12p6d)	[5s6p3d]	(17s14p8d1f)	[6s7p4d1f]	(24s33p10d2f1g)	[11s10p5d2f1g]			
Rb,Sr	(18s15p10d1f)	[6s6p5d1f]	(20s22p11d1f)	[8s8p6d1f]	(27s38p17d5f2g)	[13s12p8d3f2g]			
Y-Mo	(18s16p10d1f)	[6s7p5d1f]	(20s22p12d1f)	[8s8p6d1f]	(27s38p21d3f1g)	[13s12p9d3f1g]			
Te-Ag	(18s16p10d1f)	[6s7p5d1f]	(20s22p12d1f)	[8s8p6d1f]	(27s38p21d4f1g)	[13s12p9d4f1g]			
Cd	(18s16p10d1f)	[6s7p5d1f]	(20s22p12d1f)	[8s8p6d1f]	(26s38p21d4f1g)	[13s12p9d4f1g]			
In	(18s16p10d)	[6s7p4d]	(20s22p12d2f)	[8s8p5d2f]	(26s40p24d4f1g)	[13s13p9d4f1g]			
Sn-Xe	(18s16p10d)	[6s7p4d]	(20s22p12d2f)	[8s8p5d2f]	(27s40p24d4f1g)	[13s13p9d4f1g]			
Cs, Ba	(23s20p11d4f)	[7s7p6d1f]	(24s25p14d4f)	[11s9p7d1f]	(30s48p26d7f2g)	[16s16p11d5f2g]			
La	(23s20p14d5f)	[7s7p7d2f]	(24s25p15d5f)	[11s9p8d2f]	(30s48p29d11f2g)	[16s16p12d6f2g]			
Ce-Yb	(23s19p14d7f1g)	[7s7p7d3f1g]	(24s25p15d8f1g)	[11s9p8d4f1g]	(30s48p29d11f5g)	[16s16p12d6f3g]			
Lu	(23s20p14d6f1g)	[7s8p7d2f1g]	(24s25p15d7f1g)	[11s9p8d2f1g]	(30s48p29d11f2g)	[16s16p12d6f2g]			
Hf-Au	(23s20p14d6f)	[7s7p7d2f]	(24s25p15d7f)	[11s9p8d2f]	(30s48p29d12f1g)	[16s16p12d6f1g]			
Hg	(23s21p14d6f)	[7s8p7d2f]	(24s25p15d7f)	[11s9p8d2f]	(30s48p29d12f1g)	[16s16p12d6f1g]			
Tl-Rn	(23s22p13d6f)	[7s10p5d2f]	(24s26p15d8f)	[11s10p7d3f]	(30s48p29d13f1g)	[16s16p12d7f1g]			

Table 8.3: Comparison of the errors in ppm with respect to the large even-tempered (ET) basis set of Ref. 483 for the previously developed ET basis set of Ref. 203, the NMR-tailored x2c-SVPall-s, x2c-TZVPall-s, x2c-QZVPall-s bases, and the parent basis sets. The prefix “x2c-” is omitted for brevity. The large deviation of the 5d group between the even-tempered bases of Ref. 203 and the larger ET basis set of Ref. 483 is caused by Lanthanum. n_g denotes the number of symmetry non-equivalent nuclei of the group. σ indicates the standard deviation of the weighted overall error (WOE), see Eq. 8.24. NBF denotes the total number of basis functions in the spherical AO basis. The reference basis set uses 202,340 functions in total.

Group	n_g	Previous ET	SVPall	SVPall-s	TZVPall	TZVPall-s	QZVPall	QZVPPall	QZVPall-2c	QZVPall-s
1s	93	0.1	0.6	0.4	0.4	0.3	0.2	0.1	0.1	0.1
2s	19	0.8	7.2	5.0	6.1	5.2	0.4	0.4	0.4	0.1
2p	195	1.3	19.0	20.6	11.1	5.5	6.1	6.0	6.1	5.1
3s	14	0.2	3.2	3.8	2.5	0.7	0.2	0.2	0.3	0.3
3p	76	3.2	37.6	35.2	14.6	11.4	3.3	3.3	2.9	2.9
4s	12	5.3	27.3	29.5	20.6	15.1	2.7	2.5	2.0	2.0
3d	27	1.0	205	159	67.4	29.1	21.1	21.7	21.4	20.3
4p	24	2.2	36.6	52.2	22.2	18.5	4.5	4.5	3.8	3.8
5s	8	0.1	21.6	40.2	18.2	13.0	7.9	7.9	3.7	3.7
4d	2	2.1	53.8	151	50.7	45.4	18.8	18.4	6.3	6.2
5p	18	7.7	184	192	64.6	35.9	29.3	29.5	8.3	8.1
6s	8	16.6	134	144	134	22.9	81.1	81.1	3.4	3.4
5d	21	67.9	423	483	373	123	194	193	11.7	12.1
6p	19	9.6	461	327	487	83.9	209	208	2.2	31.8
WOE		0.002	0.03	0.03	0.02	0.01	0.008	0.008	0.003	0.002
σ		0.006	0.04	0.04	0.02	0.02	0.008	0.009	0.007	0.007
NBF		165,741	23,396	23,946	33,161	37,599	65,408	67,314	69,813	71,628

The errors for the test set are assessed with a weighted overall error (WOE) as a simple indicator for the basis set quality defined as

$$\eta = \sum_g \frac{n_g \text{MAE}_g / w_g}{n_{\text{tot}}} \quad (8.24)$$

n_g is the number of symmetry non-equivalent nuclei in each group, g , throughout the test set, w_g denotes the range of the shieldings, and n_{tot} is the total number of symmetry non-equivalent nuclei. The results are presented in Tab. 8.3 and the individual shielding constants are available in the supporting information of Ref. 482 and 483. The two even-tempered basis set result in a good agreement for all groups except the 5d block. Here, the WOE of the larger even-tempered basis sets and the previously developed even-tempered bases amounts to about 70 ppm. The x2c-SVPall-s basis sets result in a minor improvement only. Generally, double- ζ bases are not sufficiently flexible for NMR calculations of heavy elements. Therefore, at least a triple- ζ basis set should be used. Here, the extensions for NMR shieldings result in a notable improvement, the WOE is halved and especially the errors of the sixth row are significantly reduced. For instance, the error of the 6p elements is reduced from 487 ppm to 83.9 ppm. All quadruple- ζ basis sets are a considerable improvement upon the double and triple- ζ basis sets, however, the number of functions is doubled compared to the x2c-TZVPall basis and nearly increased by a factor of three compared to the x2c-SVPall bases. The x2c-QZVPall and x2c-QZVPPall bases yield nearly the same results and larger errors for the 6s, 5d, and 6p elements. These are reduced by the x2c-QZVPall-2c and x2c-QZVPall-s basis sets. The latter improves the results of the light elements and yields the same weighted overall error as the previously developed even-tempered basis sets. At first glance, the increased error for the 6p elements compared to the x2c-QZVPall-2c bases and a decreased weighted overall error may come as a surprise. However, the range of the NMR shieldings for the 6p group is very large and amounts to 3237 ppm. So, the improvement for the 2s and the 2p group out-weights this deterioration. The different results for the groups with heavier elements

are explained by the impact of the basis functions at the light element on the heavy element. Based on the results the x2c-TZVPall-s basis is recommended for general NMR shielding calculations whereas the x2c-QZVPall-s bases may be used for benchmark calculations to approach the complete basis set limit. In a density functional framework, the triple- ζ basis sets are often a reasonable choice whereas Møller–Plesset theory, which yields excellent results for the NMR shifts of light elements,^[489–492] may benefit from larger bases. The existing x2c-type auxiliary basis sets can be used with the NMR-tailored bases for ground-state calculations. These auxiliary basis sets fit the ground-state density. In contrast, tailored auxiliary basis sets are required for very accurate excited-state calculations or post-HF and post-KS treatments as these require to fit the orbital products of the two-electron integrals.^[485,493,494]

8.2.2 Comparison to Other Relativistic All-Electron Basis Sets

The NMR-tailored x2c-type basis sets are compared to other frequently used relativistic all-electron basis sets. In detail, the uncontracted ANO-RCC, ANO-R, Dyall’s double, triple, and quadruple- ζ basis sets and the segmented-contracted Sapporo basis sets of the same quality are chosen for this purpose. Note that the ANO-RCC bases^[178–182] are optimized with the DKH2 Hamiltonian and therefore employed in an uncontracted fashion as done in other studies.^[101,108,109] The recently developed ANO-R^[183] bases are optimized with the X2C Hamiltonian, however, we also employed them in the uncontracted form for consistency with the ANO-RCC basis. The ANO bases were both taken from the Basis Set Exchange Library^[487,488] and subsequently decontracted. The Dyall-VXZ (X = D, T, Q) basis sets are only available for the heavy elements beyond krypton.^[187–192,495] Contraction schemes are optimized for “fully” relativistic four-component calculations. Consequently, the Dyall basis sets are used in an uncontracted form in X2C calculations and Dyall’s suggestions for the uncontracted space are considered, i.e. linear dependencies are removed by omitting the respective functions of the SCF set. For instance, the second *d* function is removed for lanthanum. The Dyall-VDZ and VTZ bases were converted to the TURBOMOLE format by Tobias M. Pazdera, who carried out exploratory calculations. The Dyall basis sets are combined with the uncontracted cc bases for the light elements.^[161,163–165,167–169,173] The cc-pVXZ basis sets (X = D, T, Q) were taken from the ccRepo^[496] and decontracted. The Sapporo basis set family, Sapporo-XZP (X = D, Z, Q; 2012 version), optimized with the DKH3 Hamiltonian^[216–218,497] is further considered. This allows to use the segmented-contracted Sapporo basis sets in X2C calculations as X2C and DKH3 lead to similar results, X2C results are often essentially the same as with DKH4 or DKH8. However, X2C features considerably reduced computational costs and is straightforwardly applicable to analytical derivative theory. All relativistic basis sets except the Sapporo basis set family are developed with the finite nucleus model. The computational settings are the same as in the last subsection. The results are evaluated statistically as listed in Tab. 8.4 and Tab. 8.5.

As shown in Tab. 8.4, the double and triple- ζ NMR-optimized basis sets are on par with the much larger Dyall basis sets of the same quality for the light elements. For the 1s and the 2s group, the Dyall bases results in smaller errors whereas the x2c-SVPall-s and x2c-TZVPall-s basis sets perform better for the 2p group. The Sapporo-DZP basis set shows a large mean absolute error for the 2p group of 38.6 ppm. This is a nearly doubled error compared to x2c-SVPall-s with 20.6 ppm. The Sapporo-TZP bases do not exhibit such a behavior, the error is within the range of the Dyall-VTZ basis with 11.0 ppm and the x2c-TZVPall-s basis with 5.5 ppm. For the heavier elements, the Dyall-VDZ and VTZ basis perform remarkably for the d groups with very small errors. Here, the Sapporo basis sets are outperformed by all other basis sets. Especially for the 6p group, the errors are extremely large with 833 ppm for Sapporo-DZP and 649 ppm for Sapporo-TZP. These errors may be caused by the tight basis functions as the Sapporo basis is not optimized with the finite nucleus model but the point-charge model. The singularity of the respective Dirac equation does not allow

Table 8.4: Comparison of the errors in ppm with respect to the large even-tempered (ET) basis set of Ref. 483 for various double and triple- ζ basis sets as well as the uncontracted ANO-R and ANO-RCC bases. The latter are among the largest relativistic all-electron basis sets. The individual results are taken from Ref. 482 and 483. The prefix “x2c-” is omitted for the x2c-SVPall-s and x2c-TZVPall-s basis set. The segmented-contracted Sapporo basis sets for the heavy elements are optimized with the DKH3 Hamiltonian and the Dyall basis sets are employed in an uncontracted fashion together with the cc basis sets for the light elements. n_g denotes the number of symmetry non-equivalent nuclei of the group. σ indicates the standard deviation of the weighted overall error (WOE), see Eq. 8.24. NBF denotes the total number of basis functions in the spherical AO basis. The reference basis set uses 202,340 functions.

Group	n_g	Dyall-VDZ	Sapporo-DZP	SVPall-s	Dyall-VTZ	Sapporo-TZP	TZVPall-s	ANO-RCC	ANO-R
1s	93	0.4	0.6	0.4	0.2	0.2	0.3	0.1	0.1
2s	19	5.4	9.2	5.0	4.1	9.2	5.2	0.3	0.3
2p	195	25.3	38.6	20.6	11.0	10.7	5.5	4.1	4.1
3s	14	2.5	3.0	3.8	1.3	2.3	0.7	2.3	2.6
3p	76	30.7	40.0	35.2	15.8	11.5	11.4	8.8	8.9
4s	12	41.2	36.8	29.5	33.9	26.5	15.1	18.4	15.3
3d	27	28.0	114	159	21.8	71.3	29.1	9.9	10.0
4p	24	34.7	28.9	52.5	9.2	11.5	18.5	3.0	3.0
5s	8	13.0	185	40	10.2	53.8	13.0	6.7	6.8
4d	2	43.9	171	151	11.7	138.5	45.4	3.9	4.1
5p	18	163	174	192	45.4	65.6	35.9	9.5	9.8
6s	8	53.3	307	144	14.9	72.8	22.9	20.5	56.4
5d	21	117	361	483	84.2	310.3	123.9	73.8	74.2
6p	19	489	833	327	113.2	649	83.9	31.0	47.5
WOE		0.02	0.04	0.03	0.011	0.02	0.010	0.005	0.005
σ		0.04	0.07	0.04	0.016	0.03	0.02	0.009	0.010
NBF		46,013	23,396	23,946	68,163	44,896	37,599	120,867	106,966

to optimize the tighter functions. Instead, the exponents rise to infinity and optimize the singularity but not the description of the density in the core region. Due to the poor behavior for the heavy elements, the Sapporo basis sets show the largest weighted overall errors and standard deviations. The x2c-SVPall-s basis set performs slightly worse than the Dyall-VDZ basis set, however, only half of the functions are employed throughout the test set. The x2c-TZVPall-s basis set shows a slightly smaller weighted overall error of 0.010 compared to 0.011 for the Dyall-VTZ. Yet, the standard deviation of the Dyall-VTZ basis is smaller by 0.004. The very large ANO basis sets show the smallest errors for all groups except for the 3s, 4s, and the 6s elements. Consequently, the weighted overall error of the ANO basis sets is the smallest with 0.005 for both. The standard deviation is smaller with the somewhat larger ANO-RCC bases. However, the difference in the results between these two basis sets is insignificant and the ANO-R bases employ about 10% less functions throughout the test set.

The quadruple- ζ basis sets are compared in Tab. 8.5 and show considerably smaller errors than the double and triple- ζ basis sets. Note that the decontracted cc-pVQZ bases cause large errors for the Dyall-VQZ basis set and the 3d group. Even though, the results for Cu_2 , Cu_2O , Cu_2S , CuCl , CuF , CuH , and ZnF are not considered as the orbital energies are positive or a negative gap of the highest occupied molecular orbital (HOMO) and the lowest unoccupied molecular orbital (LUMO) is obtained. The poor results likely originate from linear dependencies in the cc-pVQZ basis set and lead to a large weighted overall error of 0.03 and a standard deviation of 0.06. Therefore, a subgroup of the test set is also considered for the Dyall-VQZ bases. This subgroup does not contain molecules with 3d elements and leads to reasonable errors. For the first three rows of the periodic table of elements, the results of the Dyall-VQZ, Sapporo-QZP, and the x2c-QZVPall-s basis sets are similar and only minor deviations are obvious. The x2c-QZVPall-s basis shows considerably

Table 8.5: Comparison of the errors in ppm with respect to the ET basis of Ref. 483 for the uncontracted ANO-R and ANO-RCC bases and various quadruple- ζ basis sets. The Cu_2 , Cu_2O , Cu_2S , CuCl , CuF , CuH , and ZnF were neglected for the Dyall-VQZ basis as they showed positive orbital energies or negative HOMO-LUMO gaps. The large errors of the uncontracted Dyall-VQZ basis set are caused by the 3d elements, for which the decontracted cc-pVQZ basis set was used as the Dyall bases are only available for the heavier elements. So, the test set was also statistically evaluated without considering these molecules, Dyall-VQZ (no 3d). n_g denotes the number of symmetry non-equivalent nuclei of the group. σ indicates the standard deviation of the weighted overall error (WOE), see Eq. 8.24. NBF denotes the total number of basis functions in the spherical AO representation used for the test set. The reference basis set uses 202,340 functions.

Group	n_g	ANO-RCC	ANO-R	Dyall-VQZ	Dyall-VQZ (no 3d)	Sapporo-QZP	x2c-QZVPall-s
1s	93	0.1	0.1	0.5	0.1	0.1	0.1
2s	19	0.3	0.3	0.2	0.2	1.6	0.1
2p	195	4.1	4.1	18.1	5.6	3.3	5.1
3s	14	2.3	2.6	1.1	1.1	0.5	0.3
3p	76	8.8	8.9	47.7	8.4	7.0	2.9
4s	12	18.4	15.3	13.0	13.0	21.6	2.0
3d	27	9.9	10.0	1333	–	34.0	20.3
4p	24	3.0	3.0	3.0	3.0	4.2	3.8
5s	8	6.7	6.8	4.2	4.2	40.6	3.7
4d	2	3.9	4.1	4.4	4.4	95.5	6.2
5p	18	9.5	9.8	29.3	29.3	29.6	8.1
6s	8	20.5	56.4	4.9	4.9	125	3.4
5d	21	73.8	74.2	73.4	73.4	253	12.1
6p	19	31.0	47.5	38.6	38.6	598	31.8
WOE		0.005	0.005	0.03	0.004	0.016	0.002
σ		0.009	0.010	0.06	0.010	0.018	0.007
NBF		120,867	106,966	100,965	100,965	72,704	71,628

smaller errors for the 4s and the 3d groups. The Sapporo-QZP bases deteriorate rapidly for the 5s to 6p blocks, whereas the Dyall-QZP bases are still on par with x2c-QZVPall-s for the 4p, 5s, 4d, 6s, and the 6p group. For the 5p and the 5d elements, the x2c-QZVPall-s basis outperforms the other two quadruple- ζ basis sets. Overall, the x2c-QZVPall-s also outperforms the larger ANO basis sets as shown by the smaller weighted overall error and its standard deviations. The x2c-QZVPall-s basis set features the smallest errors of all studied bases and employs nearly the same number of functions as the uncontracted Dyall-VTZ basis sets. In contrast, the x2c-type basis sets are available for all elements from hydrogen to radon and difficulties like finding suitable basis sets for the light elements do not exist.

To illustrate the impact of size of the basis set on the computational demands, the computation times are compared for $\text{W}(\text{CO})_6$. The times for the triple- ζ basis sets and the uncontracted ANO bases are listed in Tab. 8.6. In terms of basis functions, $\text{W}(\text{CO})_6$ is one of the largest molecules in the test set. The x2c-type basis sets lead to very similar computation times: about 1 minute for a single SCF iteration, 7 to 9 minutes for the X2C NMR calculations, and about 4 minutes for the DLU-X2C NMR calculations. Note that the x2c-TZVPall-s is the largest basis set for this molecule as no two-component extensions are available for carbon and oxygen. Consequently, the x2c-TZVPall and x2c-TZVPall-2c basis set are identical for these elements and the x2c-TZVPall-s features additional tight p functions. The Sapporo-TZP or the Dyall-VTZ bases lead to an increase of the computation time by a factor of 2.3 and 1.8, respectively. Here, 40 % of the total CPU time amount to the solution of the X2C response equations in the primitive space and therefore the uncontracted Dyall-VTZ results in shorter computation times for the full X2C approach. Matters are different with the DLU scheme. Here, the two-electron integrals and the solution of the CPKS equations are more demanding and consequently the Sapporo-TZP basis set results in a decreased CPU time compared to

Table 8.6: Comparison of computation time for various relativistic all-electron basis sets and $W(\text{CO})_6$. Calculations were performed on a single thread of a CPU of type Intel® Xeon® Gold 6212U CPU @ 2.40 GHz. NBF refers to the number of basis functions in the spherical AO basis. X2C-SCF denotes the computation time for the one-electron Hamiltonian in an energy calculation whereas X2C-NMR refers to the analytical derivatives in an NMR calculations. SCF refers to the computation time of a single SCF iteration and NMR to the total computation time of a NMR shielding calculation for all nuclei. For the latter, the X2C and DLU-X2C Hamiltonian are considered. Times are given in minutes.

Basis Set	NBF	X2C-SCF	SCF	X2C-NMR	DLU-NMR
x2c-TZVPall	453	0.04	0.7	7.6	3.6
x2c-TZVPall-2c	480	0.04	0.9	8.9	4.4
x2c-TZVPall-s	500	0.04	0.8	9.0	4.3
Sapporo-TZP	514	0.08	2.4	20.9	10.6
Dyall-VTZ	760	0.05	1.6	16.2	10.7
x2c-QZVPall	819	0.2	7.8	58.7	34.4
x2c-QZVPall-2c	859	0.1	6.9	42.2	26.0
x2c-QZVPall-s	895	0.1	7.8	44.9	27.3
Sapporo-QZP	850	0.2	11.9	57.4	33.3
Dyall-VQZ	1148	0.1	6.5	44.6	32.5
ANO-R(unc)	1139	0.1	10.1	66.2	54.2
ANO-RCC(unc)	1497	0.2	49.0	240.2	211.6

the Dyall-VTZ basis. The quadruple- ζ basis sets are more costly and a SCF iteration takes between 6 and 12 minutes. The X2C NMR calculations requires about 45 minutes with the x2c-type and the Dyall-VQZ basis. The Sapporo-QZP are even more demanding and the calculation amounts to nearly 1 hour. The DLU scheme reduces these computation times to about 30 minutes. The uncontracted ANO-RCC basis set employs nearly twice the number of functions than the Dyall-VTZ bases and a single SCF iterations takes 49 minutes. The NMR shielding calculations amount to 4 hours for the full X2C ansatz and more than 3.5 hours when applying the DLU scheme. Here, the two-electron integrals are the most time-consuming step and the total computation time of the X2C and the DLU-X2C calculations differ by only 30 minutes or 12%.

To sum up, the NMR-tailored basis sets employ at most four additional functions and thus do not significantly increase the total computation time but significantly improve the accuracy for triple and quadruple- ζ basis sets. The performance of the x2c-TZVPall-s basis is on par with the notably larger uncontracted Dyall-VTZ bases.

8.2.3 Comparison to Non-Relativistic NMR-Optimized Basis Sets

The NMR-tailored relativistic all-electron basis sets are further compared to the pcSseg bases of Jensen^[219,220] for light elements from hydrogen to krypton. These basis sets were optimized with the non-relativistic Hamiltonian. A subset of the test set is constructed with light elements only. This subset contains 160 molecules with 359 shielding constants and relativistic effects are of minor importance so the pcSseg basis set family can be used with the X2C Hamiltonian. Note that the Dyall basis sets are also combined with these basis sets or the correlation-consistent bases for NMR shifts in four-component calculations.^[54,55,58] The results are presented in Tab. 8.7. Here, the x2c-type basis sets result in a very consistent improvement of the accuracy with the cardinal number. The weighted overall error decreases from 0.017 for the x2c-SVPall-s to 0.002 for the x2c-QZVPall-s basis. The results of x2c-TZVPall-s bases fall within this range as the weighted overall error is 0.007. A similar behavior is evident for the standard deviation. The pcSseg basis sets feature some notable inconsistencies for pcSseg-2 and pcSseg-3. Here, the error is doubled for pcSseg-3 (3.2 ppm)

Table 8.7: Comparison of the error in ppm with respect to the even-tempered basis of Ref. 483 for the pcSseg basis sets and the Karlsruhe basis sets for molecules consisting of elements H-Kr. The prefix “x2c-” is omitted for the x2c-SVPall-s, x2c-TZVPall-s, and the x2c-QZVPall-s bases. n_g denotes the number of symmetry non-equivalent nuclei of the group. σ indicates the standard deviation of the weighted overall error (WOE), see Eq. 8.24. NBF denotes the total number of basis functions in the spherical AO representation used for the test set. The reference basis set employs 116,396 functions throughout the test set.

Group	n_g	pcSseg-0	pcSseg-1	pcSseg-2	pcSseg-3	pcSseg-4	SVPall-s	TZVPall-s	QZVPall-s
1s	76	1.5	0.2	0.1	0.0	0.0	0.4	0.2	0.1
2s	20	1.5	1.3	0.3	0.1	0.1	1.7	1.9	0.1
2p	127	46.7	14.2	3.2	6.1	0.4	16.4	4.3	2.0
3s	14	6.9	3.7	1.6	2.6	2.2	3.7	1.3	0.2
3p	63	92.6	29.2	10.9	5.7	4.1	33.9	9.2	2.7
4s	11	34.6	13.5	12.1	12.5	12.4	30.0	16.0	2.0
3d	27	934	108	30.7	21.1	17.9	159	29.1	20.2
4p	22	100	52.9	46.2	43.7	36.4	43.6	16.7	3.7
WOE		0.05	0.012	0.005	0.0047	0.0035	0.017	0.007	0.002
σ		0.08	0.014	0.004	0.0010	0.0010	0.016	0.007	0.003
NBF		6,810	12,274	23,410	43,730	70,179	12,377	20,595	39,906

compared to pcSseg-2 (6.1 ppm) for the 2p group. Note that the pcSseg-3 bases employ nearly twice the number of basis functions. The weighted overall error and the standard deviation of pcSseg-3 is smaller than for pcSseg-2.

pcSseg-0 is the smallest basis and expectedly shows large errors—especially for the 3d group with 934 ppm. The x2c-SVPall-s bases perform similar to pcSseg-1 and the two basis sets are of similar size. The x2c-TZVPall-s and the pcSseg-2 basis sets show comparable overall errors. x2c-TZVPall-s yields smaller errors for the heavy elements whereas pcSseg-2 is superior for the light elements. The latter features more basis functions by about 10 %. The x2c-QZVPall-s basis set features the smallest errors and outperforms all other bases while using less functions than pcSseg-3 and only 57 % of the functions of pcSseg-4. Especially for the 4s and the 4p groups, the x2c-QZVPall-s basis set shows smaller errors and illustrates that additional functions in the outer-core and the valence region are needed for heavier elements. For molecules consisting of light elements only, the additional tight functions proposed by Jensen are sufficient and result in an accurate description of the density in the vicinity of the nuclei.

The errors of the pcSseg bases significantly increase for the 4s, 3d, and 4p elements. Compared to the x2c-QZVPall-s basis, the pcSseg-4 basis set features sufficiently tight functions and also accurately covers the additional extensions. Therefore, the increased error is likely caused by the non-relativistic optimization of the contraction coefficients. To analyze the deficits of the pcSseg basis sets for the fourth row in detail, the pcSseg-4 basis set of As in As_4 is systematically decontracted as shown in Tab. 8.8. The decontraction of the p shell only changes the shielding constant by about 4 ppm and the decontraction of the d shell does not affect the shieldings. In contrast, the s shells are of major importance. Already decontracting the first or inner-most s shell results in a notable agreement with the reference basis set. The fully decontracted pcSseg-4 basis set excellently reproduces the reference results. Therefore, the s and p shells have to be recontracted at the X2C level as outlined in Sec. 8.2.1. The recontracted segments are listed in Sec. A.4. Recontracting the s and p segments yields a NMR shielding constant of 2248.2 ppm compared to 2248.6 ppm. Similar findings are observed for the SCF energy. The main change is caused by the inner-most s segment. Consequently, the pcSseg basis set family may be recontracted for X2C calculations or the bases may be decontracted in relativistic calculations. This is further suggested by the respective calculations for Se_8 in Tab. 8.9.

Table 8.8: Decontracted and recontracted pcSseg-4 basis sets of As in As₄. The NMR shielding constant is given in ppm whereas the energy is given in E_h. The recontracted segments are listed in Sec. A.4.

Basis	NMR Shielding Constant	SCF Energy
pcSseg-4	2210.2	-9024.146 499 40
decontracted <i>p</i>	2205.8	-9024.211 515 39
decontracted <i>d</i>	2210.8	-9024.151 924 67
decontracted <i>p</i> and <i>d</i>	2206.4	-9024.216 937 42
decontracted first <i>s</i>	2252.2	-9042.270 346 98
decontracted all <i>s</i>	2252.3	-9042.274 082 44
fully decontracted	2248.5	-9042.341 427 49
recontracted first <i>s</i>	2247.1	-9041.880 697 58
recontracted all <i>s</i>	2252.9	-9042.258 605 23
recontracted all <i>s</i> and <i>p</i>	2248.2	-9042.323 269 51
Reference	2248.5	-9042.342 063 18

Table 8.9: Decontracted pcSseg-4 basis sets of Se in Se₈. The NMR shielding constant is given in ppm whereas the energy is given in E_h.

Basis	NMR Shielding Constant	SCF Energy
pcSseg-4	790.3	-19 395.365 003 64
decontracted <i>p</i>	773.8	-19 395.516 621 63
decontracted <i>d</i>	791.1	-19 395.373 658 27
decontracted <i>s</i>	840.7	-19 437.188 669 25
fully decontracted	824.9	-19 437.346 444 44
Reference	823.1	-19 437.347 821 97

9 Assessment of the Accuracy of Relativistic Hamiltonians

9.1 NMR Shieldings and Shifts

The error introduced by the DLU scheme is assessed for various main-group and transition-metal compounds. The error is further compared to the impact of relativistic effects, the different density functional approximations, and the basis set. The calculations were originally performed in the course of Ref. 379 with the CPHF and CPKS solver of Refs. 398 and 413. Here, the convergence is checked by calculating the NMR isotropic shielding constants. In 2019, Kevin Reiter implemented a solver based on Ref. 416 for TURBOMOLE V7.5 (2020) and the convergence is checked by computing the norm of the residuum to ensure that the perturbed density matrix itself is converged. The latter leads to more accurate results and is more efficient. This solver is also used in the following chapters. Thus, all calculations in this section were redone with TURBOMOLE V7.5 (2020) and TURBOMOLE V7.5.1 (2021). Efficiency is demonstrated for large silver clusters with more than 17,000 basis functions in the primitive space and iridium complexes with more than 4,500 primitive basis functions. The finite nucleus model is employed throughout all relativistic calculations and the computational methods are described in detail in all subsections.

9.1.1 Demonstration of Gauge-Origin and Translation Invariance

All working equations for the NMR shielding constants in chapter 4 show no reference to the gauge-origin and are therefore formally gauge-origin invariant. In contrast, the integrals show a reference to the origin of the chosen coordinate system. Hence, the unperturbed and the perturbed density contribution of the NMR shielding tensor are not invariant with respect to a translation in space. The isotropic shielding constant is required to be invariant under a translation to be a physically meaningful quantity. Therefore, gauge-origin and translational invariance of the X2C and the DLU-X2C approach are demonstrated at the HF level for a small set of eight molecules: HF, HI, WO, NH₃, BiH₃, XeF₂, XeF₄, and XeF₆. The structures of the first five molecules are taken from Ref. 485 and the other structures from Ref. 101. To check the gauge-origin and translation invariance, the molecules are moved along the z axis by 120 bohr. The xenon compounds are further rotated by 60°. Dyall's VTZ basis set with additional $5s5p$ correlating functions^[187–190,495] are employed in an uncontracted form for the heavy elements and combined with the uncontracted cc-pVTZ basis set for the light elements.^[161] To avoid linear dependencies, the most diffuse primitive d functions of the SCF set are replaced with the $2d$ correlating functions as suggested by Dyall for I and Xe.^[187] Tight SCF convergence thresholds of $10^{-8} E_h$ ensure well converged orbitals and a threshold of 10^{-7} a.u. is selected for the norm of the residuum in the CPHF equations. The isotropic shielding constants are listed in Tab. 9.1. Overall, the changes upon translation and rotation are minuscule. The maximum change is found for BiH₃ with 0.02 ppm for the DLU-X2C Hamiltonian and HI with 0.006 ppm for the X2C Hamiltonian. Note that the shielding constants are in the order of 1,000 ppm. The change affects the sixth and seventh significant digit. Note that this is in line with the chosen thresholds. Thus, both Hamiltonians satisfy gauge-origin and translation invariance.

Table 9.1: Isotropic NMR shielding constants in ppm for various molecules using the X2C/HF and the DLU-X2C/HF method with the Dyall-VTZ/cc-pVTZ(unc) basis. The finite nucleus model is employed throughout. Structures are taken from Refs. 101 and 485. LA refers to the lighter atom and HA to the heavier atom, respectively. Δ Isotropic denotes the difference of the isotropic shielding constant when translating the molecule by 120 bohr along the z axis. Additionally, the xenon compounds were rotated about the z axis by 60° .

	X2C				DLU-X2C			
	LA Isotropic	Δ LA Isotropic	HA Isotropic	Δ HA Isotropic	LA Isotropic	Δ LA Isotropic	HA Isotropic	Δ HA Isotropic
HF	27.8	2×10^{-5}	409.9	-2×10^{-4}	27.8	9×10^{-5}	409.9	-8×10^{-4}
HI	30.4	-4×10^{-6}	4488.1	8×10^{-4}	30.4	-3×10^{-5}	4487.9	6×10^{-3}
WO	-372.7	-1.4×10^{-4}	36 277.3	-6×10^{-3}	-372.7	3×10^{-4}	36 277.8	2×10^{-3}
NH ₃	31.3	9×10^{-6}	261.9	2×10^{-4}	31.3	1.2×10^{-6}	261.9	5×10^{-4}
BiH ₃	27.4	-2×10^{-5}	7127.7	-5×10^{-2}	27.4	1.1×10^{-5}	7127.4	-4×10^{-3}
XeF ₂	455.2	2×10^{-6}	1981.6	1.3×10^{-4}	455.2	-4×10^{-6}	1981.6	2×10^{-5}
XeF ₄	272.3	8×10^{-4}	484.3	6×10^{-4}	272.3	-8×10^{-4}	484.5	2×10^{-3}
XeF ₆	1158.5	-6×10^{-4}	1008.8	-2×10^{-3}	58.4	-4×10^{-7}	1008.5	-1.2×10^{-3}

9.1.2 Organometallic Main-Group Alkynyls

The previous results showed that the DLU-X2C Hamiltonian still meets the physical constraints. In the following, the error of the introduced local approximation in actual calculations is assessed. For this purpose, a small test set^[383] of organometallic alkynyl compounds of the fourth main group is considered. This set consists of Tt(CCMe)₄ (Tt = Si, Ge, Sn, Pb), Me₂Tt(CCMe)₂, and Me₃Tt(CCH) to calculate the ¹³C, ²⁹Si, ⁷³Ge, ¹¹⁹Sn, and ²⁰⁷Pb NMR shifts. It was shown that for these systems a scalar-relativistic ansatz is sufficient as the main relativistic effect is the contraction of the density. The structures are taken from Ref. 383, however, the optimized geometries of the reference compounds SiMe₄ (Me = CH₃, ¹³C, ²⁹Si), GeMe₄ (⁷³Ge), SnMe₄ (¹¹⁹Sn), and PbMe₄ (²⁰⁷Pb) are not included in this reference. These structures were optimized with the spin-orbit DLU-X2C Hamiltonian^[105,107] as well as the x2c-TZVPPall-2c orbital and auxiliary basis set^[203] for the RI- J approximation. The PBE0 functional^[341,355] with a large grid^[482] (grid 4a) is selected in line with the sample compounds. The dispersion correction D3^[498] and tight SCF thresholds of $10^{-8} E_h$ are utilized. The NMR shieldings and shifts are then calculated with the same settings except for the basis sets. Here, the uncontracted Dyall-CVTZ basis set^[187,188,190,495] is used for the heavy elements (Ge, Sn, Pb) and the uncontracted cc-p(C)VTZ basis for the light elements (H, C, Si).^[161,164,167] Note that there are no core correlation functions for hydrogen and consequently cc-pCVTZ is identical to cc-pVTZ. Moreover, the two most diffuse SCF d functions of the Dyall-CVTZ bases are omitted to avoid linear dependencies. The RI- J approximation is not applied as no auxiliary basis sets are available for the Dyall basis sets. A criterion of 10^{-7} a.u. is chosen for the residuum in the CPKS equations.

The statistical evaluation of the DLU error is shown in Tab. 9.2 and the individual results are reported in Sec. A.5. The mean absolute error (MAE) is listed for each nucleus and increases with the atom number. The smallest MAE is found for C with 0.01 ppm and the largest for Pb with 0.17 ppm. The maximum errors are in the same order of magnitude and therefore clearly show the absence of outliers. The range of the NMR shifts typically increases in the same way with the atom number. Here, the range slightly decreases from carbon to silicon but then rises from 86 ppm to 601 ppm for lead. Compared to the range and the required accuracy for a comparison with experimental findings, the error introduced by DLU is negligible. In this study, the same structures are used for the X2C and the DLU-X2C NMR shieldings. Fully optimizing the molecular geometry at each level will result in a second-order error. Based on the previous implementation of geometry gradients, this error is expected to be almost vanishing as the error in the bond lengths and angles is negligible.^[107]

Table 9.2: Mean absolute error (MAE) of the DLU-X2C Hamiltonian in ^{13}C , ^{29}Si , ^{73}Ge , ^{119}Sn , and ^{207}Pb NMR shifts for a small test set of organometallic alkynyl compounds. Max. Error refers to the maximal absolute error whereas range denotes the span of the calculated shifts. Errors and range of the NMR spectra are given in ppm. The individual results are listed in the appendix, Sec. A.5. The Dyall-CVTZ/cc-pCVTZ(unc) basis set is used and the PBE0 functional (grid 4a) is selected.

	MAE	Max. Error	Range
^{13}C	0.01	0.02	109
^{29}Si	0.06	0.13	86
^{73}Ge	0.07	0.09	156
^{119}Sn	0.13	0.19	301
^{207}Pb	0.17	0.2	601

9.1.3 Xenon Fluorides

Xenon fluorides are studied for a comparison with the wavefunction-based methods of Cheng and co-workers.^[101] The impact of spin-orbit coupling is small for these molecules and the scalar-relativistic CC results can be used as benchmark values for DFT methods. Note that all electrons were correlated in the CC calculations. Furthermore, experimental results are available for all three molecules.^[499] In quantum chemistry, the xenon atom is chosen as reference whereas neat XeOF_4 is the experimental reference compound for the ^{129}Xe shifts. The two shift scales can be converted to each other by using the shifts of xenon gas at infinite dilution (-5460 ppm) at the neat XeFO_4 scale.^[500] Note that the shift at infinite dilution was obtained by extrapolation from the shift in solution. To allow for a strict comparison to the CC results, the same structures are employed and the uncontracted ANO-RCC basis sets^[179] are used. Note that the octahedral structure of XeF_6 is assumed. Very tight SCF thresholds of $10^{-9} E_h$ and CPKS thresholds of 10^{-7} a.u. are applied. The BP86,^[128,340] PBE,^[341] KT3,^[342,501] TPSS,^[346] B3LYP,^[128-130] PBE0,^[355] and TPSSh^[356] functionals are chosen to cover the most common functionals for NMR shifts. τ is generalized with the external magnetic field.^[407,461] Large grids (grid 4a) are employed for the XC part.^[482] The shifts are reported in Tab. 9.3 and the shielding constants are listed in Tab. A.5.

First, the impact of scalar relativity is significant. The shifts increase by 300 ppm (XeF_2), 550 ppm (XeF_4), and 700 ppm (XeF_6). The scalar-relativistic Hamiltonian reproduces the trend of the experimental NMR shifts: The shifts increase by about 2300 ppm from XeF_2 to XeF_4 and by 2000 ppm from XeF_2 to XeF_6 . The non-relativistic Hamiltonian tends to underestimate the NMR shifts of XeF_4 and XeF_6 . Therefore, the experimental trend is not accurately matched. Despite the pronounced relativistic effects, the MAE of DLU amounts to only 0.16 ppm and is absolutely negligible.

Second, the “pure” and hybrid density functional approximations are in reasonable agreement with the CC results and the experimental findings. All functionals overestimate the chemical shifts compared to CCSD(T), yet a considerable improvement upon HF is found. Generally, the perturbative treatment of triples in the CC methods improves the agreement with the experimental findings. However, the trend of the shifts is not accurately reproduced: the shifts increase by 2000 ppm from XeF_2 to XeF_4 and by 1700 ppm from XeF_2 to XeF_6 . The change of the shifts with the molecules is excellently described by the TPSSh functional. Overall, DFT performs well for these molecules. However, the computational settings are not very common or practical. Usually, the structure is optimized at the same or a lower level of theory and triple- ζ basis sets are commonly used for DFT calculations to restore the balance of the basis set and chosen method. This may allow for favorable error cancellation and consequently improve the agreement with the experimental results.

Table 9.3: ^{129}Xe NMR chemical shifts of xenon fluorides obtained at various levels of theory. Chemical shifts are given in ppm with respect to the isotropic shielding of the Xe atom. Method 1 uses structures from Ref. 101, which were optimized at the scalar-relativistic X2C/CCSD(T)/ANO-RCC(unc) level. The ANO-RCC(unc) basis set was used in the NMR shielding calculations of that method. Here, the mean absolute error (MAE) of the DLU scheme is 0.16 ppm. Method 2 indicates NMR calculations based on the geometry optimized at the corresponding level with the x2c-TZVPall-2c bases employed in the relativistic calculations and the def2-TZVP/TZVPall basis in the non-relativistic ones (NR). The octahedral symmetry is used for XeF_6 . The MAE of the DLU scheme with this method is 0.45 ppm. Exp. refers to the experimental value in the gas phase taken from Ref. 499. The CCSD and CCSD(T) results were taken from Ref. 101. The shielding constants of the xenon atom as reference for the NMR shifts and the xenon fluorides are listed in the appendix, Tab. A.5.

Level	Method	XeF_2			XeF_4			XeF_6		
		NR	X2C	DLU	NR	X2C	DLU	NR	X2C	DLU
HF	1	3551	4018	4018	4901	5504	5504	4289	4858	4858
BP86	1	3406	3713	3713	5616	6185	6185	5227	5903	5903
PBE	1	3383	3693	3693	5577	6147	6147	5183	5856	5856
KT3	1	3282	3594	3594	5385	5950	5950	5032	5699	5699
TPSS	1	3284	3594	3594	5412	5979	5979	5090	5762	5762
B3LYP	1	3546	3897	3897	5563	6147	6146	5145	5819	5819
PBE0	1	3412	3759	3759	5360	5931	5931	4991	5646	5645
TPSSh	1	3307	3632	3632	5344	5911	5911	5028	5694	5693
CCSD	1	3337	3698	–	4971	5507	–	4540	5130	–
CCSD(T)	1	3238	3564	–	4982	5509	–	4641	5258	–
HF	2	3165	3797	3797	4429	5299	5299	4127	4670	4670
BP86	2	3148	3654	3654	5533	6380	6380	5713	6351	6352
PBE	2	3113	3622	3622	5488	6328	6328	5661	6290	6291
KT3	2	2986	3502	3502	5161	5997	5998	5293	5918	5919
TPSS	2	3040	3538	3538	5298	6126	6127	5536	6153	6154
B3LYP	2	3288	3840	3840	5338	6223	6223	5461	6102	6103
PBE0	2	3135	3677	3677	5064	5919	5919	5148	5751	5752
TPSSh	2	3060	3574	3574	5144	5982	5982	5346	5954	5955
MP2	2	2986	3503	3503	4759	5620	5621	4992	5607	5608
Exp.			3386			5623			5425	

NMR shielding constants and shifts are further calculated with the x2c-TZVPall-2c basis sets.^[203] For consistency, the non-relativistic all-electron TZVPall basis set is used for xenon^[502] and the def2-TZVP basis set for fluorine^[198] in the non-relativistic calculations. Moreover, MP2 calculations^[491,492] are performed. The same point group symmetries as above are chosen: $D_{\infty h}$ for XeF_2 , D_{4h} for XeF_4 , and O_h for XeF_6 . Geometries were considered to be converged when the energy change falls below $10^{-6} E_h$ and the norm of the gradient is smaller than $10^{-3} E_h/\text{bohr}$. Optimized structures are listed in the supporting information of Ref. 379. Note that the potential energy surface of XeF_6 is shallow and there is sufficient evidence that both O_h and the distorted C_{3v} structure are minima.^[112] The C_{3v} structure is very likely the global minimum in the gas phase. However, the energies of the structures are sensitive regarding the basis sets, method to treat electron correlation, and special relativity.^[111,503–506] Herein, the DFT-optimized and MP2-optimized O_h structures are (local) minima as confirmed by numerical frequency calculations. In contrast, the octahedral structure is a saddle point at the HF level in line with Ref. 506. This also holds for functionals incorporating a larger amount of HF exchange. For instance, the O_h structure is a transition state at the BH&HLYP level,^[128,129,350] which uses 50 % HF exchange.^[365] Based on the normal modes, a C_{2v} symmetric transition state is found with HF. The energy of this state is lower than for the O_h structure. Due to the small energy difference,

structure conversion is likely to occur fast and also confirmed by the experimental NMR spectra, which only show one type of fluorine atoms.^[499] Therefore, the O_h symmetry is used in the NMR calculations, those results are reported in the second half of Tab. 9.3. Overall, no consistent improvement is found compared to the previous results. All functionals except for KT3, PBE0, and TPSSh severely overestimate the shifts of XeF_4 and XeF_6 . The PBE0 functional performs best by overestimating all shifts by 300 ppm. This finding agrees with previous benchmark calculations for light elements.^[407] MP2 performs well for XeF_2 and XeF_4 but does not reproduce the trend from XeF_4 to XeF_6 . MP2 essentially yields no decrease whereas the experimental shifts decrease by about 200 ppm. The most important result is, however, the negligible MAE of DLU. The error amounts to about 0.5 ppm and therefore rises compared to the computational settings above due to the structure optimization at the DLU-X2C and X2C level. Still, the DLU scheme is very accurate for heavy nuclei such as xenon.

9.1.4 Transition-Metal Oxo Compounds

The ^{17}O NMR shifts of the transition-metal oxo compounds MO_4^{x-} ($x = 2$ and $M = \text{Cr, Mo, W}$; $x = 1$ and $M = \text{Mn, Tc, Re}$; $x = 0$ and $M = \text{Fe, Ru, Os}$) are considerably affected by scalar-relativistic effects.^[380,381] As the NMR shifts are not measured at the heavy atom itself but at the neighboring atoms, ECPs are also a reasonable choice for these systems. Here, all-electron relativistic methods are compared to ECP-based and non-relativistic ansätze. The non-relativistic calculations are performed with the def2-TZVP basis for oxygen and the 3d metals,^[198] whereas the TZVPalls2 basis is used for the 4d and 5d transition metals.^[203,204,379,502] Two different choices of ECPs are considered. The Wood–Boring (WB) ECPs^[507] are used with the def2-TZVP basis set and the Dirac–Fock (DF) ECPs^[177] are used with the dhf-TZVP basis set.^[202] The X2C and DLU-X2C calculations employ the x2c-TZVPall-2c basis set.^[203] Based on the results of the previous subsection, the PBE0 functional^[355] and the BP86 functional^[128,340] are selected. Large grids (grid 4a) are employed for the numerical integration of the DFT parts. Structures were optimized at each level of theory with a SCF convergence criterion of $10^{-9} E_h$ and were considered to be converged based on an energy threshold of $10^{-6} E_h$ and a threshold of $10^{-3} E_h/\text{bohr}$ for the norm of the gradient. COSMO^[453,454] was applied to compensate the negative charge of the anionic systems. This avoids positive orbital energies of occupied states. All structures were confirmed to be local minima on the potential energy surface by numerical frequency calculations and are listed in the supporting information of Ref. 379. The optimized structures are in good agreement with the experimental findings given in Ref. 380 as the deviation of all bond lengths is below 2.5 pm. Note that the tetrahedral structure of FeO_4 is used with Fe in the oxidation state +VIII as this structure is lower in energy than the C_{2v} structure with Fe in the oxidation state +VI.^[508,509] The NMR shieldings were calculated with a criterion of 10^{-7} a.u. for the CPKS equations and the NMR shifts are obtained with respect to H_2O in the gas phase. To allow for a comparison with the experimental data,^[510] the experimentally determined vapor–liquid shift of 36 ppm^[380,381] is used. The NMR shifts are reported in Tab. 9.4.

Again, the DLU error is negligible as reflected by a MAE of 0.12 ppm and a range of about 800 ppm. For the 3d compounds, the non-relativistic and the relativistic Hamiltonians are in good agreement as expected. Due to the minor importance of relativistic effects, no ECPs are available with the standard basis sets. Already for the 4d compounds, matters are different. Here, relativistic effects need to be considered and amount to about 60 to 70 ppm. The impact of scalar relativity rises to ca. 100 ppm for the 5d molecules. The deviation between the results of the WB-ECPs and the DF-ECPs is notable for OsO_4 . Here, the results differ by 70 ppm (BP86) and 35 ppm (PBE0). The DF-ECPs yield NMR shifts close to the ones of X2C and the DLU-X2C Hamiltonian. Both methods are based on the four-component Dirac equations. The DF-ECPs are parameterized to match the properties of the 4c Hamiltonian and the X2C Hamiltonian decouples the

Table 9.4: Comparison of ^{17}O NMR shifts of transition-metal compounds calculated at various levels of theory and experimental findings. The experimental values are taken from Ref. 510 and converted to a more suitable scale as outlined in Ref. 381. To the best of the author’s knowledge, no experimental shifts were reported in the literature for FeO_4 . NR denotes the non-relativistic results, while WB-ECP and DF-ECP refer to the calculations employing Wood–Boring and Dirac–Fock ECPs for the metal atoms. All structures are optimized at the corresponding level of theory. COSMO is applied to compensate the negative charge. The MAE of the DLU scheme is 0.12 ppm and the shielding constants are listed in Tab. A.6.

	BP86					PBE0					Exp.
	NR	WB-ECP	DF-ECP	X2C	DLU	NR	WB-ECP	DF-ECP	X2C	DLU	
CrO_4^{2-}	782	–	–	764	765	845	–	–	824	824	871
MoO_4^{2-}	625	554	587	565	565	637	561	594	570	570	576
WO_4^{2-}	567	452	458	451	451	572	453	458	450	450	456
MnO_4^-	1077	–	–	1050	1050	1250	–	–	1210	1210	1255
TcO_4^-	860	736	764	769	769	919	784	800	803	803	786
ReO_4^-	761	608	595	604	604	795	620	605	615	615	605
FeO_4	1513	–	–	1465	1465	2059	–	–	1955	1956	–
RuO_4	1198	1034	1046	1054	1054	1412	1162	1178	1185	1185	1142
OsO_4	1033	868	798	806	806	1157	877	842	855	855	787

negative and positive energy subspace of the Dirac equation. Generally, the BP86 functional underestimates the shifts whereas the PBE0 results in an excellent agreement for all molecules except for CrO_4 and OsO_4 . Here, the deviations amount to ca. 50 ppm and 70 ppm. Note that the methods used herein result in a notably better agreement than the previous results^[380,381] which show a deviation of more than 200 ppm for MnO_4 . The results confirm that an ECP-based implementation^[407,511] of NMR shifts is sufficiently accurate for neighboring atom effects—at least with DF-ECPs.

9.1.5 Tungsten Compounds

^{183}W shifts are studied as an application to the sixth row of the periodic table. Here, ECPs cannot be used and an all-electron ansatz is required. The PBE0 functional^[355] and the BP86 functional^[128,340] (grid 4a) are selected again as especially PBE0 showed a robust performance in the previous studies. For the non-relativistic calculations, the def2-TZVP basis set^[198] is combined with the TZVPalls2 basis set for tungsten.^[203,204,379] The relativistic calculations use the x2c-TZVPall-2c basis set.^[203] COSMO^[453,454] is employed to compensate the charges. Tight SCF and CPKS thresholds of $10^{-9} E_h$ and 10^{-7} a.u. are applied and the structures were optimized as previously described. Numerical frequency calculations confirmed the stationary points to be local minima. Cartesian coordinates are listed in the supporting information of Ref. 379. NMR shifts are measured with respect to WO_4^{2-} and are compared to the experimental findings in Tab. 9.5. Here, the MAE of the DLU scheme amounts to 1.0 ppm and the range of the NMR shifts to more than 7750 ppm. Therefore, the DLU error is again negligible.

Overall, the non-relativistic Hamiltonian is insufficient for tungsten compounds as especially WS_4^{2-} , $\text{W}(\text{CO})_6$, and WF_6 show considerable relativistic effects between 100 and 300 ppm. The X2C Hamiltonian and the ZORA approach^[382] result in similar results for most molecules with the BP86 functional, however, larger deviations are found for WCl_6 and $\text{W}(\text{CO})_6$. At first glance, ZORA results are closer to the experimental findings but this is more likely due to error cancellation regarding the BP86 functional. In general, BP86 does not perform well for these systems as reflected by the poor results for WF_6 . In contrast, PBE0 predicts all shifts except for $\text{W}(\text{CO})_6$ within less than 200 ppm compared to the experimental data. PBE0 tends to underestimate the shifts. Note that the shifts are overestimated for WS_4^{2-} and $\text{W}(\text{CO})_6$. Despite the

Table 9.5: Comparison of non-relativistic and relativistic calculated ^{183}W shifts with experimental data taken from Refs. 513–516. The non-relativistic calculations use the def2-TZVP/TZVPalls2 basis set and the X2C/DLU-X2C calculations are performed with the x2c-TZVPall-2c bases. COSMO is employed to simulate the counter ions. The MAE introduced by the local approximation is 1.0 ppm. The shielding constants are shown in Tab. A.7. ZORA results are taken from Ref. 382.

	BP86				PBE0			Exp.
	NR	X2C	DLU	ZORA	NR	X2C	DLU	
WO_3S^{2-}	723	736	736	797	781	775	775	841
$\text{WO}_2\text{S}_2^{2-}$	1563	1609	1608	1612	1734	1728	1727	1787
WOS_3^{2-}	2454	2558	2558	2541	2769	2788	2788	2760
WS_4^{2-}	3389	3576	3575	3537	3875	3937	3936	3769
$\text{W}(\text{CO})_6$	-3802	-3828	-3832	-3679	-3681	-3816	-3820	-3446
WF_6	-454	-584	-583	-561	-830	-926	-925	-1121
WCl_6	2544	2226	2226	2011	2522	2086	2086	2181

improvement upon BP86, the shift of $\text{W}(\text{CO})_6$ is still not in a good agreement with the experimental findings and the deviation amounts to ca. 400 ppm. The structure is in a typically agreement for DFT. The bond lengths differ by 2 pm from the experimental findings.^[512] MP2 yields a shift of -4032 ppm. Therefore, a higher level of theory needs to be considered, including a better description of electron correlation and environment effects.

9.1.6 Demonstration of Efficiency

The computational costs of the X2C and the DLU-X2C Hamiltonian are compared for the silver clusters Ag_{13}^- and Ag_{55}^- , which are depicted in Fig. 9.1. For these metal clusters, the “pure” GGA functional BP86^[128,340] (grid 5a^[482]) is selected. Therefore, only the Coulomb integral derivatives within the RI- J approximation and the derivative of the XC energy for the RHS are calculated and no CPKS iterations are necessary. The x2c-SVPall orbital and auxiliary basis sets are applied and result in more than 6,000 primitive functions for the larger cluster. The computation times and the number of basis functions are listed in Tab. 9.6. The second-order response for the unperturbed density clearly dominates the CPU times in the full X2C approach already for the smaller cluster. Here, 81 % of the total computation time are needed for the second-derivative of the Hamiltonian. The calculations of the larger cluster take more than one week. Introduction of the DLU scheme reduces the computation time to 4 minutes for Ag_{13}^- and to about 5 hours for Ag_{55}^- . For the small cluster, the two-electron integrals are as demanding as all derivatives of the one-electron Hamiltonian. This changes for the larger silver cluster. Then, the DLU-X2C part amounts to 84 % of the total CPU time. This shows the efficiency of the RI- J approximation. In contrast to the full X2C ansatz, the DLU-X2C is still applicable to larger clusters like Ag_{147}^- with more than 17,000 primitive basis functions. The DLU scheme allows to also calculate all NMR shieldings of this large cluster in 5 days.

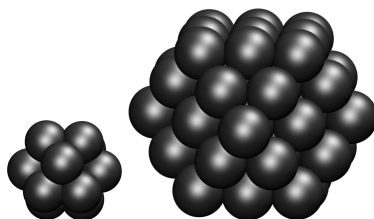


Figure 9.1: Structures of the octahedral silver clusters Ag_{13}^- (left) and Ag_{55}^- (right) taken from Ref. 105.

Table 9.6: CPU times (single thread of a CPU of type Intel® Xeon® Gold 6212 @ 2.40 GHz and TURBOMOLE V7.5 [2020]) for the important steps in an X2C and DLU-X2C NMR shielding calculation of silver cluster anions at the BP86/x2c-SVPall level of theory (grid 5a) and organometallic iridium complexes, Ir-1 and Ir-2, at the PBE0/x2c-TZVPPall-2c level (grid 4a). The RI- J approximation is used in the Coulomb integrals and SCF thresholds of $10^{-7} E_h$ (Ag clusters) and $10^{-8} E_h$ (Ir complexes) were applied. NBF denotes the number of basis functions and the parentheses refer to the corresponding space: primitive (prim), contracted (cont), and auxiliary (aux). The octahedral symmetry of the clusters is not exploited. Note that 9 iterations were needed to solve the CPKS equations with a criterion of 10^{-7} a.u. for the norm of the residuum. The time for the CPKS solver includes the first-order response with respect to the magnetic moments. Differences between the total computation time and the sum of the steps given below are due to rounding and initialization steps. Times are given in minutes and all shielding constants are calculated.

Operation	Ag ₁₃ ⁻		Ag ₅₅ ⁻		Ag ₁₄₇ ⁻	Ir-1		Ir-2	
	X2C	DLU	X2C	DLU	DLU	X2C	DLU	X2C	DLU
1st Order Response B	0.6	0.1	38.9	3.8	37.3	2.1	0.9	14.1	4.9
2nd Order Response	33.0	1.7	8615.3	240.1	6132.0	464.5	61.4	7639.0	719.3
RI- J and DFT grid	2.0	2.1	51.0	51.9	415.0	10.7	10.7	42.4	41.1
Exchange RHS	–	–	–	–	–	102.9	105.5	469.8	465.0
CPKS	5.1	0.3	1795.4	25.9	686.4	446.8	391.1	2830.5	1975.7
1st Order Response m	5.1	0.3	1795.1	25.6	679.5	67.8	7.1	1161.3	80.0
Total	40.7	4.3	10 501.0	322.0	7273.3	1027.0	569.8	10 996.1	3208.5
NBF (prim)	1,521	1,521	6,435	6,435	17,199	2,319	2,319	4,557	4,557
NBF (cont)	689	689	2,915	2,915	7,791	1,576	1,576	3,229	3,229
NBF (aux)	1,703	1,703	7,205	7,205	19,257	2,924	2,924	5,729	5,729

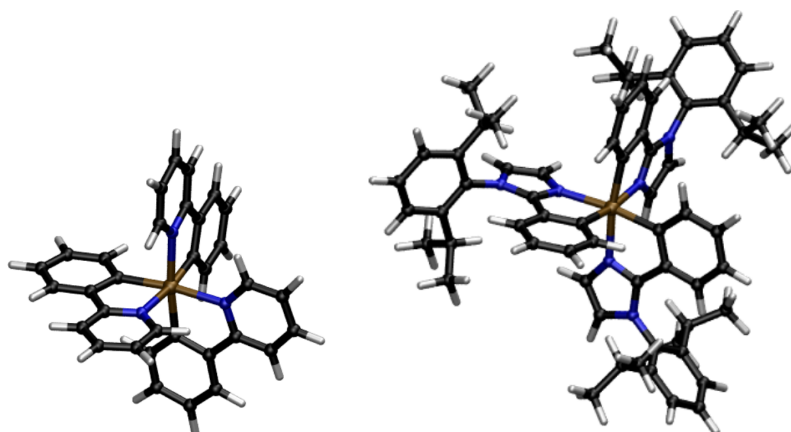


Figure 9.2: Molecular structure of the organometallic iridium complexes, denoted as Ir-1 (left) and Ir-2 (right). Ir-1 consists of 63 atoms while the larger complex consists of 139 atoms. Color scheme: hydrogen white, carbon black, nitrogen blue, and iridium brown. Structures are taken from Ref. 107.

The inclusion of HF exchange significantly changes the ratio of the one and two-electron terms as shown for the iridium complexes in Fig. 9.2. Here, the PBE0 functional^[341,355] is employed with large grids^[482] (grid 4a). The x2c-TZVPPall-2c orbital and auxiliary basis sets are chosen. The DLU-X2C calculations take about 9.5 hours and 53.5 hours. For both molecules, the evaluation of the HF exchange in the response equations is the most time-consuming step with about 69% and 62% of the total computation time. The second-order derivative of the Hamiltonian only amounts to 11% and 22%. Consequently, the exchange integrals for the RHS are more demanding for Ir-1. Matters are different for the full X2C Hamiltonian. Here, the second-order response and the CPKS integrals are balanced for Ir-1 whereas the derivative of the Hamiltonian dominates the CPU time for Ir-2 with 69% of the total time. Therefore, the DLU scheme results in balanced computational demands for large molecules without significant loss of accuracy.

9.2 NMR Indirect Spin–Spin Coupling Constants

Similar to the previous section, the accuracy of the DLU-X2C Hamiltonian for the NMR indirect spin–spin coupling constants is assessed for main-group and transition-metal elements. Furthermore, the DLU-X2C ansatz is compared to ZORA and 4c Hamiltonians. The impact of the basis set and the density functional approximations are also considered. Computational methods are described in detail in every subsection. Unless explicitly stated differently, the finite nucleus model is employed. The kinetic energy density is generalized with the paramagnetic current density.^[365]

9.2.1 Tetrel Molecules and Hydrogen Halides

The developed quasirelativistic methodology is compared to the 4c-RKB Dirac–Hartree–Fock ansatz for the tetrel hydrides and hydrogen halides.^[50,51] We adopt the same computational methods as in the 4c reference calculations. The even-tempered basis sets and structures of Ref. 50 are used for TtH_4 ($\text{Tt} = \text{C}, \text{Si}, \text{Ge}, \text{Sn}, \text{Pb}$). For HX ($\text{X} = \text{F}, \text{Cl}, \text{Br}, \text{I}$), we use the structure of Sundholm *et al.* for HF ^[517] and the experimental structures for the other molecules.^[518] The basis sets are taken from Ref. 519. A modified uncontracted aug-cc-pVTZ basis set is used for HF and HCl ,^[161,162,496,520] with a single tight p function added for F . The other molecules use the uncontracted Sadlej-pVTZ basis^[487,488,521] with additional p and d functions for H and an even-tempered basis sets for Br and I . Hartree–Fock calculations were performed with an SCF threshold of $10^{-8} E_h$ for the energy and 10^{-8} a.u. for the root mean square of the densities. A criterion of 10^{-7} a.u. for the norm of the residuum indicates the convergence of the CPHF equations. No approximations are employed for the two-electron integrals. The reduced coupling constants are reported in Tab. 9.7.

The light compounds of CH_4 , SiH_4 , HF , and HCl show essentially no relativistic effects and the finite nuclear size is not important for the results. For the heavier molecules, the impact of special relativity increases from

Table 9.7: Comparison of non-relativistic, two-component, and four-component HF results. Reduced coupling constants (${}^1K_{\text{TH}}$, ${}^2K_{\text{HH}}$, ${}^1K_{\text{HX}}$) are given in 10^{19} T J^{-2} . 4c results of the TtH_4 molecules are taken from Ref. 50 and 4c results of the HX molecules from Ref. 51. NR denotes the non-relativistic Hamiltonian. Even-tempered (ET) basis sets are used for the TtH_4 molecules.^[50] Decontracted aug-cc-pVTZ basis sets with additional tight functions are employed for HF and HCl whereas Sadlej-pVTZ bases (for H) and ET bases (for Br, I) are used for HBr and HI .^[519] Note that the 4c calculations use the finite nucleus model for the scalar potential but not the vector potential.

	Finite Nucleus					Point Charge				
	NR	X2C	DLU	mSNSO-X2C	mSNSO-DLU	X2C	DLU	mSNSO-X2C	mSNSO-DLU	4c-RKB
${}^1K_{\text{TH}}$										
CH_4	53.06	53.28	53.24	53.29	53.25	53.29	53.25	53.30	53.26	52.6
SiH_4	102.42	104.29	104.30	104.33	104.34	104.41	104.42	104.45	104.46	104.4
GeH_4	263.54	293.73	293.79	294.00	294.06	296.10	296.15	296.37	296.42	294.8
SnH_4	430.73	580.45	580.53	581.11	581.19	594.21	594.14	594.87	594.80	588.3
PbH_4	711.45	1764.62	1764.81	1766.56	1766.75	2010.97	2010.89	2012.66	2012.66	1819.0
${}^2K_{\text{HH}}$										
CH_4	-2.28	-2.29	-2.29	-2.29	-2.29	-2.29	-2.29	-2.29	-2.29	-2.27
SiH_4	-0.08	-0.05	-0.05	-0.05	-0.05	-0.05	-0.05	-0.05	-0.05	-0.05
GeH_4	-0.05	0.18	0.18	0.18	0.18	0.18	0.18	0.18	0.18	0.64
SnH_4	0.11	0.84	0.85	0.84	0.85	0.84	0.85	0.84	0.85	0.80
PbH_4	0.27	3.70	3.71	3.70	3.70	3.73	3.74	3.73	3.73	3.62
${}^1K_{\text{HX}}$										
HF	54.06	53.98	53.97	53.96	53.96	53.98	53.97	53.97	53.96	53.99
HCl	27.47	25.96	25.98	25.95	25.97	25.96	25.98	25.96	25.98	26.27
HBr	6.10	-16.25	-16.15	-16.30	-16.24	-16.33	-16.24	-16.37	-16.29	-15.82
HI	-9.28	-108.94	-108.93	-109.09	-109.09	-110.95	-110.97	-111.12	-111.12	-113.20

$30 \cdot 10^{19} \text{ T J}^{-2}$ for GeH_4 to $1100 \cdot 10^{19} \text{ T J}^{-2}$ for PbH_4 . The same holds for the impact of the nuclear charge distribution. The finite nucleus model decreases the coupling constants. The maximum change is found with $240 \cdot 10^{19} \text{ T J}^{-2}$, equaling 10 %, for PbH_4 . Overall, both the X2C and the DLU-X2C Hamiltonian result in an excellent agreement with the 4c results. The deviations rise from 0.4 % for GeH_4 to 1 % for SnH_4 and 3 % for PbH_4 . Most of the deviation for plumbane can be attributed to the missing finite nucleus effects on the vector potential in the 4c studies. The deviations for HBr and HI are in the same order of magnitude: 3 % for HBr and 4 % for HI. In an RKB basis set, the impact of the mSNSO approach is small and amounts to at most $2 \cdot 10^{19} \text{ T J}^{-2}$. This can be easily rationalized by the missing integral derivatives of the relativistically modified potential, \mathbf{W} . Thus, the mSNSO ansatz only affects the derivative of the Hamiltonian via the response equations for the decoupling matrix. Moreover, the mSNSO approximation affects the density matrix and the spinor energies in self-consistent calculations. It should be noted that even the very small impact of the mSNSO ansatz is one order of magnitude larger than the maximum DLU error of $0.19 \cdot 10^{19} \text{ T J}^{-2}$ only. Therefore, the error of the DLU scheme is negligible. Similar findings hold for the ${}^2K_{\text{HH}}$ constants of the tetrel molecules. For hydrogen, the finite nucleus model does not affect the results, however, the impact of relativity is still significant and needed to predict the correct sign for GeH_4 . Again, the quasirelativistic Hamiltonians are a good approximation of the 4c Dirac–Fock approach.

The X2C Hamiltonian agrees very well with the parent 4c approach for HF calculations. Yet, HF does not consider electron correlation and therefore a comparison with experimental data is not physically meaningful. To treat electron correlation, DFT methods are applied. Here, common conventional functionals and local hybrid functionals are considered. The BP86,^[128,340] PBE,^[341] TPSS,^[346] B3LYP,^[128–130] PBE0,^[355] TPSSh,^[356] CAM-B3LYP,^[133,529,530] LH07t-SVWN,^[138] LH12ct-SsirPW92,^[139] LHJ14,^[141] and the PSTS functional in conventional gauge^[134] combined with large integration grids^[482] (grid 4a) were selected. The DLU-X2C Hamiltonian with the finite nucleus model and the mSNSO approximation is applied. All other computational settings are unchanged and the results are presented in Tab. 9.8. As expected, all functionals improve upon HF and already the GGA functionals BP86 and PBE result in a good agreement for the tetrel

Table 9.8: Comparison of various density functional approximations. Reduced coupling constants (${}^1K_{\text{TH}}$, ${}^2K_{\text{HH}}$, ${}^1K_{\text{HX}}$) are given in 10^{19} T J^{-2} and compared to the same experimental findings of the TiH_4 molecules^[522–527] as in Ref. 50. The experimental result of HF is taken from Ref. 528. The DLU-X2C Hamiltonian including the finite nucleus model and the mSNSO ansatz is employed. The same basis sets and structures as in Tab. 9.7 are chosen. LH07t and LH12ct denote the LH07t-SVWN and the LH12ct-SsirPW92 functional. Large grids (grid 4a) are used for the numerical integration of the DFT part.

	BP86	PBE	TPSS	B3LYP	PBE0	TPSSh	CAM-B3LYP	LH07t	LH12ct	LHJ14	PSTS	Exp.
${}^1K_{\text{TH}}$												
CH_4	40.50	40.23	46.65	44.69	41.50	46.96	43.64	37.41	33.69	42.49	46.63 ^a	40.0
SiH_4	82.64	79.85	82.94	90.00	82.96	84.52	87.61	78.27	74.09	85.93	82.56	84.3
GeH_4	214.67	208.59	226.53	240.20	222.01	231.81	236.67	217.70	210.80	232.23	228.45	232
SnH_4	384.09	375.39	402.29	439.37	409.18	415.96	435.78	403.80	397.95	422.38	410.90	429
PbH_4	975.79	964.74	1053.48	1172.30	1098.03	1106.58	1187.82	1091.26	1097.10	1124.47	1092.28	–
${}^2K_{\text{HH}}$												
CH_4	–1.09	–1.00	–0.86	–1.12	–1.17	–0.95	–1.12	–1.04	–0.87	–1.05	–1.21 ^a	–1.03
SiH_4	0.01	0.06	0.82	0.40	0.06	0.79	0.47	0.21	0.16	0.45	0.75	0.22
GeH_4	0.65	0.68	1.18	1.03	0.56	1.11	1.05	0.68	0.66	1.07	1.06	0.64
SnH_4	1.22	1.23	1.67	1.75	1.12	1.62	1.73	1.26	1.23	1.75	1.48	1.27
PbH_4	3.18	3.12	3.79	4.01	3.08	3.78	3.95	3.21	3.06	4.01	3.77	–
${}^1K_{\text{HX}}$												
HF	29.39	31.03	30.27	36.44	35.29	32.18	37.15	33.63	34.36	35.66	30.81	44.2
HCl	13.28	13.90	19.22	18.49	16.61	19.94	16.66	18.20	17.35	18.55	19.12	–
HBr	–29.18	–27.57	–27.43	–20.93	–23.01	–25.34	–29.60	–17.71	–13.71	–23.20	–29.78 ^b	–
HI	–82.10	–78.21	–83.03	–72.65	–79.28	–82.81	–97.62	–75.75	–69.03	–83.74	–87.81 ^b	–

^aNorm of the residuum could only be converged below 10^{-3} a.u.

^bNorm of the residuum could only be converged below 10^{-4} a.u.

molecules with deviations below 10 % and 15 % for ${}^1K_{\text{TH}}$. The coupling constants increase with TPSS and consequently the deviation from the experimental results increases for ${}^2K_{\text{HH}}$. Hybrid density functionals increase the coupling constants of the parent “pure” functionals. B3LYP and CAM-B3LYP overestimate the couplings and PBE0 results in a good agreement with the experimental data. Note that B3LYP and CAM-B3LYP perform similarly with the exception of HI. For HI, CAM-B3LYP significantly increases the coupling constant by 20 %. The t-LMF based LHF’s, LH07t-SVWN and LH12ct-SsirPW92, tend to underestimate the coupling constants and do not improve upon the global hybrid functionals. LHJ14 is a better choice for the molecules herein and outperforms these two LHF’s for the light elements. LHJ14 yields results close to the ones of B3LYP, which is rationalized by the Becke 1988 exchange^[128] and correlation terms^[371] of LHJ14. PSTS shows very similar results as the parent TPSS and TPSSh functionals.

So far, even-tempered basis sets are employed for most atoms. The impact of the basis set is further studied by selecting the larger even-tempered basis sets of Ref. 483 as reference and considering the segmented-contracted x2c-type basis sets.^[203,483] In line with chapter 8, the basis set studies are performed with the X2C Hamiltonian in the finite nucleus model. The basis sets used in the previous Hamiltonian and DFT studies are termed 4c-Bases and the reference basis set is denoted X2C-ET. Results are shown in Tab. 9.9. Note that the 4c-Basis are no sufficient approximation of the complete basis set limit. Large deviations from the X2C-ET basis are found for HX and PbH_4 . The unfavorable performance of the 4c-Basis for the halides is caused by the modified aug-cc-pVTZ basis sets for HF and HCl and the small Saldej-pVTZ basis for hydrogen in HBr and HCl. Note that using the modified aug-cc-pVTZ for hydrogen throughout does not improve the performance. The coupling constants of HBr and HI are $-16.30 \cdot 10^{19} \text{ T J}^{-2}$ and $-109.45 \cdot 10^{19} \text{ T J}^{-2}$, respectively. The main error for Pb is caused by the missing *d* and polarization functions as the exponents of the tight functions are similar for X2C-ET.

Table 9.9: Comparison of various basis sets. Reduced coupling constants (${}^1K_{\text{TH}}$, ${}^2K_{\text{HH}}$, ${}^1K_{\text{HX}}$) are given in 10^{19} T J^{-2} . 4c-Bases denotes the basis sets of Refs. 50 and 519, see also Tab. 9.7, whereas X2C-ET refers to the even-tempered bases of Ref. 483. The X2C-ET bases are larger than the 4c-Bases. For brevity, the prefix “x2c-” for x2c-SVPall-2c etc. is omitted. The RI-*J* approximation is used for the SCF procedure with the x2c-type basis sets. The X2C Hamiltonian in the finite nucleus model at the HF level is chosen. NBF denotes the total number of basis functions in the spherical atomic orbital representation used for all molecules.

	SVPall-2c	TZVPall-2c	QZVPall-2c	QZVPall-2c-s	QZVPall-2c-j	4c-Bases	X2C-ET
${}^1K_{\text{TH}}$							
CH ₄	68.83	50.21	51.51	52.07	53.17	53.28	53.29
SiH ₄	85.74	81.95	98.74	98.73	102.38	104.29	103.94
GeH ₄	307.14	261.11	280.42	280.42	288.13	293.73	293.20
SnH ₄	510.80	521.34	557.21	557.18	576.18	580.45	581.00
PbH ₄	1542.69	1579.66	1723.55	1723.48	1770.25	1764.62	1796.69
${}^2K_{\text{HH}}$							
CH ₄	-2.05	-2.05	-2.17	-2.18	-2.21	-2.29	-2.27
SiH ₄	-0.36	-0.13	-0.03	-0.03	-0.05	-0.05	-0.04
GeH ₄	-0.27	-0.06	0.09	0.09	0.07	0.18	0.21
SnH ₄	0.39	0.60	0.79	0.79	0.83	0.84	0.90
PbH ₄	2.38	2.76	3.30	3.30	3.47	3.70	3.59
${}^1K_{\text{HX}}$							
HF	74.42	49.75	54.74	57.10	57.95	53.98	59.57
HCl	34.23	34.59	25.91	25.91	27.37	27.21	27.62
HBr	22.62	-24.97	-23.73	-23.72	-22.59	-16.25	-19.80
HI	-25.64	-96.46	-122.39	-122.39	-118.40	-108.94	-124.62
NBF	455	652	1608	1686	1719	1736	4383

A double- ζ basis set is not sufficient and shows a large deviation to the reference basis set. Even the sign of 1K for HBr is not predicted correctly. The x2c-TZVPall-2c basis set shows errors in the same range as X2C compared to 4c and the density functional results to the experimental findings. Therefore, a triple- ζ basis set may be considered sufficient for routine calculations, even though the errors are larger than for the 4c-Bases. However, the number of functions is also decreased by a factor of 3 compared to the 4c-Bases and therefore the computational costs are considerably lowered. The x2c-QZVPall-2c basis set significantly improves upon the x2c-TZVPall-2c basis. Jensen showed that tight p functions are required for the PSO term and the FC term necessitates tight s functions.^[531] Adding tight p functions by choosing the x2c-QZVPall-2c-s basis sets does not improve the results. Therefore, tight s functions are added in the same way as the tight p functions were added for the x2c-QZVPall-2c-s basis sets in Sec. 8.2.1. Thus, a single tight s function is added to the first segment by scaling the inner-most primitive with a factor of 6.5 and removing the outer-most primitive from the segment. The contraction coefficients are optimized in atomic ROHF calculations and the resulting basis set is termed x2c-QZVPall-2c-j. The bases are available in the supporting information of Ref. 431. This significantly improves upon the x2c-QZVPall-2c bases and results in a reduced deviation for all molecules except HI. The improvement for the other molecules is mainly caused by the basis set for the hydrogen atom. So, the coupling constant for HI can be improved by combining the x2c-QZVPall-2c basis set for I with x2c-QZVPall-2c-j for H. This yields $-120.13 \cdot 10^{19} \text{ T J}^{-2}$.

After demonstrating that the quasirelativistic Hamiltonian results in a good agreement with the 4c-RKB approach and considering the significant impact of the density functional approximation and the basis sets on the coupling constants, the “error” by neglecting the generalized momentum in the balance condition is assessed. Here, the DLU-X2C Hamiltonian in a finite nucleus model with the mSNSO approximation is compared to 4c-RMB results at the BP86 level from Ref. 60. For comparison, the uncontracted pcJ-2 basis set^[531] is employed for the light elements (C, Si) and the uncontracted Dyall-VTZ basis set^[190,495] for the heavy elements. $(l + 1)$ and $(l + 2)$ valence correlation and $(l + 1)$ core correlation functions were added to the Dyall basis sets. The same functionals as previously are chosen and all other computational settings are unchanged. However, the t-LMF based LHF’s are not considered due to the unfavorable performance observed previously. The results in Tab. 9.10 confirm that using the RKB instead of the more involved RMB condition is sufficient for NMR coupling constants as the relative deviation for the $^1J_{\text{TH}}$ coupling constants is below 2 % for CH₄, SiH₄, GeH₄, and SnH₄. The large deviation of 6.5 % for PbH₄ is explained by the missing finite nuclear size effects for the vector potential in the 4c calculations. Considering the impact of all other computational parameters, the RKB condition is clearly sufficient.

Table 9.10: Comparison of various density functional approximations in 4c and 2c approaches. 4c results are taken from Ref. 60. Coupling constants ($^1J_{\text{TH}}$, $^2J_{\text{HH}}$) are given in Hz and compared to the same experimental findings as in Ref. 60. The DLU-X2C Hamiltonian including the finite nucleus model and the mSNSO ansatz is employed. Large grids (grid 4a) are used for the numerical integration of the DFT part. The uncontracted Dyall-VTZ/pcJ-2 basis sets are employed.

	4c-RMB BP86	BP86	PBE	TPSS	B3LYP	PBE0	TPSSh	CAM-B3LYP	LHJ14	PSTS	Exp.
$^1J_{\text{TH}}$											
CH ₄	122.0	121.9	120.9	140.8	134.4	124.8	141.7	131.2	127.9	140.3	120.1
SiH ₄	-201.6	-198.4	-192.4	-197.6	-215.3	-199.4	-201.6	-209.3	-204.6	-198.5	-201.1
GeH ₄	-90.4	-90.1	-87.7	-94.9	-100.7	-93.2	-97.1	-99.1	-97.1	-96.1	-97.6
SnH ₄	-1742.2	-1728.0	-1690.7	-1809.9	-1975.1	-1841.6	-1871.3	-1958.5	-1896.9	-1856.7	-1933.3
PbH ₄	2345.3	2498.1	2472.5	2708.2	3007.6	2814.6	2843.9	3047.5	2879.6	2839.2	-
$^2J_{\text{HH}}$											
CH ₄	-13.50	-13.15	-12.05	-10.33	-13.49	-14.05	-11.44	-13.51	-12.66	-13.24	-12.40
SiH ₄	-0.56	-0.44	0.11	9.34	4.30	0.12	8.90	5.18	4.93	7.45	2.75
GeH ₄	7.79	7.81	8.12	13.97	12.37	6.78	13.27	12.57	12.86	11.68	7.69
SnH ₄	14.30	14.56	14.73	19.80	20.83	13.41	19.25	20.61	20.80	16.83	15.30
PbH ₄	30.87	36.67	35.77	44.44	46.59	35.36	44.23	45.85	46.21	40.84	-

9.2.2 Organometallic Main-Group Alkynyls

We study the same test set as in Sec. 9.1.2 to further compare the X2C and DLU-X2C Hamiltonian to ZORA and 4c-RMB results of Ref. 383. Therefore, structures are taken from this reference and the same basis sets as in the reference are used. The PBE^[341] and the PBE0^[355] density functional approximations are applied with large grids^[482] (grid 4a) for the numerical integration. SCF energies and densities were converged up to $10^{-8} E_h$ and 10^{-8} a.u.; a criterion of 10^{-6} a.u. was used to indicate the convergence of the CPKS equations. Results are presented in Tab. 9.11 and Tab. A.8. Note that the ZORA results are obtained with STOs^[532] and that the vector potential in the point-charge model is used in the 4c calculations.

As expected, relativistic effects are important for the Sn and Pb compounds. Here, the relativistic effects to the coupling constant of Pb–C≡C may amount to almost 800 Hz. The MAE of the DLU ansatz is 0.42 Hz with the finite nucleus model and is therefore negligible. The mean signed deviation (MSD) is 0.03 Hz and the respective standard deviation is 0.88 Hz. Note that there are no outliers as the maximum error is 2.16 Hz for Me₂Sn(CCMe)₂. The respective errors with the point-charge model are 0.44 Hz (MAE) and 0.02 Hz (MSD), while the standard deviation amounts to 0.92 Hz. Similar errors are found for the PBE functional and confirm that the error of the DLU scheme is independent of the functional. The finite nucleus model only affects the tin and lead compounds. For the latter, the finite nuclear size tends to decrease the couplings.

Table 9.11: Comparison of non-relativistic, two-component, and four-component results for alkynyl molecules at the PBE0 level. Dyall’s uncontracted CVTZ basis set is used for the heavy elements (Ge, Sn, Pb), whereas uncontracted cc-p(C)VTZ basis sets are employed for the light elements in the X2C and 4c-RMB calculations. The ZORA calculations use Slater-type basis functions. Structures, ZORA, and 4c results are taken from Ref. 383, whereas the experimental values are taken from Ref. 533. $^1J_{\text{TIC}}$ (Tt = ²⁹Si, ⁷³Ge, ¹¹⁹Sn, ²⁰⁷Pb) coupling constants are listed in Hz. NR and Me denote the non-relativistic limit and methyl groups. All X2C and DLU-X2C calculations employ the mSNSO approach.

	Finite Nucleus			Point Charge		ZORA	4c-RMB	Exp.
	NR	X2C	DLU	X2C	DLU			
$^1J_{\text{TIC}}$ for Tt(CCMe) ₄								
Si–C≡C	–125.56	–127.48	–127.46	–127.49	–127.47	–116.20	–132.32	–
Ge–C≡C	–54.09	–58.65	–58.63	–58.97	–58.94	–49.48	–60.52	–
Sn–C≡C	–904.51	–1177.51	–1175.64	–1196.64	–1194.75	–1073.64	–1223.66	–1168.0
Pb–C≡C	849.03	1674.70	1672.90	1809.68	1807.73	1505.25	1764.67	1624.5
$^1J_{\text{TIC}}$ for Me ₂ Tt(CCMe) ₂								
Si–CH ₃	–54.00	–54.64	–54.63	–54.64	–54.63	–46.08	–56.53	–
Si–C≡C	–95.88	–96.82	–96.80	–96.83	–96.81	–87.23	–100.56	–
Ge–CH ₃	–16.25	–21.13	–21.13	–21.32	–21.32	–16.94	–22.29	–
Ge–C≡C	–30.33	–35.17	–35.13	–35.30	–35.27	–30.13	–36.27	–
Sn–CH ₃	–320.52	–425.79	–425.66	–433.11	–432.99	–363.14	–440.39	–496.2
Sn–C≡C	–547.09	–590.03	–587.88	–599.35	–597.17	–550.44	–613.09	–654.6
Pb–CH ₃	276.74	469.56	469.47	508.50	508.40	373.73	491.32	574.3
Pb–C≡C	445.58	–7.38	–9.18	–5.28	–5.28	55.89	–3.40	208.0
$^1J_{\text{TIC}}$ for Me ₃ TtCCH								
Si–CH ₃	–48.12	–48.75	–48.74	–48.75	–48.74	–42.04	–51.15	–55.1
Si–C≡C	–74.51	–75.13	–75.12	–75.14	–75.12	–68.09	–77.91	–79.4
Ge–CH ₃	–16.46	–17.07	–17.07	–17.23	–17.22	–13.86	–17.66	–
Ge–C≡C	–23.08	–22.59	–22.59	–22.66	–22.66	–19.61	–23.25	–
Sn–CH ₃	–261.74	–328.72	–328.69	–319.43	–319.18	–279.85	–339.18	–303.5
Sn–C≡C	–351.81	–314.03	–313.78	–319.43	–319.18	–298.59	–326.78	–415.5
Pb–CH ₃	218.39	254.51	254.50	275.31	275.30	199.93	264.83	–
Pb–C≡C	259.34	–418.86	–419.05	–446.23	–446.43	–321.52	–440.91	–

Table 9.12: Comparison of non-relativistic and two-component results for alkynyl molecules at the PBE0 level. Dyall’s uncontracted CVTZ basis set is used for the heavy elements (Ge, Sn, Pb), whereas uncontracted cc-p(C)VTZ basis sets are employed for the light elements. The experimental values are taken from Ref. 533. $^1J_{\text{TtC}}$ (Tt = ^{29}Si , ^{73}Ge , ^{119}Sn , ^{207}Pb) coupling constants are listed in Hz. NR and Me denote the non-relativistic limit and methyl groups. All X2C and DLU-X2C calculations employ the mSNSO approach. The mean absolute error of the DLU scheme is 0.48 Hz for the finite nucleus model and 0.50 Hz for the point charge model.

Molecule	NR	Finite Nucleus		Point Charge		Exp.
		X2C	DLU	X2C	DLU	
$^1J_{\text{TtC}}$ for $\text{Tt}(\text{CCMe})_4$						
Si-C \equiv C	-123.51	-125.88	-125.86	-125.90	-125.88	-
Ge-C \equiv C	-53.31	-57.85	-57.83	-58.17	-58.14	-
Sn-C \equiv C	-889.99	-1158.58	-1156.57	-1177.39	-1175.36	-1168.0
Pb-C \equiv C	849.03	1660.61	1658.68	1794.94	1792.33	1624.5
$^1J_{\text{TtC}}$ for $\text{Me}_2\text{Tt}(\text{CCMe})_2$						
Si-CH ₃	-53.94	-54.80	-54.79	-54.81	-54.80	-
Si-C \equiv C	-95.20	-96.46	-96.46	-96.50	-96.47	-
Ge-CH ₃	-20.64	-21.79	-21.78	-21.97	-21.96	-
Ge-C \equiv C	-34.90	-36.14	-36.10	-36.29	-36.25	-
Sn-CH ₃	-331.02	-437.70	-437.56	-444.75	-444.61	-496.2
Sn-C \equiv C	-582.71	-649.27	-646.91	-659.99	-657.61	-654.6
Pb-CH ₃	301.36	524.94	524.82	566.88	566.75	574.3
Pb-C \equiv C	514.89	262.79	260.83	287.00	284.88	208.0
$^1J_{\text{TtC}}$ for Me_3TtCCH						
Si-CH ₃	-48.45	-49.10	-49.09	-49.11	-49.10	-55.1
Si-C \equiv C	-76.58	-77.31	-77.29	-77.32	-77.30	-79.4
Ge-CH ₃	-17.11	-17.80	-17.80	-17.95	-17.95	-
Ge-C \equiv C	-25.49	-25.46	-25.46	-25.55	-25.55	-
Sn-CH ₃	-275.38	-345.54	-345.40	-351.03	-350.98	-303.5
Sn-C \equiv C	-410.55	-402.22	-401.98	-409.00	-408.76	-415.5
Pb-CH ₃	244.30	309.04	308.98	334.99	334.92	-
Pb-C \equiv C	343.95	-169.59	-169.78	-179.17	-179.37	-

The quasirelativistic X2C Hamiltonian results in a good agreement with the 4c-RMB Dirac–Kohn–Sham ansatz. The coupling constants show the same trends and the deviation is typically smaller than the impact of the finite charge distribution. In contrast, ZORA does not result in such a good agreement as especially for the light elements large relative deviations are present. Also, ZORA does not accurately reproduce the coupling constants of Pb as reflected for the Pb–C \equiv C coupling constant of 55.89 Hz compared to –3.40 Hz. Compared to the experimental findings, the results for $\text{Me}_2\text{Sn}(\text{CCMe})_2$, $\text{Me}_2\text{Pb}(\text{CCMe})_2$, and Me_3SnCCH are not very convincing as the deviation is very large compared to the previous results obtained with the PBE0 functional. All magnetic properties are generally sensitive towards the molecular structure. The structures for Tab. 9.11 are optimized at the ZORA level. Considering the better agreement of the X2C and 4c Hamiltonian, the structures were reoptimized at the DLU-X2C/x2c-TZVPall-2c/PBE0 level including the dispersion correction D3.^[498] The results with these structures are given in Tab. 9.12 and the structures are provided in Ref. 431. Notably, the agreement with the experimental findings is significantly improved for all molecules—especially for the three mentioned compounds. The sign of the Pb–C \equiv C coupling constant is not predicted correctly with the ZORA-optimized structure and the deviation amounts to more than 200 Hz. Using the X2C-optimized geometry reduces this deviation to less than 60 Hz. As observed previously for NMR shifts,^[84] ZORA benefits from error cancellation in Tab. 9.11. Still, consistently using ZORA is inferior to X2C as indicated by the ZORA results in Tab. 9.11 and the X2C results in Tab. 9.12. This shows that a more sophisticated Hamiltonian than ZORA is needed for the structures of these molecules.

9.2.3 Tin Compounds

To further compare the X2C and the ZORA Hamiltonian, a set of 19 tin molecules compiled in Ref. 384 is selected. The ZORA calculations in this reference were performed with the STO TZ2P basis set^[532] and the BP86 functional.^[128,340] mSNSO DLU-X2C calculations are performed at the same structures with the x2c-TZVPPall-2c basis set^[203] and the BP86 functional (grid 4a^[482]). Moreover, the structures were reoptimized with the DLU-X2C Hamiltonian and are available in Ref. 431. DLU-X2C calculations are also carried out with the B3LYP functional^[128–130] and the x2c-QZVPall-2c basis set.^[483] COSMO^[453,454] is applied to compensate the positive or negative charge. SCF thresholds of 10^{-9} E_h and 10^{-8} a.u. for the root mean square of the density ensure well converged spinors. The CPKS equations are converged with a threshold of 10^{-6} a.u. for the residuum. To compare with, non-relativistic calculations are performed with the def2-TZVP basis set^[198] and the TZVPall bases.^[502] The results are listed in Tab. 9.13.

Generally, ZORA and DLU-X2C result in a qualitative agreement. However, some discrepancies for couplings involving hydrogen are revealed. For instance, the $^2J_{\text{SnH}}$ coupling constant of SnMe₄ is 6.74 Hz at the ZORA level and 23.45 Hz at the DLU-X2C level. ZORA severely underestimates many $^2J_{\text{SnH}}$ couplings compared to the experimental measurements.^[534–538] Furthermore, the deviation between the ZORA and the DLU-X2C results increases for the molecules containing bromine and iodine. Here, the Sn–Br coupling constants of Me₃SnBr differ by nearly 300 ppm and the deviation increases with the number of bromine atoms to 450 Hz for MeSnBr₃. A less pronounced trend is exhibited for Me₃SnI, Me₂SnI₂, and MeSnI₃. There, the deviation rises from 270 Hz to only 300 Hz.

Both ZORA and DLU-X2C do not accurately reproduce the experimental coupling constants for most molecules. Reoptimizing the structure with the more sophisticated DLU-X2C Hamiltonian is of minor importance for the agreement with the experimental data. Instead employing a larger basis set like the x2c-QZVPall-2c bases or using a hybrid functional like B3LYP has a large impact on the results. Especially the incorporation of HF exchange considerably improves the agreement with the experimental findings. The Sn–Sn coupling constant of (Me₃Sn)₂ seems to be very sensitive towards the amount of HF exchange as the result increases by 1600 Hz. Therefore, the deviation of 2000 Hz could possibly be reduced by another density functional approximation with a larger amount of HF exchange. Indeed, Becke's half and half functional, BH&HLYP, with 50% of exchange^[128,129,350] yields 5001 Hz and the range-separated functionals LC- ω PBE^[359] and ω B97X-D^[360] result in a Sn–Sn coupling constant of 4901 Hz and 3658 Hz, respectively.

The coupling constants with hydrogen atoms are notably underestimated with the chosen basis sets and the BP86 or B3LYP functional. The calculated $^2J_{\text{SnH}}$ coupling constant of SnMe₄ is 31.1 Hz with B3LYP and deviates by more than 20 Hz from the experimental result of 54.0 Hz. Based on Sec. 9.2.1, adding tight *s* functions to the basis set might improve the situation. Therefore, the x2c-QZVPall-2c-j basis set is used for SnMe₄. However, this results in a coupling constant of 33.3 Hz with the B3LYP functional. Increasing the amount of HF exchange with the BH&HLYP functional yields 58.3 Hz. Therefore, the coupling constants of these tin molecules are highly sensitive towards the admixture of HF exchange. Additionally, solvent effects may further need to be considered for a better agreement with the experimental findings.

Table 9.13: Calculated coupling constants for various Sn molecules of Ref. 384. J coupling constants are listed in Hz. ZORA results and structures are taken from Ref. 384. PC denotes the usage of the point charge model. The BP86 functional was used, and the DLU-X2C calculations use the x2c-TZVPPall-2c^[203] and the x2c-QZVPPall-2c^[483] basis sets unless explicitly noted otherwise. The prefix “x2c-” and the suffix “2c” are omitted for brevity. Experimental results are taken from the collections of Refs. 534 and 535 (in CCl_4) except for SnH_4 (Ref. 536), $(\text{Me}_3\text{Sn})_2$ (Ref. 537), SnH_3^+ , and SnH_3^- (both Ref. 538). Signs were adjusted according to the theoretical studies.

Molecule	Coupling	ZORA-optimized structures				DLU-X2C-optimized structures				Exp.
		NR	1c ZORA	2c ZORA	DLU	DLU PC	DLU	DLU QZVPPall	DLU B3LYP	
SnMe_4	$^1J_{\text{SnC}}$	-156.1	-115.93	-104.83	-133.23	-133.7	-135.7	-136.8	-255.2	-337.2
	$^2J_{\text{SnH}}$	27.3	8.45	6.74	23.45	23.5	24.6	23.1	31.1	54.0
$(\text{Me}_3\text{Sn})_2$	$^1J_{\text{SnSn}}$	1534.1	838.30	601.66	677.50	681.3	741.8	356.1	2370.3	4460
	$^1J_{\text{SnC}}$	-100.6	-31.16	-19.92	-41.92	-42.0	-45.3	-43.9	-156.9	-240
	$^2J_{\text{SnH}}$	23.8	2.97	1.07	16.55	16.6	17.5	16.3	23.6	49.5
	$^2J_{\text{SnC}}$	-30.8	-42.99	-41.46	-43.54	-43.7	-43.3	-43.7	-61.9	-56
SnH_4	$^3J_{\text{SnH}}$	-10.3	-15.90	-15.63	-16.60	-16.7	-16.6	-17.6	-16.3	-17.3
	$^1J_{\text{SnH}}$	-1211.3	-1599.63	-1549.47	-1484.28	-1489.8	-1483.9	-1662.8	-1705.5	-1930
	$^1J_{\text{SnH}}$	-1738.2	-2188.67	-2112.89	-2001.81	-2009.3	-1999.0	-2228.9	-2315.1	-2916
SnH_3^+	$^1J_{\text{SnH}}$	-60.1	26.63	81.19	221.58	222.4	205.2	183.4	105.6	109.4
SnH_3^-	$^1J_{\text{SnH}}$	-60.1	26.63	81.19	221.58	222.4	205.2	183.4	105.6	109.4
Me_3SnCl	$^1J_{\text{SnCl}}$	239.5	290.53	276.64	287.35	288.3	291.3	341.4	277.3	
	$^1J_{\text{SnC}}$	-166.0	-124.02	-112.85	-139.65	-140.2	-142.4	-148.7	-282.4	-379.7
	$^2J_{\text{SnH}}$	28.4	6.29	4.54	22.66	22.7	23.7	23.0	30.5	58.1
Me_2SnCl_2	$^1J_{\text{SnCl}}$	313.4	381.18	364.28	375.29	376.5	377.5	441.8	362.0	
	$^1J_{\text{SnC}}$	-209.8	-172.88	-162.39	-194.71	-195.5	-197.6	-212.8	-371.5	-468.4
MeSnCl_3	$^2J_{\text{SnH}}$	66.6	6.94	5.28	27.11	27.2	28.1	28.5	35.7	68.2
	$^1J_{\text{SnCl}}$	381.6	479.10	456.70	461.08	462.5	462.9	550.2	445.4	
	$^1J_{\text{SnC}}$	-324.4	-310.38	-300.50	-361.08	-362.5	-362.8	-394.5	-600.9	-693.2
SnCl_4	$^2J_{\text{SnH}}$	47.9	17.26	15.86	44.95	45.1	45.7	47.8	56.0	98.7
	$^1J_{\text{SnCl}}$	422.7	568.29	535.50	515.43	517.0	517.5	641.0	496.3	
Me_3SnBr	$^1J_{\text{SnBr}}$	1632.2	1255.87	1079.18	1372.30	1378.0	1387.1	1408.0	1411.0	
	$^1J_{\text{SnC}}$	-184.6	-113.20	-102.88	-126.57	-127.1	-129.9	-136.0	-267.6	-368.9
	$^2J_{\text{SnH}}$	31.2	5.65	3.88	21.80	21.9	22.8	22.2	29.6	57.8
Me_2SnBr_2	$^1J_{\text{SnBr}}$	1632.2	1666.69	1403.43	1756.66	1763.3	1778.2	1803.9	1823.8	
	$^1J_{\text{SnC}}$	-184.6	-145.56	-135.35	-158.86	-159.5	-161.8	-176.1	-327.5	-442.7
	$^2J_{\text{SnH}}$	31.2	4.56	2.65	23.53	23.6	24.7	25.2	31.9	66.7
MeSnBr_3	$^1J_{\text{SnBr}}$	2040.3	2085.68	1642.26	2093.04	2100.8	2118.4	2147.3	2212.7	
	$^1J_{\text{SnC}}$	-268.3	-248.27	-236.35	-275.04	-276.1	-274.9	-302.7	-487.3	-602.5
	$^2J_{\text{SnH}}$	42.4	11.22	8.98	35.11	35.2	36.4	38.7	45.2	88.5
SnBr_4	$^1J_{\text{SnBr}}$	2411.3	2442.95	1633.34	2235.30	2243.6	2265.0	2293.1	2456.0	
Me_3SnI	$^1J_{\text{SnI}}$	1656.8	1480.67	1093.32	1361.66	1373.4	1378.9	1487.6	1467.6	
	$^1J_{\text{SnC}}$	-160.9	-98.68	-88.40	-113.56	-114.0	-115.0	-120.5	-249.2	
	$^2J_{\text{SnH}}$	29.8	4.88	3.17	21.15	21.4	21.9	21.2	28.7	57.2
Me_2SnI_2	$^1J_{\text{SnI}}$	1655.8	1900.57	1262.27	1561.30	1573.9	1566.6	1710.1	1722.2	
	$^1J_{\text{SnC}}$	-160.9	-103.85	-89.42	-115.62	-116.1	-114.1	-125.7	-266.1	
	$^2J_{\text{SnH}}$	29.8	2.10	-0.15	20.47	20.5	20.4	20.7	27.4	62.4
MeSnI_3	$^1J_{\text{SnI}}$	1339.5	2261.31	1128.78	1438.36	1451.1	1401.2	1593.8	1681.7	
	$^1J_{\text{SnC}}$	-210.1	-150.76	-116.49	-154.48	-155.1	-152.6	-171.7	-325.1	
	$^2J_{\text{SnH}}$	36.7	2.84	-1.47	22.35	22.5	21.5	23.3	28.8	73.4
SnI_4	$^1J_{\text{SnI}}$	2278.8	2497.64	505.84	790.97	802.0	657.9	907.6	1149.9	
SnCl_3I	$^1J_{\text{SnCl}}$	408.5	530.35	482.23	470.51	471.9	472.2	580.7	462.9	
	$^1J_{\text{SnI}}$	2887.8	3536.61	1572.76	2287.96	2311.3	2244.0	2653.9	2712.0	
SnI_3Cl	$^1J_{\text{SnCl}}$	375.5	455.62	386.14	386.46	387.6	388.5	472.7	394.8	
	$^1J_{\text{SnI}}$	2469.2	2808.93	805.89	1207.27	1221.9	1097.5	1391.1	1057.4	

9.2.4 Application to Palladium and Platinum Complexes

To assess the accuracy of the DLU-X2C Hamiltonian for transition-metal complexes, additional investigations are performed. Here, the palladium complex $[\text{Pd}(\text{PCy}_2\text{H})_3\text{Cl}]^+$ (Cy = cyclohexyl C_6H_{11}), which is depicted in Fig. 9.3, and the platinum complex $[\text{Pt}(\text{PCy}_2\text{H})_3\text{Cl}]^+$ are studied to compare with the ZORA and 4c-RMB results of Ref. 383. Note that the optimized structure is only provided for the palladium complex in this reference. Therefore, a close comparison is only possible for this complex. Here, the same functionals and similar basis sets are employed. Therefore, the uncontracted Dyall-VDZ basis set^[189,190,495] is selected for Pd and the uncontracted cc-pVDZ basis set is used for H, C, P, and Cl.^[161,162,167,496] Furthermore, non-relativistic calculations are performed with the def2-TZVP basis sets for these elements^[198] and the TZVPalls2 bases for Pd.^[502] Moreover, calculations are performed with the x2c-TZVPall-2c basis sets^[203] and the RI-*J* approximation. The PBE^[341] and PBE0^[355] functionals are employed with a large grid (grid 4a^[482]) for the numerical integration. Positive net charges are compensated with COSMO.^[453,454] Tight SCF thresholds of $10^{-8} E_h$ and 10^{-8} a.u. for the root mean square of the density as well as a criterion of 10^{-6} a.u. for the CPKS equations ensure well converged results, which are reported in Tab. 9.14. Relativistic effects are pronounced for this complex and the Dyall-VDZ basis set is not suited for non-relativistic calculations as reflected by the large differences to the def2-TZVP/TZVPalls2 basis. The DLU-X2C Hamiltonian accurately reproduces the coupling constants of the 4c-RMB approach since the deviation for the Pd coupling constants amounts to only 15 to 20 Hz. The maximum difference is found for the $^1J_{\text{PP}}$ coupling constants of the *trans*-phosphorous atoms with about 30 Hz or 10%. Here, the ZORA Hamiltonian shows a difference of about 70 Hz. All quasirelativistic results still differ by 70 to 80 Hz from the experimental measurements.^[539]

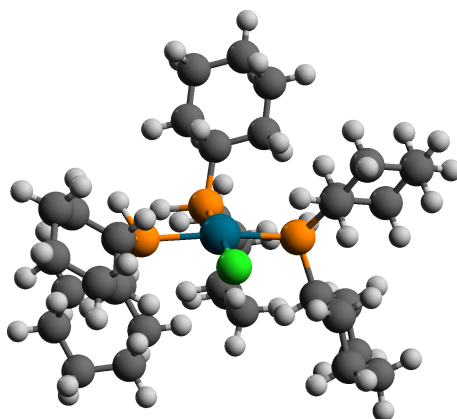


Figure 9.3: Molecular structure of $[\text{Pd}(\text{PCy}_2\text{H})_3\text{Cl}]^+$, which consists of 110 atoms. Color scheme: H white, C grey, P orange, Cl green, and Pd cyan.

Table 9.14: Coupling constants (in Hz) of $[\text{Pd}(\text{PCy}_2\text{H})_3\text{Cl}]^+$. ZORA and 4c-RMB results are taken from Ref. 383. The basis sets Dyall-VDZ/cc-pVDZ in uncontracted form, def2-TZVP/TZVPall, and x2c-TZVPall-2c are shortened to Dyall, TZVP, and TZVP-2c, respectively. Experimental results are taken from Ref. 539.

	NR		ZORA		DLU-X2C			4c-RMB		Exp.
	PBE0 Dyall	PBE0 TZVP	PBE0	PBE TZVP-2c	PBE Dyall	PBE0 TZVP-2c	PBE0 Dyall	PBE	PBE0	
$^1J_{\text{PdP}}^a$	-130.70	-119.76	-147.28	-151.37	-141.74	-167.05	-154.41	-155.65	-172.52	-
$^1J_{\text{PdP}}^b$	-191.28	-178.35	-207.32	-221.12	-219.77	-244.60	-228.80	-229.76	-243.63	-
$^1J_{\text{PH}}^a$	-18.80	264.65	268.25	222.20	247.69	263.06	270.33	251.20	280.83	355
$^1J_{\text{PH}}^b$	273.43	280.78	277.17	237.92	266.41	280.52	288.15	263.97	292.18	365
$^1J_{\text{PP}}^a$	376.13	341.95	304.48	308.68	300.46	361.77	338.39	314.18	371.15	-
$^1J_{\text{PP}}^b$	256.78	-16.01	-16.30	-14.89	-11.42	-24.79	-20.86	-13.26	-24.83	-

^aCoupling with P *trans* P

^bCoupling with P *trans* Cl

Table 9.15: Coupling constants (in Hz) of $[\text{Pd}(\text{PCy}_2\text{H})_3\text{Cl}]^+$ with various functionals and the x2c-TZVPall-2c basis set. Experimental results are taken from Ref. 539.

	BP86	PBE	TPSS	B3LYP	PBE0	TPSSh	CAM-B3LYP	Exp.
$^1J_{\text{PdP}}^a$	-145.57	-141.56	-149.36	-155.41	-152.05	-153.04	-157.94	-
$^1J_{\text{PdP}}^b$	-217.41	-212.73	-221.72	-227.95	-217.33	-223.23	-225.13	-
$^1J_{\text{PH}}^a$	257.91	248.93	295.25	282.10	275.13	303.62	282.44	355
$^1J_{\text{PH}}^b$	275.91	266.81	313.73	302.02	291.27	327.82	300.37	365
$^1J_{\text{PP}}^a$	309.16	301.07	315.61	345.05	331.87	321.41	364.70	-
$^1J_{\text{PP}}^b$	-12.87	-12.12	-12.40	-13.98	-22.40	-16.40	-21.13	-

^aCoupling with P trans P^bCoupling with P trans Cl

To reduce the gap to the experimental findings, the BP86,^[128,340] PBE,^[341] TPSS,^[346] B3LYP,^[128–130] PBE0,^[355] TPSSh,^[356] and the CAM-B3LYP^[133] functionals are considered and all structures are optimized at the x2c-TZVPall-2c/DLU-X2C level of theory. The calculations apply the RI-*J* approximation throughout and the seminumerical exchange approximation in the CPKS equations.^[311] The results in Tab. 9.15 show that the density functional approximation significantly affects the coupling constants. BP86 and PBE underestimate coupling constants by about 100 Hz, whereas a significant improvement is found for TPSS with a deviation of 60 Hz. B3LYP, CAM-B3LYP, and PBE0 perform similarly and show no notable further improvement. The best agreement is reached with the TPSSh functional, which reduces the deviation to 40–50 Hz.

The coupling constants of $[\text{Pt}(\text{PCy}_2\text{H})_3\text{Cl}]^+$ are calculated with the same computational protocol and presented in Tab. 9.16 together with the ZORA and 4c-RMB results of Ref. 383. Considering the PBE and PBE0 functional, the DLU-X2C Hamiltonian performs similar to the 4c-RMB Hamiltonian and shows a significantly smaller deviation to the experimental measurements than the ZORA approach. Note that both the ZORA and DLU-X2C results are obtained with the structure optimized at the same level of theory. Among the “pure” density functionals, TPSS performs best and shows notably larger coupling constants than BP86 and PBE. Overall, CAM-B3LYP performs best for the Pt–P couplings and the TPSSh functional performs best for the P–H couplings. The experimental trends and findings are reasonably accurate reproduced with the TPSSh and CAM-B3LYP functional.

Table 9.16: Coupling constants (in Hz) of $[\text{Pt}(\text{PCy}_2\text{H})_3\text{Cl}]^+$ with various functionals and the x2c-TZVPall-2c basis set for the DLU-X2C calculations. ZORA and 4c-RMB results (Dyall-VDZ) are taken from Ref. 383. Experimental results are taken from Ref. 539.

	DLU-X2C							ZORA	4c-RMB		Exp.
	BP86	PBE	TPSS	B3LYP	PBE0	TPSSh	CAM-B3LYP	PBE0	PBE	PBE0	
$^1J_{\text{PtP}}^a$	1589.15	1552.31	1693.37	1837.18	1809.70	1789.56	1921.08	1649.31	1665.56	2024.08	2215
$^1J_{\text{PtP}}^b$	2630.40	2571.01	2764.58	2908.47	2779.67	2831.83	2932.29	2543.61	2749.93	3088.32	3162
$^1J_{\text{PH}}^a$	274.92	265.65	312.59	299.01	290.81	320.95	297.27	285.34	269.34	298.55	357
$^1J_{\text{PH}}^b$	293.93	313.73	331.57	319.51	304.64	336.58	315.93	294.19	282.38	309.61	391
$^1J_{\text{PP}}^a$	274.17	267.87	284.54	295.33	281.63	289.37	296.89	266.48	282.89	319.43	-
$^1J_{\text{PP}}^b$	-7.91	-6.80	-9.39	-11.44	-16.77	-13.00	-17.00	-11.41	-7.44	-17.73	-

^aCoupling with P trans P^bCoupling with P trans Cl

9.2.5 Demonstration of Efficiency

The low-valent tin complex $[(\{\text{SIDipp}\}\text{P})_2\text{Sn}]$ (SIDipp = 1,3-bis(2,6-di-isopropylphenyl)-imidazolidin-2-ylidene) is chosen to illustrate the efficiency of the quasirelativistic DLU-X2C approach. The chemical properties of this complex will be studied in detail in chapter 11. This compound is depicted in Fig. 9.4 and consists of 137 atoms. The x2c-TZVPall-2c basis set^[203] and auxiliary basis^[203] for the RI- J approximation are selected, consisting of 2,408 contracted basis functions and 3,616 primitive basis functions. Moreover, the BP86,^[128,340] PBE,^[341] TPSS,^[346] B3LYP,^[128–130] PBE0,^[355] TPSSh,^[356] CAM-B3LYP,^[133,529,530] LH07t-SVWN,^[138] LH12ct-SsirPW92,^[139] LHF14,^[141] and the PSTS functional in conventional gauge^[134] combined with large integration grids^[482] (grid 4a for the conventional functionals and grid 3a for the LHF) were selected to consider the impact of the density functional approximations on the computational demands. The structures of the first six functionals are taken from Ref. 540 and the structure of the CAM-B3LYP functional is also optimized at the corresponding level of theory. For the PSTS functional, the structure of TPSSh is utilized and the other LHF calculations are carried out with the B3LYP-optimized structure. Tight SCF thresholds of $10^{-9} E_h$ and 10^{-8} a.u. for the root mean square of the density are applied and the CPKS equations are converged up to 10^{-6} a.u. for the norm of the residuum. The coupling constants are shown in Tab. 9.17 and the wall times are listed in Tab. 9.18.

Already, the “pure” density functional results are in good agreement with the experimental findings. The results range from 1342 Hz to 1410 Hz and the experimental measurements in benzene yield a coupling constant of 1334 Hz.^[540] COSMO^[453,454] is applied to treat the solvent effects with a relative permittivity of $\epsilon = 2.3$. At the BP86 level, this yields 1405 Hz and thus only changes the coupling constant of 1387 Hz without COSMO by 18 Hz. Calculations were further carried out with the x2c-TZVPall-s and the x2c-QZVPall-2c-s basis set. This results in a coupling constant of 1362 Hz and 1470 Hz. Note that the DLU error is insignificant again as the full X2C Hamiltonian yields 1387 Hz at the BP86/x2c-TZVPall-2c level of theory. Hybrid functionals increase the coupling constants of the parent GGA and meta-GGA functionals. Incorporating HF exchange increases the Sn–P coupling by 60 Hz for the PBE and PBE0 functional. For TPSS and TPSSh, only a minor increase is present. This is rationalized by the small amount of HF exchange for the TPSSh functional. Range-separation further increases the coupling constant and leads to a serious overestimate for CAM-B3LYP. The t-LMF based LHF perform solid for this molecule as reflected by couplings of 1439–1442 Hz for LH07t-SVWN and 1348–1351 Hz for LH12ct-SsirPW92. Similar to B3LYP and CAM-B3LYP, the LHF14 functional considerably overestimates the coupling constant by about 200 Hz. Only a minor improvement is found for PSTS compared to the parent TPSS and TPSSh functionals. Both the mSNSO approximation and the finite nucleus model only result in minor changes of the coupling constants.

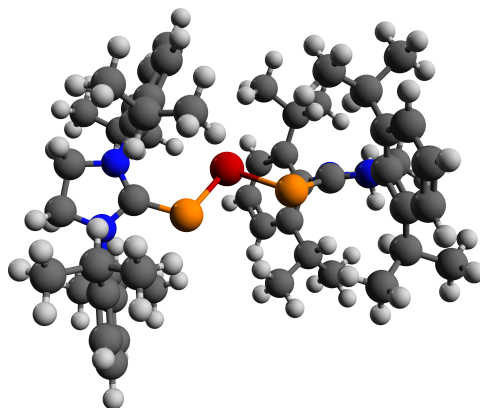


Figure 9.4: Molecular structure of $[(\{\text{SIDipp}\}\text{P})_2\text{Sn}]$ (SIDipp = 1,3-bis(2,6-di-isopropylphenyl)-imidazolidin-2-ylidene). The molecule consists of 137 atoms. Color scheme: H white, C grey, N blue, P orange, and Sn red.

Table 9.17: Results for $^1J_{\text{SnP}}$ (^{119}Sn , ^{31}P) coupling constants in Hz of the low-valent Sn phosphinidenide complex, $[(\text{SIDipp})\text{P}]_2\text{Sn}$ (SIDipp = 1,3-bis(2,6-di-isopropylphenyl)-imidazolidin-2-ylidene). The experimental result is 1334 Hz. ^[540] Structures are mainly taken from Ref. 540. Except for the LHF, the structures are optimized with the corresponding density functional approximation. For LH07t-SVWN, LH12ct-SsirPW92, LHJ14, and PSTS, we use the structure optimized with the B3LYP and the TPSSh functional. Large grids (grid 4a) are employed for the numerical integration of the exchange-correlation terms except for the LHF which utilize medium-sized grids (grid 3a). The x2c-TZVPall-2c basis set is chosen and the RI- J approximation is used in the SCF procedure with the corresponding auxiliary basis sets. Analytical HF exchange integrals are employed. The two calculated $^1J_{\text{SnP}}$ constants are averaged to compare with the experimental results.

Functional	Finite Nucleus		Point Charge	
	DLU	mSNSO-DLU	DLU	mSNSO-DLU
BP86	1387	1388	1390	1391
PBE	1342	1343	1345	1346
TPSS	1406	1407	1410	1407
B3LYP	1496	1498	1500	1498
PBE0	1401	1403	1405	1406
TPSSh	1422	1423	1426	1426
CAM-B3LYP	1540	1542	1543	1546
LH07t-SVWN	1439	1440	1440	1442
LH12ct-SsirPW92	1348	1349	1351	1351
LHJ14	1535	1536	1538	1539
PSTS	1399	1400	1402	1403

The results in this section show that the DLU-X2C Hamiltonian accurately treats relativistic effects. In contrast to the parent 4c approaches, the DLU-X2C Hamiltonian is applicable to extended molecular systems at reasonable computational costs as revealed by the wall times in Tab. 9.18. Here, timings are measured on 12 OpenMP threads of a CPU of type Intel® Xeon® Gold 6212U CPU @ 2.40 GHz. The wall time of the DLU-X2C Hamiltonian is only 4 minutes. The second-order derivative of the energy, i.e. the DSO term, takes 3 minutes whereas the derivatives for the RHS amount to 1 minute only. So, the wall time is always dominated by the two-electron integrals. The calculation with the BP86 functional takes 48 minutes in total and the XC kernel is the most time-consuming step with 40 minutes or 84 % of the computation time. This does not hold for the full X2C Hamiltonian. Here, the BP86 calculations requires more than 4 hours. The derivatives of the X2C Hamiltonian take 24 % and 72 % of the wall time. Therefore, the DLU-X2C Hamiltonian is of crucial importance for the efficiency of the quasirelativistic DFT approach.

Furthermore, it should be noted that the number of CPKS equations is small compared to the number of SCF iterations. BP86 requires 88 SCF iterations but only 6 CPKS iterations. Consequently, the SCF procedure can be more demanding than the calculation of the SSCCs for the efficient GGA and meta-GGA functionals. Matters are different for hybrid density functionals as the exchange integrals of the CPKS iterations are dominating the computation times. The SCF calculation of the B3LYP functional takes less than 10 hours (115 SCF iterations), whereas the SSCC calculation amounts to 1 day 21 hours and 9 minutes (8 CPKS iterations). The exchange integrals take 98 % of the total wall time. Similar timings are obtained for the other hybrid density functionals like PBE0 and TPSSh. The range-separated CAM-B3LYP functional requires 11 CPKS iterations and the calculation is the most time-consuming taking nearly 3 days. These wall times can be significantly reduced by the application of the seminumerical exchange approximation to the CPKS equations. Limiting the approximation to the CPKS equations allows to use a very small integration grid (grid -1) without loss of accuracy. This reduces the wall times to a range of 5.5 to 10 hours without altering the couplings by more than 1 Hz. The exchange integrals still dominate the wall times by requiring more than 70 % of the total time.

Table 9.18: Wall times and iterations for the ground-state density and the two Sn–P coupling constants with the DLU-X2C Hamiltonian in the finite nucleus model on a CPU of type Intel® Xeon® Gold 6212U CPU @ 2.40 GHz using 12 OpenMP threads. The code was compiled with Intel® Fortran Compiler 19.0.1.144. Timings are listed in minutes. Initial orbitals are generated with the extended Hückel method. The RI- J approximation is employed for the SCF procedure. LHF’s evaluate the XC and the HF exchange contribution simultaneously. Therefore, no separate timings are listed for the HF exchange part. The difference of the three steps to the total wall time of the SSCCs can be attributed to the transformation of the integrals and the density response into the spinor basis as part of the generalized (block) conjugate gradient or Davidson solver. Note that LHF’s use a medium-sized grid (3a) whereas all other functionals employ large grids (4a). This significantly improves the SCF convergence of the LHF’s. Upon application of the seminumerical exchange approximation for the CPKS equations, the computation times for the SSCCs of the hybrid functionals are reduced to 323 minutes (B3LYP), 339 minutes (PBE0), 596 minutes (TPSSh), and 454 minutes (CAM-B3LYP).

Functional	SCF		SSCCs				
	Iter.	Total Time	Iter.	1e Part	Exchange	XC Kernel	Total Time
BP86	88	88	6	4	–	43	50
PBE	97	96	6	4	–	38	44
TPSS	94	100	7	4	–	190	199
B3LYP	115	591	8	4	2650	49	2709
PBE0	132	744	9	4	3227	59	3297
TPSSh	128	627	8	4	2842	220	3072
CAM-B3LYP	110	777	11	4	4237	69	4318
LH07t-SVWN	75	2591	8	4	–	2140	2150
LH12ct-SsirPW92	65	2256	8	4	–	2237	2247
LHJ14	71	2478	9	4	–	2634	2645
PSTS	81	2888	8	4	–	2288	2298

The described multigrid approach for the XC kernel and the seminumerical approximation is only applicable to the global and range-separated hybrid density functionals in a straightforward manner. Therefore, the LHF are more demanding as shown by wall times of 35.8 and 44.1 hours. The SCF calculations are more demanding than the SSCC calculations due to the required integration bounds for numerical stability. Compared to the previous implementation in TURBOMOLE V7.5,^[294,305,311,315,363] the bounds and numerical thresholds were tightened by two orders of magnitude to ensure a smooth convergence. The previous settings required more than 5 days for the SCF iterations to converge and the total number of SCF calculations was 223 for LH07t-SVWN. This shows that LHF’s are numerically cumbersome and the efficiency is notably decreased compared to the parent global hybrid functionals, which allow for a more efficient application of the seminumerical exchange approximation. Furthermore, the timings clearly show that the calculations of the two Sn–P coupling constants is less demanding than the SCF calculations for the “pure” density functionals. For hybrid functionals, the SSCC calculations are not significantly more costly than the SCF calculations. Therefore, SSCC calculations are possible for large molecules and the most time-consuming step of a standard quantum chemical protocol is the optimization of the structure, which requires multiple SCF and gradient calculations.

10 Assessment of the Accuracy of Density Functional Approximations

The impact of the density functional approximation is assessed for NMR coupling constants and shifts in comparison to high-level coupled-cluster theory and experimental findings. The “pure” density functionals BP86,^[128,340] PBE,^[341] KT3,^[342,501] and TPSS^[346] are included. Hybrid density functional approximations considered in the benchmark calculations are BH&HLYP,^[128,129,350] B3LYP,^[128–130] PBE0,^[355] and TPSSH.^[356] The range-separated hybrid density functionals LC- ω PBE,^[359,529,530] ω B97X-D,^[360,529,530] CAM-B3LYP,^[133,529,530] CAM-QTP-00,^[361,529,530] and CAM-QTP-02^[362,529,530] are further included. LHF s are represented by LH07t-SVWN,^[138] LH12ct-SsirPW92,^[139] LH14t-calPBE,^[140] LH20t,^[370] LHJ14,^[141] and the PSTS functional in conventional gauge.^[134] The LHJ14 and the PSTS functionals are applied to NMR properties for the first time. Note that the a_1 -only variant of PSTS is used as only closed-shell systems are studied. The large number of functionals allows for a broad and comprehensive overview. All calculations employ a large grid^[294,315,482] (grid 4 in non-relativistic approaches and grid 4a in X2C calculations) for the numerical integration of the exchange-correlation contributions. Coupling constants are calculated with and without the paramagnetic current density to generalize the kinetic energy density, τ , for meta-GGA-based functionals and LHF s. For NMR shieldings and shifts, both generalizations described in chapter 7 are applied; the generalization with the external magnetic field^[461] and the paramagnetic current density.^[458–460,462] The latter is denoted by a “c” at the beginning of the functional name throughout this chapter. The NMR shifts of LH14t-calPBE and LH20t are obtained by neglecting the derivatives with respect to the magnetic field of the calibration function. Cartesian coordinates of the optimized structures and all individual results are listed in the supporting information of Ref. 365.

The existing LHF implementations of the NMR properties^[415,432,467] were reworked to increase the efficiency. The guidelines for the memory handling described in Ref. 223 were considered to reduce the memory demands for large molecules. Furthermore, the gradient routines implemented in Ref. 364 were reworked to support a shared memory parallelization with OpenMP and Fork-SMP.^[541] This allows for structure optimizations of midsize or large molecules. Moreover, the integral screening methods discussed in Ref. 311 were implemented together with Christof Holzer for all LHF routines. This replaces the previous screening based on junctions^[304] with a more robust screening based on the Schwarz inequality combined with a suitable aliasing and dealiasing scheme. This scheme leads to a smooth SCF convergence for diffuse basis sets and also reduces the overall scaling of local hybrid functional calculations from $\mathcal{O}(N^3)$ to $\mathcal{O}(N^2)$ or even lower, where N measures the size of the system.

10.1 NMR Indirect Spin–Spin Coupling Constants

NMR coupling constants are calculated for a small test set of 13 molecules consisting of CO, H₂O, OHF, OF₂, HCN, FCN, HCCH, FCCH, FCCF, FNO, H₂CO, HFCO, and F₂CO with 45 spin–spin coupling constants. The DFT results are compared to the CC3 calculations of Ref. 116. Based on the large impact of the basis set in the previous chapter, CC benchmark values are essential for a meaningful assessment of the density functional itself. However, no such benchmark values are available for a heavy element test set and tailored basis sets are only available for the light elements.^[531,542] Consequently, the NMR coupling studies in this chapter are restricted to light elements. Here, the same computational protocol as for the CC3 results is applied. Structures were optimized with the aug-cc-pVQZ basis set^[161,164,496,520] at each level of theory. The optimized structures are available in Ref. 365. NMR coupling constants are then obtained with the aug-ccJ-pVTZ basis set, which is constructed by augmenting the ccJ-pVTZ^[542] bases from the Basis Set Exchange library^[487,488] with the functions of Ref. 520. Tight SCF thresholds of 10⁻⁹ E_h and 10⁻⁹ a.u. for the root mean square of the density matrix as well as a CPKS threshold of 10⁻⁶ a.u. ensure that all results are well converged. The statistical evaluation of the results is presented in Tab. 10.1. A mean absolute percent-wise error (MAPE) is used for the analysis as the coupling constants are within a range of 1500 Hz.

The “pure” density functional approximations result in large errors for the coupling constants. The errors amount to about 40 % for the ¹*J* couplings and to 40–50 % for the ²*J* and ³*J* coupling constants. TPSS does not significantly improve the agreement compared to the GGA functionals. The corresponding hybrid functional TPSSh also does not considerably change the errors. For the ¹*J* couplings, the error is reduced from 38.20 % to 29.30 % and the respective error of the ²*J* or ³*J* coupling is reduced to 29.40 %. The GGA hybrid functionals result in a much better agreement with the CC3 results. Here, the errors are about 20 % (¹*J*) and 25 % (^{2/3}*J*). Note that the unfavorable performance of TPSSh can be mainly attributed to the couplings involving fluorine and oxygen. The impact of the current density is small as it only affects the PSO term of meta-GGAs and the corresponding hybrid functionals. The respective one-electron integrals are purely imaginary and antisymmetric. Therefore, the magnetic XC kernel requires an iterative procedure for the PSO term. For the studied molecules, 2 CPKS equations are needed. The FC and the SD terms are symmetric and the contribution of the antisymmetric magnetic XC kernel vanishes like for electric polarizabilities. The FC term is the dominant term for the studied molecules and the PSO term is comparably small.^[116] Nevertheless, the current-dependent generalization of τ restores the iso-orbital constraint in DFT.

Range-separated hybrid functionals like ω B97X-D and CAM-QTP-02 outperform the global hybrid functionals for the ¹*J* coupling constants. In contrast to the latter, ω B97X-D is also able to deliver very accurate ²*J* and ³*J* coupling constants with a significantly decreased standard deviation indicating that no outliers are present. A position-dependent admixture of Hartree–Fock exchange in LHF_s does not result in a consistent improvement. The t-LMF based functionals LH07t-SVWN, LH14t-calPBE, and LH20t yield smaller errors than PBE0 and LH20t slightly improves upon ω B97X-D for the ¹*J* coupling constants. However, these functionals show larger deviations for the ²*J* and ³*J* couplings than ω B97X-D. Other local hybrid functionals such as LH12ct-SsirPW92 and LHJ14 show no remarkable improvement as the deviations are larger than for B3LYP. Furthermore, PSTS does not improve upon the parent TPSS and TPSSh functionals and leads to errors of more than 100 % for F₂CO and OHF. In contrast, the errors rise for ¹*J* couplings and only a minor decrease is exhibited for the other couplings. Also, the current-dependent generalization of τ does not notably change the results for the t-LMF-based functionals, which control the amount of HF exchange with the iso-orbital indicator. Instead, the maximum change is found for PSTS (¹*J*) and LHJ14 (^{2/3}*J*). The generalization of the kinetic energy density does not increase the computational costs for the local hybrid functionals as the calculation of HF exchange contribution is more demanding. Therefore,

Table 10.1: Mean absolute percent-wise error (MAPE) and respective standard deviation (STD) for a the spin-spin coupling constants of CO, H₂O, OHF, OF₂, HCN, FCN, HCCH, FCCH, FCCF, FNO, H₂CO, HFCO, and F₂CO. CC3 results serve as reference herein.^[116] Coupling constants with an absolute value below 7 Hz are neglected in the statistical evaluation. A “c” at the beginning of the functional name indicates that the current-dependent correction for the kinetic energy density is used. The aug-ccJ-pVTZ basis set is employed. Individual coupling constants are given in Ref. 365.

	¹ <i>J</i>		^{2/3} <i>J</i>	
	MAPE	STD	MAPE	STD
KT3	43.38	49.35	48.25	49.81
BP86	44.44	47.52	45.69	55.44
PBE	40.60	44.17	43.89	47.11
TPSS	38.20	36.75	39.11	39.62
cTPSS	39.01	36.75	39.11	40.12
BH&HLYP	23.92	22.51	25.56	24.90
B3LYP	23.76	17.58	26.23	25.47
PBE0	19.48	17.40	23.98	23.83
TPSSh	29.30	26.54	29.40	30.89
cTPSSh	30.10	26.43	31.22	31.25
LC- ω PBE	19.97	19.20	27.77	22.85
ω B97X-D	14.81	12.35	18.50	15.31
CAM-B3LYP	18.58	11.50	26.35	19.03
CAM-QTP-00	27.07	31.13	38.01	41.16
CAM-QTP-02	15.20	15.93	24.64	19.86
LH07t-SVWN	18.94	20.79	19.44	22.90
cLH07t-SVWN	19.04	20.85	19.86	22.94
LH12ct-SsirPW92	25.16	24.06	29.64	27.98
cLH12ct-SsirPW92	25.16	24.09	29.68	27.93
LH14t-calPBE	17.34	16.00	19.57	19.33
cLH14t-calPBE	17.39	16.00	19.73	19.28
LH20t	13.43	12.46	22.48	18.38
cLH20t	13.32	12.31	21.83	18.00
PSTS	31.07	29.80	30.41	33.64
cPSTS	34.51	33.78	31.31	36.06
LHJ14	24.47	23.27	31.67	30.27
cLHJ14	23.16	22.96	29.54	29.23

the current-dependent generalization of the kinetic energy density is the default choice and ensures a gauge invariant formalism.

To conclude, most local hybrid functionals based on the t-LMF sufficiently reproduce the coupling constants of the high-level CC3 model. The recently developed LH20t functional performs best for the ¹*J* coupling constants whereas LH07t-SVWN and LH14t-calPBE yield smaller errors for the ^{2/3}*J* couplings. On the contrary, the LH12ct-SsirPW92 functional is outperformed by all global GGA hybrid functionals. TPSS, TPSSh, and PSTS are not suited for the coupling constants in this test set and PSTS even leads to a deterioration compared to the parent TPSSh functional. For the studied molecules, the range-separated functionals tend to perform best. Overall, ω B97X-D shows the smallest deviation to the approximate coupled-cluster CC3 results.

10.2 NMR Shieldings and Shifts

The NMR shieldings and shifts are studied for both light and heavy elements. For the light elements, the DFT results are assessed with CCSD(T) results.^[310,543] The first test set of Stoychev and co-workers^[310] considers the NMR shielding constants of H, C, N, O, F, and P, whereas the test set of Flaig *et al.*^[543] considers the ¹H and ¹³C NMR shifts. Here, the same geometries and basis sets as in the coupled-cluster calculations are used making the results strictly comparable and ensure that only the impact of the density functional approximations for NMR shieldings and shifts without any other effects is assessed.

Furthermore, the ¹⁷O NMR shifts of the transition-metal oxo compounds,^[380,381] the ¹²⁹Xe shifts of the xenon fluorides,^[499] and the ¹⁸³W shifts of the tungsten compounds^[382] of Sec. 9.1 are studied with the functionals described in the previous subsection. Here, the experimental findings serve as reference and the NMR-tailored x2c-TZVPall-s basis sets are used throughout to allow for a meaningful comparison. Moreover, the structures are optimized at each level of theory for this purpose. The optimized structures are provided in the supporting information of Ref. 365. All results are statistically evaluated with the mean absolute error, mean signed error, and the respective standard deviation.

10.2.1 NMR Shielding Constants of Organic Compounds

The NMR shieldings of CH₄, (CH₃)₂CO, furan, CO, CF₄, HF, H₂O, OF₂, F₂, NH₃, N₂, N₂O, PN, PH₃, and PF₃ are calculated with the original pcSseg-4 basis set and compared to the CCSD(T) results.^[310] SCF thresholds of 10⁻⁹ E_h and 10⁻⁹ a.u. for the root mean square of the density matrix ensure well converged MOs. The norm of the residuum in the CPKS equations^[416] is required to be less than 10⁻⁷ a.u. to ensure converged NMR shielding constants. Due to the range of the shieldings, the results are separately evaluated for H, C, and the group of N, O, F, and P shielding constants.

The results for the H shieldings are presented in Fig. 10.1. Here, HF and the “pure” density functional approximations lead to comparably large errors of more than 0.3 ppm. The GGA global hybrid functionals reduce these errors to about 0.1–0.2 ppm and the standard deviation is reduced in a similar way. Again, some range-separated functionals worsen the results and the errors are in the same range as those of the GGA functionals while CAM-B3LYP and CAM-QTP-00 perform remarkably well. Most LHF do not result in a notable improvement for the shielding constants of hydrogen. LH07t-SVWN, LH12ct-SsirPW92, PSTS, and LHJ14 show rather large errors. Yet, the smallest MAE is found for LH14t-calPBE with 0.11 ppm.

The C shieldings in Fig. 10.2 reveal a different picture. The KT3 functional performs best (MAE = 6.27 ppm) and the global hybrid functionals are no significant improvement compared to the parent GGA and meta-GGA functionals. Instead, range-separated hybrids consistently reduce the errors compared to the global hybrids. Among the LHF, the LH12ct-SsirPW92 functional performs best with a mean absolute error of 7.36 ppm.

The errors for N, O, F, and P are presented in Fig. 10.3. BP86, PBE, and TPSS show errors in the range of 30 to 50 ppm whereas the NMR-optimized KT3 functional again yields a very small mean absolute error of 23.80 ppm. Conventional hybrid functionals only result in minor changes for the parent PBE and TPSS functional. Range-separated functionals yield errors in the same range as KT3, however, the standard deviation rises. ωB97X-D shows a MAE of 20.45 ppm only while the MSD amounts to -44.50 ppm. The t-LMF functionals perform similarly. LH12ct-SsirPW92 features the smallest MAE of 20.45 ppm and a MSD of -12.11 ppm. PSTS slightly reduces the errors of TPSS and TPSSh, whereas LHJ14 does not yield accurate shielding constants and shows the largest mean absolute error of all functionals with 59.24 ppm.

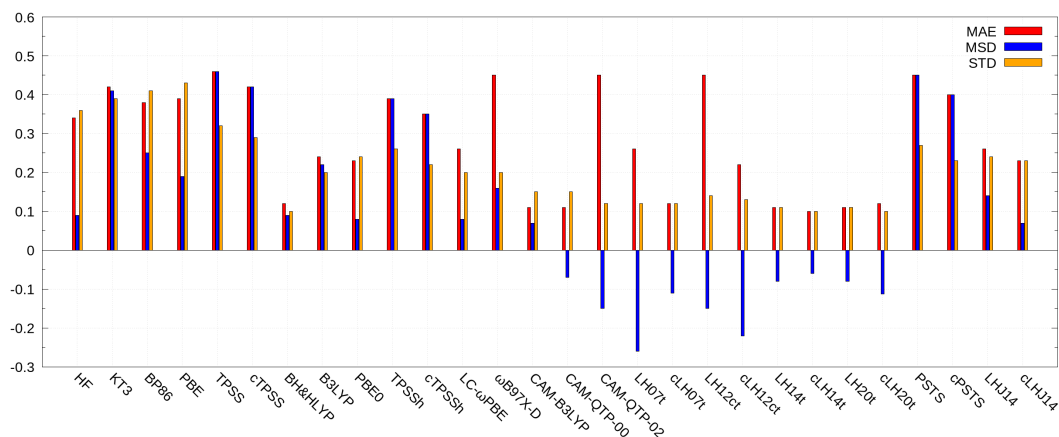


Figure 10.1: Comparison of various functionals for ^1H NMR shieldings in ppm. Errors are measured with respect to pcSseg-4/CCSD(T).^[310] LH07t, LH12ct, and LH14t refer to the functionals LH07t-SVWN, LH12ct-SsirPW92, and LH14t-calPBE, respectively. The inclusion of the current density to restore gauge-origin invariance instead of the external vector potential in the generalized kinetic energy density is denoted by a “c” at the beginning of the functional name. MAE, MSD, and STD denote the mean absolute error, mean signed error, and the standard deviation regarding the latter.

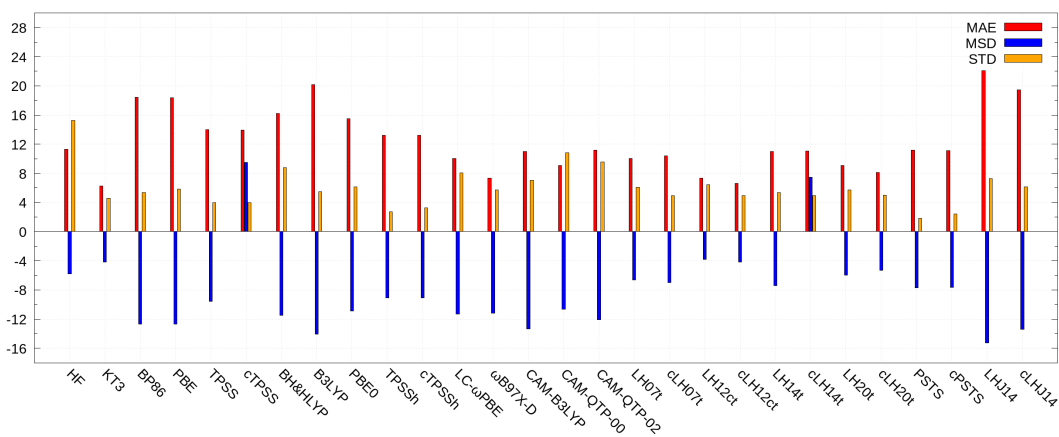


Figure 10.2: Comparison of various functionals for ^{13}C NMR shieldings in ppm.

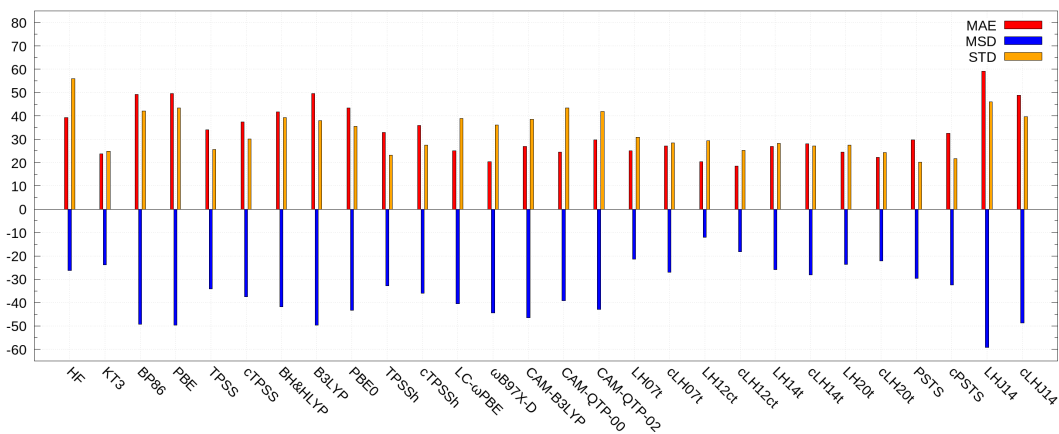


Figure 10.3: Comparison of various functionals for ^{15}N , ^{17}O , ^{19}F , and ^{31}P NMR shieldings.

The current-density formalism for the generalized kinetic energy density, τ , results in a notable improvement for the shieldings of almost all τ -dependent functionals. The comparably large error of LH12ct-SsirPW92 for H shieldings is halved to 0.22 ppm. This confirms the previous findings for LH12ct-SsirPW92 and this test set^[415,467] compared to a broader selection of functionals. For LH14t-calPBE and LH20t, the good performance for H shieldings is preserved. Also, the errors of the meta-GGA based global and local hybrid functionals are consistently reduced. The current-density formalism does not sufficiently improve the NMR shieldings of LHJ14. Considering the cost–balance ratio, the semi-empirical GGA functional KT3 is a solid choice for the shielding constants of these molecules as it yields similar errors as the current-dependent LH12ct-SsirPW92 functional at a fraction of the computational costs.

10.2.2 ^1H and ^{13}C NMR Shifts of Organic Compounds

The ^1H and ^{13}C NMR shifts are calculated for a larger set of 29 organic compounds with respect to tetramethylsilane (TMS, SiMe_4). Here, the def2-TZVP basis set is selected and all other computational parameters are unchanged compared to the previous subsection. The results are depicted in Fig. 10.4 and Fig. 10.5. Here, the non-empirical GGA functionals show large errors for the ^1H shifts. BP86 (MAE = 0.20 ppm) and PBE (MAE = 0.22 ppm) show larger deviations than HF (MAE = 0.17 ppm). The errors are significantly reduced with the TPSS functional. For instance, the MAE is 0.15 ppm and the performance is on par with KT3. The latter yields a reduced MSD but a larger standard deviation. Global hybrid and range-separated functionals improve upon the underlying GGA functionals with MAEs between 0.14 ppm and 0.18 ppm. Range-separation does not notably affect the NMR shifts and the BH&HLYP functionals yields the smallest errors with an MAE of 0.14 ppm and a MSD of 0.13 ppm. The small amount of HF exchange in the TPSSh functional results in similar errors like TPSS. TPSS, TPSSh, and BH&HLYP perform best among the conventional functionals. Most t-LMF functionals tend to reduce the error with LH12ct-SsirPW92 being an exception as it increases the errors compared to BH&HLYP. The highly parameterized LH20t functional shows the smallest errors and performs best for ^1H shifts. PSTS shows the same MAE of 0.11 ppm but a significantly larger standard deviation. Again, LHJ14 yields relatively large absolute errors and a large standard deviation. The maximum error is found for H_2CO with 0.85 ppm. Still, the MAE of all hybrid functionals is below 0.20 ppm.

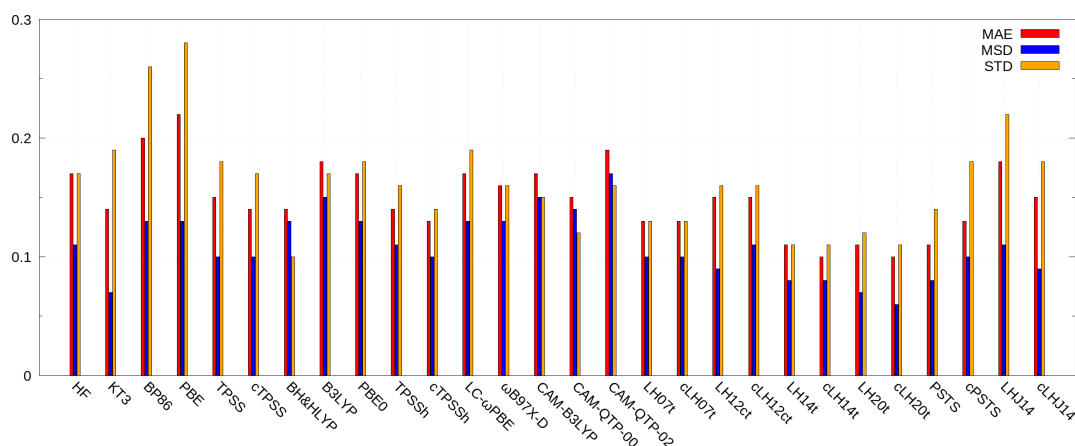


Figure 10.4: Comparison of various functionals for ^1H NMR shifts (in ppm) with respect to the def2-TZVP/CCSD(T) level.^[543] TMS was chosen as reference for the chemical shifts. The inclusion of the current density to restore gauge-origin invariance instead of the external vector potential in the generalized kinetic energy density is denoted by a “c” at the beginning of the functional name. The suffix of the t-LMF based functionals is omitted for brevity.

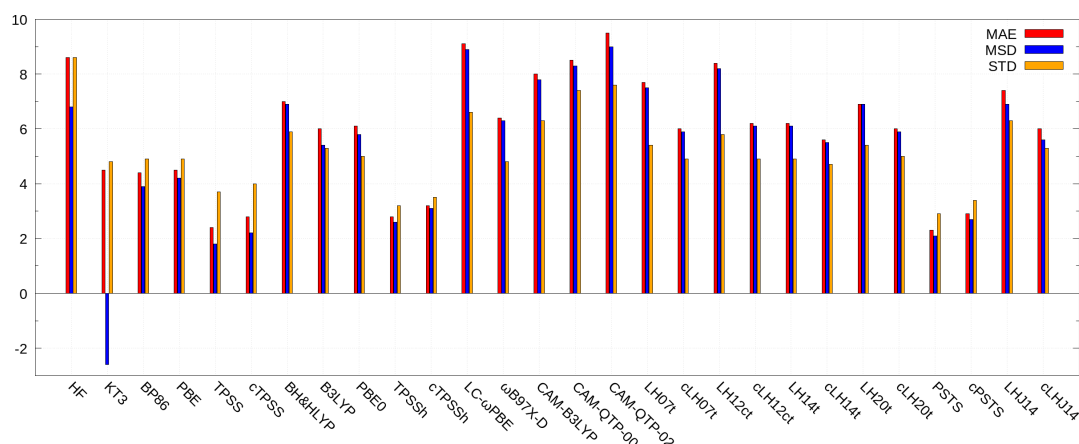


Figure 10.5: Comparison of various functionals for ^{13}C NMR shifts (in ppm) with respect to the def2-TZVP/CCSD(T) level.^[543] TMS was chosen as reference for the chemical shifts.

For the ^{13}C NMR shifts, the GGA functionals perform remarkably well with an error of about 5 ppm. Here, the corresponding hybrid functionals lead to a deterioration with MAEs of 6 to 7 ppm. Range-separated hybrids such as LC- ω PBE and CAM-B3LYP further increase the error to 9 ppm. In contrast, the incorporation of τ by TPSS and TPSSH improves upon the GGA density functional approximations. The errors are about 2 ppm for TPSS. The t-LMF functionals lead to similar results like the global hybrid functionals with errors above 6 ppm. LHI14 performs on par with these functionals. Due to the underlying TPSS form, the PSTS functional features the best agreement with the coupled-cluster data among the LHF. Note that all functionals except for KT3 show a positive mean signed deviation. KT3 features a negative MSD just like the preceding KT2 functional in Ref. 543. Based on the excellent agreement of TPSS with the CCSD(T) reference, the Laplacian or the kinetic energy density is of major importance for accurate ^1H and ^{13}C NMR shifts. This is also confirmed by the impact of the choice for the generalization of τ . Overall, the current-density dependent form results in smaller errors for the t-LMF and z-LMF based LHF. Matters are different for TPSS, TPSSH, and PSTS, for which the error is increased when using the paramagnetic current density instead of the external magnetic field to restore the gauge-origin invariance of τ . The improvement for the t-LMFs is rationalized by the preserved iso-orbital constraint of the current-dependent generalization.

10.2.3 NMR Shifts of Transition-Metal Oxo Compounds

As a transition to the NMR shifts of heavy nuclei, the ^{17}O NMR shifts of CrO_4^{2-} , MoO_4^{2-} , WO_4^{2-} , MnO_4^- , TcO_4^- , ReO_4^- , FeO_4 , RuO_4 , and OsO_4 are studied at the DLU-X2C/x2c-TZVPall-s level of theory. Structures are optimized at each level of theory and COSMO^[453,454] is applied to all charged molecules. A SCF threshold of $10^{-9} E_h$ is chosen and the norm of the residuum is converged to 10^{-7} a.u. in the NMR calculations. The NMR shifts are obtained with H_2O as reference. For a comparison, the experimental shifts^[510] are converted to a more suitable scale^[380,381] with the vapor-liquid shift of H_2O . According to these references, solvent effects may amount to roughly 20–30 ppm. The results are depicted in Fig. 10.6. HF is omitted as the errors are larger than 200 ppm and electron correlation clearly needs to be treated.

First, the “pure” density functional approximations show mean absolute errors between 50 ppm and 80 ppm and mean signed errors in the same order of magnitude. In contrast to the organic compounds, TPSS does not result in an improvement compared to BP86 or PBE. Instead, these perform better than TPSS for the transition-metal compounds investigated herein. As expected, KT3 loses some ground compared to the previous studies as KT3 was designed for the NMR shifts of light main-group compounds.

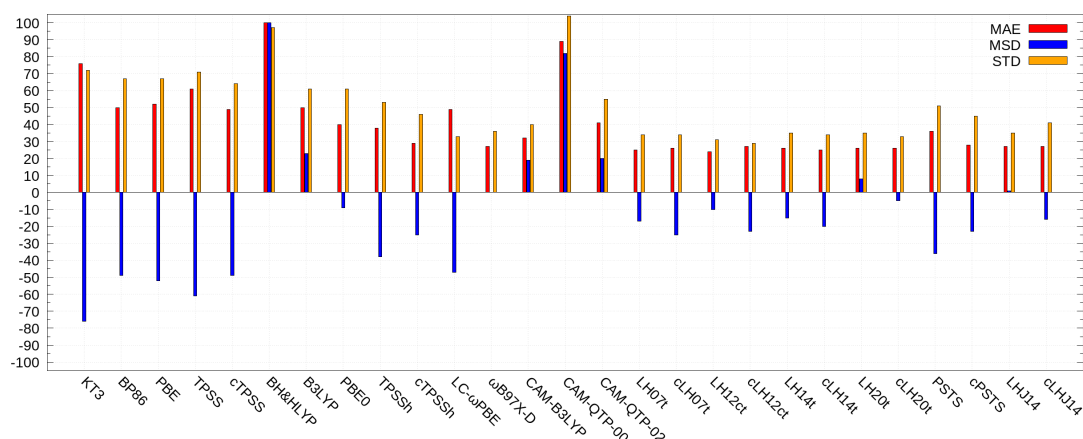


Figure 10.6: Comparison of various functionals for ^{17}O NMR shifts (in ppm) of transition-metal oxo compounds. Calculated with the DLU-X2C Hamiltonian and the x2c-TZVPall-s basis sets. Net charges are compensated with COSMO. Experimental references are taken from Ref. 381, which converted the original measurements^[510] with respect to H_2O using the experimental vapor–liquid shift.

Second, a static amount of exchange results in an improvement and the errors are reduced to 40–50 ppm. However, a very large amount of HF exchange as for BH&HLYP shows poor results—just like HF itself. A more sophisticated incorporation of exchange as in $\omega\text{B97X-D}$ or CAM-B3LYP reduces the errors to about 30 ppm. $\omega\text{B97X-D}$ yields a mean signed error of 0 ppm. Yet, range-separation is not an *a priori* improvement as indicated by the unfavorable performance of CAM-QTP-00.

Third, the t-LMF based LHF's show similar errors as the range-separated functionals but the standard deviation is often decreased. Note that all t-LMF functionals lead to essentially the same MAE and standard deviation. Also, the impact of the different generalizations for τ is insignificant for these indicators. Only the MSD is affected and the paramagnetic current density increases the absolute value of the MSD for LHF's except for LH20t. On the contrary, the current-dependent choice leads to a minor yet steady improvement for TPSS, TPSSh, and PSTS, which perform similar. Overall, the LHJ14 functional shows the best results among the local hybrid functionals. The MAE is 27 ppm and the MSD amounts to 1 ppm. Therefore, the findings for LHJ14 significantly differ from the previous subsections. In contrast to PSTS, the results with LHJ14 differ notably from B3LYP, which also consists of Becke's 1988 exchange term.^[128]

10.2.4 NMR Shifts of Xenon Fluorides

The xenon fluorides of Sec. 9.1.3 are studied with the set of functionals. Here, the same settings as in the previous subsection are adopted. Only the root mean square of the density is required to be smaller than 10^{-8} a.u. to ensure well converged orbitals for heavy elements. All structures are optimized at the respective level of theory. Symmetry constraints are applied for all molecules: $D_{\infty h}$ for XeF_2 , D_{4h} for XeF_4 , and O_h for XeF_6 . Note that the optimized structure of XeF_6 is a saddle point with BH&HLYP, CAM-QTP-00, CAM-QTP-02, and HF. The shifts are measured with respect to the xenon atom. Spin–orbit coupling is of minor importance for the NMR shifts. Based on the CCSD(T) results^[101] and the spin-orbit treatment in Ref. 544, the experimental shifts should be underestimated by 200 ppm for XeF_2 and overestimated by 100 ppm for XeF_4 , and 100 ppm for XeF_6 . The ^{129}Xe NMR shifts are listed in Tab. 10.2 and the shielding constants are available in Ref. 365. Most LHF's result in a reasonable agreement with the reference for XeF_2 . TPSS, TPSSh, and PSTS even lead to an excellent agreement with the desired scalar-relativistic result for XeF_2 . Yet, they do not perform remarkably well for XeF_4 and XeF_6 . CAM-QTP-00 performs best for these molecules, while CAM-QTP-02 yields a sufficiently accurate shift for XeF_6 . Most functionals fail to accurately predict

the trend from XeF_4 to XeF_6 (-250 ppm). “Pure” density functional approximations tend to significantly underestimate this trend whereas the opposite holds for the range-separated hybrid functionals. The t-LMF functionals and LHJ14 show a rather accurate decrease. The current-dependent τ notably affects the shifts of LH07t-SVWN and LH12ct-SsirPW92 decreasing them by about 100–200 ppm whereas the other shifts are not significantly altered. Overall, B3LYP and LH20t rather systematically overestimate all shifts by 200–300 ppm. The latter correctly describes the trend of the shifts.

Table 10.2: Comparison of ^{129}Xe NMR shifts (in ppm) with various density functionals at the DLU-X2C/x2c-TZVPall-s level. CCSD(T) results are taken from Ref. 101. The uncontracted ANO-RCC basis set^[179] is used therein and all electrons are correlated. Differences between the CCSD(T) results and the experimental findings can mainly be addressed to spin–orbit coupling as shown by the correction Δ SO obtained in Ref. 544. The experimental shifts are measured with respect to neat XeOF_4 ^[499] and converted with the shift for the xenon atom.^[500]

	XeF_2	XeF_4	XeF_6
HF	3814	5312	4669
KT3	3523	5998	5900
BP86	3671	6378	6326
PBE	3644	6328	6264
TPSS	3553	6122	6129
cTPSS	3516	6071	6089
BH&HLYP	3885	6231	6083
B3LYP	3864	5830	5443
PBE0	3695	5924	5733
TPSSh	3588	5981	5933
cTPSSh	3556	5935	5896
LC- ω PBE	3888	5987	5527
ω B97X-D	3882	6072	5733
CAM-B3LYP	3969	6171	5793
CAM-QTP-00	3911	5733	5189
CAM-QTP-02	3990	5981	5434
LH07t-SVWN	3854	6164	5989
cLH07t-SVWN	3761	6041	5857
LH12ct-SsirPW92	3849	6057	5838
cLH12ct-SsirPW92	3749	5918	5693
LH14t-calPBE	3763	6026	5843
cLH14t-calPBE	3743	5995	5808
LH20t	3751	5862	5600
cLH20t	3771	5883	5610
PSTS	3565	5924	5897
cPSTS	3535	5882	5863
LHJ14	3730	6135	5952
cLHJ14	3820	6255	6055
CCSD(T)	3564	5509	5258
Δ SO	-222	108	–
Exp.	3386	5623	5425

10.2.5 NMR Shifts of Tungsten Compounds

The tungsten compounds of Sec. 9.1.5 serve as an illustrative application to transition-metal shifts. The shifts are calculated at the optimized structure of each functional with the DLU-X2C Hamiltonian and the x2c-TZVPall-s basis set. COSMO^[453,454] is applied to WO_4^{2-} , WO_3S^{2-} , $\text{WO}_2\text{S}_2^{2-}$, WOS_3^{2-} , and WS_4^{2-} to compensate the negative charge. The same thresholds as in Sec. 10.2.3 are applied, i.e. the root mean square of the density is converged up to the default setting of 10^{-6} a.u., and the point-group symmetry of the molecules is exploited. As spin-orbit coupling is of minor importance for the shifts,^[382] the experimental findings^[513–516] serve as reference. The ^{183}W NMR shifts are calculated with respect to WO_4^{2-} and the evaluation is presented in Fig. 10.7.

BP86 performs best among the “pure” density functionals with a MAE of 228 ppm and a MSD of -34 ppm. KT3 yields the largest errors. As reflected by the poor results for BH&HLYP, a balanced admixture of HF exchange is of crucial importance for an improvement upon the GGA and meta-GGA functionals. Here, PBE0 and TPSSh result in a good agreement with the experimental findings with MAEs of 119 ppm and 150 ppm. The respective MSDs are 40 ppm and -35 ppm. Range-separated hybrid functionals lead to increased errors. The mean absolute errors for the more robust representatives LC- ω PBE, ω B97X-D, and CAM-B3LYP functional range from 211 ppm to 252 ppm. LHF based on the t-LMF also do not reduce the errors compared to PBE0 and TPSSh. The MAEs range from 192 ppm for LH14t-calPBE to 231 ppm for LH12ct-SsirPW92. So, the performance is similar to the range-separated hybrid functionals. In contrast, PSTS and LHJ14 improve upon TPSSh with a MAE of 148 ppm and 137 ppm. The MSDs amount to only -20 ppm and 0 ppm. Moreover, the standard deviation is slightly reduced. Notably, the current-dependent generalization of the kinetic energy density very consistently reduces the errors with the exception of LHJ14. The MAE of TPSSh and PSTS is reduced to about 100 ppm and the MSD is reduced to -34 ppm and -18 ppm, respectively.

To consider the cost–balance ratio of a density functional approximation, the wall times are reported for the SCF procedure and the NMR shielding calculations in Tab. 10.3 and Tab. 10.4. The wall times are measured on a single thread of a Intel® Xeon® Gold 6212U CPU @ 2.40 GHz. Note that only the timings of selected functionals are presented, i.e. BP86, KT3, BH&HLYP, CAM-QTP-00, and CAM-QTP-02 are omitted. Still, every functional class considered herein is represented by at least one functional. The SCF timings reveal the following picture.

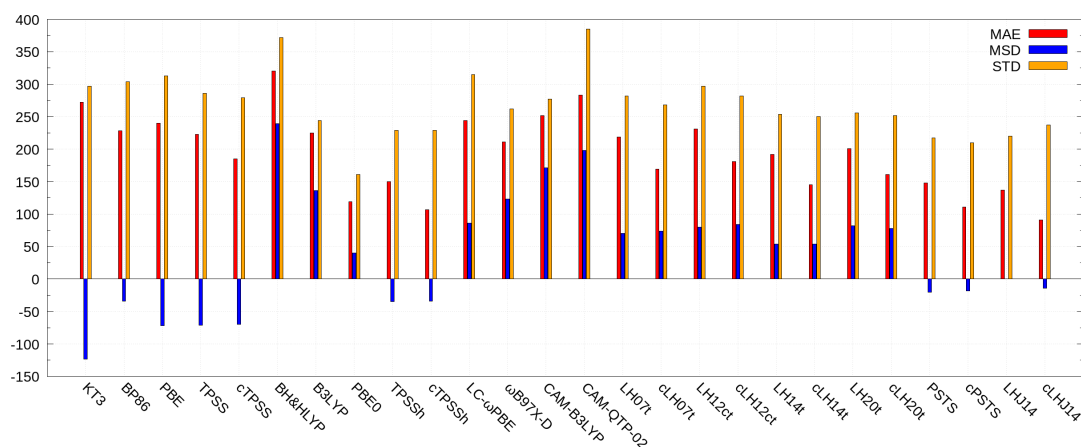


Figure 10.7: Comparison of various functionals for ^{183}W NMR shifts (in ppm) of eight compounds with respect to WO_4^{2-} . Calculated are performed at the DLU-X2C/x2c-TZVPall-s level of theory and using COSMO for the charged systems. Experimental results are taken from Refs. 513–516. CAM-QTP-00 is omitted due to a large standard deviation of 456 ppm. Likewise, HF results in a MAE of 646 ppm.

Table 10.3: Wall times of the full SCF procedure in seconds on a CPU of type Intel® Xeon® Gold 6212U CPU @ 2.40 GHz using one thread. The code was compiled with Intel® Fortran Compiler 19.0.1.144. Point-group symmetry is exploited. A core Hamiltonian guess is used for the initial orbitals to start the SCF procedure.

	PBE	TPSS	B3LYP	PBE0	TPSSh	LC- ω PBE	ω B97X-D	CAM-B3LYP	LH07t	LH12ct	LH14t	LH20t	PSTS	LHJ14
WO ₄ ²⁻	58	62	83	81	78	105	97	103	153	146	131	127	123	138
WO ₃ S ²⁻	393	398	398	314	403	598	682	645	1559	1457	1529	1427	1335	1499
WO ₂ S ₂ ²⁻	474	439	446	424	501	935	837	753	1720	1764	1406	2087	1854	1650
WOS ₃ ²⁻	388	499	457	502	570	844	837	796	1704	1855	1780	1722	1861	2201
WS ₄ ²⁻	435	486	471	542	570	169	156	165	162	2175	1932	1891	1883	2291
WF ₆	54	46	67	72	68	99	100	102	124	112	109	110	111	118
WCl ₆	58	69	84	70	70	153	137	127	123	154	159	138	157	175
W(CO) ₆	185	207	202	189	179	306	286	314	302	350	361	380	404	339
TOTAL	2044	2206	2207	2194	2438	3209	3132	3005	5846	8014	7407	7881	7726	8411

Table 10.4: Wall times of the NMR shielding calculations in seconds on a CPU of type Intel® Xeon® Gold 6212U CPU @ 2.40 GHz using one thread. The code was compiled with Intel® Fortran Compiler 19.0.1.144. Point-group symmetry is exploited.

	PBE	TPSS	B3LYP	PBE0	TPSSh	LC- ω PBE	ω B97X-D	CAM-B3LYP	LH07t	LH12ct	LH14t	LH20t	PSTS	LHJ14
WO ₄ ²⁻	10	9	36	35	32	40	42	38	48	45	46	49	36	48
WO ₃ S ²⁻	50	62	163	148	140	227	201	198	581	576	518	543	485	499
WO ₂ S ₂ ²⁻	44	58	153	157	144	280	231	214	530	569	537	675	578	526
WOS ₃ ²⁻	46	60	159	164	182	282	251	256	550	605	583	624	616	654
WS ₄ ²⁻	52	61	179	194	183	56	56	49	58	757	675	730	619	704
WF ₆	13	11	36	40	36	45	47	43	47	47	47	50	46	48
WCl ₆	13	17	50	41	18	61	62	58	61	59	65	58	57	58
W(CO) ₆	39	45	95	40	81	136	138	142	121	141	135	138	127	131
Total	267	323	871	818	816	1127	1027	998	1996	2798	2606	2867	2563	2668

Global hybrid functionals lead to similar total computation times as the “pure” density functionals as they lead to a more rapid SCF convergence behavior. The time amounts to about 2000–2500 seconds. The range-separated hybrid functionals increase the timings by about 50% as the integral evaluation with the damping scheme is more involved. Most LHF’s result in a significantly increased computation time. The timings are increased by about a factor of 4 compared to PBE. The only exception is LH07t-SVWN due to the very rapid convergence in the case of WS₄²⁻.

Similar findings hold for the NMR shielding calculations. PBE and TPSS result in very short computation times and the calculation of all shielding constants amounts to less than 6 minutes. The timings are prolonged to about 12 minutes with global hybrid functionals and to more than 16 minutes with range-separated hybrid functionals. The computation times of the latter are more than doubled for LHF’s. Here, the wall times range from 33 to 48 minutes. This considerable increase of the computational costs is caused by the comparably large grids for the seminumerical exchange approximation. The DFT exchange and correlation terms require larger grids for the numerical integration than the HF exchange.^[310] Therefore, a multigrid approach with a small grid for HF exchange and a larger grid for the DFT exchange and correlation terms can be highly efficient as shown by the timings in Tab. 10.5. Here, the RI-*J* approximation and smaller grids (grid 2a) are applied together with the seminumerical exchange approximation for left-hand side of the CPKS equations only. Application of the seminumerical approximation to these integrals only allows to use a very small grid (grid -1) without loss of accuracy. Such a multigrid approach is not straightforwardly applicable to LHF’s. Therefore, LHF’s are still more demanding than the conventional hybrid functionals. The overall timings are notably reduced due to the smaller grid for the XC energy. The timings for LHF’s are still increased by a factor of 7 to 8 compared to PBE and by a factor of 2 compared to the global hybrids. This demonstrates that the additional flexibility with a position-dependent admixture of HF exchange comes at the prize of increased computational costs for NMR properties as the density in the vicinity of the nucleus requires a sufficient grid for the DFT exchange and correlation contribution.

Table 10.5: Wall times of the NMR shielding calculations in seconds (grid 2a RI- J , and seminumerical exchange with grid -1 for the left-hand side of the CPKS equations in the global and range-separated hybrid calculations). Calculations are carried out with a CPU of type Intel® Xeon® Gold 6212U CPU @ 2.40 GHz using one thread. The code was compiled with Intel® Fortran Compiler 19.0.1.144.

	PBE	TPSS	B3LYP	PBE0	TPSSh	LC- ω PBE	ω B97X-D	CAM-B3LYP	LH07t	LH12ct	LH14t	LH20t	mPSTS	LHJ14
WO_4^{2-}	7	7	13	14	14	15	17	14	22	20	21	21	20	23
WO_3S^{2-}	17	20	55	60	57	83	71	72	189	181	188	202	182	179
$\text{WO}_2\text{S}_2^{2-}$	17	20	58	60	59	85	77	74	206	265	203	212	182	190
WOS_3^{2-}	16	21	73	64	66	91	83	90	203	218	213	231	196	203
WS_4^{2-}	8	8	16	15	16	19	19	18	26	26	25	26	22	29
WF_6	10	11	17	18	17	21	19	19	23	22	22	23	24	24
WCl_6	12	10	20	23	19	25	23	24	27	28	29	30	28	33
$\text{W}(\text{CO})_6$	24	32	51	30	47	57	58	57	63	63	61	64	63	60
Total	112	129	302	284	295	394	367	367	758	824	762	810	717	740

10.2.6 Summary

In many cases, global and range-separated functionals result in improved NMR shieldings and shifts. The NMR-tailored GGA KT3 performs well for the light elements and is able to reach or surpass the accuracy of global hybrid functionals. The additional flexibility of the fully local admixture of HF exchange should provide an improved description of the electronic structure and lead to better results for NMR properties. However, this is not consistently reflected in the obtained results and the studied LHF only lead to minor improvements compared to popular global or range-separated hybrids such as B3LYP, PBE0, TPSSh, or CAM-B3LYP. Often, LHF even lead to a deterioration. The most robust LHF for NMR shieldings and shifts is PSTS, which provides a very consistent improvement upon the parent TPSS and TPSSh functionals. The other LHF and LMF show no clear trend and the situation is less clear cut. Here, the results are highly dependent on the test set and molecular class. For light elements, most t-LMF based functionals and PSTS are superior to many global hybrids and the LHJ14 functional. For heavy elements, the t-LMF based functionals loose some ground and the LHJ14 functional performs remarkably. Therefore, the t-LMF and the z-LMF do not results in a consistent improvement compared to global hybrid functionals incorporating a static amount of exchange. Note that all LHF lead to increased computational costs compared to the global and range-separated functionals with the seminumerical exchange approximation. To conclude, all classes of LHF and LMF require more work to reach the robustness of the conventional hybrid functionals PBE0 and TPSSh.

11 Application to Phosphinidenide Complexes

The first “parent” phosphinidenide complex was synthesized in 2010.^[545] Here, the PH group is stabilized with a N-heterocyclic carbene (NHC) but the stabilization is also possible with cyclic (alkyl)(amino)carbenes (cAACs).^[546] This allows to prepare low-valent group 14 compounds with the oxidation state +II.^[547] The synthesis of Ge, Sn, and Pb complexes with sterically demanding ligands is shown in Fig. 11.1. The compounds **3–7** were prepared by Markus Balmer in the group of Carsten von Hänisch and their properties will be analyzed with quantum chemical methods to study the bonding situation. Compound **3** with a V-shaped structure of the GeP₂ group and compound **6** are depicted in Fig. 11.2. The molecular structure of the compounds **4** and **5** is similar to that of **3** and the same holds for **6** and **7**. First, the compounds **3–5** are discussed. Second, the properties of **6** and **7** are described. Selected bond lengths and angles are listed in Tab. 11.1. Experimentally, the structures were determined with X-ray spectroscopy in the solid state. These findings are compared to the optimized structure at the DFT level.

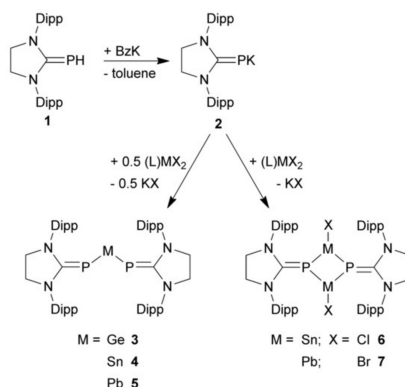


Figure 11.1: Synthesis of the phosphinidenide complexes. Dipp = 1,3-bis(2,6-diisopropylphenyl)imidazolium-2-ylidene and Bz = benzyl. The ligand to prepare the compounds **3–7** is SIMes, SIMes = 1,3-bis(2,4,6-trimethylphenyl)imidazolium-2-ylidene. Details on the conditions, solvents, etc. can be found in Ref. 540.

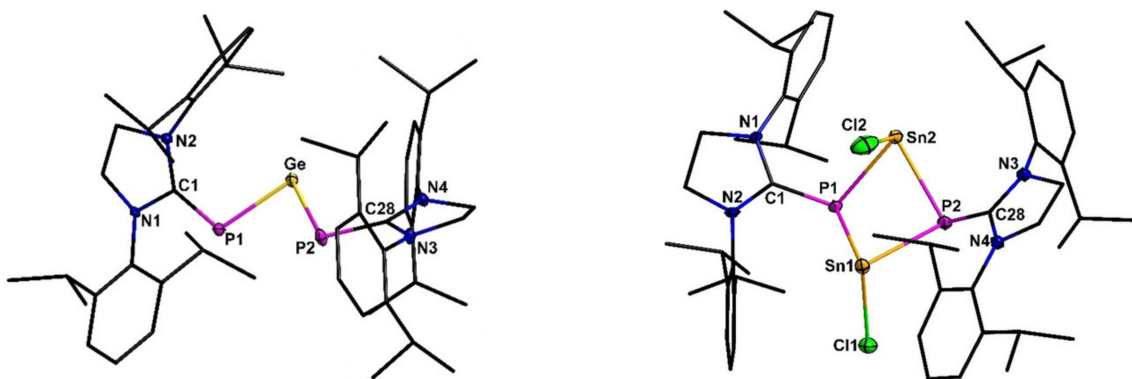


Figure 11.2: Molecular structure of compound **3** (left) and **6** (right). Hydrogen atoms are omitted for clarity. Thermal ellipsoids represent a 50% probability level, carbon atoms are shown as wire frame for better visibility.

Table 11.1: Structural data on compounds **3–5**. Experimental structures (Exp.) are determined with X-ray spectroscopy and the theoretically optimized structures are obtained at the DLU-X2C/x2c-TZVPall level of theory with grid 4a for the numerical integration of the XC parts. The Cartesian coordinates are available in the supporting information of Ref. 540.

	3	4	5
d(C–P) in pm			
Exp.	177.0–177.3	176.5–176.8	174.3–175.4
BP86	178.03–178.04	177.43–177.45	176.98–177.03
PBE	177.93–177.95	177.32–177.34	176.84–176.87
TPSS	178.00–178.03	177.35–177.39	176.80–176.84
B3LYP	177.92–177.95	177.37–177.41	176.89–177.08
PBE0	176.84–176.89	176.16–176.16	175.56–175.57
TPSSh	177.66–177.68	176.88–176.95	176.30–176.35
d(C–M) in pm			
Exp.	229.6–230.2	249.2–249.9	258.0–258.2
BP86	233.59–233.62	253.95–253.97	262.70–262.72
PBE	233.00–233.00	253.27–253.34	262.04–262.08
TPSS	232.23–232.30	252.82–252.87	262.00–262.09
B3LYP	233.32–233.39	253.72–253.79	262.94–263.35
PBE0	230.56–230.61	250.57–250.59	259.19–259.20
TPSSh	231.74–232.04	251.64–251.70	260.64–260.89
\angle (C–P–M) in °			
Exp.	104.8–105.7	104.1–105.8	103.3–105.6
BP86	107.46–107.51	108.52–108.53	108.90–109.01
PBE	106.33–106.46	107.10–107.17	107.51–107.67
TPSS	107.06–107.16	107.57–107.62	107.76–107.86
B3LYP	107.88–107.94	107.95–108.00	107.56–108.01
PBE0	105.79–105.83	106.55–106.63	107.30–107.45
TPSSh	106.44–106.53	106.91–107.15	107.04–107.28
\angle (P–M–P) in °			
Exp.	87.4	85.8	84.6
BP86	86.61	85.11	84.96
PBE	86.59	85.49	85.15
TPSS	86.37	85.39	84.98
B3LYP	88.47	88.47	90.03
PBE0	87.85	86.74	85.91
TPSSh	87.65	86.11	85.91

The structures are optimized with the scalar-relativistic DLU- X2C Hamiltonian^[105,107] in the finite nucleus model employing the x2c-TZVPall orbital and auxiliary basis set^[203] for the multipole-accelerated resolution to the identity (MARI-*J*) approximation.^[120] The BP86,^[128,340] PBE,^[341] TPSS,^[346] B3LYP,^[128–130] PBE0,^[355] and TPSSh^[356] functionals are employed with large grids^[482] (grid 4a). SCF iterations are converged up to 10^{-9} E_h and 10^{-9} a.u. for the root mean square of the density matrix. Based on the structural data, the TPSSh functional performs best and all bond lengths are overestimated by 1–2 pm. The trend of the bond lengths and the angles is well described. The impact of dispersion interaction on the structure is small as the optimization using the D4 dispersion correction^[548] and the BP86 functional shortens the C–P and M–P bonds by 1–2 pm. The C–P–M angle of the compounds **3**, **4**, and **5** is reduced by 3.2°, 5.3°, and

Table 11.2: Spectroscopic data on compounds **3–5**. NMR shifts are calculated with the scalar-relativistic DLU-X2C Hamiltonian and the x2c-TZVPall-s bases whereas the SSCCs are obtained with the quasirelativistic DLU-X2C Hamiltonian and the x2c-TZVPall-2c basis set. Based on the data, the large deviation of the calculated and the measured ^{31}P shifts is caused by spin-orbit interactions. The signs of the coupling constants are corrected by the quantum chemical calculations. Excitation energies are calculated with the semiK approximation for the time-dependent DFT studies. The first maxima correspond to singlet excitations.

	3	4	5
$\delta^{31}\text{P}$ in ppm			
Exp.	145	121	117
BP86	217	220	242
PBE	207	204	222
TPSS	171	166	181
B3LYP	214	220	250
PBE0	166	156	169
TPSSh	160	149	161
$J(\text{M-P})$ in Hz			
Exp.	–	1334	–1673
BP86	–	1387	–1527
PBE	–	1342	–1457
TPSS	–	1406	–1692
B3LYP	–	1496	–1644
PBE0	–	1401	–1766
TPSSh	–	1422	–1799
$\delta^{13}\text{C}_{\text{NHC}}$ in ppm			
Exp.	191	192	186
BP86	197	200	160
PBE	198	199	199
TPSS	195	197	198
B3LYP	210	212	213
PBE0	204	206	202
TPSSh	199	201	201
First absorption maxima UV/Vis in nm			
Exp.	543	554	569
PBE0	482	499	508
TPSSh	507	528	539

6.6° , whereas the P–M–P angle rises by 0.2° , 1.5° , and 4.7° . Therefore, neglecting dispersion corrections in the other calculations is a reasonable approximation. A comparison with known bond lengths of other germanium and tin phosphinidenide complexes^[549,550] suggests that $p\pi-p\pi$ interactions are present. $p\pi-p\pi$ interactions are further indicated by the low-field shifted ^{31}P NMR signals in Tab. 11.2. Other germanium substituted phosphinidenides show signals at -11.4 ppm for $\text{K}[(\text{SIMesP})_3\text{Ge}]$ ^[549] or -114.7 ppm for $(\text{SIDipp})\text{PGePh}_3$.^[550] So, electron density is transferred from the phosphorous atoms to the metal atom. A similar downfield shift is present for **4** with 121.4 ppm and **5** with 116.8 ppm. In contrast to **4** and **5**, no splitting of the NMR signal is observed for compound **3**. The phosphorous shifts are a demanding case for DFT as the results are very functional-dependent. Note that the calculated shifts use PH_3 as reference instead of aqueous H_3PO_4 . The shifts are converted to the experimental scale with the absolute shielding

constants of 328.35 ppm and 594.45 ppm.^[551] Furthermore, the x2c-TZVPall-s orbital^[482] and x2c-TZVPall auxiliary basis set^[203] are applied in the NMR shift calculations. The robust hybrid density functional approximations PBE0 and TPSSh yield a sufficient agreement for **3** and **4**. Larger deviations occur for **5** and the trend from **4** to **5** is not correctly reproduced. The experimentally determined shifts decrease, whereas the calculated shifts increase. This discrepancy is likely caused by the missing treatment of spin-orbit interaction. The calculated 1J coupling constants with the spin-orbit DLU-X2C Hamiltonian, the x2c-TZVPall-2c basis set,^[203] and the semiK approximation for the CPKS equations^[311] results in a good agreement with the experimental findings. The coupling constants of the lead compound are typically predicted within a range of 100 Hz, which is a remarkable agreement with the experimental findings and shows that indeed the spin-orbit interaction needs to be considered for accurate NMR parameters of these complexes. GGA functionals underestimate the coupling constants whereas the TPSS and the hybrid functionals overestimate the coupling constants. The position of the first maxima in the UV/Vis spectra is also in good agreement with the TPSSh calculations.

This agreement of the theoretically and the experimentally obtained analytical data allows for an analysis of the bonding situation. Wiberg bond indices^[552] (WBI) in Tab. 11.3 indeed confirm the presumption of a $p\pi-p\pi$ bonding interaction. The WBI of P-M is larger than 1 for all methods and molecules. The impact of spin-orbit coupling on the WBI was found to be small. Therefore, the multibond character is clearly indicated. The WBI for the C-P bond increases with the mass of M and the WBI of the P-M bond decreases. This shows that the two π -bonds are contrary effects and the π -system is delocalized over the complete C-P-M-P-C bonds as shown by the frontier molecular orbitals of compound **4** in Fig. 11.3. The HOMO-2 shows the $p\pi-p\pi$ interaction of the M-P bond while the HOMO-1 describes the C-P π bond. Thus, these orbitals explain the WBIs. The HOMO contains a significant contribution from the lone pairs of the tetrel atom. Notably, the energy difference between the HOMO-1 and the HOMO is small and amounts to 0.1 eV (**3**), 0.1 eV (**4**), and 0.05 eV (**5**). The antibonding M-P π -orbital is the LUMO, which is 1.8 eV higher in energy than the HOMO. Incorporating HF exchange by the TPSSh functional, increases the gap to 2.4 eV. The frontier orbitals of the germanium and the lead compound describe the same orbitals and are very similar. Therefore, compound **5** features a notable $p\pi-p\pi$ Pb-P interaction and a multibond character.

Table 11.3: WBI of the compounds **3–5** at the scalar-relativistic DLU-X2C/x2c-TZVPall level of theory. The impact of spin-orbit coupling on the WBI was found to be small at the TPSS level and typically changes the WBI by 0.01.

	3	4	5
WBI (C-P)			
BP86	1.39	1.42	1.45
PBE	1.38	1.42	1.45
TPSS	1.29	1.33	1.37
B3LYP	1.43	1.46	1.48
PBE0	1.39	1.43	1.46
TPSSh	1.33	1.34	1.38
WBI (P-M)			
BP86	1.22	1.15	1.11
PBE	1.21	1.14	1.11
TPSS	1.20	1.13	1.08
B3LYP	1.23	1.15	1.11
PBE0	1.22	1.14	1.10
TPSSh	1.20	1.13	1.08

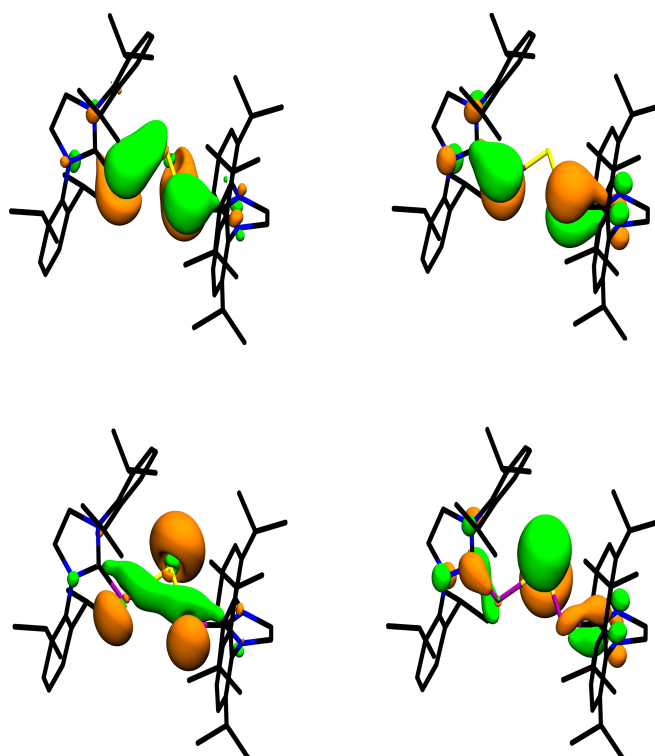


Figure 11.3: Frontier orbitals of compound **4**. Calculated at the DLU-X2C/x2c-TZVPall/TPSS level of theory. Orbital shapes are drawn with an isovalue of 0.04 a.u.; the HOMO–2 at the top left shows the $\pi\pi$ – $\pi\pi$ Sn–P interaction, whereas the HOMO–1 at the top right shows the C–P π interaction. The HOMO (bottom left) consists of the lone pairs at Pb and the LUMO (bottom right) describes the π -orbital of the Sn–P bond. Hydrogen atoms are omitted for clarity.

The compounds **6** and **7** featuring two tetrel atoms contain a central P_2M_2 cycle with a butterfly conformation. The theoretically optimized and the experimentally determined structures result in a similar agreement like for the monomer compounds **3**–**5**. For **6**, the P–Sn bond lengths range from 259.6 to 266.3 pm in the solid state and the four calculated bond lengths at the TPSSh level are 263.77 pm, 265.42 pm, 268.64 pm, and 269.85 pm. So, the deviation is larger than for the previously studied molecules but still in a very reasonable agreement and the bond lengths are similar to known P–Sn^{II} molecules.^[553] Likewise, the experimental P–Pb bond lengths of **7** are within 269.2–276.9 pm, which is in accordance with the TPSSh optimized structure. Here, the bond lengths cover a range from 271.50 to 279.43 pm. Tab. 11.4 shows that the spectroscopic data are also well described by PBE0 and TPSSh. The tin compound shows a ^{31}P NMR signal at –66 ppm and a $^1J_{\text{SnP}}$ coupling constant of 998 Hz. The hybrid density functionals PBE0 and TPSSh yield a NMR shift of –50 ppm and –45 ppm and a NMR coupling constant of 1067 Hz and 1028 Hz. All functionals are in very good agreement with the experimental findings of the coupling constant. The deviation amounts to less than 80 Hz. This suggests that compound **6** is still dimeric in solution for the NMR experiments. The ^{31}P NMR spectrum of compound **7** shows a signal at –48 ppm with a $^1J_{\text{PbP}}$ coupling constant of 1205 Hz. GGA functionals underestimate the coupling constant by 500 Hz whereas the PBE0 functional results in a remarkable agreement. This shows that a sophisticated treatment of relativistic effects and electron correlation is important for the NMR properties of the phosphinidenide complexes with heavy elements. The scalar-relativistic NMR shifts are in reasonable agreement for all compounds except for **5**. However, the NMR coupling constants necessitate a quasirelativistic or two-component framework as the Fermi-contact and the spin-dipole interaction are spin-orbit effects according to the Dirac equation. Therefore, NMR shifts can be calculated within a scalar-relativistic treatment while NMR coupling constants are only meaningful considering also spin-orbit interaction. Overall, the PBE0 and TPSSh functionals perform well and confirm the results of the previous chapter.

Table 11.4: Spectroscopic data on compounds **6** and **7**. NMR shifts are calculated with the scalar-relativistic DLU-X2C Hamiltonian and the x2c-TZVPall-s bases whereas the SSCCs are obtained with the quasirelativistic DLU-X2C Hamiltonian and the x2c-TZVPall-2c basis set. The signs of the coupling constants are corrected by the quantum chemical calculations. Excitation energies are calculated with the semiK approximation for the time-dependent DFT studies.

	BP86	PBE	TPSS	B3LYP	PBE0	TPSSh	Exp.
$\delta^{31}\text{P}$ in ppm							
6	5	7	-34	-6	-50	-45	-66
7	14	9	-24	4	-35	-40	-48
$J(\text{M-P})$ in Hz							
6	923	902	971	1057	1067	1028	998
7	-755	-726	-912	-932	-1277	-1091	-1205

The shifts and the bond lengths of **6** and **7** suggest that no multibond character is present and no electron density is transferred to the metal atom. This is confirmed by the WBI reported in Tab. 11.5. The compounds **6** and **7** show no $p\pi-p\pi$ interactions as the WBI for the P-M bonds are 0.70–0.77 for **6** and 0.66–0.75 for **7**.

Table 11.5: WBI of the compounds **6** and **7** at the scalar-relativistic DLU-X2C/x2c-TZVPall level of theory. The number of the atoms is described in Fig. 11.2.

	BP86	PBE	TPSS	B3LYP	PBE0	TPSSh
6						
C1-P1	1.25	1.21	1.14	1.26	1.21	1.12
C28-P2	1.25	1.21	1.14	1.25	1.20	1.14
P1-Sn1	0.73	0.73	0.71	0.70	0.72	0.70
P2-Sn1	0.73	0.74	0.71	0.74	0.74	0.73
P1-Sn2	0.79	0.79	0.76	0.79	0.79	0.77
P2-Sn2	0.79	0.78	0.76	0.77	0.76	0.75
7						
C1-P1	1.26	1.24	1.15	1.27	1.21	1.15
C28-P2	1.28	1.25	1.17	1.30	1.22	1.16
P1-Pb1	0.78	0.78	0.75	0.76	0.78	0.75
P2-Pb1	0.77	0.76	0.74	0.76	0.77	0.75
P1-Pb2	0.68	0.69	0.66	0.69	0.70	0.67
P2-Pb2	0.68	0.68	0.67	0.67	0.67	0.66

12 Application to All-Metal Aromaticity

12.1 Aromaticity and IUPAC Criteria

Originally, aromatic compounds were defined as unsaturated, cyclic planar organic molecules which show a highly symmetric ring structure and a tendency to retain the ring structure in reactions.^[554] In organic chemistry, aromatic compounds generally show an electrophilic substitution in Friedel–Crafts reactions.^[555] The parent compound is benzene, whose structure was discussed by Kekulé.^[556,557] The six electron aromatic structure was later postulated by Crocker in 1922^[558] and by Armit and Robinson in 1925.^[559] Note that Armstrong already suggested a sextet-like structure by the six aromatic “affinities” in his work on the *meta* and *ortho-para* directing substituents.^[560] Quantum chemical methods were applied to the “benzene problem” by Hückel^[285–287] and lead to the $(4n + 2)$ rule for aromaticity and the $(4n)$ rule for antiaromaticity. Hückel’s theory describes a cyclic and delocalized system of π -electrons in unsaturated, cyclic planar molecules and allows to understand the structure and chemical properties of benzene. Here, all bonding MOs are doubly occupied and all antibonding MOs are unoccupied. The resonance energy of the delocalized π -system may be calculated with Hückel MO theory or modern quantum chemical methods. The resonance energy of the π -electrons can also be graphically calculated with the Frost–Musulin circle.^[561] Later, the concept of aromaticity was extended to account for heteroaromatic systems like pyridine or porphine as well as spiro-aromatic and Möbius-aromatic compounds. Aromaticity has proven to be an extremely valuable concept in chemistry, however, it is not possible to simply “measure” aromaticity. Therefore, the following criteria of aromaticity for cyclic molecular systems are introduced by the International Union of Pure and Applied Chemistry (IUPAC):^[562]

1. Energetic criterion: The thermodynamic stability of aromatic compounds is enhanced compared to the acyclic analogues. Therefore, a tendency to retain the structural type is found in chemical reactions.
2. Structural criterion: “The lesser the alternation of bond lengths in the rings, the greater is the aromaticity of the molecule.”^[562]
3. Magnetic criterion: A diamagnetic or diatropic ring current is induced by an external magnetic field.

The magnetic criterion is based on Ampère’s circuital law. Here, the external magnetic field induces a ring current due to the delocalized electrons.^[16–19] Consider a planar, cyclic molecule with a delocalized π -system and a magnetic field perpendicular to the molecular plane. According to Lenz’s law, the diatropic ring current flows in a clockwise direction and a paratropic ring current in the counterclockwise direction. For aromatic systems, the diatropic ring current dominates whereas antiaromatic systems possess a net paratropic ring current. This is evident from the anisotropy of the magnetic susceptibility^[563] or the characteristic shifts in NMR spectra. The diatropic ring current deshields the hydrogen atoms outside the benzene ring and the ^1H NMR signal is found at about 7 ppm.^[3] The ring current is also accessible in quantum chemical studies and can be calculated directly with the gauge-including magnetically induced current (GIMIC) method^[423,424,427] or indirectly with the nucleus-independent chemical shifts (NICS).^[18,564] The GIMIC method calculates the magnetically induced current density numerically on a grid and provides a current or delocalization pathway. To quantify the ring current, an integration plane is placed through a bond or atom to numerically integrate

the current through that plane. This allows to calculate the current strength. Note that the GIMIC method is generally applicable to molecules as long as an integration plane can be constructed. Therefore, more complicated multiring structures can be studied straightforwardly.^[565] On the contrary, the NICS method places a ghost atom at the ring center and calculates the isotropic NMR shielding constant at this atom. The sign is reverted to comply with the common NMR scale. A negative NICS value indicates aromaticity whereas a positive NICS value is found for antiaromatic systems like cyclobutadiene. NICS values may also be calculated on a grid to obtain a so-called NICS profile.^[18] Current strengths and NICS of selected hydrocarbon and heteroaromatic compounds calculated in this work are shown in Fig. 12.1 (a and b). Here, we focus on monocyclic compounds. According to the $(4n + 2)$ rule, the cyclobutadiene dianion is aromatic with 6 π -electrons and a rare example of such a four-membered cycle is $\text{Li}_2[(\text{Me}_3\text{SiC})_4]$.^[566] The largest NICS value of the hydrocarbons is found for the cyclopropenyl cation with -21.7 ppm, whereas the maximum ring current is obtained for [18]annulene with 28.0 nA/T. Overall, the ring current tends to increase with the number of π -electrons. The large NICS value of the cyclopropenyl cation with just 2 π -electrons is rationalized by the small distance of the delocalized π -system to the ring center, where the ghost atom is placed. The distance of the carbon atoms to the ring center amounts to 78.82 pm. Very similar trends are observed for the heteroaromatic molecules (Fig. 12.1 b). $\text{K}[(\text{B}^t\text{Bu})_2\text{CCH}(\text{SiMe}_3)_2]$ serves as a rare example of a three-membered cycle^[567] and features the largest NICS value with -15.8 ppm and a ring current strength of 10.2 nA/T. Porphine shows the strongest current with 25.3 nA/T and all π -electrons participate as the current splits at the pyrrole ring into an inner route via the nitrogen atom and an outer route via the C–C backbone.^[423,565]

The discussed criteria are not restricted to organic compounds. Thus, also inorganic, non-metal aromatic molecules (Fig. 12.1 c) exist. Compared to the large number and variety of hydrocarbon and heteroaromatic compounds, only a few purely inorganic aromatic molecules with up to 10 atoms are known.^[568] Borane derivatives with a B_3 and B_4 group are examples for 2π -electron systems.^[569–572] Most molecules of this class feature 6 π -electrons like the $(\text{RSi})_4^{2-}$ moiety in $[\{\eta^4\text{-(RSi)}_4\}\text{Ru}(\text{CO})_3]$ ($\text{R} = \text{SiMe}^t\text{Bu}$),^[573] S_2N_2 ,^[574] or the Ch_4^{2+} ($\text{Ch} = \text{S}, \text{Se}, \text{Te}$) molecules^[575,576] and the Pn_4^{2-} ($\text{Pn} = \text{P}, \text{As}$) systems.^[577,578] Note that S_2N_2 , Se_4^{2+} , and Te_4^{2+} are σ -antiaromatic and π -aromatic as shown by NICS calculations above the molecular plane.^[579] Here, the NICS values are calculated at the ring center with a varying distance above the molecular plane and cutting out the σ -contributions in the GIMIC calculations by proper construction of the integration plane. Other notable known aromatic compounds are P_2N_3^- ,^[580] Pn_5^- ($\text{Pn} = \text{P}, \text{As}$),^[581] and Pn_6 ($\text{Pn} = \text{P}, \text{As}$).^[581] Larger S–N rings with 10 and 14 π -electrons are also experimentally secured.^[568] The ring currents and NICS values are in the same order of magnitude as for the hydrocarbon and heteroaromatic molecules.

Furthermore, metals allow for a great degree of delocalization and therefore considerable ring currents and aromatic properties based on the magnetic criterion may be expected. However, only small aromatic compounds consisting of metal atoms only are experimentally described in the literature (Fig. 12.1 d). First, the group of Robinson discussed the aromatic character of $[(\text{R}\text{Ga})_3]^{2-}$ ($\text{R} = \text{C}_6\text{H}_3\text{-2,6-(C}_6\text{H}_2\text{-2,4,6-Me}_3)_2$) with 2 π -electrons^[582,583] and subsequently the Al compound was synthesized.^[584] The ring current of the first amounts to 2.9 nA/T and the compound is considered to be weakly aromatic based on the magnetic criterion. Its NICS value is much larger due to the short distance of the ghost atom to the Ga–Ga bonds amounting to 68.50 pm. In 2001, the class of all-metal aromatic compounds was brought to the spotlight by the Tr_4^{2-} cycles in $[\text{MTr}_4]^-$ with $\text{M}/\text{Tr} = \text{Li}/\text{Al}, \text{Na}/\text{Al}, \text{Cu}/\text{Al}, \text{Na}/\text{Ga}, \text{and Na}/\text{In}$.^[585,586] These anions were prepared in gas-phase experiments. The Tr_4^{2-} cycles feature a square planar structure and show significant current strengths and NICS values of 27.6 nA/T and -31.8 ppm. Today, three-membered, four-membered, and five-membered cycles are known. The Sb_3^{3-} moiety in $[(\text{Sb}_3)_2\text{Au}_3]^{3-}$, the “[Ga_4] $^{4-}$ ” group in $[(\text{Ar}^*\text{Ga})_2\text{Ga}_2]^{2-}$ with $\text{Ar}^* = \text{C}_6\text{H}_3\text{-2,6-(C}_6\text{H}_2\text{-2,4,6-iPr}_3)_2$,^[587] and Hg_4^{6-} in Ref. 588 sustain notable ring currents. Together with Tt_5^{6-} ($\text{Tt} = \text{Sn}, \text{Pb}$)^[589] and Pn_5^- ($\text{Pn} = \text{Sb}, \text{Bi}$)^[590] these compounds form the class of all-metal aromatic molecules.^[591]

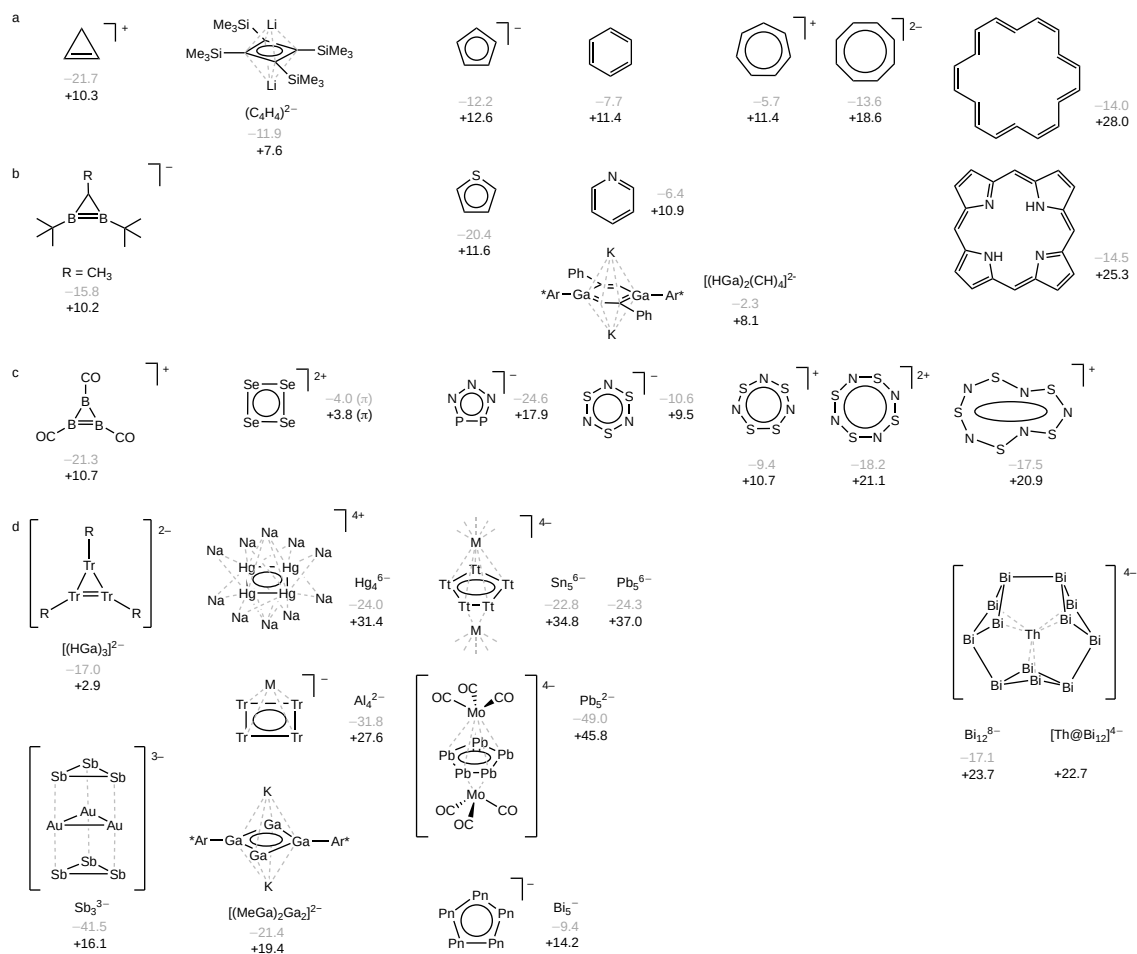


Figure 12.1: Survey of different classes of experimentally secured molecules exhibiting $(4n + 2)$ π -aromaticity. NICS values in ppm (grey) and ring currents in nA/T (black) were calculated at the RI- J /def(2)-TZVP/PBE/grid 3^[198,294,312,315,341,592,593] level of theory. COSMO^[453,454] is applied to the charged systems. Simplifications of the molecules for the calculations are shown. All structures are optimized at the corresponding level of theory. SCF energies were converged up to 10^{-8} E_h and a threshold of 10^{-7} a.u. was used for the response of the orbitals (norm of the residuum) in the NMR calculations. From left to right: molecules with three to eight atoms and examples with more than eight atoms (rightmost) contributing to the $(4n + 2)$ π -aromatic system. Missing entries indicate that no example has been reported for the respective class.

a: Representatives of hydrocarbon aromatic molecules with the well-known aromatic systems like the cyclopentadienyl anion and benzene. $\text{Li}_2[(\text{Me}_3\text{SiC})_4]$ is included as a rare example of a four-membered cycle.^[566] [18]annulene is shown as an example of a large homoaromatic compound.^[594]

b: Representatives of heteroaromatic molecules with $\text{K}[(\text{B})_2\text{CCH}(\text{SiMe}_3)_2]$ as a rare example of a three-membered cycle^[567] and $[(\text{Ar}^*\text{Ga})_2(\text{CH}_2)(\text{CPh})_2]^{2-}$ as a representative of metallaaromatic molecules; $\text{Ar}^* = \text{C}_6\text{H}_3\text{-2,6-(C}_6\text{H}_3\text{-2,6-iPr}_2)_2$.^[595] Porphin is shown as an example of a large heteroaromatic compound.

c: Examples of purely inorganic, non-metal aromatic molecules with the gas-phase species $[\text{B}_3(\text{CO})_3]^+$ as a rare example of a three-membered cycle.^[569] Note that S_2N_2 , Se_4^{2+} , and Te_4^{2+} are σ -antiaromatic and π -aromatic as already observed previously based on NICS profiles.^[579] Here, NICS(0) and NICS(1) are calculated. NICS(1) denotes that the ghost atom is placed in the ring center but 1 Å above the molecular plane. The NICS(0) describes the aromaticity of all contributions and NICS(1) excludes the contribution of the σ -electrons. Therefore, the integration plane for GIMIC similarly excludes the σ -contributions. Larger S–N rings with 10 or 14 π electrons are known.^[574]

d: Survey of all known types of molecules exhibiting all-metal π -aromaticity, with their stabilizing atoms or groups: $\text{Tr} = \text{Al, Ga}$ and $\text{R} = \text{C}_6\text{H}_3\text{-2,6-(C}_6\text{H}_2\text{-2,4,6-Me}_3)_2$ in $[(\text{RTr})_3]^{2-}$; ^[582-584] Tr_4^{2-} of $\text{M/Tr} = \text{Li/Al, Na/Al, Cu/Al, Na/In, Na/Ga}$ in the gas-phase species $[\text{MTr}_4]^-$; ^[585,586] $[(\text{Ar}^*\text{Ga})_2\text{Ga}_2]^{2-}$ with $\text{Ar}^* = \text{C}_6\text{H}_3\text{-2,6-(C}_6\text{H}_2\text{-2,4,6-iPr}_2)_2$; ^[587] Ti_5^{6-} with $\text{Ti} = \text{Sn, Pb}$; ^[589] $\text{Pn} = \text{Sb, Bi}$ in the gas-phase species Pn_5^- . ^[590] NICS values and ring currents are given for one homologue only, as results within the homologous series are similar. Note that the values refer to total ring currents unless explicitly noted otherwise. This may include additional contributions of σ -aromaticity. The weakly π -antiaromatic compounds Pn_4^{2-} ($\text{Pn} = \text{Sb, Bi}$)^[596,597] are not listed here. The all-metal aromatic compounds are further studied in Tab. 12.1 with both ECP-based and all-electron relativistic approaches. $[\text{Th}@\text{Bi}_{12}]^{4-}$ is discussed in detail in the next section.

Table 12.1: Current strengths and NICS of known all-metal aromatic compounds at the RI-*J*/def2-TZVP/PBE/grid 3 level with the non-relativistic (NR) or ECP-based Hamiltonian and at the RI-*J*/x2c-TZVPall-s/PBE/grid 3a level with the scalar-relativistic DLU-X2C Hamiltonian in the finite nucleus model. COSMO is applied to model the counter ions of the charged systems. Note that ECPs are used for heavier atoms than Kr. DLU-X2C calculations are only performed for molecules with heavier atoms than Kr to compare with the ECP-based ansatz. All structures are optimized at the corresponding level of theory. SCF energies were converged up to $10^{-8} E_h$ and a threshold of 10^{-7} a.u. was used for the response of the orbitals (norm of the residuum) in the NMR calculations. Current strengths are given in nA/T and NICS values in ppm. Like in Ref. 583, large substituents are omitted to focus on the aromatic moiety and to allow for a straightforward placement of the integration plane for the current strengths. Note that Sb_4^{2-} and Bi_4^{2-} are antiaromatic based on the magnetic criterion. This also holds at the more sophisticated def2-TZVPD/PBE0/grid 3 level of theory.^[200,355]

	NR/ECP: def(2)-TZVP		DLU-X2C: x2c-TZVPall-s	
	GIMIC	NICS	GIMIC	NICS
Sb_3^{3-}	16.1	-41.5	13.4	-41.1
$(AlH)_3^{2-}$	3.6	-18.6	-	-
$(GaH)_3^{2-}$	2.9	-17.0	-	-
Al_4^{2-}	27.6	-31.8	-	-
Ga_4^{2-}	29.3	-34.0	-	-
In_4^{2-}	29.7	-31.5	30.0	-30.8
$(Ga(CH_3))_2Ga_2^{2-}$	19.4	-21.4	-	-
Sb_4^{2-}	-4.9	5.4	-4.5	3.7
Bi_4^{2-}	-5.5	5.5	-5.6	4.2
Hg_4^{6-}	31.8	-25.0	33.1	-27.9
Ge_5^{6-}	37.7	-27.7	-	-
Sn_5^{6-}	34.8	-22.8	32.7	-19.3
Pb_5^{6-}	37.0	-24.3	36.1	-23.4
Sb_5^-	16.5	-12.5	15.6	-11.2
Bi_5^-	14.2	-9.4	13.9	-9.8
Pb_5^{2-}	45.8	-49.0	46.4	-50.2

Fig. 12.1 provides a comprehensive overview of known inorganic and all-metal aromatic molecules with the same computational methods. Here, ECPs are used for NMR and GIMIC calculations of heavy elements. The derivation of the GIMIC methods assumes that the Biot-Savart-like expression for the NMR shielding tensor and the expression based on analytical energy derivatives in quantum chemistry lead to the same result at all points in space. However, the NMR shielding tensor of an atom with an ECP is not strictly meaningful as the core electrons are missing. Therefore, the calculations are repeated with the all-electron scalar-relativistic DLU-X2C Hamiltonian in Tab. 12.1. The good agreement of the two approaches indicates that the core electrons are of minor importance for the ring currents. Therefore, both approaches can be used. Besides Pb_5^{2-} , the largest NICS values are obtained for Sb_3^{3-} whereas the largest ring currents are found for Ge_5^{6-} . This shows that NICS is less suited for small membered cycles as the ghost atom is extremely shielded by the nearby ring current. For the larger cycles, both methods result in a qualitative agreement.

12.2 Pushing the Limits of Aromaticity with $[\text{Th}@\text{Bi}_{12}]^{4-}$

The previously discussed all-metal aromatic systems are rather small and most species are stabilized by sterically demanding ligands, metal ions, transition-metal complex moieties, or by incorporation into a intermetallic solid. This allows for a significant ring current, however, these approaches are not applicable to larger systems. In contrast, endohedral clusters may stabilize an aromatic ring system from the inside. This idea forms the basis for the synthesis of the anionic cluster $[\text{Th}@\text{Bi}_{12}]^{4-}$. This compound was prepared by Armin Eulenstein, Niels Lichtenberger, Robert Wilson, and Lars Deubner in the groups of Stefanie Dehnen and Florian Kraus.^[598] The molecular structure is depicted in Fig. 12.2. The molecule consists of a torus-shaped Bi_{12}^{8-} unit and a central Th^{4+} ion. The magnetic measurements by Rudolphe Clérac confirm the assignment of the formal charges and the closed-shell configuration. According to Fig. 12.2, the Bi_{12}^{8-} torus consists of four Bi_4 rings. So, two different Bi–Bi bonds are present. The bonds between the Bi_4 rings (d_A) are only slightly shorter than the bonds within the Bi_4 cycle (d_B). Thus, the cluster is highly symmetric with nearly equal bond lengths. The bond lengths of about 304 pm are significantly shorter than common Bi–Bi single bonds. This indicates that a multibond character due to π -interactions is present. Therefore, the structural criterion is fulfilled. The energetic criterion is more involved as non-cyclic analogues are not known. Still, the cluster anion is stable in the solid state and in solution as well as in the gas phase. Consequently, there are sufficient experimental findings to further investigate the aromaticity with quantum chemical calculations.

Quantum chemical studies of the molecular and electronic structure are carried out with ECPs methods. We use an ECP-78 for Th^[592] and the respective def-TZVP basis set and an ECP-60 for Bi^[593] in combination with the def2-TZVP basis set.^[198] The RI-*J* approximation is employed with the corresponding auxiliary basis sets.^[312] The negative charge is compensated by COSMO. The structure was optimized at the def(2)-TZVP basis set level and using the PBE functional^[341] with modified grids^[294,315] (grid m3) by Florian Weigend. The molecular structure is excellently reproduced by these computational settings and the deviations amount to about 1 pm. The HOMO in Fig. 12.3 confirms the presumption of a delocalized π -system. This is further indicated by an incomplete Boys local procedure.^[599] Here, 33 localized orbitals describing the two-center Bi–Bi bonds (Fig. 12.3 c and d) and the Th–Bi bonds (Fig. 12.3 e) are formed but one delocalized

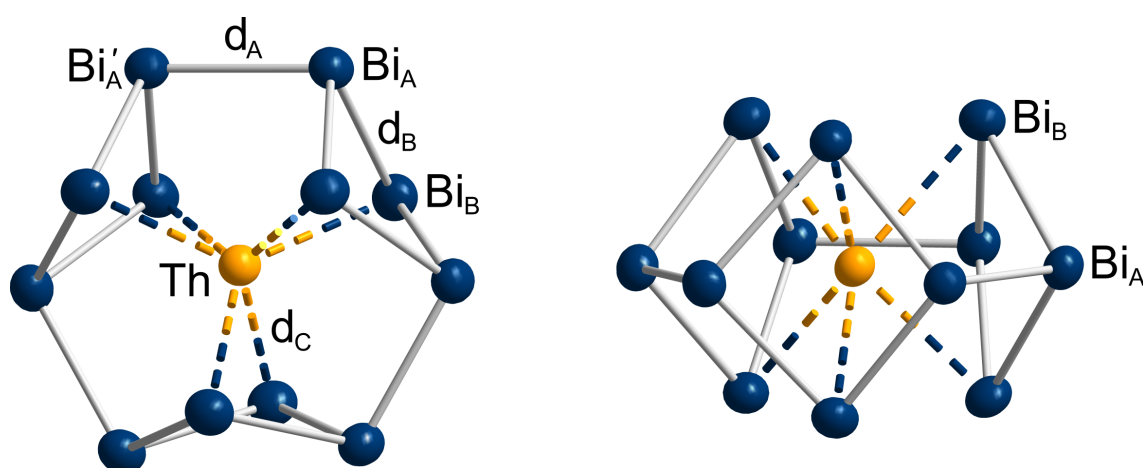


Figure 12.2: Molecular structure of $[\text{Th}@\text{Bi}_{12}]^{4-}$ in $[\text{K}(\text{crypt-222})]_4[\text{Th}@\text{Bi}_{12}]\cdot 2\text{en}$, with crypt = 4,7,13,16,21,24-hexaoxa-1,10-diazabicyclo[8.8.8]hexacosane and en = ethane-1,2-diamine. The molecule is shown in two different orientations with displacement ellipsoids drawn at the 50% probability level at 100(2) K. The structure was determined with a single-crystal X-ray structure analysis by the experimentally working groups. Ranges of selected distances in pm: $\text{Bi}_A\text{--Bi}'_A = d_A$ 304.020(14)–307.85(13) pm, $\text{Bi}_A\text{--Bi}_B = d_B$ 304.40(11)–313.2(1) pm, $\text{Th--Bi}_A = d_C$ 321.04(11)–325.71(9) pm, $\text{Th--Bi}_B = d_D$ 352.51(13)–359.08(9) pm.

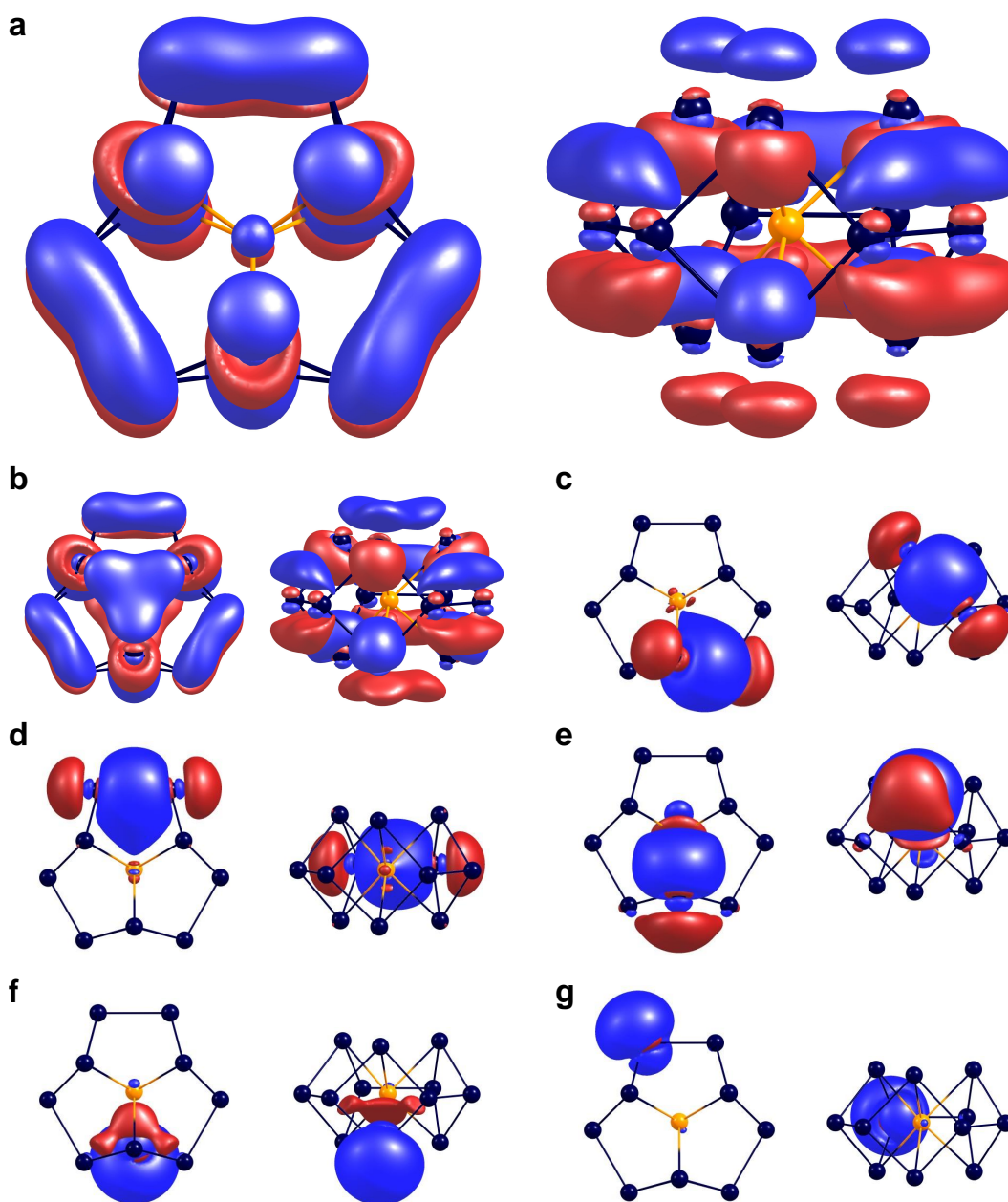


Figure 12.3: HOMO of the cluster anion $[\text{Th}@\text{Bi}_{12}]^{4-}$ and localized molecular orbitals (LMOs) from a Boys localization procedure^[599] at the def(2)-TZVP/PBE/grid m3 level of theory in top and side views. **a:** The HOMO (character a_2'' in D_{3h} symmetry). **b:** The LMO with the highest energy expectation value shows contributions from all 12 Bi atoms and has almost the same shape as the HOMO, which indicates intrinsic electron delocalization. **c:** Two-center LMO representing a Bi–Bi bond within a Bi_4 ring. **d:** Two-center LMO representing a Bi–Bi bond between two Bi_4 rings. **e:** Two-center LMO representing a Bi–Th bond. **f:** One-center LMO representing a lone pair at a Bi atom above/below the equatorial plane of the molecule. **g:** One-center LMO representing a lone pair at a Bi atom within the equatorial plane of the molecule. Contours are drawn at isovalues of ± 0.02 a.u. in blue and red, for approximately the same orientation of the molecule as shown in Fig. 12.2. Orbitals were visualized by Florian Weigend.

orbital remains. The HOMO–LUMO gap amounts to 0.425 eV and a TD-DFT calculation at the def(2)-TZVP/PBE/grid m3 level reveals the lowest triplet excitation energy to be located at 0.351 eV, being accessible with infrared light (2831 cm^{-1} and 3532 nm). To sum up, the experimental and quantum chemical findings suggest that two of the three criteria of aromaticity are fulfilled and form the starting point for an analysis of the magnetically induced current density.

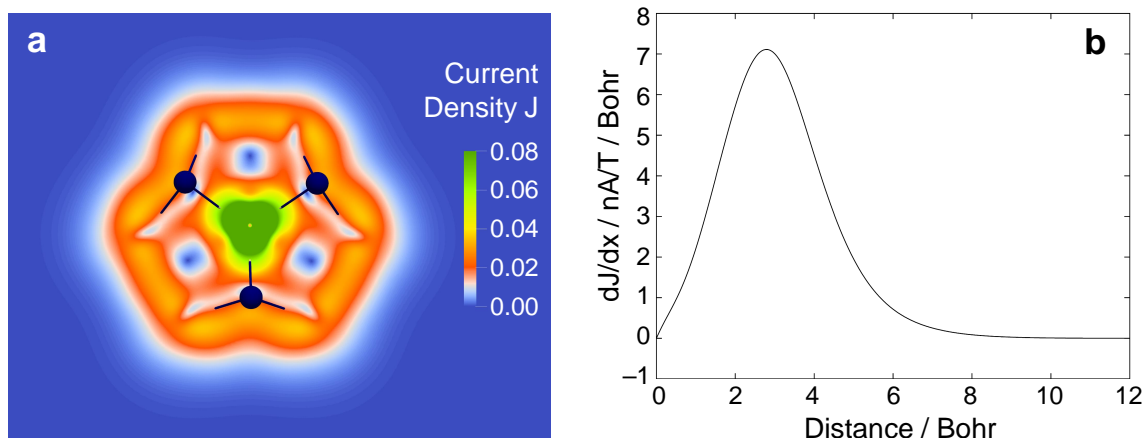


Figure 12.4: Calculated ring currents in $[\text{Th}@\text{Bi}_{12}]^{4-}$. **a:** Plot of the magnetically induced current density (in atomic units), 2 bohr above the plane of Bi_A atoms and the central Th atom. The magnetic field is perpendicular to the molecular plane. **b:** Profile of the magnetically induced current density to determine the boundaries for the numerical integration. The origin is at the zero point of the magnetically induced current density between the $\text{Bi}_A-\text{Bi}'_A$ bond and the Th atom. The integration plane is shown in Fig. 12.5.

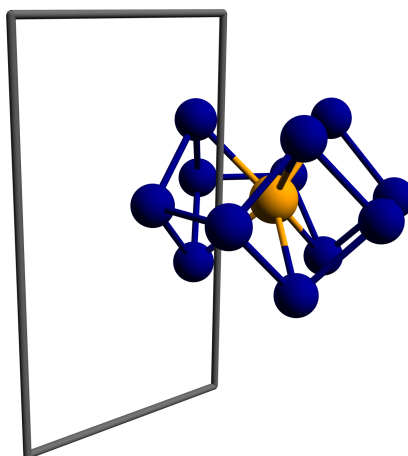


Figure 12.5: Integration plane for the magnetically induced current density calculations of $[\text{Th}@\text{Bi}_{12}]^{4-}$.

The magnetic criterion of aromaticity is studied with the ECP-based ansatz described above and scalar-relativistic all-electron DLU-X2C calculations^[105,107,379] employing the finite nucleus model throughout. The DLU-X2C calculations use two different basis sets, namely the Jorge-DKH-TZP^[213,487,488,600] and the Dyall-VTZ basis.^[187,188,190,495,601] Note that we have deleted the inner-most g function from the $6d/7s$ correlating set of Th to remove linear dependencies of the Dyall-VTZ basis set and the RI- J approximation is not applied as no auxiliary basis sets are available. The theoretical studies of the magnetic criterion are performed with the BP86,^[128,340] PBE,^[341] TPSS,^[346] B3LYP,^[128-130] PBE0,^[355] TPSSH,^[356] LC- ω PBE,^[359,529,530] ω B97X-D,^[360,529,530] and the CAM-B3LYP^[133,529,530] functional, as well as the LH07t-SVWN,^[138] LH12ct-SsirPW92,^[139] LH14t-calPBE,^[140] LH20t,^[370] LHJ14,^[141] and the PSTS functional in conventional gauge.^[134] The numerical integration of the DFT parts is performed with medium sized grids; grid 3 in ECP calculations^[294,315] and grid 3a in DLU-X2C calculations.^[482] Based on the pronounced dependence on the considered nuclei for NMR calculations, this large number of functionals is considered. We note in passing that these are the first magnetically induced current density calculations with local hybrid functionals. SCF convergence thresholds of $10^{-8} E_h$ ensure well converged orbitals and a threshold 10^{-7} a.u. is used for the norm of the residuum in the CPKS equations to ensure a sufficiently converged response of the density matrix. The magnetically induced current density is studied with the GIMIC code.^[423,424,427]

A plot of the magnetically induced current density is shown in Fig. 12.4. The left-hand side of this figure shows the magnetically induced current density calculated 2 bohr above the molecular plane of $[\text{Th}@\text{Bi}_{12}]^{4-}$. This molecular plane consists of the Bi_A atoms and the central Th atom. The right-hand side shows the profile of the magnetically induced current density through the $\text{Bi}_A\text{--Bi}'_A$ bond, which is used to determine the boundaries for the numerical integration of the current density to obtain the current strengths. The respective integration plane perpendicular to the molecular plane is depicted in Fig. 12.5. For the current profile calculation, this plane is partitioned into small slices with a length of 0.02 bohr and a height of 8 bohr above and below the molecular plane. The torus-shaped current density is structurally similar to that in planar rings. Therefore, the π -system may be described as a belt and simplified to a cycle. Net ring current strengths are listed in Tab. 12.2. The ECP-based approaches result in a diatropic net ring current of 22.4–26.5 nA/T and the DLU-X2C Hamiltonian tends to increase that ring current to 23.2–26.2 nA/T with the Dyll-VTZ basis and 24.7–27.5 nA/T with the Jorge-DKH-TZP basis set. Remarkably, this is about twice the ring current of benzene with 11.4 nA/T (TPSSh) and roughly the same ring current of porphine with 25.3 nA/T (TPSSh). Note that both benzene and porphine feature a significantly larger number of π -electrons. Benzene is a 6π and porphine a 26π -aromatic molecule, whereas the ring current of $[\text{Th}@\text{Bi}_{12}]^{4-}$ is mainly caused by 2 π -electrons. The increased ring current may be rationalized by the greater tendency for delocalization of metals. Therefore, $[\text{Th}@\text{Bi}_{12}]^{4-}$ is clearly aromatic based on the magnetic criterion.

Table 12.2: Current strengths in nA/T of $[\text{Th}@\text{Bi}_{12}]^{4-}$ with various computational methods. The inclusion of the current density to restore gauge-origin invariance instead of the external vector potential in the generalized kinetic energy density is denoted by a “c” at the beginning of the functional name. ECP calculations are carried out with the def2-TZVP basis set for Bi and def-TZVP for Th. The RI-*J* approximation is only applied in the ECP calculations.

	def(2)-TZVP/ECP	Dyll-VTZ/DLU-X2C	Jorge-DKH-TZP/DLU-X2C
BP86	22.4	23.2	24.7
PBE	22.7	23.4	24.8
TPSS	22.9	23.3	24.8
cTPSS	23.1	23.3	24.9
B3LYP	24.1	24.6	25.9
PBE0	25.1	25.4	25.5
TPSSh	24.0	24.2	25.5
cTPSSh	24.1	24.4	25.6
LC- ω PBE	26.5	25.9	27.5
ω B97X-D	25.8	25.9	27.4
CAM-B3LYP	25.3	25.3	26.8
LH07t-SVWN	23.9	26.2	24.7
cLH07t-SVWN	24.0	24.7	25.8
LH12ct-SsirPW92	24.5	25.3	26.2
cLH12ct-SsirPW92	24.6	25.4	26.2
LH14t-calPBE	24.0	24.9	26.0
cLH14t-calPBE	24.1	24.9	26.0
LH20t	25.1	25.4	26.4
cLH20t	24.9	25.4	26.3
PSTS	24.0	24.4	25.6
cPSTS	24.2	24.6	25.6
LHJ14	24.2	24.7	26.5
cLHJ14	23.4	23.8	26.0

The impact of the central Th^{4+} ion on the aromaticity is further studied. Therefore, the ring current of the bare and hypothetical Bi_{12}^{8-} ring is calculated. Moreover, this allows for an application of the NICS method, where a ghost atom is placed at the center of the cluster. Due to the absence of the Th atom, the NMR-tailored x2c-type basis sets^[203,482,483] are also used to calculate the NICS and ring current. Results are presented in Tab. 12.3. The ring current amounts to about 23 nA/T at the ECP level and ranges from about 21 nA/T to 23 nA/T when considering all electrons. This shows that Th^{4+} ion is mainly needed to stabilize the cycle and to allow for a synthetic access. The NICS values also clearly indicate the aromaticity with -17 ppm (ECP) and -15 to -19 ppm (DLU-X2C). To compare with, the ring currents and NICS values of Al_4^{2-} are 27.6 nA/T and -31.8 ppm at the def2-TZVP/PBE level of theory. The ring currents are rather similar. Notably, Al_4^{2-} features 2 π -electrons delocalized over a small four-membered ring and for $[\text{Th}@\text{Bi}_{12}]^{4-}$ or Bi_{12}^{8-} the same number of electrons is delocalized over 12 atoms. The greater difference for the NICS values is explained by the distance of the ghost atom to the delocalized π -system. For Al_4^{2-} , the distance of the ghost atom to the Al atoms is 126.47 pm, whereas the distance amounts to 236.28 pm for Bi_{12}^{8-} .

Furthermore, the number of π -electrons in the Bi_{12} torus is increased to study whether a $(4n + 2)$ rule applies. The hypothetical 4 π -electrons system Bi_{12}^{10-} features a triplet ground state like the square planar cyclobutadiene. At the ECP/def2-TZVP level of theory, the triplet state is lower in energy by 9.76 kJ/mol with BP86, 8.54 kJ/mol with PBE, 8.01 kJ/mol with TPSS, and 9.74 kJ/mol with TPSSh. Using the fractional occupation number (FON) approach^[602] with a proper damping level of 9 a.u. smoothly converges to the triplet state. On the contrary, the hypothetical 6 π -electrons system Bi_{12}^{12-} sustains a large net diatropic ring current of more than 40 nA/T and NICS values of about -33 ppm with triple- ζ basis sets as listed in Tab. 12.4. Therefore, Bi_{12}^{12-} is aromatic based on the magnetic criterion and may even show a record ring current. However, a synthetic access to such a highly negative charged polybismuthide is not very likely.

To conclude, $[\text{Th}@\text{Bi}_{12}]^{4-}$ is aromatic based on the formulated criteria and sustains a large ring current despite featuring 2 π -electrons only. Therefore, the limits and boundaries of all-metal aromaticity are pushed by $[\text{Th}@\text{Bi}_{12}]^{4-}$.

Table 12.3: Current strengths (in nA/T) and NICS (in ppm) of B_{12}^8 with various computational methods. The RI- J approximation is used with the def(2)-TZVP and the x2c-type basis sets. The def(2)-TZVP basis set employs ECPs whereas all other basis sets are combined with the DLU-X2C Hamiltonian.

	def(2)-TZVP		Dyall-VTZ		Jorge-DKH-TZP		x2c-SVPall-s		x2c-TZVPall-s		x2c-QZVPall-s	
	GIMIC	NICS	GIMIC	NICS	GIMIC	NICS	GIMIC	NICS	GIMIC	NICS	GIMIC	NICS
BP86	23.4	-16.8	23.3	-17.6	23.0	-15.3	21.0	-15.5	21.8	-16.3	23.0	-18.0
PBE	23.7	-17.1	23.4	-17.8	23.2	-15.4	21.1	-15.6	22.0	-16.5	22.8	-18.2
TPSS	23.4	-17.1	23.1	-17.7	22.8	-15.7	20.8	-15.7	21.7	-16.5	23.1	-18.0
cTPSS	24.0	-16.1	23.3	-17.9	22.9	-15.8	20.9	-15.8	21.9	16.7	23.0	-18.2
B3LYP	23.6	-17.0	23.4	-17.6	23.0	-15.3	20.8	-16.3	21.9	-16.6	23.1	-17.9
PBE0	24.2	-17.9	23.1	-17.7	23.4	-16.9	21.2	-15.6	22.3	-17.3	23.6	-18.7
TPSSh	23.7	-17.5	23.4	-18.0	23.0	-16.3	20.9	-16.2	21.9	-16.9	23.1	-18.3
cTPSSh	23.8	-17.6	23.6	-18.2	23.1	-16.3	21.0	-16.3	22.1	-17.0	23.2	-18.5
LC- ω PBE	23.1	-17.4	22.8	-17.6	22.0	-17.2	19.6	-16.2	21.2	-16.7	22.5	-17.7
ω B97X-D	23.6	-17.3	23.6	-17.7	22.9	-17.1	20.4	-16.6	21.8	-16.8	23.3	-17.9
CAM-B3LYP	23.2	-16.9	23.0	-17.3	22.3	-16.8	20.2	-16.4	21.4	-16.5	22.8	-17.5
LH07t-SVWN	23.7	-17.1	23.0	-16.4	23.5	-17.8	20.8	-16.3	21.9	-16.7	23.3	-18.1
cLH07t-SVWN	23.8	-17.2	23.6	-17.9	23.1	-16.4	21.0	-16.4	22.1	-16.8	23.4	-18.2
LH12ct-SsirPW92	23.9	-17.3	23.7	-17.9	23.3	-16.7	20.9	-16.5	22.1	-16.9	23.5	-18.2
cLH12ct-SsirPW92	23.9	-17.3	23.8	-17.9	23.3	-16.7	21.1	-16.5	22.2	-16.9	23.5	-18.2
LH14t-calPBE	23.9	-17.4	23.7	-18.0	23.2	-16.5	21.0	-16.5	22.1	-16.9	23.5	-18.4
cLH14t-calPBE	23.8	-17.4	23.7	-18.0	23.2	-16.5	21.0	-16.4	22.1	-16.9	23.4	-18.4
LH20t	23.9	-17.5	23.8	-18.1	23.4	-16.9	20.9	-16.5	22.0	-16.9	23.7	-18.5
cLH20t	23.6	-17.4	23.5	-18.1	23.2	-16.8	20.6	-16.5	21.7	-16.8	23.3	-18.4
PST	23.7	-17.4	23.5	-18.0	23.0	-16.4	20.9	-16.3	22.0	-16.9	23.1	-18.3
cPST	23.8	-17.6	23.6	-18.2	23.1	-16.4	21.1	-16.4	22.2	-17.1	23.2	-18.4
LH14	24.1	-17.7	24.2	-18.4	23.3	-17.2	21.1	-16.5	22.2	-16.8	24.1	-18.8
cLH14	23.2	-17.6	23.1	-18.2	22.7	-17.1	20.4	-16.5	21.3	-16.8	23.0	-18.6

Table 12.4: Current strengths (in nA/T) and NICS (in ppm) of Bi₁₂⁴⁻ with various computational methods. The RI-*J* approximation is used with the def(2)-TZVP and the x2c-type basis sets. The def(2)-TZVP basis set employs ECPs whereas all other basis sets are combined with the DLU-X2C Hamiltonian.

	def(2)-TZVP		Dyall-VTZ		Jorge-DKH-TZP		x2c-SVPall-s		x2c-TZVPall-s		x2c-QZVPall-s	
	GIMC	NICS	GIMC	NICS	GIMC	NICS	GIMC	NICS	GIMC	NICS	GIMC	NICS
	BP86	42.0	-33.4	41.1	-34.2	41.0	-32.1	36.2	-31.3	37.9	-32.6	40.4
PBE	42.9	-34.0	41.9	-34.8	41.8	-32.7	36.9	-31.7	38.7	-33.2	41.1	-35.3
TPSS	42.6	-33.9	41.7	-34.7	41.8	-33.5	36.5	-31.6	38.6	-33.1	40.9	-35.2
cTPSS	42.8	-34.3	41.9	-35.1	42.0	-33.6	36.7	-31.8	38.8	-33.4	41.2	-35.5
B3LYP	40.7	-33.2	39.6	-33.8	40.0	-32.1	35.1	-30.9	36.6	-32.3	38.9	-34.3
PBE0	43.0	-34.8	41.7	-35.6	42.1	-33.8	36.7	-32.2	38.7	-33.9	41.0	-36.1
TPSSh	42.8	-34.3	41.6	-35.1	41.8	-33.5	36.5	-31.9	38.6	-33.5	40.9	-35.6
cTPSSh	43.0	-34.7	41.9	-35.4	42.0	-33.6	36.7	-32.1	38.8	-33.7	41.1	-35.8
LC- ω PBE	39.6	-33.5	38.3	-34.4	34.5	-30.5	14.2	-21.2	25.7	-27.8	37.4	-34.9
ω B97X-D	39.3	-33.2	37.9	-34.0	38.5	-32.5	32.1	-30.0	33.8	-31.5	37.1	-34.4
CAM-B3LYP	38.8	-32.5	37.6	-33.3	38.2	-31.5	32.3	-29.3	33.7	-30.9	37.0	-33.8
LH07t-SVWN	41.4	-33.8	40.9	-33.0	40.3	-34.6	35.6	-31.5	37.3	-32.9	39.7	-35.0
cLH07t-SVWN	41.6	-34.0	40.5	-34.8	41.0	-33.1	35.8	-31.6	37.5	-33.0	39.8	-35.1
LH12ct-SsirPW92	41.5	-34.1	40.4	-35.0	41.2	-33.4	35.6	-31.7	37.4	-33.2	39.7	-35.3
cLH12ct-SsirPW92	41.8	-34.3	40.5	-35.0	41.0	-33.1	35.8	-31.6	37.5	-33.0	39.8	-35.4
LH14t-calPBE	42.0	-34.1	41.0	-34.9	41.3	-33.2	36.0	-31.6	37.9	-33.1	40.3	-35.2
cLH14t-calPBE	42.0	-34.1	40.9	-34.9	41.3	-33.5	35.8	-31.8	37.6	-33.2	40.2	-35.2
LH20t	43.2	-34.8	42.1	-35.6	42.2	-34.1	36.4	-32.1	38.8	-33.8	41.3	-35.9
cLH20t	42.6	-34.6	41.4	-35.4	41.2	-33.1	35.9	-31.6	37.8	-33.1	40.6	-35.7
PSTS	42.6	-34.2	41.6	-35.0	41.7	-33.5	36.6	-31.9	38.6	-33.4	40.9	-35.4
cPSTS	42.9	-34.6	41.8	-35.4	41.9	-33.6	36.8	-32.1	38.8	-33.7	41.1	-35.7
LHJ14	43.0	-34.3	42.5	-35.3	41.4	-33.2	36.1	-31.2	38.4	-32.9	41.9	-35.6
cLHJ14	41.4	-33.7	40.5	-34.7	40.5	-32.9	35.0	-30.9	36.9	-32.4	39.7	-33.8

12.3 Ring Currents and NICS of $[\text{K}_2\text{Zn}_{20}\text{Bi}_{16}]^{6-}$

Zinc does not show a tendency to form clusters in the condensed phase and Zn usually adapts the +II oxidation state due to the stability of the closed d shell. Molecular Zn clusters can still be prepared via heterometallic cluster synthesis. The cluster anion $[\text{K}_2\text{Zn}_{20}\text{Bi}_{16}]^{6-}$ with a homoatomic $\{\text{Zn}_{12}\}$ subunit featuring Zn–Zn bonds was synthesized by Armin Eulenstein.^[603] The structure is shown in Fig. 12.6. The $\{\text{Zn}_{12}\}$ subunit is formed with the Zn3–Zn6 and the symmetry equivalent bonds in the cluster center. This unit is enclosed by a macrocycle consisting of eight Zn atoms (Zn1, Zn2, and symmetry equivalent atoms) and the 16 Bi atoms. A Boys localization procedure^[599] reveals multicenter bonds and thus inherent electron delocalization. Therefore, the cluster may sustain a ring current due to the cyclic shape and the embedded $\{\text{Zn}_{12}\}$ subunit. This forms the starting point for an analysis of the magnetically induced current density with the GIMIC method and nucleus-independent chemical shifts. The NICS method is applicable as a ghost atom can be placed at the center of the molecule. The distance of the ghost atom to the neighboring zinc atoms is 188.88 pm and thus larger than for Al_4^{2-} with 126.47 pm towards the aluminum atoms. Accordingly, the distance of the ghost atom to the Zn5–Zn6 bond amounts to 139.62 pm. Hence, the distance is sufficiently large to allow for a reasonable NICS value.

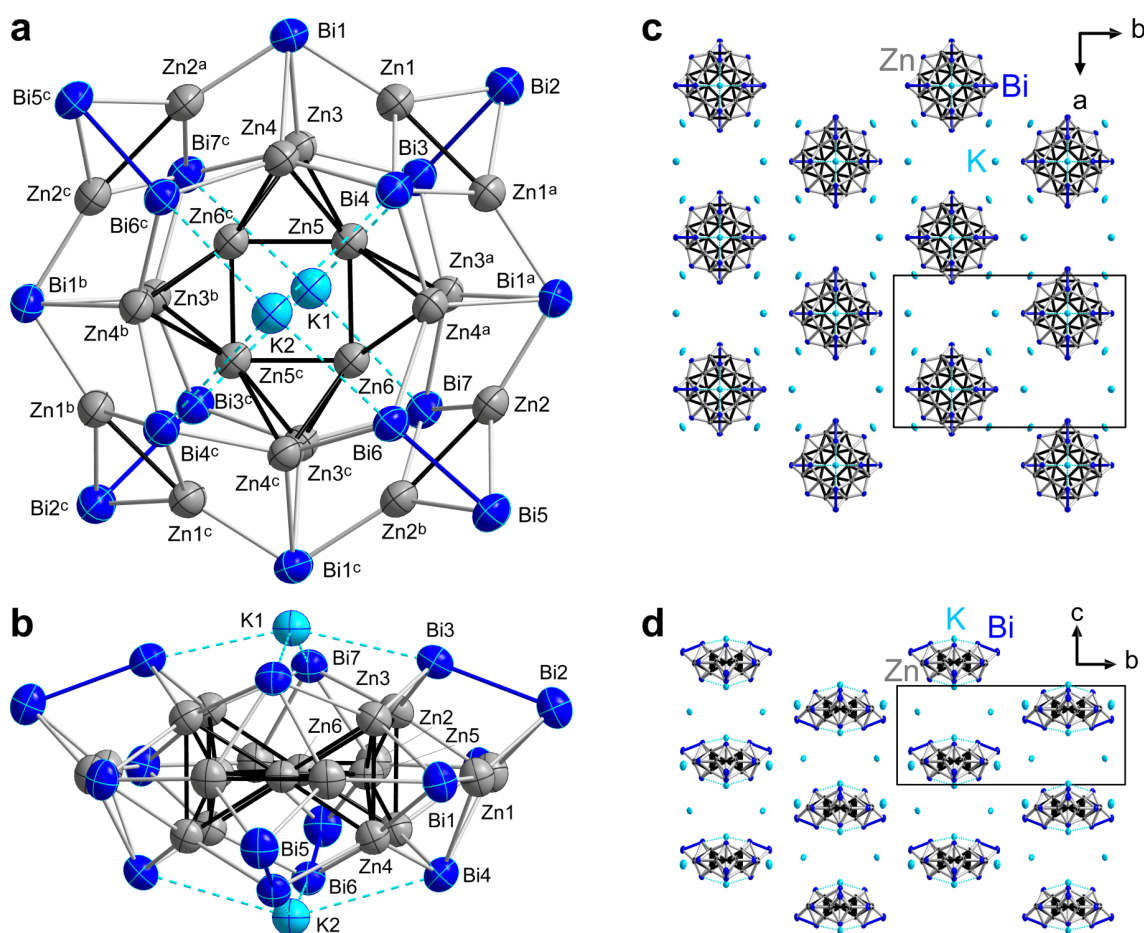


Figure 12.6: a: View of the oblate molecule $[\text{K}_2\text{Zn}_{20}\text{Bi}_{16}]^{6-}$ in $[\text{K}(\text{crypt-222})]_6[\text{K}_2\text{Zn}_{20}\text{Bi}_{16}]$ possessing idealized D_{2h} symmetry, which is reduced to crystallographic C_{2v} symmetry. b: Side view, upon an additional rotation about the C_2 axis running through K1 and K2 (by about 45° with regard to the orientation above). Displacement ellipsoids are drawn at 30% probability. c: View of packing of $[\text{K}_2\text{Zn}_{20}\text{Bi}_{16}]^{6-}$ anions and K^+ cations along the crystallographic c axis. d: View of packing anions and cations along the crystallographic b axis. C, N, and H atoms are not shown for clarity. The structure was examined by Werner Massa.

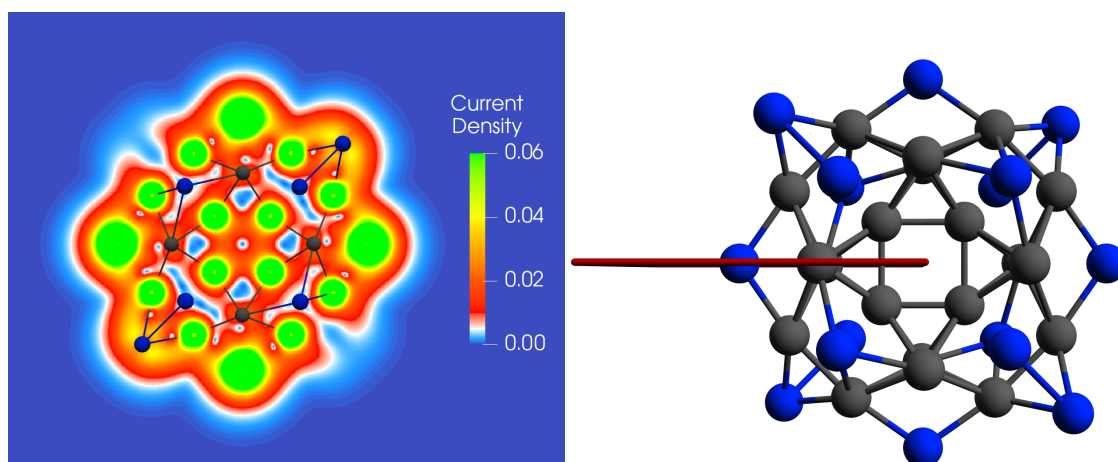


Figure 12.7: **Left:** Plot of the magnetically induced current density of $[\text{Zn}_{20}\text{Bi}_{16}]^{8-}$ in atomic units calculated 1 bohr above the plane of the Zn5 and Zn6 atoms at the dhf-TZVP/TPSS (grid 3) level of theory. The corresponding plot 1 bohr below the plane is identical apart from a rotation by 90° along an axis perpendicular to the molecular plane. **Right:** Integration plane to obtain the current strength based on a numerical integration of the magnetically induced current density. The integration plane, which starts at the center of the cluster, is shown in red. This integration plane is perpendicular to the molecular plane and parallel to the applied external magnetic field.

The magnetically induced current density is studied with an ECP-based approach as the placement of an integration plane is more involved for this cluster. Here, the integration plane is placed through a heavy atom like Bi and the additional core electrons described with the DLU-X2C ansatz would require very tight integration thresholds to avoid a significant loss of accuracy. Exemplary calculations did not finish within a month as the GIMIC code is not as efficient as the NMR shielding implementation. Consequently, the magnetically induced current density is obtained with the dhf-TZVP orbital and auxiliary basis set for the RI- J approximation^[202] combined with a small-core ECP for Bi.^[593] Based on the previous studies in Sec. 12.2, the TPSS functional is chosen and the kinetic energy density is generalized with the external magnetic field.^[407,461] Medium-sized grids (grid 3) are employed for the numerical integration of the XC parts.^[294,315] COSMO^[453,454] is applied to model the counter ions, however, the radius for the cavity of zinc was set to 222.3 pm. The SCF procedure is converged up to $10^{-7} E_h$ and the CPKS equations for the NMR shieldings are considered to be converged with a threshold of 10^{-7} a.u. for the norm of the residuum. The magnetically induced current density is then obtained with the GIMIC code,^[423,424,427] which requires the perturbed density of a NMR shielding calculation. For a better placement of the integration plane, the K^+ ions are neglected in these calculations. The impact of the K^+ ions on the induced current density is studied below with the NICS ansatz, for which the ECP-based treatment described above and the scalar-relativistic all-electron DLU-X2C Hamiltonian^[105,107,379] in the finite nucleus model are considered. The latter employs the NMR-tailored x2c-TZVPall-s basis sets^[482] and the x2c-TZVPall auxiliary basis set^[203] together with suitable grids (grid 3a) for the DFT part.^[482]

A plot of the magnetically induced current density of $[\text{Zn}_{20}\text{Bi}_{16}]^{8-}$ is depicted in the left-hand side of Fig. 12.7. The right-hand side shows the integration plane for the current strength calculation. The plot shows a ring current and the current strength amounts to 0.43–7.0 nA/T. Here, only a range is given as the integration plane is placed through a heavy metal atom and these atoms show a strong current density in the plot (marked in green). To compare with, the aromatic molecules porphine and zinc porphyrine sustain a diatropic net ring current of 25.4 nA/T and 25.1 nA/T. Benzene possesses a ring current of 11.5 nA/T at the same level of theory. The current strength depends on the number of electrons, the surface, and the topology.^[19] Therefore, a direct comparison of the degree of aromaticity of $[\text{Zn}_{20}\text{Bi}_{16}]^{8-}$ and benzene or porphine is not possible. Still, a qualitative assignment of the aromaticity based on the magnetic criterion is valid.

The NICS values reveal a similar picture with -4.2 ppm for $[\text{Zn}_{20}\text{Bi}_{16}]^{8-}$ and -4.4 ppm for $[\text{K}_2\text{Zn}_{20}\text{Bi}_{16}]^{6-}$. DLU-X2C calculations yield NICS values of -4.2 ppm and -3.6 ppm, respectively. Therefore, the K^+ ions are of minor importance for the ring current and are mainly needed for the stabilization and the synthetic access. For comparison, the NICS values of porphine and benzene are -14.6 ppm and -8.0 ppm, respectively. Thus, the cluster $[\text{K}_2\text{Zn}_{20}\text{Bi}_{16}]^{6-}$ may be classified as weakly aromatic based on the magnetic criterion.

Non-aromatic compounds show significantly decreased NICS values and current strengths. The heterometallic compound $[\text{Hg}_8\text{Te}_{16}]^{8-}$ with a porphine-like structure only shows a ring current of 0.24 nA/T.^[604] The NICS value is 1.2 ppm with the DLU-X2C Hamiltonian. As expected, the ECP-based Hamiltonian with the def2-TZVP basis^[198] and auxiliary basis set^[312] results in essentially the same NICS value of 1.3 ppm. Here, the NICS values are positive and essentially vanish.

13 Summary and Conclusions

In this work, the relativistic (one-electron) exact two-component (X2C) theory is applied to nuclear magnetic resonance (NMR) shielding tensors and NMR indirect spin–spin coupling constants. For NMR shieldings, a scalar-relativistic framework is considered whereas the coupling constants use a quasirelativistic framework. The latter describes scalar-relativistic effects as well as spin–orbit interactions. Compared to the non-relativistic approach, X2C results in a considerable increase of the computational costs. Therefore, the diagonal local approximation to the unitary decoupling transformation (DLU) is derived and implemented for NMR properties. The highly efficient DLU ansatz drastically reduces the computational demands, making routine calculations of large molecules with more than 100 atoms and several thousand basis functions possible. With this implementation, all shielding constants of the very large Ag_{147}^- cluster employing more than 17,000 uncontracted and nearly 8,000 contracted basis functions are calculated in just 5 days with a single thread and a “pure” density functional approximation. Further speed-ups are obtained by using the available shared-memory parallelization. The error introduced by DLU is assessed for main-group and transition-metal compounds. It is found to be negligible as it typically amounts to less than 1 ppm even for heavy elements. To compare with, the impact of relativistic effects typically amounts to a few hundred ppm and the range of the respective NMR spectra covers a few thousand ppm. The error is further assessed in comparison with the impact of the density functional approximation and the basis set. Similarly, the NMR indirect spin–spin coupling constants of organometallic complexes with more than 130 atoms and about 2,500 contracted basis functions are obtained in about 5 hours using 12 threads with a triple- ζ basis set and hybrid density functionals without loss of accuracy. Here, the DLU scheme results in a speed-up by a factor of 60 compared to the full X2C approach and the well established resolution of the identity approximation as well as the seminumerical exchange approximation are applied to the two-electron integrals. For the first time in X2C theory, the finite nucleus model is used for both the scalar and vector potential. The quasirelativistic Hamiltonian accurately reproduces the results of the “fully” relativistic four-component ansatz for both main-group and transition-metal compounds such as palladium and platinum complexes requiring only a fraction of the computational resources. The DLU error is assessed for small main-group molecules and organometallic alkynyl compounds and amounts to less than 0.5 Hz for the organometallic alkynyl compounds of Si, Ge, Sn, and Pb. In contrast, the finite nuclear size effects significantly change the coupling constants of Sn and Pb molecules as the Fermi-contact interaction is very sensitive towards the density in the vicinity of the nuclei.

Electron correlation is treated within density functional theory (DFT) up to the fourth rung of Jacob’s ladder consisting of global, range-separated, and local hybrid functionals. This results in the first implementation of NMR coupling constants at the quasirelativistic X2C level within a density functional framework. Previous approaches were restricted to HF theory and their applicability is therefore limited. In the presented DFT framework, the kinetic energy density is generalized using the paramagnetic current density to ensure gauge invariance and to restore the iso-orbital constraint. For the first time, this generalization is applied to NMR coupling constants in non-relativistic and relativistic quantum chemistry. Furthermore, the modern class of local hybrid functionals (LHFs), which allow for a position-dependent admixture of HF exchange, is applied to relativistic NMR coupling constants for the first time. Additionally, the first application of LHFs, which are not based on the simple iso-orbital indicator, to NMR shifts is presented. The impact of different density functional approximations is assessed throughout the periodic table of elements. In these benchmark

studies, the local hybrid functionals show some potential in their application to NMR properties, however, the currently available LHF's are not as robust as the popular PBE0 and TPSSh functionals. Therefore, more work is needed for the class of LHF's to reach the performance of the well established global and range-separated hybrid functionals.

The NMR properties are sensitive towards the basis set. Therefore, tailored basis sets for NMR shifts are developed with double, triple, and quadruple- ζ quality. For this purpose, analytical basis set gradients are derived and implemented at the scalar-relativistic X2C level. Tight p functions are added to describe the density in the vicinity of the nuclei. Additionally, p and d functions are employed for the outer-core and the valence region of heavier elements. The accuracy of the tailored basis sets is assessed for a large test set of 255 closed-shell molecules and compared to other frequently used basis sets. Here, the developed basis sets perform similar to the much larger basis sets of Dyall, which are probably the most commonly used relativistic all-electron basis sets to date. The NMR-tailored x2c-TZVPall-s and x2c-QZVPall-s basis sets result in the same accuracy as the Dyall-VTZ or Dyall-VQZ bases at notably reduced computational costs. First steps towards optimized basis sets for NMR coupling constants were presented. Yet, further work is needed to ensure balanced errors for all elements up to radon.

The three main parameters of a quantum chemical calculation are the Hamiltonian, the method used for treating electron correlation, and the basis set. The thorough consideration and assessment of these three parameters for main-group and transition-metal systems allows for a robust and efficient computational methodology of NMR shifts and coupling constants throughout the periodic table of elements. The developed implementation is applied to phosphinidene complexes of the fourth main group as well as all-metal Th–Bi and Zn–Bi clusters. The DLU-X2C Hamiltonian results in a remarkable agreement with the experimental NMR and UV/Vis spectra of the phosphinidene complexes of Ge, Sn, and Pb. Using the introduced tools, the $p\pi$ – $p\pi$ bonding character between phosphorus and lead could be confirmed for the first ever synthesized compound exhibiting this bonding interaction. Furthermore, the magnetic properties of the anionic cluster $[\text{Th}@\text{Bi}_{12}]^{4-}$ are analyzed and the magnetically induced current density is calculated based on the NMR shielding implementation. Magnetically induced current density studies reveal a considerable ring current in the $\{\text{Bi}_{12}\}$ moiety of the cluster and therefore confirm the all-metal aromaticity based on the magnetic criterion. The aromaticity is further illustrated by the highly symmetric structure and the (nearly) identical Bi–Bi bond lengths. To compare with, the larger cluster $[\text{K}_2\text{Zn}_{20}\text{Bi}_{16}]^{6-}$ sustains a notably decreased ring current. Therefore, $[\text{Th}@\text{Bi}_{12}]^{4-}$ is the largest known substantially all-metal aromatic compound, which is experimentally secured. This demonstrates that the DLU-X2C Hamiltonian is an efficient, robust, and versatile tool for chemical applications. In future developments, the methodology can be extended to the electron paramagnetic resonance (EPR) hyperfine coupling constants and g tensors straightforwardly as the one-electron terms are available from the implementation of NMR shifts and coupling constants of closed-shell systems.

A Appendix

A.1 Integral Evaluation in the Finite Nucleus Model

The integral evaluation is demonstrated for the potential integral in a finite nucleus model. The integral evaluation herein differs from the previously presented scheme,^[106] which used the recurrence relations for the Gauss–Rys method.^[157–159,605] Herein, the Gauss–Rys integration will be used for the integration of the variable stemming from the Laplace transformation of the potential operator. The integration over the electronic coordinate, \vec{r} , will be carried out with Gauss–Hermite quadrature. Therefore, all integrals for NMR properties are evaluated with the same methods.^[606] The integral derivatives of the potential and the relativistically modified potential are obtained by linear combinations as discussed in Sec. 4.3.1.

First, the combination of Gauss–Rys and Gauss–Hermite integration will be illustrated for the point-charge model as an introduction. Consider the potential integral of a nucleus C in the CAO basis

$$V_{AB}^C = N_A N_B \int_V \frac{e^{-ar_A^2} e^{-br_B^2} (x - A_x)^{i_x} (y - A_y)^{i_y} (z - A_z)^{i_z} (x - B_x)^{j_x} (y - B_y)^{j_y} (z - B_z)^{j_z}}{|\vec{r} - \vec{R}_C|} d\vec{r}, \quad (\text{A.1})$$

where the basis functions are denoted by A and B , which also denote the atom center. The exponents are a and b , respectively. A short-hand notation $r = |\vec{r}|$ is employed. The angular momentum numbers are i and j . \int_V indicates that the integration is carried out over the complete three-dimensional space. Using the Gaussian product theorem of Eq. 3.5 yields

$$V_{AB}^C = \kappa_{AB} \int_V \frac{e^{-pr_P^2} (x - A_x)^{i_x} (y - A_y)^{i_y} (z - A_z)^{i_z} (x - B_x)^{j_x} (y - B_y)^{j_y} (z - B_z)^{j_z}}{r_C} d\vec{r} \quad (\text{A.2})$$

with the prefactor and the new variables

$$\kappa_{AB} = N_A N_B \exp(-\mu R_{AB}^2), \quad (\text{A.3})$$

$$\mu = \frac{ab}{a+b}, \quad (\text{A.4})$$

$$p = a+b, \quad (\text{A.5})$$

$$P_v = \frac{aA_v + bB_v}{a+b} \quad \text{with } v \in \{x, y, z\}. \quad (\text{A.6})$$

The denominator in the integral is simplified by using a Laplace transformation^[151]

$$\frac{1}{r_C} = \frac{1}{\sqrt{\pi}} \int_{-\infty}^{\infty} e^{-t^2 r_C^2} dt. \quad (\text{A.7})$$

Therefore, the integral becomes

$$V_{AB}^C = \frac{\kappa_{AB}}{\sqrt{\pi}} \int_{-\infty}^{\infty} \int_V \tilde{r}_A^i \tilde{r}_B^j e^{-pr_P^2} e^{-t^2 r_C^2} d\vec{r} dt \quad (\text{A.8})$$

with

$$\tilde{r}_A^i = (x - A_x)^{i_x} (y - A_y)^{i_y} (z - A_z)^{i_z}, \quad (\text{A.9})$$

$$\tilde{r}_B^j = (x - B_x)^{j_x} (y - B_y)^{j_y} (z - B_z)^{j_z}. \quad (\text{A.10})$$

The two exponential functions in the integral are again simplified with the Gaussian product theorem

$$V_{AB}^C = \frac{\kappa_{AB}}{\sqrt{\pi}} \int_{-\infty}^{\infty} \int_V \tilde{r}_A^i \tilde{r}_B^j e^{-(p+t^2)r_S^2} e^{-\frac{pt^2}{p+t}R_{PC}^2} d\vec{r} dt \quad (\text{A.11})$$

with the center S given by

$$S_v = \frac{pP_v + t^2C_v}{p + t^2} \quad \text{with } v \in \{x, y, z\}. \quad (\text{A.12})$$

The substitution $t^2 = pu^2$ with $dt = \sqrt{p} du$ leads to

$$V_{AB}^C = \frac{2\kappa_{AB}\sqrt{p}}{\sqrt{\pi}} \int_0^{\infty} \left\{ \int_V \tilde{r}_A^i \tilde{r}_B^j e^{-p(1+u^2)r_N^2} d\vec{r} \right\} e^{-p\frac{u^2}{1+u^2}R_{PC}^2} du \quad (\text{A.13})$$

with

$$N_v = \frac{pP_v + pu^2C_v}{p + pu^2} \quad \text{with } v \in \{x, y, z\}. \quad (\text{A.14})$$

The integral boundaries regarding u are shifted by exploiting the symmetry and adding a factor of two. The three-dimensional integral in curly brackets, $\{ \}$, is separable into the individual Cartesian components. Thus, it is separated into three one-dimensional integrals. A further substitution is made

$$q^2 = \frac{u^2}{1+u^2} \Leftrightarrow u^2 = \frac{q^2}{1-q^2} \rightarrow du = (1-q^2)^{3/2} dq \quad (\text{A.15})$$

with $q \in [0, 1]$. Therefore, the integral becomes

$$V_{AB}^C = \frac{2\kappa_{AB}\sqrt{p}}{\sqrt{\pi}} \int_0^1 \left\{ \int_V \tilde{r}_A^i \tilde{r}_B^j e^{-p\left(1+\frac{q^2}{1-q^2}\right)r_N^2} d\vec{r} \right\} \frac{e^{-pq^2R_{PC}^2}}{(1-q^2)^{3/2}} dq. \quad (\text{A.16})$$

As the Cartesian components of the integral in curly brackets are separable, we may consider the x component now

$$\int_{-\infty}^{\infty} x_A^{i_x} x_B^{j_x} \exp \left[\left(1 + \frac{q^2}{1-q^2} \right) \left(x - \frac{pP_x + p\frac{q^2}{1-q^2}C_x}{p + \frac{pq^2}{1-q^2}} \right) \right] dx. \quad (\text{A.17})$$

We now aim at rearranging this integral for an application of the Gauss–Hermite quadrature. To do so, the substitution

$$\tilde{x} = \left[\left(1 + \frac{q^2}{1-q^2} \right) \left(x - \frac{pP_x + p\frac{q^2}{1-q^2}C_x}{p + \frac{pq^2}{1-q^2}} \right) \right] \rightarrow dx = d\tilde{x} \frac{1}{\sqrt{p(1+q^2/(1-q^2))}} \quad (\text{A.18})$$

is applied and the x integral finally results in

$$\frac{1}{\sqrt{p(1+q^2/(1-q^2))}} \int_{-\infty}^{\infty} e^{-\tilde{x}^2} \underbrace{\left[\frac{\tilde{x}}{\sqrt{p\left(1+\frac{pq^2}{1-q^2}\right)}} + \frac{pP_x + \frac{q^2}{1-q^2}C_x}{p + \frac{pq^2}{1-q^2}} - X_A \right]^{i_x} \left[m - X_B \right]^{j_x}}_{=m(\tilde{x},q)} d\tilde{x}. \quad (\text{A.19})$$

The Gauss–Hermite quadrature evaluates a Gaussian integral according to

$$\int_{-\infty}^{\infty} e^{-x^2} f(x) dx = \sum_{k=1}^n w_k f(x_k), \quad (\text{A.20})$$

where x_k are the roots of the Hermite polynomial H_n and the weights are calculated by^[607,608]

$$w_k = \frac{2^{n-1} n! \sqrt{\pi}}{n^2 (H_{n-1}(x_k))^2}. \quad (\text{A.21})$$

By applying Gauss–Hermite integration, this integral is evaluated as

$$\frac{1}{\sqrt{p(1+q^2/(1-q^2))}} \underbrace{\sum_{k=1}^{n_H} w_k (m_k(\tilde{x}, q) - X_A)^i (m_k(\tilde{x}, q) - X_B)^j}_{=[\text{x-GH}(\tilde{x}, q)]}, \quad (\text{A.22})$$

where the sum runs from 1 to $n_H = \frac{i+j}{2} + 1$ and w_k is the corresponding weight function. m_k is calculated with the roots of the Hermite polynomial of order k , \tilde{x}_k . Note that in TURBOMOLE the weights are multiplied by $\sqrt{\pi}$. Inserting the expression for x in Eq. A.16 and interchanging the Cartesian components for y and z yields

$$V_{AB}^C = \frac{2\kappa_{AB}}{p\sqrt{\pi}} \int_0^1 e^{-pq^2 R_{PC}^2} [\text{x-GH}(\tilde{x}, q)] [\text{y-GH}(\tilde{y}, q)] [\text{z-GH}(\tilde{z}, q)] dq. \quad (\text{A.23})$$

Now the Gauss–Rys integration method is applied to the integration with respect to q . Therefore, this integration is carried out as a weighted sum with the roots of the Rys polynomials^[155,156]

$$\int_0^1 P_L(q^2) e^{-Oq^2} dq = \sum_{l=1}^N P_L(q_l^2) w_l, \quad (\text{A.24})$$

where $P_L(q^2)$ is a polynomial of order L and N is larger or equal than $L/2$. w_l is the integration weight and q_l is a root of the Rys polynomial, $R_N(q, O)$. So, the roots depend on the exponent $O = pR_{PC}^2$. Consequently, the potential integral follows as

$$V_{AB}^C = \frac{2\kappa_{AB}}{p\sqrt{\pi}} \sum_{l=1}^{n_R} w_l [\text{x-GH}(\tilde{x}, q)] [\text{y-GH}(\tilde{y}, q)] [\text{z-GH}(\tilde{z}, q)] \quad (\text{A.25})$$

with $n_R = \frac{i+j}{2} + 1$. Note that m in $[\text{x-GH}]$ etc. depends on the Gauss–Hermite and the Gauss–Rys roots. Resubstituting u and q as well as x results in

$$V_{AB}^C = \frac{2\kappa_{AB}}{p\sqrt{\pi}} \sum_{l=1}^{n_R} w_l \sum_{k=1}^{n_H} w_k \underbrace{\left(\frac{x_k}{\sqrt{p + pu_l^2}} + \frac{pP_x + pu_l^2 C_x}{p + pu_l^2} - X_A \right)}_{=g(x,u)}^{i_x} \left(g(x, u) - B_A \right)^{j_x} \dots \quad (\text{A.26})$$

The Rys roots and weights are obtained based on Ref. 609. The integral evaluation is carried out with two nested loops. The outer loop performs the Gauss–Rys integration and the inner loop the Gauss–Hermite quadrature.

Second, the finite nucleus model is considered. Here, the potential integral is given as

$$V_{AB} = N_A N_B N_C \int_V \int_V \frac{\tilde{r}_A^i \tilde{r}_B^j e^{-ar_A^2} e^{-br_B^2} e^{-\zeta(R-R_C)^2}}{|\vec{r} - \vec{R}|} d\vec{r} d\vec{R}, \quad (\text{A.27})$$

where N_C is the normalization of the Gaussian charge distribution, $N_C = (\zeta/\pi)^{3/2}$. Similar to the previous integral, we make use of the Gaussian product theorem for the Gaussian A and B as well as the Laplace transformation to arrive at

$$V_{AB} = N_A N_B N_C \frac{e^{-\mu R_{AB}^2}}{\sqrt{\pi}} \int_{-\infty}^{\infty} \int_V \int_V \tilde{r}_A^i \tilde{r}_B^j e^{-pr_P^2} e^{-\zeta(\vec{R}-\vec{R}_C)^2} e^{-t^2(\vec{r}-\vec{R})^2} d\vec{r} d\vec{R} dt. \quad (\text{A.28})$$

Further using the Gaussian product theorem for the charge density and the Laplace-transformation term

$$e^{-\zeta(R-R_C)^2} e^{-t^2(r-R)^2} = \exp\left(-(\zeta+t^2)\left(\vec{R} - \frac{\zeta\vec{R}_C + t^2\vec{r}}{\zeta+t^2}\right)^2\right) \exp\left(-r_C^2 \frac{\zeta t^2}{\zeta+t^2}\right) \quad (\text{A.29})$$

allows separate \vec{R} and to carry out the integration over \vec{R} in spherical coordinates. Defining

$$\tilde{\vec{R}} = \vec{R} - \frac{\zeta\vec{R}_C + t^2\vec{r}}{\zeta+t^2} \quad (\text{A.30})$$

results in the integration over \vec{R} according to

$$4\pi \int_0^{\infty} \tilde{R}^2 e^{-(\zeta+t^2)\tilde{R}^2} d\tilde{R} = \frac{4\pi}{4} \frac{\sqrt{\pi}}{(\zeta+t^2)^{3/2}} = \left(\frac{\pi}{\zeta+t^2}\right)^{3/2}. \quad (\text{A.31})$$

Hence, the integral is simplified to

$$V_{AB} = \pi \kappa_{AB} N_C \int_{-\infty}^{\infty} \int_V \tilde{r}_A^i \tilde{r}_B^j \exp(-pr_P^2) \frac{1}{(\zeta+t^2)^{3/2}} \exp\left(-r_C^2 \frac{\zeta t^2}{\zeta+t^2}\right) d\vec{r} dt. \quad (\text{A.32})$$

The Gaussian product theorem is applied again to shift the dependence on the electronic coordinate to one Gaussian

$$V_{AB} = \pi \kappa_{AB} N_C \int_{-\infty}^{\infty} \int_V \tilde{r}_A^i \tilde{r}_B^j \frac{\exp\left(-\left(p + \frac{\zeta t^2}{\zeta+t^2}\right) r_S^2\right)}{(\zeta+t^2)^{3/2}} \exp\left(-R_{PC}^2 \frac{p\zeta t^2 / (\zeta+t^2)}{p + \zeta t^2 / (\zeta+t^2)}\right) d\vec{r} dt. \quad (\text{A.33})$$

The center of the Gaussian with the electronic coordinate is given by

$$S_v = \frac{pP_v + \zeta t^2 C_v / (\zeta+t^2)}{p + \zeta t^2 / (\zeta+t^2)} \quad \text{with } v \in \{x, y, z\}. \quad (\text{A.34})$$

For the application of the Gauss–Rys quadrature, the substitution

$$u^2 = \frac{t^2}{\zeta+t^2} \Leftrightarrow t^2 = \frac{\zeta u^2}{1-u^2} \longrightarrow dt = \sqrt{\zeta} (1-u^2)^{-3/2} du \quad (\text{A.35})$$

is introduced to change the integration boundaries as $u \in [0, 1]$. Therefore, the boundaries are now in the proper range for the Gauss–Rys method. The substitution further yields $(\zeta+t^2)^{3/2} = (1-u^2)^{-3/2} \zeta^{3/2}$ and $S_v = (pP_v + \zeta u^2 C_v) / (p + \zeta u^2)$.

Hence, the potential integral follows as

$$V_{AB} = 2\pi\kappa_{AB}\tilde{N}_C\sqrt{\zeta}\int_0^1\int_V\tilde{r}_A^i\tilde{r}_B^j\exp\left(-\left(p+\zeta u^2\right)r_S^2\right)\exp\left(-R_{PC}^2\frac{p\zeta u^2}{p+\zeta u^2}\right)d\vec{r}du \quad (\text{A.36})$$

with $\tilde{N}_C = \pi^{-3/2}$. Now, the integral over the electronic coordinates can be separated into the Cartesian components to use the Gauss–Hermite quadrature. We aim at rewriting the second term for an easier application of the Gauss–Rys scheme. Therefore, the substitution

$$\chi^2 = \frac{p+\zeta}{\zeta u^2+p}u^2 \Leftrightarrow u^2 = \frac{p\chi^2}{p+\zeta-\zeta\chi^2} \rightarrow d\chi = \frac{p+\zeta}{(p+\zeta-\zeta\chi^2)^{3/2}}\sqrt{p}du \quad (\text{A.37})$$

is introduced. Note that $\chi \in [0, 1]$. Inserting this into the integral equation results in

$$V_{AB} = 2\pi\kappa_{AB}\tilde{N}_C\sqrt{\zeta p(p+\zeta)}\int_0^1\left\{\int_V\tilde{r}_A^i\tilde{r}_B^j\exp\left[-\left(p+\zeta u^2\right)r_S^2\right]d\vec{r}\right\}\frac{\exp\left(-\rho R_{PC}^2\chi^2\right)}{(p+\zeta-\zeta\chi^2)^{3/2}}d\chi, \quad (\text{A.38})$$

where we defined $\rho = p\zeta/(p+\zeta)$. The integration in curly brackets is now done with Gauss–Hermite integration by separating the three Cartesian components. Consider the Cartesian component x for the integral in curly brackets

$$\int_{-\infty}^{\infty}x_A^{i_x}x_B^{j_x}\exp\left[-\left(p+\zeta u^2\right)x_S^2\right]dx. \quad (\text{A.39})$$

Application of the substitution

$$\tilde{x}^2 = \left(p+\zeta u^2\right)x_S^2 \Leftrightarrow x = \frac{\tilde{x}}{\sqrt{p+\zeta u^2}} + S_x \rightarrow dx = \frac{1}{\sqrt{p+\zeta u^2}}d\tilde{x} \quad (\text{A.40})$$

simplifies the x integral to

$$\int_{-\infty}^{\infty}\left(\frac{\tilde{x}}{\sqrt{p+\zeta u^2}} + X_{SA}\right)^{i_x}\left(\frac{\tilde{x}}{\sqrt{p+\zeta u^2}} + X_{SB}\right)^{j_x}\frac{1}{\sqrt{p+\zeta u^2}}e^{-\tilde{x}^2}d\tilde{x}. \quad (\text{A.41})$$

Note that \tilde{x} depends on the variable of the Laplace integration, u or χ . This integral is computed with Gauss–Hermite quadrature according to

$$\underbrace{\sum_{k=1}^{n_H}w_k\left(\frac{\tilde{x}_k}{\sqrt{p+\zeta u^2}} + X_{SA}\right)^{i_x}\left(\frac{\tilde{x}_k}{\sqrt{p+\zeta u^2}} + X_{SB}\right)^{j_x}}_{\text{x-GH}(\tilde{x},u)}\frac{1}{\sqrt{p+\zeta u^2}}, \quad (\text{A.42})$$

where \tilde{x}_k are the roots of the Hermite polynomials. The integrals over y and z are obtained in the same manner. Therefore, the potential integral reads

$$V_{AB} = 2\pi\kappa_{AB}\tilde{N}_C\sqrt{\frac{\zeta}{p+\zeta}}\int_0^1\left\{\left[\text{x-GH}(\tilde{x},u)\right]\left[\text{y-GH}(\tilde{y},u)\right]\left[\text{z-GH}(\tilde{z},u)\right]\right\}\exp\left(-\rho R_{PC}^2\chi^2\right)d\chi \quad (\text{A.43})$$

and the application of the Gauss–Rys quadrature is straightforward.

The roots χ_l and weights w_l are obtained with ρR_{PC}^2 . The integral evaluation reads

$$V_{AB} = 2\pi\kappa_{AB}\tilde{N}_C\sqrt{\frac{\zeta}{p+\zeta}}\sum_{l=1}^{n_R}w_l\left[\text{x-GH}(\tilde{x},u_l)\right]\left[\text{y-GH}(\tilde{y},u_l)\right]\left[\text{z-GH}(\tilde{z},u_l)\right], \quad (\text{A.44})$$

where u_l is obtained after the resubstitution as

$$u_l^2 = \frac{p\chi_l^2}{p+\zeta-\zeta\chi_l^2}. \quad (\text{A.45})$$

The center S_v for the Gauss–Hermite scheme follows as

$$S_{v,l} = \frac{pP_v + \zeta u_l^2 C_v}{p + \zeta u_l^2}. \quad (\text{A.46})$$

So, \tilde{x} and the roots for the Gauss–Hermite scheme can be computed for a given Rys root. Therefore, the Gauss–Hermite integration is performed inside a loop for the Gauss–Rys method. The integral evaluation was verified by comparison to the previous implementation using Gauss–Rys integration throughout^[106] and an implementation with the Obara–Saika scheme^[152–154] for the three-center RI- J integrals^[197,297,298] as discussed in Ref. 204. Furthermore, the point-charge limit was verified by using a finite nucleus exponent in the order of 10^9 .

A.2 Expectation Values in X2C and DLU-X2C

The calculation of expectation values in X2C and related decoupling approaches such as Douglas–Kroll–Hess theory requires additional care.^[31,242] Similar to the two-electron interactions in Sec. 2.6, neglecting the unitary transformation for the expectation values results in a picture-change error. The electronic 4c spinors and the 2c spinors are related by the unitary decoupling transformation

$$\Psi_i^+ = U \begin{pmatrix} \varphi_i^+ \\ 0 \end{pmatrix}. \quad (\text{A.47})$$

Consider the expectation value of a property operator \hat{P} in the four-component space and its transformation to the two-component space

$$\langle \Psi_i^+ | \hat{P} | \Psi_i^+ \rangle = \langle U \varphi_i^+ | \hat{P} | U \varphi_i^+ \rangle = \langle \varphi_i^+ | (U^\dagger \hat{P} U)^+ | \varphi_i^+ \rangle \neq \langle \varphi_i^+ | \hat{P}_{\text{NR}} | \varphi_i^+ \rangle, \quad (\text{A.48})$$

where $(U^\dagger \hat{P} U)^+$ indicates the electronic block of the transformed property operator and \hat{P}_{NR} denotes the non-relativistic operator. Thus, the unitary decoupling transformation has to be applied to the respective property operator of the expectation value. In X2C, this is carried out with the matrix representation of the property operator. Therefore, the picture-change correction is performed in three steps:

1. Set up the four-component operator.
2. Form the matrix representation of this operator by the basis set expansion considering the proper balance condition.
3. Perform the unitary transformation of the operator in its matrix representation.

The picture-change correction was implemented for the electric dipole and quadrupole moments, the magnetic dipole moment of the electron, and the nuclear electric field integrals. The picture-change correction is then performed according to

$$\mu_{\text{lg},u}^+ = \begin{pmatrix} U^{LL,\dagger} & U^{SL,\dagger} \end{pmatrix} \mathbb{D}_{\text{op}} \begin{pmatrix} U^{LL} \\ U^{SL} \end{pmatrix}, \quad (\text{A.49})$$

where \mathbb{D}_{op} denotes the matrix representation of the operator in the four-component space. Generally, electric operators are even, i.e. only the large-large and the small-large block contain non-vanishing elements. Magnetic operators are odd and only the large-small and the small-large block possess non-trivial contributions. This follows from the principle of minimal coupling

$$\hat{\vec{p}} \longrightarrow \hat{\vec{p}} + \frac{1}{c} \vec{A}, \quad (\text{A.50})$$

$$\vec{F} \longrightarrow \vec{F} - q\phi, \quad (\text{A.51})$$

where \vec{F} denotes the electric field, q the particle charge, and ϕ the electrostatic potential with $\hat{V} = -\phi_{\text{nuc}}$ for the interaction of the nuclei and the electrons. Owing to the structure of the Dirac–Hamilton operator in Eq. 2.7, the momentum operator and its generalization form the large-small and the small-large block of the Dirac matrix.

A.2.1 Electronic Moments: Dipole and Quadrupole Moment

The dipole moment operator, $\hat{\mu} = -\vec{r}$, in length gauge is a potential or electric operator. Thus, it is an even operator and only the large-large and the small-small block of the Dirac matrix contain non-zero elements

$$\mathbb{D}_{\text{lg},u} = \begin{pmatrix} \boldsymbol{\mu}_u & \mathbf{0}_2 \\ \mathbf{0}_2 & \frac{1}{4c^2} \tilde{\boldsymbol{\mu}}_u \end{pmatrix} \quad (\text{A.52})$$

with $u \in \{x, y, z\}$. Here, $\boldsymbol{\mu}_u$ is block-diagonal in the two-component space

$$\boldsymbol{\mu}_u = \begin{pmatrix} \boldsymbol{\mu}_u & \mathbf{0} \\ \mathbf{0} & \boldsymbol{\mu}_u \end{pmatrix} \quad \text{with} \quad \boldsymbol{\mu}_{\kappa\nu,u} = \langle \lambda_\kappa | \hat{\mu}_u | \lambda_\nu \rangle \quad (\text{A.53})$$

and the elements $\tilde{\boldsymbol{\mu}}$ denotes the relativistically modified dipole moment, which arises due to the restricted kinetic balance condition. After applying the Dirac identity, $\tilde{\boldsymbol{\mu}}$ is written with real matrices only

$$\tilde{\boldsymbol{\mu}} = \begin{pmatrix} \tilde{\boldsymbol{\mu}}^0 + i\tilde{\boldsymbol{\mu}}^z & \tilde{\boldsymbol{\mu}}^y + i\tilde{\boldsymbol{\mu}}^x \\ -\tilde{\boldsymbol{\mu}}^y + i\tilde{\boldsymbol{\mu}}^x & \tilde{\boldsymbol{\mu}}^0 - i\tilde{\boldsymbol{\mu}}^z \end{pmatrix}, \quad (\text{A.54})$$

where the individual matrices are defined as

$$(\tilde{\boldsymbol{\mu}}^0)_{\kappa\nu,u} = \langle \lambda_\kappa | \hat{p}_x \hat{\mu}_u \hat{p}_x + \hat{p}_y \hat{\mu}_u \hat{p}_y + \hat{p}_z \hat{\mu}_u \hat{p}_z | \lambda_\nu \rangle, \quad (\text{A.55})$$

$$(\tilde{\boldsymbol{\mu}}^x)_{\kappa\nu,u} = \langle \lambda_\kappa | \hat{p}_y \hat{\mu}_u \hat{p}_z - \hat{p}_z \hat{\mu}_u \hat{p}_y | \lambda_\nu \rangle, \quad (\text{A.56})$$

$$(\tilde{\boldsymbol{\mu}}^y)_{\kappa\nu,u} = \langle \lambda_\kappa | \hat{p}_z \hat{\mu}_u \hat{p}_x - \hat{p}_x \hat{\mu}_u \hat{p}_z | \lambda_\nu \rangle, \quad (\text{A.57})$$

$$(\tilde{\boldsymbol{\mu}}^z)_{\kappa\nu,u} = \langle \lambda_\kappa | \hat{p}_x \hat{\mu}_u \hat{p}_y - \hat{p}_y \hat{\mu}_u \hat{p}_x | \lambda_\nu \rangle. \quad (\text{A.58})$$

These integrals are evaluated based on Gauss–Hermite integration. The picture-change corrected dipole moments follow as

$$\boldsymbol{\mu}_{\text{lg},u}^+ = \begin{pmatrix} U^{LL,\dagger} & U^{SL,\dagger} \\ U^{LL} & U^{SL} \end{pmatrix} \begin{pmatrix} \boldsymbol{\mu}_u & \mathbf{0}_2 \\ \mathbf{0}_2 & \frac{1}{4c^2} \tilde{\boldsymbol{\mu}}_u \end{pmatrix} \begin{pmatrix} U^{LL} \\ U^{SL} \end{pmatrix}. \quad (\text{A.59})$$

The electric quadrupole moments are obtained in the same way by replacing x , y , and z in the dipole operator with x^2 , xy , xz , y^2 , yz , and z^2 .

In excited-state calculations, the dipole operator is also calculated in velocity gauge. In the limit of a complete basis set, the transition dipole moments are identical in length and velocity gauge. So, the difference of the two gauge choices serves as an estimate of the basis set completeness.^[610] In the following, we will discuss the scalar-relativistic ansatz as only this was implemented herein. The dipole operator in velocity gauge is introduced into the one-electron Dirac Hamiltonian, \hat{h}_{D} , by the principle of minimal coupling and a gauge transformation^[387,388] leading to

$$\hat{h}_{\text{D}} = (\beta - I_4) c^2 + c\vec{\alpha} \cdot \left(\hat{\vec{p}} + \frac{1}{c} \vec{A} \right), \quad (\text{A.60})$$

where the vector potential, \vec{A} , is defined via the electric field, \vec{F} , as

$$\vec{A}(t) = -c \int_0^t \vec{F}(t') dt'. \quad (\text{A.61})$$

Thus, the dipole operator is an odd operator in velocity gauge. As discussed in Sec. 4.2, the vector potential has to be formally included in the balance condition to result in the exact non-relativistic limit. Considering the scalar-relativistic effects only yields the spin-free Dirac matrix of the dipole operator in velocity gauge

$$\mathbf{D}_{\text{vg},u} = -\frac{1}{i\Omega} \begin{pmatrix} \mathbf{0} & \mathbf{p}_u \\ \mathbf{p}_u & \mathbf{0} \end{pmatrix}. \quad (\text{A.62})$$

Here, Ω refers to the excitation energy of a transition and the expectation value has to be formed with the respective transition density. The picture-change corrected dipole moments in velocity gauge to be contracted with the transition density matrix are

$$\boldsymbol{\mu}_{\text{vg},u}^{\dagger} = -\frac{1}{i\Omega} \begin{pmatrix} \mathbf{U}^{LL,\dagger} & \mathbf{U}^{SL,\dagger} \end{pmatrix} \begin{pmatrix} \mathbf{0} & \mathbf{p}_u \\ \mathbf{p}_u & \mathbf{0} \end{pmatrix} \begin{pmatrix} \mathbf{U}^{LL} \\ \mathbf{U}^{SL} \end{pmatrix}. \quad (\text{A.63})$$

As the momentum integrals are already available in standard quantum chemistry codes, the picture-change correction of the dipole moments in velocity gauge requires no new integrals to be implemented.

A.2.2 Magnetic Dipole Moment of the Electron

The magnetic dipole moment of the electron is given in the 4c space as^[611]

$$\hat{\mathbf{m}} = -(\hat{\mathbf{r}} \times \hat{\boldsymbol{\alpha}}) \quad (\text{A.64})$$

in units of Bohr's magneton. In the non-relativistic limit, this yields the common expression

$$\hat{\mathbf{m}} = -\left(\hat{\mathbf{l}} + 2\hat{\mathbf{s}}\right) \quad (\text{A.65})$$

with the orbital angular momentum, $\hat{\mathbf{l}}$, and the electron spin, $\hat{\mathbf{s}}$. The orbital angular momentum describes the diamagnetic contribution whereas the electron spin refers to the paramagnetic contribution. The magnetic dipole moment in the 4c Dirac picture features non-zero elements only for the large-small and the small-large part. In a basis set expansion with the restricted kinetic balance condition, the matrix elements read

$$(\mathbf{m}^{\text{LS}})_{\kappa\nu,u} = \langle \lambda_{\kappa} | [\hat{\mathbf{r}} \times \hat{\boldsymbol{\sigma}}]_u (\hat{\boldsymbol{\sigma}} \cdot \hat{\mathbf{p}}) | \lambda_{\nu} \rangle, \quad (\text{A.66})$$

$$(\mathbf{m}^{\text{SL}})_{\kappa\nu,u} = \langle \lambda_{\kappa} | (\hat{\boldsymbol{\sigma}} \cdot \hat{\mathbf{p}}) [\hat{\mathbf{r}} \times \hat{\boldsymbol{\sigma}}]_u | \lambda_{\nu} \rangle. \quad (\text{A.67})$$

Note that the large-small and the small-large block are not Hermitian, but the Dirac matrix is still Hermitian as the magnetic moment is an observable and the relation $\mathbf{m}_u^{\text{LS}} = \mathbf{m}_u^{\text{SL},\dagger}$ holds. Separating these matrix elements into spin-free and spin-dependent terms results in

$$(\mathbf{m}^{\text{LS}})_{\kappa\nu,u} = -\sigma_0 \langle \lambda_{\kappa} | \hat{\mathbf{l}}_u | \lambda_{\nu} \rangle + \sum_i \sigma_i \langle \lambda_{\kappa} | \delta_{ui} \hat{\mathbf{r}} \cdot \vec{\nabla} - \hat{r}_i \partial_u | \lambda_{\nu} \rangle, \quad (\text{A.68})$$

where the scalar-relativistic contribution is simply the orbital angular momentum. Therefore, only the spin-dependent contributions have to be implemented based on Gauss–Hermite integration.

A.2.3 Nuclear Electric Field Integrals

The nuclear electric field is given as

$$\vec{F}_{\text{nuc}} = -\vec{\nabla}\phi_{\text{nuc}} = \vec{\nabla}\hat{V}. \quad (\text{A.69})$$

In the point-charge model the nuclear electric field is directly obtained as

$$\vec{F}_{\text{nuc}} = \sum_I Z_I \frac{\vec{r} - \vec{R}_I}{|\vec{r} - \vec{R}_I|^3}. \quad (\text{A.70})$$

The Dirac matrix possesses non-vanishing integrals for the large-large and the small-small block like the dipole moments in length gauge. Therefore, the matrix elements in a restricted kinetically balanced basis set of the large-large block read

$$(\mathbf{F}_{\text{nuc}})_u = \begin{pmatrix} (\mathbf{F}_{\text{nuc}})_u & \mathbf{0} \\ \mathbf{0} & (\mathbf{F}_{\text{nuc}})_u \end{pmatrix} \quad (\text{A.71})$$

and the elements of the small-small block are given as

$$\left(\tilde{\mathbf{F}}_{\text{nuc}}\right)_u = \begin{pmatrix} \left(\tilde{\mathbf{F}}_{\text{nuc}}^0\right)_u + i\left(\tilde{\mathbf{F}}_{\text{nuc}}^z\right)_u & \left(\tilde{\mathbf{F}}_{\text{nuc}}^y\right)_u + i\left(\tilde{\mathbf{F}}_{\text{nuc}}^x\right)_u \\ -\left(\tilde{\mathbf{F}}_{\text{nuc}}^y\right)_u + i\left(\tilde{\mathbf{F}}_{\text{nuc}}^x\right)_u & \left(\tilde{\mathbf{F}}_{\text{nuc}}^0\right)_u - i\left(\tilde{\mathbf{F}}_{\text{nuc}}^z\right)_u \end{pmatrix}, \quad (\text{A.72})$$

where the individual matrices are defined as

$$(\mathbf{F}_{\text{nuc}})_{\kappa\nu,u} = \langle \lambda_\kappa | (\nabla_u \hat{V}) | \lambda_\nu \rangle, \quad (\text{A.73})$$

$$\left(\tilde{\mathbf{F}}_{\text{nuc}}^0\right)_{\kappa\nu,u} = \langle \lambda_\kappa | \hat{p}_x (\nabla_u \hat{V}) \hat{p}_x + \hat{p}_y (\nabla_u \hat{V}) \hat{p}_y + \hat{p}_z (\nabla_u \hat{V}) \hat{p}_z | \lambda_\nu \rangle, \quad (\text{A.74})$$

$$\left(\tilde{\mathbf{F}}_{\text{nuc}}^x\right)_{\kappa\nu,u} = \langle \lambda_\kappa | \hat{p}_y (\nabla_u \hat{V}) \hat{p}_z - \hat{p}_z (\nabla_u \hat{V}) \hat{p}_y | \lambda_\nu \rangle, \quad (\text{A.75})$$

$$\left(\tilde{\mathbf{F}}_{\text{nuc}}^y\right)_{\kappa\nu,u} = \langle \lambda_\kappa | \hat{p}_z (\nabla_u \hat{V}) \hat{p}_x - \hat{p}_x (\nabla_u \hat{V}) \hat{p}_z | \lambda_\nu \rangle, \quad (\text{A.76})$$

$$\left(\tilde{\mathbf{F}}_{\text{nuc}}^z\right)_{\kappa\nu,u} = \langle \lambda_\kappa | \hat{p}_x (\nabla_u \hat{V}) \hat{p}_y - \hat{p}_y (\nabla_u \hat{V}) \hat{p}_x | \lambda_\nu \rangle. \quad (\text{A.77})$$

The integral derivatives in the point-charge model are evaluated using a combination of Gauss–Rys integration and Gauss–Hermite quadrature. The picture-change correction is performed like in Sec. A.2.1. The finite nucleus integrals may be evaluated using translational invariance. The derivative of the electric field or the second derivative of the electrostatic potential is the electric field gradient, which is sensitive to picture-change correction effects.^[612]

A.3 Static Polarizabilities in X2C and DLU-X2C

The electrostatic field is included in the potential by the principle of minimal coupling.^[387,388] For a static homogeneous electric field, \vec{F} , the potential becomes

$$\hat{V} = \hat{V}(0) + \vec{F} \cdot \vec{r} \quad \text{with} \quad \hat{V}(0) = \hat{V}(\vec{F} = 0). \quad (\text{A.78})$$

Similar to Sec. 4.1, the total energy may be expressed with a Taylor expansion

$$E(\vec{F}) = E(0) + \sum_u \left. \frac{\partial E(\vec{F})}{\partial F_u} \right|_{\vec{F}=0} F_u + \sum_{u,v} \frac{1}{2} \left. \frac{\partial^2 E(\vec{F})}{\partial F_u \partial F_v} \right|_{\vec{F}=0} F_u F_v + \dots \quad (\text{A.79})$$

where the first and second order term define the permanent electric dipole moment vector, $\vec{\mu}$, and the static polarizability tensor, α , as

$$\mu_u = - \left. \frac{\partial E(\vec{F})}{\partial F_u} \right|_{\vec{F}=0}, \quad (\text{A.80})$$

$$\alpha_{uv} = - \left. \frac{\partial^2 E(\vec{F})}{\partial F_u \partial F_v} \right|_{\vec{F}=0}. \quad (\text{A.81})$$

The norm of the dipole vector defines the (scalar) dipole moment and the mean trace of the polarizability tensor forms the (isotropic) polarizability. Including the potential of Eq. A.78 in the one-electron Dirac matrix in Eq. 2.31 leads to the explicit energy expression to calculate the dipole moment and the polarizability. For electric properties, the derivative of the unitary transformation matrix to form the derivative in X2C is negligible.^[263,613] Thus, the components of the dipole vector in an X2C framework read

$$\mu_u = - \text{tr}(\mathbf{D}\mu_u^+) \quad (\text{A.82})$$

and the polarizability tensor follows as

$$\alpha_{uv} = - \text{tr} \left(\left. \frac{\partial \mathbf{D}}{\partial F_u} \right|_0 \mu_v^+ \right), \quad (\text{A.83})$$

with the picture-change corrected dipole integrals, μ_u^+ , described in Sec. A.2.1. Eq. A.83 requires to solve the CPHF or CPKS equations. The occupied-occupied block vanishes as the overlap integrals do not depend on the external electric field. The occupied-virtual block is obtained by solving the response equation

$$\begin{pmatrix} \mathbf{A} & \mathbf{B} \\ \mathbf{B}^* & \mathbf{A}^* \end{pmatrix} \begin{pmatrix} \mathbf{X} \\ \mathbf{Y} \end{pmatrix} = \begin{pmatrix} \mathbf{P}^\nu \\ \mathbf{P}^{\nu*} \end{pmatrix} \quad (\text{A.84})$$

with the RHS vectors \mathbf{P} and $\mathbf{P}^{\nu*}$ containing the picture-change corrected dipole integrals as outlined in chapter 6.

Static polarizabilities are calculated for ferrocene, ruthenocene, and osmocene. The structures of the eclipsed and the staggered conformer were optimized with the scalar-relativistic DLU-X2C Hamiltonian in the finite nucleus model.^[105,107] Spin-orbit effects are negligible for the molecular structures of the metallocenes. The x2c-TZVPPall basis set^[203] and the respective auxiliary basis set^[203] for the RI- J approximation are selected. Tight SCF thresholds of $10^{-8} E_h$ for the energy and 10^{-8} a.u. for the root mean square of the

Table A.1: Static polarizabilities (in atomic units) of the cyclopentadienyl (Cp) complexes of Fe, Ru, and Os.^[443] The scalar-relativistic DLU-X2C calculations are denoted as sc-DLU-X2C while DLU-X2C refers to self-consistent treatment of spin-orbit coupling in a two-component formalism. Note that the DLU-X2C-BHLYP calculation did not converge for the eclipsed conformer. The experimental results are taken from Ref. 614.

	Fe(Cp) ₂		Ru(Cp) ₂		Os(Cp) ₂	
	Eclipsed					
Functional	sc-DLU-X2C	DLU-X2C	sc-DLU-X2C	DLU-X2C	sc-DLU-X2C	DLU-X2C
TPSS	124.3	124.3	133.4	133.4	132.6	132.9
TPSSh	121.4	121.4	130.9	130.9	130.5	130.5
BH&HLYP	114.2	–	125.4	125.4	125.3	125.4
PBE0	118.7	118.7	128.6	128.6	128.4	128.4
CAM-B3LYP	118.2	118.2	128.1	128.1	127.8	127.8
LH12ct-SsirPW92	119.2	119.6	128.6	129.1	128.3	128.8
	Staggered					
Functional	sc-DLU-X2C	DLU-X2C	sc-DLU-X2C	DLU-X2C	sc-DLU-X2C	DLU-X2C
TPSS	124.2	124.2	133.5	133.5	133.0	133.0
TPSSh	121.2	121.2	130.9	130.9	130.6	130.7
BH&HLYP	114.0	114.1	125.4	125.4	125.4	125.4
PBE0	118.5	118.5	128.6	128.6	128.5	128.5
CAM-B3LYP	118.0	118.0	128.1	128.1	127.9	127.9
LH12ct-SsirPW92	119.0	119.4	128.6	129.1	128.4	128.9
EXP	126.1		133.1		138.5	

density matrix are applied. The TPSS,^[346] TPSSh^[356] BH&HLYP,^[128,129,350] PBE0,^[355] and the CAM-B3LYP,^[133] functional were selected with a large grid for the numerical integration of the XC part (grid 4a).^[482] No symmetry constraints were imposed as the initial structure ensures that the eclipsed or the staggered conformer is optimized. Structures are optimized up to an energy threshold of $10^{-6} E_h$ and a gradient vector residual norm of $10^{-3} E_h/\text{bohr}$. The eclipsed conformation is preferred at the level of theory.

The static polarizabilities were calculated with the above functionals and the LH12ct-SsirPW92 functional,^[139] which utilizes the PBE0-optimized geometry. The two-component DFT calculations employ the x2c-TZVPPall-2c basis set^[203] and the modified SNSO approach^[255,260] to account for spin-orbit effects on the two-electron integrals. The results are listed in Tab. A.1. Notably, the two conformers yield nearly identical polarizabilities and the impact of spin-orbit coupling on the results is minuscule for all functionals except for LH12ct-SsirPW92 (0.5 a.u.). The polarizability at the TPSS level is in a good agreement with the experimental results for ferrocene and ruthenocene. The polarizability tends to increase with the amount of HF exchange in the hybrid functionals. Therefore, all hybrid functionals considerably underestimate the polarizability. All methods fail to describe the trend from ruthenocene to osmocene. Experimentally, the polarizability rises from ferrocene to osmocene whereas the calculations show a decrease from ruthenocene to osmocene. The regression is predicted correctly at the GW-BSE@PBE0 level of theory^[443] indicating that a more sophisticated treatment of electron correlation might be necessary for osmocene. Another potential source of “error” is the employed basis set. The polarizability is sensitive towards very diffuse basis functions,^[200] which are not included in the x2c-TZVPPall-2c basis set.

A.4 Recontracted pcSseg-4 Basis Set for As

The recontacted pcSseg-4 basis set for As as discussed in Sec. 8.2.3 is given below. Only the recontacted segments are listed. The original pcSseg-4 basis set is available in Ref. 220 or via the Basis Set Exchange library.^[487,488]

```

15 s
46921900.000      0.36768751771E-04
6822920.0000     0.12679484265E-03
1535100.0000     0.30953575089E-03
433853.00000     0.72563030852E-03
141855.00000     0.16434578029E-02
51542.900000     0.37059539422E-02
20317.600000     0.83553392102E-02
8519.7100000     0.18813188294E-01
3758.8400000     0.41527662155E-01
1731.5300000     0.86835472998E-01
836.30900000     0.16049897132
419.47800000     0.25684874274
212.18900000     0.31221157854
107.92600000     0.21455060767
54.267200000     0.55457968489E-01
 7 s
2497.6700000     -0.17660579091E-02
774.91900000     -0.12302980453E-01
300.49600000     -0.57797936826E-01
133.46600000     -0.92054450139E-01
32.475000000     0.41621518517
17.141100000     0.47102665019
9.4086900000     0.26772841881
 5 s
129.51300000     0.28238537923E-02
32.687600000     -0.52615193307E-01
17.006400000     -0.19672561513
9.0042800000     -0.12321667089
5.2731800000     0.32834843290
 7 p
484852.00000     0.10313113613E-04
74592.700000     0.48151385284E-04
18102.000000     0.19249356340E-03
6028.6500000     0.67925032092E-03
2371.7300000     0.23039233324E-02
1040.7100000     0.73051436325E-02
483.85200000     0.22232616300E-01

```

A.5 NMR Shielding Constants and Shifts of the Organometallic Main-Group Molecules

The NMR shielding constants of the reference compounds are listed in Tab. A.2. The shieldings and shifts of the sample compounds are reported in Tabs. A.3 and A.4. Molecular structures of the sample compounds are taken from Ref. 383. These were optimized with the ZORA Hamiltonian. Note that the structures of the reference compounds are not listed in this reference. So, the structures of the reference compounds are optimized at the spin-orbit DLU-X2C level with the x2c-TZVPPall-2c/PBE0/D3 method^[203,355,498] and included in the supporting information of Ref. 379. All NMR calculations are performed with the Dyllall-CVTZ/cc-pCVTZ(unc) basis^[161,164,167,187,188,190,495] and the PBE0 functional (grid 4a^[482]).

Table A.2: NMR isotropic shielding constants (in ppm) of the reference compounds used to calculate the NMR chemical shifts. All structures were optimized at the spin-orbit DLU-X2C/x2c-TZVPPall-2c/PBE0 level of theory. The dispersion correction D3 is applied and large grids (grid 4a) are used for the numerical integration of the XC terms. Structures were confirmed to be local (minima) on the potential energy surface by numerical frequency calculations. The NMR shielding constants are calculated with the Dyllall-CVTZ/cc-pCVTZ(unc) basis sets.

Nucleus	X2C	DLU
¹³ C	187	187
²⁹ Si	344	344
⁷³ Ge	1329	1329
¹¹⁹ Sn	2529	2528
²⁰⁷ Pb	5432	5431

Table A.3: ¹³C NMR isotropic shielding constants σ and shifts δ in ppm. Tt denotes the heavy atom. Me is used as an abbreviation for the methyl group, CH₃. Structures are taken from Ref. 383. The PBE0 functional (grid 4a) and the Dyllall-CVTZ/cc-pCVTZ(unc) basis sets are applied.

	X2C				DLU			
	σ Tt-Me	δ Tt-Me	σ Tt-CC	δ Tt-CC	σ Tt-Me	δ Tt-Me	σ Tt-CC	δ Tt-CC
Si(CCMe) ₄	–	–	100	87	–	–	100	87
Ge(CCMe) ₄	–	–	101	86	–	–	101	86
Sn(CCMe) ₄	–	–	103	84	–	–	103	84
Pb(CCMe) ₄	–	–	101	86	–	–	101	86
Me ₂ Si(CCMe) ₂	183	4	97	90	183	4	97	90
Me ₂ Ge(CCMe) ₂	181	6	95	92	181	6	95	92
Me ₂ Sn(CCMe) ₂	190	–3	98	89	190	–3	98	89
Me ₂ Pb(CCMe) ₂	177	10	92	95	177	10	92	95
Me ₃ Si(CCH)	185	2	89	98	185	2	89	98
Me ₃ Ge(CCH)	182	5	87	100	182	5	87	99
Me ₃ Sn(CCH)	188	–1	87	100	188	–1	87	100
Me ₃ Pb(CCH)	178	9	81	106	178	9	81	106

Table A.4: ^{29}Si , ^{73}Ge , ^{119}Sn , and ^{207}Pb NMR isotropic shielding constants σ and shifts δ in ppm. The PBE0 functional (grid 4a) and the Dyall-CVTZ/cc-pCVTZ(unc) basis sets are applied.

	X2C		DLU	
	σ	δ	σ	δ
$\text{Si}(\text{CCMe})_4$	449	-105	449	-105
$\text{Me}_2\text{Si}(\text{CCMe})_2$	390	-46	390	-46
$\text{Me}_3\text{Si}(\text{CCH})$	363	-19	363	-19
$\text{Ge}(\text{CCMe})_4$	1531	-201	1531	-201
$\text{Me}_2\text{Ge}(\text{CCMe})_2$	1429	-100	1429	-100
$\text{Me}_3\text{Ge}(\text{CCH})$	1375	-46	1375	-46
$\text{Sn}(\text{CCMe})_4$	2951	-422	2951	-423
$\text{Me}_2\text{Sn}(\text{CCMe})_2$	2727	-198	2727	-199
$\text{Me}_3\text{Sn}(\text{CCH})$	2650	-121	2650	-121
$\text{Pb}(\text{CCMe})_4$	6258	-826	6257	-826
$\text{Me}_2\text{Pb}(\text{CCMe})_2$	5878	-447	5878	-447
Me_3PbCCH	5657	-226	5657	-226

A.6 NMR Shielding Constants of Xenon and the Xenon Fluorides

The shielding constants of the xenon atom and the xenon fluorides are reported in Tab. A.5. The calculations utilize the uncontracted ANO-RCC basis set^[179] for comparison with the coupled-cluster results of Cheng and co-workers.^[101] Moreover, a consistent computational protocol is used, where the structure is optimized at the same level of theory as the NMR calculations. Here, the non-relativistic calculations are performed with a proper basis sets^[198,502] and the relativistic calculations employ the x2c-TZVPall-2c basis set.^[203]

Table A.5: ¹²⁹Xe NMR isotropic shielding constants of xenon and xenon fluorides obtained at various levels of theory. Method 1 uses structures from Ref. 101, which were optimized at the scalar-relativistic X2C/CCSD(T)/ANO-RCC(unc) level. The ANO-RCC(unc) basis set was used in the NMR shielding calculations of that method. Method 2 indicates NMR calculations based on the geometry optimized at the corresponding level with the x2c-TZVPall-2c bases employed in the relativistic calculations and the def2-TZVP/TZVPall basis in the non-relativistic ones (NR). The octahedral symmetry is used for XeF₆.

Level	Method	Xe			XeF ₂			XeF ₄			XeF ₆		
		NR	X2C	DLU	NR	X2C	DLU	NR	X2C	DLU	NR	X2C	DLU
HF	1	5642	5865	5865	2091	1847	1847	741	362	362	1353	1007	1007
BP86	1	5643	5867	5867	2237	2154	2154	27	-318	-318	416	-36	-36
PBE	1	5643	5867	5867	2259	2174	2174	66	-281	-281	459	10	11
KT3	1	5651	5875	5875	2370	2282	2282	267	-75	-74	619	176	176
TPSS	1	5686	5910	5910	2402	2316	2316	274	-69	-68	595	149	149
B3LYP	1	5643	5867	5867	2096	1970	1970	80	-280	-280	498	47	47
PBE0	1	5643	5866	5866	2231	2107	2107	282	-65	-64	652	221	221
TPSSh	1	5682	5907	5907	2376	2275	2275	338	-4	-4	654	213	214
HF	2	5642	5863	5863	2477	2066	2066	1213	565	565	1516	1193	1193
BP86	2	5642	5865	5865	2494	2211	2211	109	-514	-515	-71	-486	-487
PBE	2	5642	5865	5865	2529	2243	2243	154	-463	-464	-19	-425	-426
KT3	2	5648	5871	5871	2663	2369	2369	488	-126	-126	355	-47	-48
TPSS	2	5680	5908	5908	2640	2370	2370	382	-218	-219	144	-245	-246
B3LYP	2	5642	5865	5865	2355	2025	2025	304	-358	-358	181	-237	-238
PBE0	2	5642	5865	5865	2507	2187	2187	578	-55	-55	494	114	113
TPSSh	2	5677	5904	5904	2617	2330	2330	533	-78	-78	331	-50	-51
MP2	2	5666	5863	5863	2680	2361	2360	907	242	242	674	255	254

A.7 NMR Shielding Constants of Transition-Metal Oxo Compounds

The isotropic shielding constants of the nine transition-metal oxo compounds are shown in Tab. A.6. The shielding constant of the reference compound H₂O to calculate the chemical shifts is 334 ppm at all levels of theory. Note that ECPs are not available for the 3d group and consequently the results are the same as with the non-relativistic Hamiltonian.

Table A.6: Comparison of ¹⁷O NMR isotropic shielding constants of transition metal compounds calculated at various levels of theory. The shielding constant of H₂O is 334 ppm at all levels of theory. NR denotes the non-relativistic calculations, while WB-ECP and DF-ECP refer to the calculations employing Wood–Boring^[507] and Dirac–Fock ECPs^[177] for the metal atoms. All structures are optimized at the corresponding level of theory. COSMO^[453,454] is applied to compensate the negative charge.

	BP86					PBE0				
	NR	WB-ECP	DF-ECP	X2C	DLU	NR	WB-ECP	DF-ECP	X2C	DLU
CrO ₄ ²⁻	-457	-	-	-439	-439	-511	-	-	-490	-490
MoO ₄ ²⁻	-300	-229	-261	-240	-240	-303	-227	-260	-236	-236
WO ₄ ²⁻	-241	127	-132	-126	-126	-238	-119	-124	-116	-117
MnO ₄ ⁻	-751	-	-	-724	-724	-916	-	-	876	-876
TcO ₄ ⁻	-535	-410	-439	-444	-443	-585	-450	-466	-469	-469
ReO ₄ ⁻	-436	-283	-270	-279	-279	-461	-286	-271	-281	-281
FeO ₄	-1187	-	-	-1140	-1140	-1725	-	-	-1621	-1622
RuO ₄	-872	-708	-720	-729	-729	-1078	-828	-844	-851	-851
OsO ₄	-707	-543	-472	-481	-481	-823	-543	-508	-521	-521

A.8 NMR Shielding Constants of Tungsten Compounds

The shielding constants of the eight tungsten molecules are presented in Tab. A.7. In line with the previous sections, the non-relativistic calculations are carried out with a non-relativistic basis set and the all-electron relativistic calculations use a corresponding basis set. The NMR shifts are obtained with respect to WO_4^{2-} .

Table A.7: Comparison of non-relativistic and relativistic calculated ^{183}W isotropic shielding constants. The non-relativistic calculations use the def2-TZVP/TZVPalls2 basis set^[198,203,204,379] and the relativistic calculations are performed with the x2c-TZVPall-2c bases.^[203] COSMO^[433,454] is employed to simulate the counter ions of the charged systems.

	BP86			PBE0		
	NR	X2C	DLU	NR	X2C	DLU
WO_4S^{2-}	252	927	926	501	1193	1192
WO_3S^{2-}	-470	191	191	-280	417	417
$\text{WO}_2\text{S}_2^{2-}$	-1310	-682	-682	-1233	-535	-535
WOS_3^{2-}	-2201	-1632	-1631	-2268	-1595	-1596
WS_4^{2-}	-3136	-2650	-2649	-3374	-2744	-2743
$\text{W}(\text{CO})_6$	4055	4755	4759	4182	5008	5012
WF_6	707	1510	1509	1331	2119	2118
WCl_6	-2291	-1300	-1300	-2021	-893	-893

A.9 PBE Results for the NMR Coupling Constants of Alkynyl Compounds

The coupling constants of the alkynyl compounds with the structures of Ref. 383 are given in Tab. A.8.

Table A.8: Comparison of non-relativistic, two-component, and four-component results for alkynyl molecules at the PBE level. Dyll’s uncontracted CVTZ basis sets^[187,188,190,495] are used for the heavy elements (Ge, Sn, Pb), whereas uncontracted cc-p(C)VTZ basis sets^[161,162,164,167,496] are employed for the light elements. Structures and 4c results are taken from Ref. 383, whereas the experimental values are taken from Ref. 533. $^1J_{\text{TtC}}$ (Tt = ^{29}Si , ^{73}Ge , ^{119}Sn , ^{207}Pb) coupling constants are listed in Hz. Note that the structures are optimized with the PBE0^[355] functional.^[383] NR and Me denote the non-relativistic limit and methyl groups. All X2C and DLU-X2C calculations employ the mSNSO approach.

	NR	Finite Nucleus		Point Charge		4c-RMB	EXP
		X2C	DLU	X2C	DLU		
$^1J_{\text{TtC}}$ for Tt(CCMe) ₄							
Si-C≡C	-114.09	-116.63	-116.60	-116.64	-116.62	-121.05	-
Ge-C≡C	-46.33	-50.54	-50.51	-50.81	-50.78	-52.10	-
Sn-C≡C	-786.86	-994.76	-992.78	-1010.99	-1008.99	-1033.64	-1168.0
Pb-C≡C	757.95	1265.31	1263.49	1371.41	1369.44	1340.32	1624.5
$^1J_{\text{TtC}}$ for Me ₂ Tt(CCMe) ₂							
Si-CH ₃	-44.76	-45.35	-45.33	-45.35	-45.34	-46.96	-
Si-C≡C	-86.18	-87.07	-87.04	-87.08	-87.05	-90.31	-
Ge-CH ₃	-14.17	-14.95	-14.94	-15.03	-15.02	-15.36	-
Ge-C≡C	-27.53	-27.89	-27.85	-28.04	-28.00	-28.77	-
Sn-CH ₃	-232.22	-283.59	-283.44	-288.23	-288.08	-293.47	-496.2
Sn-C≡C	-452.94	-440.63	-438.28	-448.09	-445.72	-456.94	-654.6
Pb-CH ₃	193.04	207.67	207.55	224.06	223.93	219.48	574.3
Pb-C≡C	350.37	-169.60	-171.51	-177.01	-179.08	-172.64	208.0
$^1J_{\text{TtC}}$ for Me ₃ TtCCH							
Si-CH ₃	-39.03	-39.67	-39.65	-39.67	-39.66	-41.17	-55.1
Si-C≡C	-64.87	-65.86	-65.84	-65.86	-65.84	-68.12	-79.4
Ge-CH ₃	-10.35	-11.15	-11.15	-11.21	-11.21	-11.51	-
Ge-C≡C	-16.76	-15.88	-15.88	-15.97	-15.97	-16.30	-
Sn-CH ₃	-124.46	-194.55	-194.51	-197.42	-197.38	-201.25	-303.5
Sn-C≡C	-148.78	-182.41	-182.16	-184.64	-184.40	-188.91	-415.5
Pb-CH ₃	123.45	35.51	35.47	38.69	38.65	39.03	-
Pb-C≡C	177.08	-530.90	-531.07	-566.13	-566.31	-554.57	-

A.10 PBE Results for the NMR Coupling Constants of Alkynyl Compounds with X2C-Optimized Structures

The coupling constants of the alkynyl compounds with the structure optimized at the DLU-X2C/x2c-TZVPall-2c/PBE level are shown in Tab. A.9.

Table A.9: Comparison of non-relativistic and two-component results for alkynyl molecules at the PBE level. Dyall's uncontracted CVTZ basis sets^[187,188,190,495] are used for the heavy elements (Ge, Sn, Pb), whereas uncontracted cc-p(C)VTZ basis sets^[161,162,164,167,496] are employed for the light elements. The experimental values are taken from Ref. 533. $^1J_{\text{TtC}}$ (Tt = ^{29}Si , ^{73}Ge , ^{119}Sn , ^{207}Pb) coupling constants are listed in Hz. NR and Me denote the non-relativistic limit and methyl groups. All X2C and DLU-X2C calculations employ the mSNSO approach. The mean absolute error of the DLU scheme is 0.49 Hz for the finite nucleus model and 0.51 Hz for the point charge model.

Molecule	NR	Finite Nucleus		Point Charge		EXP
		X2C	DLU	X2C	DLU	
$^1J_{\text{TtC}}$ for $\text{Tt}(\text{CCMe})_4$						
Si-C \equiv C	-113.23	-115.22	-115.20	-115.24	-115.21	-
Ge-C \equiv C	-47.50	-50.09	-50.06	-50.36	-50.33	-
Sn-C \equiv C	-783.71	-984.82	-982.68	-1000.88	-998.72	-1168.0
Pb-C \equiv C	757.93	1273.84	1271.86	1380.24	1378.10	1624.5
$^1J_{\text{TtC}}$ for $\text{Me}_2\text{Tt}(\text{CCMe})_2$						
Si-CH ₃	-45.15	-45.77	-45.76	-45.78	-45.76	-
Si-C \equiv C	-86.08	-87.04	-87.01	-87.05	-87.02	-
Ge-CH ₃	-14.33	-15.84	-15.83	-15.93	-15.92	-
Ge-C \equiv C	-28.77	-29.22	-29.18	-29.38	-29.34	-
Sn-CH ₃	-241.74	-301.80	-301.64	-306.73	-306.56	-496.2
Sn-C \equiv C	-486.78	-501.93	-499.34	-510.34	-507.73	-654.6
Pb-CH ₃	224.33	267.71	267.57	289.47	289.31	574.3
Pb-C \equiv C	424.15	56.93	54.81	66.01	63.72	208.0
$^1J_{\text{TtC}}$ for Me_3TtCCH						
Si-CH ₃	-39.83	-40.41	-40.40	-40.41	-40.40	-55.1
Si-C \equiv C	-67.91	-68.35	-68.33	-68.35	-68.33	-79.4
Ge-CH ₃	-13.40	-12.15	-12.14	-12.21	-12.21	-
Ge-C \equiv C	-18.88	-18.96	-18.96	-19.07	-19.07	-
Sn-CH ₃	-172.03	-216.99	-216.92	-220.38	-220.31	-303.5
Sn-C \equiv C	-297.90	-269.01	-268.77	-272.65	-272.41	-415.5
Pb-CH ₃	182.69	88.28	88.21	95.90	95.82	-
Pb-C \equiv C	249.83	-325.75	-325.92	-345.72	-345.90	-

List of Figures

2.1	Workflow of the X2C transformation	13
2.2	Workflow of the DLU-X2C transformation	17
3.1	Comparison of the original and the modified PSTS functional	32
4.1	Algorithm for the unperturbed density contribution of the NMR shielding tensor	56
5.1	Algorithm for the first derivatives of the DLU-X2C Hamiltonian	71
8.1	Analysis of deficits for the existing triple- ζ bases	91
9.1	Structure of the octahedral silver clusters Ag_{13}^- and Ag_{55}^-	107
9.2	Molecular structure of the organometallic iridium complexes	108
9.3	Molecular structure of $[\text{Pd}(\text{PCy}_2\text{H})_3\text{Cl}]^+$	117
9.4	Molecular structure of $[(\{\text{SIDipp}\}\text{P})_2\text{Sn}]$	119
10.1	Comparison of various functionals for ^1H NMR shieldings in ppm	127
10.2	Comparison of various functionals for ^{13}C NMR shieldings in ppm	127
10.3	Comparison of various functionals for ^{15}N , ^{17}O , ^{19}F , and ^{31}P NMR shieldings	127
10.4	Comparison of various functionals for ^1H NMR shifts	128
10.5	Comparison of various functionals for ^{13}C NMR shifts	129
10.6	Comparison of various functionals for ^{17}O NMR shifts	130
10.7	Comparison of various functionals for ^{183}W NMR shifts	132
11.1	Synthesis of the phosphinidenide complexes	135
11.2	Structures of the phosphinidenide complexes	135
11.3	Frontier orbitals of compound 4	139
12.1	Survey of different classes of molecules exhibiting $(4n + 2)$ π -aromaticity	143
12.2	Molecular structure of $[\text{Th}@\text{Bi}_{12}]^{4-}$	145
12.3	HOMO and LMOs of $[\text{Th}@\text{Bi}_{12}]^{4-}$	146
12.4	Calculated ring currents in $[\text{Th}@\text{Bi}_{12}]^{4-}$	147
12.5	Integration plane for $[\text{Th}@\text{Bi}_{12}]^{4-}$	147
12.6	Molecular structure of $[\text{K}_2\text{Zn}_{20}\text{Bi}_{16}]^{6-}$	152
12.7	Magnetically induced current density of $[\text{Zn}_{20}\text{Bi}_{16}]^{8-}$	153

List of Tables

8.1	Exponents of the first segment for carbon	92
8.2	x2c-SVPall-s, x2c-TZVPall-s, and x2c-TZVPall-s basis sets	93
8.3	Evaluation of the NMR-tailored basis sets	94
8.4	Comparison to other frequently used double and triple- ζ all-electron relativistic basis sets	96
8.5	Comparison to other frequently used quadruple- ζ all-electron relativistic basis sets	97
8.6	Computation time for various relativistic basis sets	98
8.7	Comparison to the pcSseg basis sets	99
8.8	Shieldings with recontracted pcSseg-4 basis sets of As for X2C	100
8.9	Shieldings with decontracted pcSseg-4 basis sets of Se for X2C	100
9.1	Demonstration of gauge and translational invariance	102
9.2	Statistical evaluation of the DLU error for organometallic compounds	103
9.3	^{129}Xe NMR chemical shifts of xenon fluorides at various levels of theory	104
9.4	Comparison of ^{17}O NMR shifts of transition-metal compounds	106
9.5	Comparison of non-relativistic and relativistic calculated ^{183}W shifts	107
9.6	Computation times of Ag clusters and iridium complexes	108
9.7	Comparison of non-relativistic, two-component, and four-component HF results	109
9.8	Comparison of various density functional approximations for TtH_4 and HX	110
9.9	Comparison of various basis sets for TtH_4 and HX	111
9.10	Comparison to 4c-RMB results for TtH_4 and HX	112
9.11	Comparison of non-relativistic, two-component, and four-component results for alkynyl molecules at the PBE0 level	113
9.12	Comparison of non-relativistic and two-component results for alkynyl molecules at the PBE0 level with optimized structures	114
9.13	Calculated coupling constants for various Sn molecules	116
9.14	Coupling constants of $[\text{Pd}(\text{PCy}_2\text{H})_3\text{Cl}]^+$	117
9.15	DFT results for the coupling constants of $[\text{Pd}(\text{PCy}_2\text{H})_3\text{Cl}]^+$	118
9.16	Coupling constants of $[\text{Pt}(\text{PCy}_2\text{H})_3\text{Cl}]^+$	118
9.17	Coupling constants of $[(\{\text{SIDipp}\}\text{P})_2\text{Sn}]$	120
9.18	Wall times for the SCF procedure and the SSCC calculation of $[(\{\text{SIDipp}\}\text{P})_2\text{Sn}]$	121
10.1	Assessment of density functional approximations for NMR couplings	125
10.2	Comparison of ^{129}Xe NMR shifts	131
10.3	Wall times of the full SCF procedure for tungsten compounds	133
10.4	Wall times of the NMR shielding calculations of tungsten compounds	133
10.5	Wall times of the NMR shielding calculations with the RI- J and semiK approximation	134
11.1	Structural data on compounds 3–5	136
11.2	Spectroscopic data on compounds 3–5	137
11.3	WBI of the compounds 3–5	138
11.4	Spectroscopic data on compounds 6 and 7	140
11.5	WBI of the compounds 6 and 7	140
12.1	Current strengths and NICS of known all-metal aromatic compounds	144

12.2	Current strengths and NICS of $[\text{Th}@\text{Bi}_{12}]^{4-}$	148
12.3	Current strengths and NICS of Bi_{12}^{8-}	150
12.4	Current strengths and NICS of Bi_{12}^{12-}	151
A.1	Static polarizabilities of metallocenes	168
A.2	NMR shieldings of the reference compounds for the alkynyl compounds	170
A.3	^{13}C NMR isotropic shielding constants and shifts of the alkynyl compounds	170
A.4	^{29}Si , ^{73}Ge , ^{119}Sn and ^{207}Pb NMR shieldings and shifts of the alkynyl compounds	171
A.5	^{129}Xe NMR isotropic shielding constants of xenon and xenon fluorides	172
A.6	Comparison of ^{17}O NMR shieldings of transition metal compounds	173
A.7	Comparison of non-relativistic and relativistic calculated ^{183}W shieldings	174
A.8	Comparison of non-relativistic and two-component results for alkynyl molecules with PBE	175
A.9	Comparison of non-relativistic and two-component results for alkynyl molecules at the PBE level with optimized structures	176

Acronyms and Symbols

Acronyms and Abbreviations

1c	one-component
2c	two-component
4c	four-component
AO	(spherical) atomic orbital
BLAS	basic linear algebra subroutines
Bz	benzyl
cAAC	cyclic (alkyl)(amino)carbenes
CAM	Coulomb attenuating method
CAO	Cartesian atomic orbital
CC	coupled cluster
CCSD(T)	coupled-cluster singles and doubles
CCSD(T)	coupled-cluster singles, doubles, and perturbative triples
COSMO	conductor-like screening model
CPHF	coupled-perturbed Hartree–Fock
CPKS	coupled-perturbed Kohn–Sham
CPU	central processing unit
crypt-222	4,7,13,16,21,24-hexaoxa-1,10-diazabicyclo[8.8.8]hexacosane
Cy	cyclohexyl
DF	Dirac–Fock
DFT	density functional theory
Dipp	1,3-bis(2,6-diisopropylphenyl)imidauolin-2-ylidene
DKH	Douglas–Kroll–Hess
DLU	diagonal local approximation to the unitary decoupling transformation
DSO	diamagnetic spin–orbit
ECP	effective-core potential

en	ethane-1,2-diamine
EPR	electron paramagnetic resonance
ET	even-tempered
FC	Fermi-contact
FON	fractional occupation number
GGA	generalized gradient approximation
GHF	generalized Hartree–Fock
GIAO	gauge-including atomic orbitals
GIMIC	gauge-including magnetically induced current
GKS	generalized Kohn–Sham
GPU	graphics processing unit
GTO	Gaussian-type orbital
GW-BSE	Bethe–Salpeter equation in the Green’s function <i>GW</i> approximation
HF	Hartree–Fock
HOMO	highest occupied molecular orbital
IAO	linear-independent AO basis
IUPAC	International Union of Pure and Applied Chemistry
KIT	Karlsruhe Institute of Technology
LCAO	linear combination of atomic orbitals
LHF	local hybrid functional
LHS	left-hand side
LMF	local mixing function
lr	long range
LSDA	local spin density approximation
MAE	mean absolute error
MAPE	mean absolute percent-wise error
MARI-<i>J</i>	multipole-accelerated resolution of the identify
MSD	mean signed deviation
meta-GGA	meta-generalized gradient approximation
Me	methyl
MO	molecular orbital
MP2	second-order Møller–Plesset perturbation theory

NHC	N-heterocyclic carbene
NICS	nucleus-independent chemical shift
NMR	nuclear magnetic resonance
NR	non-relativistic
OMP	open multi-processing (OpenMP)
PSO	paramagnetic spin-orbit
RI-<i>J</i>	resolution of the identity approximation to the Coulomb integrals
RHF	restricted Hartee-Fock
RHS	right-hand side
RKB	restricted kinetic balance
RKS	restricted Kohn-Sham
RMB	restricted magnetic balance
RMS	root mean square
ROHF	restricted open-shell Hartree-Fock
RPA	random phase approximation
RSH	range-separated hybrid
SAO	symmetry-adapted atomic orbital
SCF	self-consistent field
SD	spin-dependent in the context of the relativistic integrals
SD	spin-dipole term in the context of NMR couplings
semiK	seminumerical exchange
SF	spin-free
SIDipp	1,3-bis(2,6-di-isopropylphenyl)-imidazolidin-2-ylidene
SIMes	1,3-bis(2,4,6-trimethylphenyl)imidazolidine-2-ylidene
SNSO	screened nuclear spin-orbit
mSNSO	modified screened nuclear spin-orbit
SO	spin-orbit
sr	short range
SSCC	spin-spin coupling constant
STD	standard deviation
STO	Slater-type orbital
^tBu	<i>tert</i> -butyl

TD-DFT	time-dependent density functional theory
TMS	tetramethylsilane, SiMe ₄
UKS	unrestricted Kohn–Sham
WB	Wood–Boring
WBI	Wiberg bond index
WOE	weighted overall error
X2C	exact two-component
XC	exchange correlation
ZORA	zeroth-order regular approximation

Constants

c	speed of light, $c = 137.0359990840$ a.u.
π	pi: 3.1415926 . . .

Latin Symbols and Variables

\vec{A}	vector potential
\vec{B}	external magnetic field
E	energy
\vec{F}	electric field
f^{H}	Hartree kernel
f^{XC}	exchange-correlation kernel
$G_{\mu\nu\kappa\omega}$	two-electron integrals
\mathcal{G}	nuclear integral for the vector potential of the magnetic moments
i	imaginary unit, $\sqrt{-1}$
J	NMR coupling constant in Herz
\vec{j}	current density
K	reduced NMR coupling constant
l	angular momentum quantum number
M	isotope or atomic mass number
\vec{m}	electron magnetic dipole moment
\vec{m}_I	nuclear magnetic moments
m_l	magnetic quantum number
Q	(m)SNSO screening parameter
\vec{r}	position vector of the electron
\vec{R}	position vector of the nucleus
t	time or integration variable
w_I	weight function for the finite nucleus model
Z	charge of the nucleus

Greek Symbols and Variables

$\alpha \beta$	spin functions
λ_μ	spin-free one-component basis function
$\lambda_\mu(\vec{B}, \vec{r})$	GIAO
ϵ	orbital or spinor energy, or energy density in DFT equations
Λ	gauge function
ϕ_μ	spin-dependent two-component basis functions
φ	two-component spinor
Ψ	wave function
ψ	molecular orbital
ρ	density
σ	Pauli matrices
τ	kinetic energy density
Ω	excitation energy
ζ	exponent of a basis function or the finite charge distribution

Matrices

Γ	two-electron density matrix
Π	generalized momentum matrix
\mathbf{A}, \mathbf{B}	electronic Hessian matrices
D	Dirac matrix
C	coefficient matrix for the LCAO ansatz
C_L, C_S	coefficient matrix for the X2C or Dirac Hamiltonian
J	Coulomb matrix
K	exchange matrix
L^{NESC}, L	NESC matrix
M	metric
O^λ	orbital rotation matrix for CPHF and CPKS
r	eigenvalues of the renormalization matrix
R	renormalization matrix
P	RHS vector
Q^λ	RHS matrix of the Sylvester equation
S	overlap matrix
\tilde{S}	normalization matrix of the large component
T	kinetic energy
X	decoupling matrix
U	unitary transformation matrix
U^λ	unitary orbital rotation matrix for X2C response equations
V	external or electron-nuclei potential
V_R	eigenvectors of the renormalization matrix
V_R^\dagger	generalized inverse of V_R
W	relativistically modified potential
Z	energy-weighted density matrix

Operators and Math symbols

$!!$	double factorial
\Leftrightarrow	equivalence, rearranging
$\langle \Psi $	bra
$ \Psi\rangle$	ket
$\Gamma(a)$	gamma function
$\hat{\mu}$	electronic dipole moment operator
$[A, B]$	commutator of A and B , $[A, B] = AB - BA$
$\mathbf{0}$	matrix consisting of zeros only
$\mathbf{1}$	identity matrix
I_4	(4×4) identity matrix (operator) for the Dirac equation
$\vec{\alpha} \vec{\beta}$	trace-less quantities of the Dirac equation
Δ	Laplace operator, Hessian
ϵ_{uvw}	Levi-Civita tensor
\exp	exponential function
Im	imaginary part
$\vec{\nabla}$	nabla operator, gradient
$\hat{\pi}$	generalized momentum operator
\hat{F}	Fock operator
\hat{g}	two-particle interaction operator
\hat{H}	Molecular Hamiltonian
\hat{h}	One-electron Hamiltonian
\hat{J}	Coulomb operator
\hat{K}	exchange operator
$\hat{\mathcal{K}}$	ZORA operator
\hat{l}	angular momentum operator
\otimes	direct product
$P(a, x)$	lower incomplete gamma function
\hat{p}	momentum operator
Re	real part
\hat{R}	renormalization operator

\hat{s}	spin operator
\hat{T}	kinetic energy operator
\hat{V}	electron-nucleus potential, external potential
\hat{V}^{XC}	exchange-correlation potential
\hat{X}	decoupling operator
\hat{Y}	energy-dependent operator for the relation of the large and small functions

Permissions to Print

This work contains material, that has already been published in scientific journals. The permission to use this material in print and electronic form was obtained from the corresponding copyrights-holder.

- Section 3.5.5, chapters 7 and 10, as well as current strengths and NICS values in Sec. 12.2 for all functionals except for BP86, PBE, TPSS, and TPSSh: Reproduced (adapted) with permission from *Assessing the Accuracy of Local Hybrid Density Functional Approximations for Molecular Response Properties*, Christof Holzer, Yannick J. Franzke, Max Kehry, *J. Chem. Theory Comput.* **17**, 2928–2947 (2021). Copyright 2021 The Authors. Published by American Chemical Society.
- Sections 4.1, 4.2, 4.3, 4.4, 4.6, 9.1, A.5, A.6, A.7, and A.8: Reproduced (adapted) with permission from *NMR Shielding Tensors and Chemical Shifts in Scalar-Relativistic Local Exact Two-Component Theory*, Yannick J. Franzke, Florian Weigend, *J. Chem. Theory Comput.* **15**, 1028–1043 (2019). Copyright 2019 American Chemical Society.
- Chapter 5, Sections 9.2, A.9, and A.10, as well as NMR couplings in chapter 11: Reproduced (adapted) from the author’s original manuscript *NMR Indirect Spin–Spin Coupling Constants in a Modern Quasi-Relativistic Density Functional Framework*, Yannick J. Franzke, F. Mack, F. Weigend, *J. Chem. Theory Comput.* **17**, 3974–3994 (2021). Copyright 2021 The Authors. Published by American Chemical Society.
- Chapter 6, Sections A.2 and A.3: Reproduced (adapted) from the authors’ original manuscript *Quasirelativistic two-component core excitations and polarizabilities from a damped-response formulation of the Bethe–Salpeter equation*, Max Kehry, Yannick J. Franzke, Christof Holzer, Wim Klopper. This article has been accepted for publication in *Mol. Phys.* **118**, e1755064 (2020), published by Taylor & Francis.
- Chapter 8: Reproduced (adapted) with permission from *Segmented Contracted Error-Consistent Basis Sets of Quadruple- ζ Valence Quality for One- and Two-Component Relativistic All-Electron Calculations*, Yannick J. Franzke, Lucas Spiske, Patrik Pollak, Florian Weigend, *J. Chem. Theory Comput.* **16**, 5658–5674 (2020). Copyright 2020 American Chemical Society.
- Chapter 8: Reproduced (adapted) with permission from *Error-consistent segmented contracted all-electron relativistic basis sets of double- and triple-zeta quality for NMR shielding constants*, Yannick J. Franzke, Robert Treß, Tobias M. Pazdera, Florian Weigend, *Phys. Chem. Chem. Phys.* **21**, 16658 (2019). Published by the PCCP Owner Societies. This article is licensed under a Creative Commons Attribution 3.0 Unported Licence. Material from this article can be used in other publications provided that the correct acknowledgement is given with the reproduced material. The link to the respective license is <http://creativecommons.org/licenses/by/3.0/> (retrieved April 23, 2021).

- Chapter 11: Reproduced (adapted) with permission from *Low-Valent Group 14 Phosphinidenide Complexes [(SIDippP)₂M] Exhibit P-M pπ-pπ Interaction (M = Ge, Sn, Pb)*, Markus Balmer, Yannick J. Franzke, Florian Weigend, Carsten von Hänisch, *Chem. Eur. J.* **26**, 192–197 (2020). Published by Wiley-VCH. This article is licensed under a Creative Commons Attribution 4.0 International CC BY 4.0 License. This is an open access article distributed under the terms of the Creative Commons CC BY license, which permits unrestricted use, distribution, and reproduction in any medium, provided the original work is properly cited. The link to the respective license is <http://creativecommons.org/licenses/by/4.0/> (retrieved April 29, 2021).
- Sections 12.1 and 12.2: Reproduced (adapted) with permission from *Substantial π-aromaticity in the anionic heavy-metal cluster [Th@Bi₁₂]⁴⁻*, Armin R. Eulenstein, Yannick J. Franzke, Niels Lichtenberger, Robert J. Wilson, H. Lars Deubner, Florian Kraus, Rudolphe Clérac, Florian Weigend, Stephanie Dehnen, *Nat. Chem.* **13**, 149–155 (2021). Published by Springer Nature.
- Section 12.3: Reproduced (adapted) with permission from *Stabilizing a metalloid {Zn₁₂} unit within a polymetallide environment in [K₂Zn₂₀Bi₁₆]⁶⁻*, Armin R. Eulenstein, Yannick J. Franzke, Patrick Bügel, Werner Massa, Florian Weigend, Stephanie Dehnen, *Nat. Commun.* **11**, 5122 (2020). Published by Springer Nature. This article is licensed under a Creative Commons Attribution 4.0 International License, which permits use, sharing, adaptation, distribution and reproduction in any medium or format, as long as you give appropriate credit to the original author(s) and the source, provide a link to the Creative Commons license, and indicate if changes were made. The link to the respective license is <http://creativecommons.org/licenses/by/4.0/> (retrieved April 29, 2021).

List of Publications

Corresponding authors are marked with an asterisk (*) whereas † marks equal contribution.

15. *NMR Indirect Spin–Spin Coupling Constants in a Modern Quasi-Relativistic Density Functional Framework*
Y. J. Franzke*, F. Mack, F. Weigend
J. Chem. Theory Comput. **17**, 3974–3994 (2021).
14. *Assessing the Accuracy of Local Hybrid Density Functional Approximations for Molecular Response Properties*
C. Holzer†*, **Y. J. Franzke†***, M. Kehry
J. Chem. Theory Comput. **17**, 2928–2947 (2021).
13. *Substantial π -aromaticity in the anionic heavy-metal cluster $[Th@Bi_{12}]^{4-}$*
A. R. Eulenstein†, **Y. J. Franzke†**, N. Lichtenberger, R. J. Wilson, H. L. Deubner, F. Kraus, R. Clérac, F. Weigend*, S. Dehnen*
Nat. Chem. **13**, 149–155 (2021).
12. *Stabilizing a metalloid $\{Zn_{12}\}$ unit within a polymetallide environment in $[K_2Zn_{20}Bi_{16}]^{6-}$*
A. R. Eulenstein†, **Y. J. Franzke†**, P. Bügel, W. Massa, F. Weigend*, S. Dehnen*
Nat. Commun. **11**, 5122 (2020).
11. *Segmented Contracted Error-Consistent Basis Sets of Quadruple- ζ Valence Quality for One- and Two-Component Relativistic All-Electron Calculations*
Y. J. Franzke*, L. Spiske, P. Pollak, F. Weigend*
J. Chem. Theory Comput. **16**, 5658–5674 (2020).
10. *TURBOMOLE: Modular program suite for ab initio quantum-chemical and condensed-matter simulations*
S. G. Balasubramani, G. P. Chen, S. Coriani, M. Diedenhofen, M. S. Frank, **Y. J. Franzke***, F. Furche*, R. Grotjahn, M. E. Harding, C. Hättig*, A. Hellweg, B. Helmich-Paris, C. Holzer, U. Huniar, M. Kaupp, A. Marefat Khah, S. Karbalaei Khani, T. Müller, F. Mack, B. D. Nguyen, S. M. Parker, E. Perlt, D. Rappoport, K. Reiter, S. Roy, M. Rückert, G. Schmitz, M. Sierka, E. Tapavicza, D. P. Tew, C. van Wüllen, V. K. Voora, F. Weigend, A. Wodynski, J. M. Yu
J. Chem. Phys. **152**, 184107 (2020).
9. *Quasirelativistic two-component core excitations and polarisabilities from a damped-response formulation of the Bethe–Salpeter equation*
M. Kehry, **Y. J. Franzke**, C. Holzer, W. Klopper*
Mol. Phys. **118**, e1755064 (2020).
8. *Preparation and luminescence properties of a M_{16} heterometallic coinage metal chalcogenide cluster*
A. M. Polgar, **Y. J. Franzke**, S. Lebedkin, F. Weigend*, J. F. Corrigan*
Dalton Trans. **49**, 593–597 (2020).

7. *Low-Valent Group 14 Phosphinidenide Complexes [(SIDippP)₂M] Exhibit P-M pπ-pπ Interaction (M = Ge, Sn, Pb)*
M. Balmer, **Y. J. Franzke**, F. Weigend, C. von Hänisch*
Chem. Eur. J. **26**, 192–197 (2020).
6. *Error-consistent segmented contracted all-electron relativistic basis sets of double- and triple-zeta quality for NMR shielding constants*
Y. J. Franzke*, R. Treß, T. M. Pazdera, F. Weigend*
Phys. Chem. Chem. Phys. **21**, 16658–16664 (2019).
5. *NMR Shielding Tensors and Chemical Shifts in Scalar-Relativistic Local Exact Two-Component Theory*
Y. J. Franzke*, F. Weigend*
J. Chem. Theory Comput. **15**, 1028–1043 (2019).
4. *The Identity of “Ternary” A/Tl/Pb or K/Tl/Bi Solid Mixtures and Binary Zintl Anions Isolated From Their Solutions*
N. Lichtenberger, **Y. J. Franzke**, F. Weigend, S. Dehnen*
Chem. Eur. J. **24**, 12022–12030 (2018).
3. *Efficient implementation of one- and two-component analytical energy gradients in exact two-component theory*
Y. J. Franzke*, N. Middendorf, F. Weigend*
J. Chem. Phys. **148**, 104110 (2018).
2. *Calculations of current densities and aromatic pathways in cyclic porphyrin and isoporphyrin arrays*
Y. J. Franzke, D. Sundholm*, F. Weigend
Phys. Chem. Chem. Phys. **19**, 12794–12803 (2017).
1. *{μ-PbSe}: A Heavy CO Homologue as an Unexpected Ligand*
G. Thiele, **Y. Franzke**, F. Weigend, S. Dehnen*
Angew. Chem. Int. Ed. **54**, 11283–11288 (2015).

German version: *{μ-PbSe}: ein schweres CO-Homolog als ungewöhnlicher Ligand*
G. Thiele, **Y. Franzke**, F. Weigend, S. Dehnen*
Angew. Chem. **127**, 11437–11442 (2015).

Bibliography

- [1] J. Mason, ed., *Multinuclear NMR* (Springer US, New York, USA, 1987).
- [2] K. Wüthrich, *Angew. Chem. Int. Ed.* **42**, 3340 (2003).
- [3] H. Friebolin, *Basic One- and Two-Dimensional NMR Spectroscopy*, 5th ed. (Wiley-VCH, Weinheim, Germany, 2010).
- [4] “nmrshiftdb2,” An open-source NMR web database, see <https://nmrshiftdb.nmr.uni-koeln.de/> (retrieved April 5, 2021).
- [5] “SDBSWeb,” Spectral Database for Organic Compounds by the Japanese National Institute of Advanced Industrial Science and Technology, see <https://sdfs.db.aist.go.jp> (retrieved April 5, 2021).
- [6] T. Helgaker, M. Jaszuński, and K. Ruud, *Chem Rev.* **99**, 293 (1999).
- [7] J. Vaara, *Phys. Chem. Chem. Phys.* **9**, 5399 (2007).
- [8] T. Helgaker, M. Jaszuński, and M. Pecul, *Prog. Nucl. Magn. Reson. Spectrosc.* **53**, 249 (2008).
- [9] J. Jaźwiński, “Theoretical aspects of indirect spin-spin couplings,” in *Nuclear Magnetic Resonance*, Vol. 42, edited by J. Wojcik and K. Kamienska-Trela (The Royal Society of Chemistry, Cambridge, United Kingdom, 2013) pp. 152–180.
- [10] M. Kaupp, M. Bühl, and V. G. Malkin, eds., *Calculation of NMR and EPR Parameters: Theory and Applications* (Wiley-VCH, Weinheim, Germany, 2004).
- [11] S. Mitzinger, J. Bandemehr, K. Reiter, J. Scott McIndoe, X. Xie, F. Weigend, J. F. Corrigan, and S. Dehnen, *Chem. Commun.* **54**, 1421 (2018).
- [12] R. J. Wilson, F. Hastreiter, K. Reiter, P. Büschelberger, R. Wolf, R. M. Gschwind, F. Weigend, and S. Dehnen, *Angew. Chem. Int. Ed.* **57**, 15359 (2018).
- [13] J. Gauss, *Ab initio Berechnung chemischer NMR-Verschiebung unter Berücksichtigung der Elektronenkorrelation*, Habilitationsschrift, University of Karlsruhe (TH), Germany (1993).
- [14] K. Reiter, *Weiterentwicklung und Anwendung von quantenchemischen Methoden zur Berechnung von Molekülen im Magnetfeld*, Dissertation, Karlsruhe Institute of Technology (KIT), Germany (2018).
- [15] M. Repisky, S. Komorovsky, R. Bast, and K. Ruud, “Relativistic calculations of nuclear magnetic resonance parameters,” in *Gas Phase NMR*, edited by K. Jackowski and M. Jaszuński (The Royal Society of Chemistry, Cambridge, United Kingdom, 2016) Chap. 8, pp. 267–303.
- [16] P. Lazzarotti, *Prog. Nucl. Magn. Reson. Spectrosc.* **36**, 1 (2000).
- [17] P. R. von Schleyer and H. Jiao, *Pure & Appl. Chem.* **68**, 209 (1996).
- [18] Z. Chen, C. S. Wannere, C. Corminboeuf, R. Puchta, and P. v. R. Schleyer, *Chem. Rev.* **105**, 3842 (2005).

- [19] D. Sundholm, H. Fliegl, and R. J. F. Berger, *Wiley Interdiscip. Rev.: Comput. Mol. Sci.* **6**, 639 (2016).
- [20] E. Schrödinger, *Ann. Phys.* **384**, 361 (1926).
- [21] E. Schrödinger, *Ann. Phys.* **384**, 489 (1926).
- [22] E. Schrödinger, *Ann. Phys.* **385**, 437 (1926).
- [23] E. Schrödinger, *Ann. Phys.* **386**, 109 (1926).
- [24] A. Einstein, *Ann. Phys.* **322**, 891 (1905).
- [25] P. A. M. Dirac, *Proc. Roy. Soc. Lond. A* **117**, 610 (1928).
- [26] P. Pyykkö, *Chem. Rev.* **88**, 563 (1988).
- [27] K. G. Dyall and K. Fægri Jr., *Introduction to Relativistic Quantum Chemistry* (Oxford University Press, New York, USA, 2007).
- [28] M. Reiher and A. Wolf., *Relativistic Quantum Chemistry – The Fundamental Theory of Molecular Science*, 2nd ed. (Wiley-VCH, Weinheim, Germany, 2015).
- [29] W. Liu, ed., *Handbook of Relativistic Quantum Chemistry* (Springer, Berlin, Heidelberg, Germany, 2017).
- [30] W. Liu, *Mol. Phys.* **108**, 1679 (2010).
- [31] T. Saue, *ChemPhysChem* **12**, 3077 (2011).
- [32] P. Pyykkö, *Annu. Rev. Phys. Chem.* **63**, 45 (2012).
- [33] P. Pyykkö, *Chem. Rev.* **112**, 371 (2012).
- [34] J. Autschbach, *J. Chem. Phys.* **136**, 150902 (2012).
- [35] W. Liu, *J. Chem. Phys.* **152**, 180901 (2020).
- [36] W. Liu, *J. Chem. Phys.* **152**, 249901 (2020).
- [37] N. Bartlett, *Gold Bulletin* **31**, 22 (1998).
- [38] P. Pyykkö, *Chem. Soc. Rev.* **37**, 1967 (2008).
- [39] R. Ahuja, A. Blomqvist, P. Larsson, P. Pyykkö, and P. Zaleski-Ejgierd, *Phys. Rev. Lett.* **106**, 018301 (2011).
- [40] P. Pyykkö, “Relativistic Quantum Chemistry,” in *Advances in Quantum Chemistry*, Vol. 11, edited by P.-O. Löwdin (Academic Press, New York, USA, 1978) pp. 353–409.
- [41] F. Calvo, E. Pahl, M. Wormit, and P. Schwerdtfeger, *Angew. Chem. Int. Ed.* **52**, 7583 (2013).
- [42] A. Einstein, *Ann. Phys.* **323**, 639 (1905).
- [43] M. Dolg, “Relativistic effective core potentials,” in *Relativistic Electronic Structure Theory, Theoretical and Computational Chemistry*, Vol. 11, edited by P. Schwerdtfeger (Elsevier, Amsterdam, The Netherlands, 2002) Chap. 14, pp. 793–862.
- [44] M. Dolg and X. Cao, *Chem. Rev.* **112**, 403 (2012).

- [45] M. Dolg, "Relativistic effective core potentials," in *Handbook of Relativistic Quantum Chemistry*, edited by W. Liu (Springer, Berlin, Heidelberg, Germany, 2017) Chap. 14, pp. 449–478.
- [46] D. Figgen, K. A. Peterson, M. Dolg, and H. Stoll, *J. Chem. Phys.* **130**, 164108 (2009).
- [47] B. Swirles and D. R. Hartree, *Proc. Royal Soc. Lond. A* **152**, 625 (1935).
- [48] T. Saue, *Principles and Applications of Relativistic Molecular Calculations*, Ph.D. thesis, University of Oslo, Norway (1997).
- [49] G. A. Aucar, T. Saue, L. Visscher, and H. J. A. Jensen, *J. Chem. Phys.* **110**, 6208 (1999).
- [50] T. Enevoldsen, L. Visscher, T. Saue, H. J. A. Jensen, and J. Oddershede, *J. Chem. Phys.* **112**, 3493 (2000).
- [51] L. Visscher, T. Enevoldsen, T. Saue, H. J. A. Jensen, and J. Oddershede, *J. Comput. Chem.* **20**, 1262 (1999).
- [52] S. S. Gomez, R. H. Romero, and G. A. Aucar, *J. Chem. Phys.* **117**, 7942 (2002).
- [53] C. A. Giménez, A. F. Maldonado, and G. A. Aucar, *Theor. Chem. Acc.* **135**, 201 (2016).
- [54] M. Iliáš, T. Saue, T. Enevoldsen, and H. J. A. Jensen, *J. Chem. Phys.* **131**, 124119 (2009).
- [55] M. Olejniczak, R. Bast, T. Saue, and M. Pecul, *J. Chem. Phys.* **136**, 014108 (2012).
- [56] M. Olejniczak, R. Bast, T. Saue, and M. Pecul, *J. Chem. Phys.* **136**, 239902 (2012).
- [57] S. Komorovský, M. Repiský, O. L. Malkina, V. G. Malkin, I. Malkin Ondřík, and M. Kaupp, *J. Chem. Phys.* **128**, 104101 (2008).
- [58] S. Komorovský, M. Repiský, O. L. Malkina, and V. G. Malkin, *J. Chem. Phys.* **132**, 154101 (2010).
- [59] S. Komorovský, M. Repiský, K. Ruud, O. L. Malkina, and V. G. Malkin, *J. Phys. Chem. A* **117**, 14209 (2013).
- [60] M. Repiský, S. Komorovský, O. L. Malkina, and V. G. Malkin, *Chem. Phys.* **356**, 236 (2009).
- [61] Y. Xiao, D. Peng, and W. Liu, *J. Chem. Phys.* **126**, 081101 (2007).
- [62] Y. Xiao, W. Liu, L. Cheng, and D. Peng, *J. Chem. Phys.* **126**, 214101 (2007).
- [63] L. Cheng, Y. Xiao, and W. Liu, *J. Chem. Phys.* **130**, 144102 (2009).
- [64] Y. Xiao, Q. Sun, and W. Liu, *Theor. Chem. Acc.* **131**, 1080 (2012).
- [65] L. L. Foldy and S. A. Wouthuysen, *Phys. Rev.* **78**, 29 (1950).
- [66] J.-L. Heully, I. Lindgren, E. Lindroth, S. Lundqvist, and A.-M. Mårtensson-Pendrill, *J. Phys. B: At. Mol. Phys.* **19**, 2799 (1986).
- [67] M. Douglas and N. M. Kroll, *Ann. Phys. (NY)* **82**, 89 (1974).
- [68] B. A. Hess, *Phys. Rev. A* **33**, 3742 (1986).
- [69] G. Jansen and B. A. Hess, *Phys. Rev. A* **39**, 6016 (1989).
- [70] M. Reiher, *Theor. Chem. Acc.* **116**, 241 (2006).

- [71] M. Reiher, *Wiley Interdiscip. Rev.: Comput. Mol. Sci.* **2**, 139 (2012).
- [72] R. Fukuda, M. Hada, and H. Nakatsuji, *J. Chem. Phys.* **118**, 1015 (2003).
- [73] S. Lubber, I. M. Ondák, and M. Reiher, *Chem. Phys.* **356**, 205 (2009).
- [74] M. Hayami, J. Seino, and H. Nakai, *J. Chem. Phys.* **148**, 114109 (2018).
- [75] C. Chang, M. Pelissier, and P. Durand, *Phys. Scr.* **34**, 394 (1986).
- [76] E. van Lenthe, E. J. Baerends, and J. G. Snijders, *J. Phys. Chem.* **99**, 4597 (1993).
- [77] R. van Leeuwen, E. van Lenthe, E. J. Baerends, and J. G. Snijders, *J. Chem. Phys.* **101**, 1272 (1994).
- [78] S. Faas, J. Snijders, J. van Lenthe, E. van Lenthe, and E. Baerends, *Chem. Phys. Lett.* **246**, 632 (1995).
- [79] S. K. Wolff, T. Ziegler, E. van Lenthe, and E. J. Baerends, *J. Chem. Phys.* **110**, 7689 (1999).
- [80] J. Autschbach and T. Ziegler, *J. Chem. Phys.* **113**, 936 (2000).
- [81] J. Autschbach and T. Ziegler, *J. Chem. Phys.* **113**, 9410 (2000).
- [82] J. Autschbach, *J. Chem. Phys.* **129**, 094105 (2008).
- [83] J. Autschbach, *J. Chem. Phys.* **130**, 209901 (2009).
- [84] J. Autschbach, *Mol. Phys.* **111**, 2544 (2013).
- [85] W. Kutzelnigg and W. Liu, *J. Chem. Phys.* **123**, 241102 (2005).
- [86] W. Liu and W. Kutzelnigg, *J. Chem. Phys.* **126**, 114107 (2007).
- [87] W. Liu and D. Peng, *J. Chem. Phys.* **125**, 044102 (2006).
- [88] W. Liu and D. Peng, *J. Chem. Phys.* **125**, 149901 (2006).
- [89] D. Peng, W. Liu, Y. Xiao, and L. Cheng, *J. Chem. Phys.* **127**, 104106 (2007).
- [90] M. Iliaš and T. Saue, *J. Chem. Phys.* **126**, 064102 (2007).
- [91] W. Liu and D. Peng, *J. Chem. Phys.* **131**, 031104 (2009).
- [92] J. Sikkema, L. Visscher, T. Saue, and M. Iliaš, *J. Chem. Phys.* **131**, 124116 (2009).
- [93] K. G. Dyall, *J. Chem. Phys.* **106**, 9618 (1997).
- [94] K. G. Dyall, *J. Chem. Phys.* **109**, 4201 (1998).
- [95] K. G. Dyall and T. Enevoldsen, *J. Chem. Phys.* **111**, 10000 (1999).
- [96] K. G. Dyall, *J. Chem. Phys.* **115**, 9136 (2001).
- [97] L. Cheng, S. Stopkowicz, and J. Gauss, *Int. J. Quantum Chem.* **114**, 1108 (2014).
- [98] D. Cremer, W. Zou, and M. Filatov, *Wiley Interdiscip. Rev.: Comput. Mol. Sci.* **4**, 436 (2014).
- [99] Q. Sun, W. Liu, Y. Xiao, and L. Cheng, *J. Chem. Phys.* **131**, 081101 (2009).
- [100] Q. Sun, Y. Xiao, and W. Liu, *J. Chem. Phys.* **137**, 174105 (2012).

- [101] L. Cheng, J. Gauss, and J. F. Stanton, *J. Chem. Phys.* **139**, 054105 (2013).
- [102] T. Yoshizawa, W. Zou, and D. Cremer, *J. Chem. Phys.* **146**, 134109 (2017).
- [103] T. Yoshizawa and M. Hada, *J. Chem. Phys.* **147**, 154104 (2017).
- [104] D. Peng and M. Reiher, *J. Chem. Phys.* **136**, 244108 (2012).
- [105] D. Peng, N. Middendorf, F. Weigend, and M. Reiher, *J. Chem. Phys.* **138**, 184105 (2013).
- [106] Y. J. Franzke, *Effiziente Implementierung ein- und zweikomponentiger analytischer Gradienten im Rahmen der quasirelativistischen Exact-Two-Component-Theorie*, M.Sc. thesis, Karlsruhe Institute of Technology (KIT), Germany (2017).
- [107] Y. J. Franzke, N. Middendorf, and F. Weigend, *J. Chem. Phys.* **148**, 104410 (2018).
- [108] L. Cheng and J. Gauss, *J. Chem. Phys.* **135**, 084114 (2011).
- [109] L. Cheng and J. Gauss, *J. Chem. Phys.* **135**, 244104 (2011).
- [110] L. Cheng and J. Gauss, *J. Chem. Phys.* **134**, 244112 (2011).
- [111] L. Cheng, J. Gauss, and J. F. Stanton, *J. Chem. Phys.* **142**, 224309 (2015).
- [112] M. Gawrilow, H. Beckers, S. Riedel, and L. Cheng, *J. Chem. Phys. A* **122**, 119 (2018).
- [113] J. Gauss and J. F. Stanton, *J. Chem. Phys.* **102**, 251 (1995).
- [114] J. Gauss and J. F. Stanton, "Electron-correlated approaches for the calculation of NMR chemical shifts," in *Advances in Chemical Physics* (John Wiley & Sons, New York, USA, 2002) Chap. 6, pp. 355–422.
- [115] A. M. Teale, O. B. Lutnæs, T. Helgaker, D. J. Tozer, and J. Gauss, *J. Chem. Phys.* **138**, 024111 (2013).
- [116] R. Faber, S. P. A. Sauer, and J. Gauss, *J. Chem. Theory Comput.* **13**, 696 (2017).
- [117] R. Stratmann, G. E. Scuseria, and M. J. Frisch, *Chem. Phys. Lett.* **257**, 213 (1996).
- [118] C. A. White, B. G. Johnson, P. M. Gill, and M. Head-Gordon, *Chem. Phys. Lett.* **253**, 268 (1996).
- [119] C. Ochsenfeld, C. A. White, and M. Head-Gordon, *J. Chem. Phys.* **109**, 1663 (1998).
- [120] M. Sierka, A. Hogekamp, and R. Ahlrichs, *J. Chem. Phys.* **118**, 9136 (2003).
- [121] V. Sychrovský, J. Gräfenstein, and D. Cremer, *J. Chem. Phys.* **113**, 3530 (2000).
- [122] T. Helgaker, M. Watson, and N. C. Handy, *J. Chem. Phys.* **113**, 9402 (2000).
- [123] T. W. Keal, T. Helgaker, P. Sałek, and D. J. Tozer, *Chem. Phys. Lett.* **425**, 163 (2006).
- [124] A. D. Becke, *J. Chem. Phys.* **140**, 18A301 (2014).
- [125] N. Mardirossian and M. Head-Gordon, *Mol. Phys.* **115**, 2315 (2017).
- [126] J. P. Perdew and K. Schmidt, *AIP Conf. Proc.* **577**, 1 (2001).
- [127] G. I. Csonka, J. P. Perdew, and A. Ruzsinszky, *J. Chem. Theory Comput.* **6**, 3688 (2010).
- [128] A. D. Becke, *Phys. Rev. A* **38**, 3098 (1988).

- [129] C. Lee, W. Yang, and R. G. Parr, *Phys. Rev. B* **37**, 785 (1988).
- [130] P. J. Stephens, F. J. Devlin, C. F. Chabalowski, and M. J. Frisch, *J. Phys. Chem.* **98**, 11623 (1994).
- [131] Y. Tawada, T. Tsuneda, S. Yanagisawa, T. Yanai, and K. Hirao, *J. Chem. Phys.* **120**, 8425 (2004).
- [132] T. M. Henderson, B. G. Janesko, and G. E. Scuseria, *J. Phys. Chem. A* **112**, 12530 (2008).
- [133] T. Yanai, D. P. Tew, and N. C. Handy, *Chem. Phys. Lett.* **393**, 51 (2004).
- [134] J. P. Perdew, V. N. Staroverov, J. Tao, and G. E. Scuseria, *Phys. Rev. A* **78**, 052513 (2008).
- [135] J. Jaramillo, G. E. Scuseria, and M. Ernzerhof, *J. Chem. Phys.* **118**, 1068 (2003).
- [136] A. D. Becke, *J. Chem. Phys.* **109**, 2092 (1998).
- [137] T. M. Maier, A. V. Arbuznikov, and M. Kaupp, *Wiley Interdiscip. Rev.: Comput. Mol. Sci.* **9**, e1378 (2018).
- [138] H. Bahmann, A. Rodenberg, A. V. Arbuznikov, and M. Kaupp, *J. Chem. Phys.* **126**, 011103 (2007).
- [139] A. V. Arbuznikov and M. Kaupp, *J. Chem. Phys.* **136**, 014111 (2012).
- [140] A. V. Arbuznikov and M. Kaupp, *J. Chem. Phys.* **141**, 204101 (2014).
- [141] E. R. Johnson, *J. Chem. Phys.* **141**, 124120 (2014).
- [142] P. de Silva and C. Corminboeuf, *J. Chem. Phys.* **142**, 074112 (2015).
- [143] S. Huzinaga, *Comput. Phys. Rep.* **2**, 281 (1985).
- [144] F. Jensen, *Wiley Interdiscip. Rev.: Comput. Mol. Sci.* **3**, 273 (2013).
- [145] J. G. Hill, *Int. J. Quantum Chem.* **113**, 21 (2013).
- [146] D. A. Pantazis and F. Neese, *Wiley Interdiscip. Rev.: Comput. Mol. Sci.* **4**, 363 (2014).
- [147] F. Weigend, "Error-balanced Segmented Contracted Gaussian Basis Sets," in *Computational Methods in Lanthanide and Actinide Chemistry* (John Wiley & Sons, Chichester, United Kingdom, 2015) Chap. 7, pp. 181–194.
- [148] K. A. Peterson and K. G. Dyall, "Gaussian Basis Sets for Lanthanide and Actinide Elements," in *Computational Methods in Lanthanide and Actinide Chemistry* (John Wiley & Sons, Chichester, United Kingdom, 2015) Chap. 8, pp. 195–216.
- [149] S. Reine, T. Helgaker, and R. Lindh, *Wiley Interdiscip. Rev.: Comput. Mol. Sci.* **2**, 290 (2012).
- [150] W. J. Hehre, R. F. Stewart, and J. A. Pople, *J. Chem. Phys.* **51**, 2657 (1969).
- [151] S. F. Boys, *Proc. Roy. Soc. Lond. A* **200**, 542 (1950).
- [152] S. Obara and A. Saika, *J. Chem. Phys.* **84**, 3963 (1986).
- [153] S. Obara and A. Saika, *J. Chem. Phys.* **89**, 1540 (1988).
- [154] R. Ahlrichs, *Phys. Chem. Chem. Phys.* **8**, 3072 (2006).
- [155] H. King and M. Dupuis, *J. Comput. Phys.* **21**, 144 (1976).
- [156] M. Dupuis, J. Rys, and H. F. King, *J. Chem. Phys.* **65**, 111 (1976).

- [157] J. Rys, M. Dupuis, and H. F. King, *J. Comput. Chem.* **4**, 154 (1983).
- [158] M. Dupuis and A. Marquez, *J. Chem. Phys.* **114**, 2067 (2001).
- [159] H. F. King, *J. Phys. Chem. A* **120**, 9348 (2016).
- [160] L. E. McMurchie and E. R. Davidson, *J. Comput. Phys.* **26**, 218 (1978).
- [161] T. H. Dunning, *J. Chem. Phys.* **90**, 1007 (1989).
- [162] D. E. Woon and T. H. Dunning, *J. Chem. Phys.* **98**, 1358 (1993).
- [163] D. E. Woon and T. H. Dunning, *J. Chem. Phys.* **100**, 2975 (1994).
- [164] D. E. Woon and T. H. Dunning, *J. Chem. Phys.* **103**, 4572 (1995).
- [165] A. K. Wilson, D. E. Woon, K. A. Peterson, and T. H. Dunning, *J. Chem. Phys.* **110**, 7667 (1999).
- [166] T. H. Dunning, K. A. Peterson, and A. K. Wilson, *J. Chem. Phys.* **114**, 9244 (2001).
- [167] K. E. Peterson and T. H. Dunning, *J. Chem. Phys.* **117**, 10548 (2002).
- [168] N. B. Balabanov and K. A. Peterson, *J. Chem. Phys.* **123**, 064107 (2005).
- [169] J. G. Hill and K. A. Peterson, *J. Chem. Phys.* **147**, 244106 (2017).
- [170] D. H. Bross and K. A. Peterson, *Theor. Chem. Acc.* **133**, 1434 (2013).
- [171] M. Vasiliiu, K. A. Peterson, J. K. Gibson, and D. A. Dixon, *J. Phys. Chem. A* **119**, 11422 (2015).
- [172] K. A. Peterson and C. Puzzarini, *Theor. Chem. Acc.* **114**, 283 (2005).
- [173] B. P. Prascher, D. E. Woon, K. A. Peterson, T. H. Dunning, and A. K. Wilson, *Theor. Chem. Acc.* **128**, 69 (2011).
- [174] K. A. Peterson, *J. Chem. Phys.* **142**, 074105 (2015).
- [175] Q. Lu and K. A. Peterson, *J. Chem. Phys.* **145**, 054111 (2016).
- [176] R. Feng and K. A. Peterson, *J. Chem. Phys.* **147**, 084108 (2017).
- [177] K. A. Peterson, D. Figgen, M. Dolg, and H. Stoll, *J. Chem. Phys.* **126**, 124101 (2007).
- [178] P.-O. Widmark, P.-Å. Malmqvist, and B. O. Roos, *Theor. Chim. Acta* **77**, 291 (1990).
- [179] B. O. Roos, R. Lindh, P.-Å. Malmqvist, V. Veryazov, and P.-O. Widmark, *J. Phys. Chem. A* **108**, 2851 (2004).
- [180] B. O. Roos, V. Veryazov, and P.-O. Widmark, *Theor. Chem. Acc.* **111**, 345 (2004).
- [181] B. O. Roos, R. Lindh, P.-Å. Malmqvist, V. Veryazov, and P.-O. Widmark, *J. Phys. Chem. A* **109**, 6575 (2005).
- [182] B. O. Roos, R. Lindh, P.-Å. Malmqvist, V. Veryazov, P.-O. Widmark, and A. C. Borin, *J. Phys. Chem. A* **112**, 11431 (2008).
- [183] J. P. Zobel, P.-O. Widmark, and V. Veryazov, *J. Chem. Theory Comput.* **16**, 278 (2020).
- [184] P.-O. Widmark, J. P. Zobel, V. P. Vysotskiy, T. Tsuchiya, and V. Veryazov, *J. Chem. Phys.* **149**, 194102 (2018).

- [185] D. Claudino, R. Gargano, and R. J. Bartlett, *J. Chem. Phys.* **144**, 104106 (2016).
- [186] K. G. Dyall, *Theor. Chem. Acc.* **99**, 366 (1998).
- [187] K. G. Dyall, *Theor. Chem. Acc.* **108**, 335 (2002).
- [188] K. G. Dyall, *Theor. Chem. Acc.* **109**, 284 (2003).
- [189] K. G. Dyall, *Theor. Chem. Acc.* **112**, 403 (2004).
- [190] K. G. Dyall, *Theor. Chem. Acc.* **115**, 441 (2006).
- [191] K. G. Dyall and A. S. P. Gomes, *Theor. Chem. Acc.* **125**, 97 (2009).
- [192] A. S. P. Gomes, K. G. Dyall, and L. Visscher, *Theor. Chem. Acc.* **127**, 369 (2010).
- [193] K. G. Dyall, *Theor. Chem. Acc.* **129**, 603 (2011).
- [194] A. Schäfer, H. Horn, and R. Ahlrichs, *J. Chem. Phys.* **97**, 2571 (1992).
- [195] A. Schäfer, C. Huber, and R. Ahlrichs, *J. Chem. Phys.* **100**, 5829 (1994).
- [196] F. Weigend, F. Furche, and R. Ahlrichs, *J. Chem. Phys.* **119**, 12753 (2003).
- [197] K. Eichkorn, F. Weigend, O. Treutler, and R. Ahlrichs, *Theor. Chem. Acc.* **97**, 119 (1997).
- [198] F. Weigend and R. Ahlrichs, *Phys. Chem. Chem. Phys.* **7**, 3297 (2005).
- [199] R. Gulde, P. Pollak, and F. Weigend, *J. Chem. Theory Comput.* **8**, 4062 (2012).
- [200] D. Rappoport and F. Furche, *J. Chem. Phys.* **133**, 134105 (2010).
- [201] M. K. Armbruster, W. Klopper, and F. Weigend, *Phys. Chem. Chem. Phys.* **8**, 4862 (2006).
- [202] F. Weigend and A. Baldes, *J. Chem. Phys.* **133**, 174102 (2010).
- [203] P. Pollak and F. Weigend, *J. Chem. Theory Comput.* **13**, 3696 (2017).
- [204] P. Pollak, *Technische Weiterentwicklung und Anwendung quasirelativistischer Allelektronenmethoden*, Dissertation, Karlsruhe Institute of Technology (KIT), Germany (2017).
- [205] F. E. Jorge, A. Canal Neto, G. G. Camiletti, and S. F. Machado, *J. Chem. Phys.* **130**, 064108 (2009).
- [206] G. A. Ceolin, R. C. de Berrêdo, and F. E. Jorge, *Theor. Chem. Acc.* **132**, 1339 (2013).
- [207] L. S. C. Martins, F. E. Jorge, M. L. Franco, and I. B. Ferreira, *J. Chem. Phys.* **145**, 244113 (2016).
- [208] C. T. Campos, G. A. Ceolin, A. Canal Neto, F. E. Jorge, and F. N. N. Pansini, *Chem. Phys. Lett.* **516**, 125 (2011).
- [209] A. Canal Neto and F. E. Jorge, *Chem. Phys. Lett.* **582**, 158 (2013).
- [210] F. E. Jorge, L. S. C. Martins, and M. L. Franco, *Chem. Phys. Lett.* **643**, 84 (2016).
- [211] C. T. Campos, A. Z. de Oliveira, I. B. Ferreira, F. E. Jorge, and L. S. C. Martins, *Chem. Phys. Lett.* **675**, 1 (2017).
- [212] R. C. de Berrêdo and F. E. Jorge, *J. Mol. Struct.: THEOCHEM* **961**, 107 (2010).

- [213] A. Z. de Oliveira, C. T. Campos, F. E. Jorge, I. B. Ferreira, and P. A. Fantin, *Comput. Theor. Chem.* **1135**, 28 (2018).
- [214] C. L. Barros, P. J. P. de Oliveira, F. E. Jorge, A. C. Neto, and M. Campos, *Mol. Phys.* **108**, 1965 (2010).
- [215] C. T. Campos and F. E. Jorge, *Mol. Phys.* **111**, 167 (2013).
- [216] T. Noro, M. Sekiya, and T. Koga, *Theor. Chem. Acc.* **131**, 1124 (2012).
- [217] M. Sekiya, T. Noro, T. Koga, and T. Shimazaki, *Theor. Chem. Acc.* **131**, 1247 (2012).
- [218] T. Noro, M. Sekiya, and T. Koga, *Theor. Chem. Acc.* **132**, 1363 (2013).
- [219] F. Jensen, *J. Chem. Theory Comput.* **4**, 719 (2008).
- [220] F. Jensen, *J. Chem. Theory Comput.* **11**, 132 (2015).
- [221] R. Ahlrichs, M. Bär, M. Häser, H. Horn, and C. Kölmel, *Chem. Phys. Lett.* **162**, 165 (1989).
- [222] F. Furche, R. Ahlrichs, C. Hättig, W. Klopper, M. Sierka, and F. Weigend, *Wiley Interdiscip. Rev.: Comput. Mol. Sci.* **4**, 91 (2014).
- [223] S. G. Balasubramani, G. P. Chen, S. Coriani, M. Diedenhofen, M. S. Frank, Y. J. Franzke, F. Furche, R. Grotjahn, M. E. Harding, C. Hättig, A. Hellweg, B. Helmich-Paris, C. Holzer, U. Huniar, M. Kaupp, A. Marefat Khah, S. Karbalaeei Khani, T. Müller, F. Mack, B. D. Nguyen, S. M. Parker, E. Perlt, D. Rappoport, K. Reiter, S. Roy, M. Rückert, G. Schmitz, M. Sierka, E. Tapavicza, D. P. Tew, C. van Wüllen, V. K. Voora, F. Weigend, A. Wodyński, and J. M. Yu, *J. Chem. Phys.* **152**, 184107 (2020).
- [224] Developers' version of TURBOMOLE V7.5.1 2021, a development of University of Karlsruhe and Forschungszentrum Karlsruhe GmbH, 1989-2007, TURBOMOLE GmbH, since 2007; available from <https://www.turbomole.org> (retrieved November 22, 2020).
- [225] P. A. M. Dirac, *Math. Proc. Camb. Philos. Soc.* **35**, 416 (1939).
- [226] H. A. Lorentz, *Proc. R. Neth. Acad. Arts Sci.* **6**, 809 (1904).
- [227] P. A. M. Dirac and R. H. Fowler, *Proc. Roy. Soc. Lond. A* **126**, 360 (1930).
- [228] M. Born and R. Oppenheimer, *Ann. Phys.* **389**, 457 (1927).
- [229] Y. Ishikawa, R. Baretty, and R. Binning, *Chem. Phys. Lett.* **121**, 130 (1985).
- [230] O. Visser, P. Aerts, D. Hegarty, and W. Nieuwpoort, *Chem. Phys. Lett.* **134**, 34 (1987).
- [231] W. Johnson and G. Soff, *At. Data Nucl. Data Tables* **33**, 405 (1985).
- [232] L. Visscher and K. G. Dyall, *At. Data Nucl. Data Tables* **67**, 207 (1997).
- [233] K. G. Dyall and K. Fægri Jr., *Chem. Phys. Lett.* **201**, 27 (1993).
- [234] J. A. Gaunt, *Proc. Roy. Soc. Lond. A* **122**, 513 (1929).
- [235] G. Breit, *Phys. Rev.* **34**, 553 (1929).
- [236] G. E. Brown and D. G. Ravenhall, *Proc. Roy. Soc. Lond. A* **208**, 552 (1951).
- [237] J. Sucher, *Int. J. Quantum Chem.* **25**, 3 (1984).

- [238] J. Sucher, Phys. Rev. Lett. **55**, 1033 (1985).
- [239] J. Sucher, Phys. Rev. A **22**, 348 (1980).
- [240] J. Sucher, Phys. Rev. A **23**, 388 (1981).
- [241] M. H. Mittleman, Phys. Rev. A **24**, 1167 (1981).
- [242] D. Peng and M. Reiher, Theor. Chem. Acc. **131**, 1081 (2012).
- [243] W. Kutzelnigg, Chem. Phys. **225**, 203 (1997).
- [244] W. Pauli, Z. Phys. **43**, 601 (1927).
- [245] F. Jensen, *Introduction to Computational Chemistry*, 2nd ed. (John Wiley & Sons, Chichester, United Kingdom, 2007).
- [246] R. S. Mulliken, Science **157**, 13 (1967).
- [247] W. Kutzelnigg, Angew. Chem. Int. Ed. Engl. **35**, 572 (1996).
- [248] R. E. Stanton and S. Havriliak, J. Chem. Phys. **81**, 1910 (1984).
- [249] W. Kutzelnigg, Int. J. Quantum Chem. **25**, 107 (1984).
- [250] K. G. Dyall, I. P. Grant, and S. Wilson, J. Phys. B: At. Mol. Phys. **17**, 493 (1984).
- [251] K. G. Dyall, J. Chem. Phys. **100**, 2118 (1994).
- [252] C. C. J. Roothaan, Rev. Mod. Phys. **23**, 69 (1951).
- [253] G. G. Hall, Proc. Roy. Soc. Lond. A **205**, 541 (1951).
- [254] W. Zou, M. Filatov, and D. Cremer, J. Chem. Theory Comput. **8**, 2617 (2012).
- [255] J. C. Boettger, Phys. Rev. B **62**, 7809 (2000).
- [256] S. Majumder, A. V. Matveev, and N. Rösch, Chem. Phys. Lett. **382**, 186 (2003).
- [257] J. E. Peralta and G. E. Scuseria, J. Chem. Phys. **120**, 5875 (2004).
- [258] C. van Wüllen and C. Michauk, J. Chem. Phys. **123**, 204113 (2005).
- [259] M. Filatov, W. Zou, and D. Cremer, J. Chem. Phys. **139**, 014106 (2013).
- [260] W. Zou, M. Filatov, and D. Cremer, J. Chem. Phys. **142**, 214106 (2015).
- [261] B. A. Heß, C. M. Marian, U. Wahlgren, and O. Gropen, Chem. Phys. Lett. **251**, 365 (1996).
- [262] J. Liu and L. Cheng, J. Chem. Phys. **148**, 144108 (2018).
- [263] T. Yoshizawa, W. Zou, and D. Cremer, J. Chem. Phys. **145**, 184104 (2016).
- [264] H. Hellmann, *Einführung in die Quantenchemie* (Franz Deuticke, Leipzig, Germany, 1936).
- [265] R. P. Feynman, Phys. Rev. **56**, 340 (1939).
- [266] M. Repiský, S. Komorovský, E. Malkin, O. L. Malkina, and V. G. Malkin, Chem. Phys. Lett. **488**, 94 (2010).

- [267] W. Zou, M. Filatov, and D. Cremer, *J. Chem. Phys.* **134**, 244117 (2011).
- [268] J. E. Peralta, J. Uddin, and G. E. Scuseria, *J. Chem. Phys.* **122**, 084108 (2005).
- [269] L. Gagliardi, N. C. Handy, A. G. Ioannou, C.-K. Skylaris, S. Spencer, A. Willetts, and A. M. Simper, *Chem. Phys. Lett.* **283**, 187 (1998).
- [270] N. Lichtenberger, Y. J. Franzke, W. Massa, F. Weigend, and S. Dehnen, *Chem. Eur. J.* **24**, 12022 (2018).
- [271] J. C. Slater, *Phys. Rev.* **34**, 1293 (1929).
- [272] T. Helgaker, P. Jørgensen, and J. Olsen, *Molecular Electronic-Structure Theory* (John Wiley & Sons, Chichester, United Kingdom, 2000).
- [273] W. Pauli, *Z. Phys.* **31**, 765 (1925).
- [274] M. K. Armbruster, *Entwicklung und Implementierung zweikomponentiger Hartree-Fock- und Dichtefunktionalmethoden*, Dissertation, University of Karlsruhe (TH), Germany (2007).
- [275] M. K. Armbruster, F. Weigend, C. van Wüllen, and W. Klopper, *Phys. Chem. Chem. Phys.* **10**, 1748 (2008).
- [276] G. te Velde, F. M. Bickelhaupt, E. J. Baerends, C. Fonseca Guerra, S. J. A. van Gisbergen, J. G. Snijders, and T. Ziegler, *J. Comput. Chem.* **22**, 931 (2001).
- [277] J. Held, M. Hanrath, and M. Dolg, *J. Chem. Theory Comput.* **14**, 6197 (2018).
- [278] R. Ahlrichs, P. Scharf, and K. Jankowski, *Chem. Phys.* **98**, 381 (1985).
- [279] D. R. Hartree, *Math. Proc. Camb. Philos. Soc.* **24**, 89 (1928).
- [280] V. Fock, *Z. Phys.* **61**, 126 (1930).
- [281] C. J. Cremer, *Essentials of Computational Chemistry: Theories and Models*, 2nd ed. (John Wiley & Sons, Chichester, United Kingdom, 2004).
- [282] A. Szabo and N. S. Ostlund, *Modern Quantum Chemistry*, revised 1st ed. (McGraw-Hill, New York, USA, 1989).
- [283] T. Koopmans, *Physica* **1**, 104 (1934).
- [284] A. Baldes and F. Weigend, *Mol. Phys.* **111**, 2617 (2013).
- [285] E. Hückel, *Z. Phys.* **70**, 204 (1931).
- [286] E. Hückel, *Z. Phys.* **72**, 310 (1931).
- [287] E. Hückel, *Z. Phys.* **76**, 628 (1932).
- [288] R. Hoffmann, *J. Chem. Phys.* **39**, 1397 (1963).
- [289] P.-O. Löwdin, *Int. J. Quantum Chem.* **55**, 77 (1995).
- [290] C. Møller and M. S. Plesset, *Phys. Rev.* **46**, 618 (1934).
- [291] C. D. Sherrill and H. F. Schaefer, "The configuration interaction method: Advances in highly correlated approaches," in *Advances in Quantum Chemistry*, Vol. 34, edited by P.-O. Löwdin, J. R. Sabin, M. C. Zerner, and E. Brändas (Academic Press, San Diego, USA, 1999) pp. 143–269.

- [292] J. Čížek, *J. Chem. Phys.* **45**, 4256 (1966).
- [293] R. J. Bartlett and M. Musiał, *Rev. Mod. Phys.* **79**, 291 (2007).
- [294] O. Treutler, *Entwicklung und Anwendung von Dichtefunktionalmethoden*, Dissertation, University of Karlsruhe (TH), Germany (1995).
- [295] E. J. Baerends, D. E. Ellis, and P. Ros, *Chem. Phys.* **2**, 41 (1973).
- [296] O. Vahtras, J. Almlöf, and M. W. Feyereisen, *Chem. Phys. Lett.* **213**, 514 (1993).
- [297] K. Eichkorn, O. Treutler, H. Öhm, M. Häser, and R. Ahlrichs, *Chem. Phys. Lett.* **242**, 283 (1995).
- [298] F. Weigend, M. Kattannek, and R. Ahlrichs, *J. Chem. Phys.* **130**, 164106 (2009).
- [299] R. A. Friesner, *Chem. Phys. Lett.* **116**, 39 (1985).
- [300] R. A. Friesner, *J. Chem. Phys.* **85**, 1462 (1986).
- [301] R. A. Friesner, *J. Chem. Phys.* **86**, 3522 (1987).
- [302] M. N. Ringnalda, M. Belhadj, and R. A. Friesner, *J. Chem. Phys.* **93**, 3397 (1990).
- [303] T. J. Martinez and E. A. Carter, “Pseudospectral methods applied to the electron correlation problem,” in *Modern Electronic Structure Theory – Part II*, edited by D. R. Yarkony (World Scientific Press, Singapore, 1995) Chap. 17, pp. 1132–1165.
- [304] F. Neese, F. Wennmohs, A. Hansen, and U. Becker, *Chem. Phys.* **356**, 98 (2009).
- [305] P. Plessow and F. Weigend, *J. Comput. Chem.* **33**, 810 (2012).
- [306] R. Izsák, A. Hansen, and F. Neese, *Mol. Phys.* **110**, 2413 (2012).
- [307] R. Izsák, F. Neese, and W. Klopper, *J. Chem. Phys.* **139**, 094111 (2013).
- [308] A. Yachmenev and W. Klopper, *Mol. Phys.* **111**, 1129 (2013).
- [309] H. Laqua, J. Kussmann, and C. Ochsenfeld, *J. Chem. Theory Comput.* **14**, 3451 (2018).
- [310] G. L. Stoychev, A. A. Auer, R. Izsák, and F. Neese, *J. Chem. Theory Comput.* **14**, 619 (2018).
- [311] C. Holzer, *J. Chem. Phys.* **153**, 184115 (2020).
- [312] F. Weigend, *Phys. Chem. Chem. Phys.* **8**, 1057 (2006).
- [313] M. Häser and R. Ahlrichs, *J. Comput. Chem.* **10**, 104 (1989).
- [314] H. Horn, H. Weiß, M. Häser, M. Ehrig, and R. Ahlrichs, *J. Comput. Chem.* **12**, 1058 (1991).
- [315] O. Treutler and R. Ahlrichs, *J. Chem. Phys.* **102**, 346 (1995).
- [316] W. Kohn, A. D. Becke, and R. G. Parr, *J. Phys. Chem.* **100**, 12974 (1996).
- [317] W. Kohn, *Rev. Mod. Phys.* **71**, 1253 (1999).
- [318] R. G. Parr and Y. Weitao, *Density-functional theory of atoms and molecules*, 1st ed. (Oxford University Press, New York, USA, 1989).
- [319] L. H. Thomas, *Math. Proc. Camb. Philos. Soc.* **23**, 542–548 (1927).

- [320] E. Fermi, *Z. Phys.* **48**, 73 (1928).
- [321] P. A. M. Dirac, *Math. Proc. Camb. Philos. Soc.* **26**, 376–385 (1930).
- [322] E. Teller, *Rev. Mod. Phys.* **34**, 627 (1962).
- [323] P. Hohenberg and W. Kohn, *Phys. Rev. B* **136**, 864 (1964).
- [324] M. Levy, *Proc. Natl. Acad. Sci. USA* **76**, 6062 (1979).
- [325] M. Levy, *Int. J. Quantum Chem.* **110**, 3140 (2010).
- [326] E. H. Lieb, *Int. J. Quantum Chem.* **24**, 243 (1983).
- [327] W. Kohn and L. J. Sham, *Phys. Rev.* **140**, A1133 (1965).
- [328] J. A. Pople, P. M. Gill, and B. G. Johnson, *Chem. Phys. Lett.* **199**, 557 (1992).
- [329] A. D. Becke, *J. Chem. Phys.* **88**, 2547 (1988).
- [330] C. Van Wüllen, *J. Comput. Chem.* **20**, 51 (1999).
- [331] C. Van Wüllen, *J. Comput. Chem.* **23**, 779 (2002).
- [332] F. Wang, G. Hong, and L. Li, *Chem. Phys. Lett.* **316**, 318 (2000).
- [333] L. Goerigk and S. Grimme, *Wiley Interdiscip. Rev.: Comput. Mol. Sci.* **4**, 576 (2014).
- [334] S. Grimme, *J. Chem. Phys.* **124**, 034108 (2006).
- [335] S. Grimme and M. Steinmetz, *Phys. Chem. Chem. Phys.* **18**, 20926 (2016).
- [336] S. Śmiga, O. Franck, B. Mussard, A. Buksztel, I. Grabowski, E. Luppi, and J. Toulouse, *J. Chem. Phys.* **145**, 144102 (2016).
- [337] S. H. Vosko, L. Wilk, and M. Nusair, *Can. J. Phys.* **58**, 1200 (1980).
- [338] A. D. Becke, *J. Chem. Phys.* **84**, 4524 (1986).
- [339] A. D. Becke, *J. Chem. Phys.* **107**, 8554 (1997).
- [340] J. P. Perdew, *Phys. Rev. B* **33**, 8822 (1986).
- [341] J. P. Perdew, K. Burke, and M. Ernzerhof, *Phys. Rev. Lett.* **77**, 3865 (1996).
- [342] T. W. Keal and D. J. Tozer, *J. Chem. Phys.* **121**, 5654 (2004).
- [343] A. D. Becke, *Int. J. Quantum Chem.* **23**, 1915 (1983).
- [344] J. P. Perdew and L. A. Constantin, *Phys. Rev. B* **75**, 155109 (2007).
- [345] A. D. Becke, *J. Chem. Phys.* **112**, 4020 (2000).
- [346] J. Tao, J. P. Perdew, V. N. Staroverov, and G. E. Scuseria, *Phys. Rev. Lett.* **91**, 146401 (2003).
- [347] J. Sun, A. Ruzsinszky, and J. P. Perdew, *Phys. Rev. Lett.* **115**, 036402 (2015).
- [348] Y. Zhao and D. G. Truhlar, *Theor. Chem. Acc.* **120**, 215 (2008).
- [349] A. D. Becke, *J. Chem. Phys.* **98**, 5648 (1993).

- [350] A. D. Becke, *J. Chem. Phys.* **98**, 1372 (1993).
- [351] J. Harris and R. O. Jones, *J. Phys. F: Metal Phys* **4**, 1170 (1974).
- [352] O. Gunnarsson and B. I. Lundqvist, *Phys. Rev. B* **13**, 4274 (1976).
- [353] D. C. Langreth and J. P. Perdew, *Phys. Rev. B* **15**, 2884 (1977).
- [354] J. Harris, *Phys. Rev. A* **29**, 1648 (1984).
- [355] C. Adamo and V. Barone, *J. Chem. Phys.* **110**, 6158 (1999).
- [356] V. N. Staroverov, G. E. Scuseria, J. Tao, and J. P. Perdew, *J. Chem. Phys.* **119**, 12129 (2003).
- [357] P. W. Gill, R. D. Adamson, and J. A. Pople, *Mol. Phys.* **88**, 1005 (1996).
- [358] T. Leininger, H. Stoll, H.-J. Werner, and A. Savin, *Chem. Phys. Lett.* **275**, 151 (1997).
- [359] O. A. Vydrov and G. E. Scuseria, *J. Chem. Phys.* **125**, 234109 (2006).
- [360] J.-D. Chai and M. Head-Gordon, *Phys. Chem. Chem. Phys.* **10**, 6615 (2008).
- [361] Y. Jin and R. J. Bartlett, *J. Chem. Phys.* **145**, 034107 (2016).
- [362] R. L. A. Haiduke and R. J. Bartlett, *J. Chem. Phys.* **149**, 131101 (2018).
- [363] H. Bahmann and M. Kaupp, *J. Chem. Theory Comput.* **11**, 1540 (2015).
- [364] S. Klawohn, H. Bahmann, and M. Kaupp, *J. Chem. Theory Comput.* **12**, 4254 (2016).
- [365] C. Holzer, Y. J. Franzke, and M. Kehry, *J. Chem. Theory Comput.* **17**, 2928 (2021).
- [366] C. F. von Weizsäcker, *Z. Phys.* **96**, 431 (1935).
- [367] A. V. Arbuznikov, H. Bahmann, and M. Kaupp, *J. Phys. Chem. A* **113**, 11898 (2009).
- [368] A. D. Becke, *J. Chem. Phys.* **119**, 2972 (2003).
- [369] A. D. Becke, *J. Chem. Phys.* **122**, 064101 (2005).
- [370] M. Haasler, T. M. Maier, R. Grotjahn, S. Gückel, A. V. Arbuznikov, and M. Kaupp, *J. Chem. Theory Comput.* **16**, 5645 (2020).
- [371] A. D. Becke, *J. Chem. Phys.* **88**, 1053 (1988).
- [372] L. A. Curtiss, K. Raghavachari, P. C. Redfern, and J. A. Pople, *J. Chem. Phys.* **112**, 7374 (2000).
- [373] A. Görling and M. Levy, *Phys. Rev. A* **50**, 196 (1994).
- [374] C. A. Jiménez-Hoyos, B. G. Janesko, G. E. Scuseria, V. N. Staroverov, and J. P. Perdew, *Mol. Phys.* **107**, 1077 (2009).
- [375] F. Liu, E. Proynov, J.-G. Yu, T. R. Furlani, and J. Kong, *J. Chem. Phys.* **137**, 114104 (2012).
- [376] L. A. Curtiss, K. Raghavachari, P. C. Redfern, and J. A. Pople, *J. Chem. Phys.* **106**, 1063 (1997).
- [377] Y. Zhao, B. J. Lynch, and D. G. Truhlar, *J. Phys. Chem. A* **108**, 2715 (2004).
- [378] J. Tao, V. N. Staroverov, G. E. Scuseria, and J. P. Perdew, *Phys. Rev. A* **77**, 012509 (2008).

- [379] Y. J. Franzke and F. Weigend, *J. Chem. Theory Comput.* **15**, 1028 (2019).
- [380] M. Kaupp, V. G. Malkin, O. L. Malkina, and D. R. Salahub, *J. Am. Chem. Soc.* **117**, 1851 (1995).
- [381] M. Kaupp, V. G. Malkin, O. L. Malkina, and D. R. Salahub, *J. Am. Chem. Soc.* **117**, 8492 (1995).
- [382] A. Rodriguez-Forteza, P. Alemany, and T. Ziegler, *J. Phys. Chem. A* **103**, 8288 (1999).
- [383] T. B. Demissie, *J. Chem. Phys.* **147**, 174301 (2017).
- [384] A. Bagno, G. Casella, and G. Saielli, *J. Chem. Theory Comput.* **2**, 37 (2006).
- [385] J. Vícha, S. Komorovský, M. Repiský, R. Marek, and M. Straka, *J. Chem. Theory Comput.* **14**, 3025 (2018).
- [386] M. Gell-Mann, *Nuovo. Cim.* **4**, 848 (1956).
- [387] L. D. Landau and E. M. Lifshitz, *Course of theoretical physics*, 4th ed., Vol. 2: The classical theory of fields (Pergamon Press, Oxford, United Kingdom, 1998).
- [388] J. Jackson, *Classical Electrodynamics*, 3rd ed. (John Wiley & Sons, New York, USA, 1999).
- [389] A. Bohr and V. F. Weisskopf, *Phys. Rev.* **77**, 94 (1950).
- [390] A. C. Hennum, W. Klopper, and T. Helgaker, *J. Chem. Phys.* **115**, 7356 (2001).
- [391] F. London, *J. Phys. Radium* **8**, 397 (1937).
- [392] R. Ditchfield, *J. Chem. Phys.* **56**, 5688 (1972).
- [393] R. Ditchfield, *Mol. Phys.* **27**, 789 (1974).
- [394] R. Ditchfield, *Mol. Phys.* **27**, 789 (1974).
- [395] W. Kutzelnigg, *Phys. Rev. A* **67**, 032109 (2003).
- [396] E. Anderson, Z. Bai, C. Bischof, S. Blackford, J. Demmel, J. Dongarra, J. Du Croz, A. Greenbaum, S. Hammarling, A. McKenney, and D. Sorensen, *LAPACK Users' Guide*, 3rd ed. (Society for Industrial and Applied Mathematics, Philadelphia, USA, 1999).
- [397] K. Wolinski, J. F. Hinton, and P. Pulay, *J. Am. Chem. Soc.* **112**, 8251 (1990).
- [398] M. Häser, R. Ahlrichs, H. P. Baron, P. Weis, and H. Horn, *Theor. Chim. Acta* **83**, 455 (1992).
- [399] C. L. Lawson, R. J. Hanson, D. R. Kincaid, and F. T. Krogh, *ACM Trans. Math. Softw.* **5**, 308 (1979).
- [400] L. S. Blackford, J. Demmel, J. Dongarra, I. Duff, S. Hammarling, G. Henry, M. Heroux, L. Kaufman, A. Lumsdaine, A. Petitet, R. Pozo, K. Remington, and R. C. Whaley, *ACM Trans. Math. Softw.* **28**, 135 (2002).
- [401] L. Cheng and J. Gauss, *J. Chem. Phys.* **141**, 164107 (2014).
- [402] A. Pausch and W. Klopper, *Mol. Phys.* **118**, e1736675 (2020).
- [403] R. M. Stevens, R. M. Pitzer, and W. N. Lipscomb, *J. Chem. Phys.* **38**, 550 (1963).
- [404] J. A. Pople, R. Krishnan, H. B. Schlegel, and J. S. Binkley, *Int. J. Quantum Chem.* **16**, 225 (1979).
- [405] S. F. O'Shea and D. P. Santry, *Theor. Chim. Acta* **37**, 1 (1975).

- [406] R. A. Smith, *SIAM J. Appl. Math.* **16**, 198 (1968).
- [407] K. Reiter, F. Mack, and F. Weigend, *J. Chem. Theory Comput.* **14**, 191 (2018).
- [408] M. Beer, J. Kussmann, and C. Ochsenfeld, *J. Chem. Phys.* **134**, 074102 (2011).
- [409] N. C. Handy and H. F. Schaefer, *J. Chem. Phys.* **81**, 5031 (1984).
- [410] P. Pulay, *Mol. Phys.* **17**, 197 (1969).
- [411] H. Weiss, R. Ahlrichs, and M. Häser, *J. Chem. Phys.* **99**, 1262 (1993).
- [412] S. M. Parker and F. Furche, "Response Theory and Molecular Properties," in *Frontiers of Quantum Chemistry*, edited by M. Wójcik, H. Nakatsuji, B. Kirtman, and Y. Ozaki (Springer, Singapore, 2018) pp. 69–86.
- [413] U. Huniar, *Berechnung der chemischen Verschiebung der NMR mit Methoden der Dichtefunktionaltheorie (DFT)*, Diploma thesis, University of Karlsruhe (TH), Germany (1999).
- [414] F. Mack, *Chemische Abschirmungskonstanten mit meta-GGA-Funktionalen: Implementierung und Testrechnungen*, M.Sc. thesis, Karlsruhe Institute of Technology (KIT), Germany (2017).
- [415] C. J. Schattenberg, K. Reiter, F. Weigend, and M. Kaupp, *J. Chem. Theory Comput.* **16**, 931 (2020).
- [416] F. Furche, B. T. Krull, B. D. Nguyen, and J. Kwon, *J. Chem. Phys.* **144**, 174105 (2016).
- [417] P. Deglmann, F. Furche, and R. Ahlrichs, *Chem. Phys. Lett.* **362**, 511 (2002).
- [418] V. Malkin, O. Malkina, and D. Salahub, *Chem. Phys. Lett.* **204**, 80 (1993).
- [419] G. Schreckenbach and T. Ziegler, *J. Phys. Chem.* **99**, 606 (1995).
- [420] F. Furche, *J. Chem. Phys.* **114**, 5982 (2001).
- [421] R. Bauernschmitt and R. Ahlrichs, *J. Chem. Phys.* **104**, 9047 (1996).
- [422] M. E. Casida, *J. Mol. Struct.: THEOCHEM* **914**, 3 (2009).
- [423] J. Jusélius, D. Sundholm, and J. Gauss, *J. Chem. Phys.* **121**, 3952 (2004).
- [424] H. Fliegl, S. Taubert, O. Lehtonen, and D. Sundholm, *Phys. Chem. Chem. Phys.* **13**, 20500 (2011).
- [425] P. Lazzeretti, *J. Chem. Phys.* **148**, 134109 (2018).
- [426] P. Lazzeretti, M. Malagoli, and R. Zanasi, *Chem. Phys. Lett.* **220**, 299 (1994).
- [427] "GIMIC," Version 2.1.4 (merge 3a5f0eb, 2019), available from <https://github.com/qmcurrents/gimic> (retrieved November 26, 2020).
- [428] N. F. Ramsey, *Phys. Rev.* **91**, 303 (1953).
- [429] W. Kutzelnigg, *Theor. Chim. Acta* **73**, 173 (1988).
- [430] T. Yoshizawa, *Chem. Phys.* **518**, 112 (2019).
- [431] Y. J. Franzke, F. Mack, and F. Weigend, *J. Chem. Theory Comput.* **17**, 3974 (2021).
- [432] F. Mack, C. J. Schattenberg, M. Kaupp, and F. Weigend, *J. Phys. Chem. A* **124**, 8529 (2020).

- [433] D. R. Lide, ed., *CRC Handbook of Chemistry and Physics*, 78th ed. (CRC Press, Boca Raton, USA, 1997).
- [434] N. Stone, *At. Data Nucl. Data Tables* **90**, 75 (2005).
- [435] H. Fukui, T. Baba, Y. Shiraishi, S. Imanishi, K. Kudo, K. Mori, and M. Shimoji, *Mol. Phys.* **102**, 641 (2004).
- [436] S. Hamaya, H. Maeda, M. Funaki, and H. Fukui, *J. Chem. Phys.* **129**, 224103 (2008).
- [437] B. Sandhoefer, S. Kossmann, and F. Neese, *J. Chem. Phys.* **138**, 104102 (2013).
- [438] J. Autschbach, *J. Chem. Theory Comput.* **13**, 710 (2017).
- [439] A. Wodyński and M. Kaupp, *J. Phys. Chem. A* **123**, 5660 (2019).
- [440] R. Feng, T. J. Duignan, and J. Autschbach, *J. Chem. Theory Comput.* **17**, 255 (2021).
- [441] F. Furche and D. Rappoport, in *Computational Photochemistry*, Theoretical and Computational Chemistry, Vol. 16, edited by M. Olivucci (Elsevier, Amsterdam, The Netherlands, 2005) Chap. III, pp. 93–128.
- [442] M. Filatov, W. Zou, and D. Cremer, *J. Phys. Chem. A* **116**, 3481 (2012).
- [443] M. Kehry, Y. J. Franzke, C. Holzer, and W. Klopper, *Mol. Phys.* **118**, e1755064 (2020).
- [444] H. Fukui and T. Baba, *J. Chem. Phys.* **117**, 7836 (2002).
- [445] M. Kühn and F. Weigend, *J. Chem. Theory Comput.* **9**, 5341 (2013).
- [446] M. Kühn, *Zweikomponentige Methoden im Rahmen der zeitabhängigen Dichtefunktionaltheorie*, Dissertation, Karlsruhe Institute of Technology (KIT), Germany (2015).
- [447] C. Holzer, *Die GW-Methode und Bethe–Salpeter–Gleichung in der Quantenchemie: Theorie und Anwendung*, Dissertation, Karlsruhe Institute of Technology (KIT), Germany (2018).
- [448] M. Kühn and F. Weigend, *J. Chem. Phys.* **142**, 034116 (2015).
- [449] R. Bauernschmitt, M. Häser, O. Treutler, and R. Ahlrichs, *Chem. Phys. Lett.* **264**, 573 (1997).
- [450] OpenMP Architecture Review Boards, “OpenMP API shared-memory parallel programming,” <https://www.openmp.org> (retrieved December 4, 2020).
- [451] E. P. Almaraz and F. Furche, Initial OpenMP version of aoforce and escf, released with TURBOMOLE V6.3 (2011).
- [452] C. Holzer and Y. J. Franzke, OpenMP version of ridft, rdgrad, and egrad with contributions to mpshift, dscf, and grad; improved OpenMP version of aoforce and escf, released with TURBOMOLE V7.4 (2019) and further improved in TURBOMOLE V7.5 (2020).
- [453] A. Klamt and G. Schüürmann, *J. Chem. Soc., Perkin Trans. 2*, 799 (1993).
- [454] A. Schäfer, A. Klamt, D. Sattel, J. C. W. Lohrenz, and F. Eckert, *Phys. Chem. Chem. Phys.* **2**, 2187 (2000).
- [455] C. Holzer and W. Klopper, *J. Chem. Phys.* **150**, 204116 (2019).
- [456] E. R. Davidson, *J. Comput. Phys.* **17**, 87 (1975).

- [457] G. L. Sleijpen and H. A. Van der Vorst, *SIAM Rev.* **42**, 267 (2000).
- [458] J. F. Dobson, *J. Chem. Phys.* **98**, 8870 (1993).
- [459] A. D. Becke, *J. Chem. Phys.* **117**, 6935 (2002).
- [460] J. Tao, *Phys. Rev. B* **71**, 205107 (2005).
- [461] S. N. Maximoff and G. E. Scuseria, *Chem. Phys. Lett.* **390**, 408 (2004).
- [462] J. E. Bates and F. Furche, *J. Chem. Phys.* **137**, 164105 (2012).
- [463] G. Vignale and M. Rasolt, *Phys. Rev. Lett.* **59**, 2360 (1987).
- [464] E. I. Tellgren, S. Kvaal, and T. Helgaker, *Phys. Rev. A* **89**, 012515 (2014).
- [465] E. I. Tellgren, S. Kvaal, E. Sagvolden, U. Ekström, A. M. Teale, and T. Helgaker, *Phys. Rev. A* **86**, 062506 (2012).
- [466] M. Hoffmann-Ostenhof and T. Hoffmann-Ostenhof, *Phys. Rev. A* **16**, 1782 (1977).
- [467] C. J. Schattenberg and M. Kaupp, *J. Chem. Theory Comput.* **17**, 1469 (2021).
- [468] S. N. Maximoff, J. E. Peralta, V. Barone, and G. E. Scuseria, *J. Chem. Theory Comput.* **1**, 541 (2005).
- [469] H. Kramers, *Proc. R. Neth. Acad. Arts Sci.* **33**, 959 (1930).
- [470] T. M. Maier, H. Bahmann, and M. Kaupp, *J. Chem. Theory Comput.* **11**, 4226 (2015).
- [471] F. Wang, T. Ziegler, E. van Lenthe, S. van Gisbergen, and E. J. Baerends, *J. Chem. Phys.* **122**, 204103 (2005).
- [472] J. Gao, W. Zou, W. Liu, Y. Xiao, D. Peng, B. Song, and C. Liu, *J. Chem. Phys.* **123**, 054102 (2005).
- [473] K. Faegri Jr. and J. Almlof, *J. Comput. Chem.* **7**, 396 (1986).
- [474] C. Broyden, *J. Inst. Math. Appl.* **6**, 76 (1970).
- [475] R. Fletcher, *Comput. J.* **13**, 317 (1970).
- [476] D. Goldfarb, *Math. Comput.* **24**, 23 (1970).
- [477] D. Shanno, *Math. Comput.* **24**, 647 (1970).
- [478] C. C. J. Roothaan, *Rev. Mod. Phys.* **32**, 179 (1960).
- [479] J. Rice and R. Amos, *Chem. Phys. Lett.* **122**, 585 (1985).
- [480] M. Häser, *J. Chem. Phys.* **95**, 8259 (1991).
- [481] “Molecular test set for general purpose basis sets,” (2017), the test set contains the following 361 compounds: H₂, Li₂, Li₂O, Li₄C₄H₁₂, Li₄Cl₄, Li₄H₄, Li₈, LiBH₄, LiCl, LiF, LiH, Li₂S, Li₃P, Be₂F₄, Be₂H₄, Be₄, BeC₂H₆, BeF₂O₂H₄, BeH₂, BeS, B₂H₆, B₃N₃H₆, B₄H₄, BF₃, BH₃CO, BH₃, BH₃NH₃, C₂H₂, C₂H₃N, C₂H₄, C₂H₆, C₄H₄, C₆H₆, CF₄, H₂CO₂, H₂CO, CH₃N, CH₃OH, CH₄, HCN, HNC, HNO, HNO₂, HNO₃, N₂H₂, N₂H₄, N₂, N₄, NF₃, NH₃, NH₄F, CO₂, CO, H₂CO₃, H₂O₂, H₂O, OF₂, HF, F₂, Na₂O, Na₂S, Na₃N, Na₃P, NaCl, NaF, NaH, Mg₄, MgCl₂, MgF₂, MgF, MgH₂, Al₂O₃, Al₂S₃, AlCl₃, AlF₃, AlH₃, AlN, SiCl₄, SiF₄, SiH₄, SiO₂, SiS₂, H₃PO₄, HCP, P₂, P₄, PF₃, PF₅, PH₃, CS₂, H₂SO₄, H₂S, H₂S₂, S₂, S₅, SF₂, SF₄, SF₆, Cl₂, ClF₃, ClF, HCl, CaCl₂, CaF₂,

- CaH₂, K₂S, K₃P, KBr, KCl, KF, KH, KI, ScCl₃, ScF₃, ScH₃, ScO, TiCl₄, Ti(CO)₄, TiF₃, TiF₄, TiH₄, TiO₂, TiO, TiS₂, VH₅, VOF₃, VO, CrCl₃, Cr(CO)₆, CrF₃, CrO₃, MnF₂, MnO₂, MnO₃F, MnO₄⁻, MnO, MnS, Fe(CO)₅, FeF₂, FeF₄, FeO, ferrocene, CoCl₃, CoF₂, CoF₃, Ni(CO)₄, NiF₂, NiF₃, NiO, Cu₂, Cu₂O, Cu₂S, CuCl, CuCN, CuF, CuH, ZnCl₂, ZnF₂, ZnH₂, Zn(CH₃)₂, GaCl₃, GaCl, GaF₂, GaF, GaH₃, GaO, GeCl₄, GeF₃, GeF₄, GeH₄, GeO₂, GeO, As₄, As₄S₄, AsCl₃, AsH₃, Se₈, H₂Se, SeO₂, SeO, Br₂, BrCl, HBr, CHBr₃, RbF, RbH, RbO, SrF₂, SrF, SrH₂, SrO, SrS, YF₃, YF, YO, ZrF₃, ZrF, ZrO₂, ZrO, NbF₃, NbO₂F, NbO₂, NbO, Mo(CO)₆, MoF₃, MoH, MoO₂, MoO₃, Tc₂O₇, TcO₃F, TcO, Ru(CO)₅, RuF, RuO₂, RuO₄, RuO, RhF₄, RhF₆, RhF, RhO, Pd(CO)₄, PdF, Ag₂, AgCl, CdF₂, Cd(CH₃)₂, InCl₃, InCl, InH₃, InH, InO, SnF₃, SnH₄, SnO₂, SnO, SbCl₆⁻, SbF₃, SbF, SbH₃, SbO₂, TeF₃, TeH₂, TeO₂, TeO, I₂, ICl, HI, IO₄⁻, CsF, CsH, CsO, BaF₂, BaF, BaH₂, BaO, BaS, La₂O₃, LaF₃, LaH₂, LaI₂, LaI₃, CeF₃, CeF, CeH₂, CeO, PrCl, PrF₃, PrH₂, NdF₃, NdH₂, NdO, PmF, PmH₂, PmO, SmCl₂, SmF, SmH₂, EuCl, EuF₂, EuF₃, EuH₂, GdF₂, GdF₃, GdF, GdH₂, TbF, DyCl₃, DyF, HoF₃, HoO, ErCl₂, ErF₃, TmCl₃, TmCl, TmF₂, Yb₂, YbCl, YbF₃, YbH₂, Lu₂, Lu₂N, Lu₂O, LuBr₃, LuCl₃, LuF₂, LuF₃, LuF, LuH₃, LuI₃, HfF₃, HfF, HfO₂, HfO, TaF₃, TaF, TaO₂F, W(CO)₆, WF₃, WH, WO₂, WO₃, WO, ReH, ReO₂, ReO₃F, ReO₃, ReO, Os(CO)₅, OsO₂, OsO₃, OsO₄, OsOF₅, IrF₆, Pt(CO)₄, PtO₂, PtO, Au₂, Au₃⁻, AuCl₃, AuCl, Hg₂Cl₂, HgF₂, Hg(CH₃)₂, TlCl₃, TlCl, TiH₃, TiH, TlO, PbH₄, PbO₂, PbO, PbF₃, Bi₄, BiCl₆⁻, BiF₃, BiF, BiH₃, BiO₂, PoO₂, PoO, At₂.
- [482] Y. J. Franzke, R. Treß, T. M. Pazdera, and F. Weigend, *Phys. Chem. Chem. Phys.* **21**, 16658 (2019).
- [483] Y. J. Franzke, L. Spiske, P. Pollak, and F. Weigend, *J. Chem. Theory Comput.* **16**, 5658 (2020).
- [484] “Molecular test set for the nmr shieldings constants,” (2019), the test set contains the following 255 compounds: Ag₂, AgCl, Al₂O₃, Al₂S₃, AlCl₃, AlF₃, AlH₃, Ar₂, As₄, As₄S₄, AsCl₃, AsH₃, At₂, AtCl, AtF₃, Au₂, AuCl, B₂H₆, B₃N₃H₆, B₄H₄, Ba₄, BaF₂, BaH₂, BaO, BaS, Be₂F₄, Be₂H₄, Be₄, BeC₂H₆, BeF₂O₂H₄, BeH₂, BeS, BF₃, BH₃, BH₃CO, BH₃NH₃, BiF₃, BiH₃, Br₂, BrCl, C₂H₂, C₂H₃N, C₂H₄, C₂H₆, C₄H₄, C₆H₆, CF₄, CH₂O, CH₂O₂, CH₃N, CH₄, CO, CO₂, Ca₄, CaCl₂, CaF₂, CaH₂, Cd₂, Cd₂Cl₂, Cd(CH₃)₂, Cl₂, ClF, ClF₃, Cr(CO)₆, CrO₃, Cs₂, CsF, CsH, Cu₂, Cu₂O, Cu₂S, CuCl, CuCN, CuF, CuH, F₂, Fe(CO)₅, ferrocene, GaCl, GaCl₃, GaF, GaH₃, GeCl₄, GeF₄, GeH₄, GeO, GeO₂, H₂, H₂CO₃, H₂O, H₂O₂, H₂SO₄, H₃PO₄, HBr, HCBBr₃, HCl, HCN, HCP, He₂, HF, HfO, HfO₂, Hg₂, Hg₂Cl₂, HgF₂, Hg(CH₃)₂, HI, HCN, HNO₂, HNO₃, H₂S, H₂S₂, I₂, ICl, InCl, InCl₃, InH, InH₃, K₂, K₂S, K₃P, KBr, KCl, KF, KH, KI, Kr₂, LaCl₃, LaF₃, LaH₃, Li₂, Li₂O, Li₄C₄H₁₂, Li₄Cl₄, Li₄H₄, Li₈, LiBH₄, LiCl, LiF, LiH, Li₂S, Mg₄, MgCl₂, MgF₂, MgH₂, Mo₂, Mo(CO)₆, MoO₃, N₂, N₂H₂, N₂H₄, N₄, Na₂, NF₃, NH₃, NH₄F, Na₂O, Na₂S, Na₃N, Na₃P, NaCl, NaF, NaH, NbO₂F, Ne₂, Ni(CO)₄, OF₂, Os(CO)₅, OsO₃, OsO₄, P₂, PF₃, PF₅, PH₃, PLi₃, PbH₄, PbO, PbO₂, PdBr₂, Pd(CO)₄, PoBr₂, PoCl₄, PoF₂, PoF₆, PoO₂, Pt(CO)₄, PtO₂, Rb₂, RbF, RbH, Re₂O₇, Rn₂, RnF₂, Ru(CO)₅, RuO₂, RuO₄, S₅, SF₂, SF₄, SF₆, SbF₃, SbH₃, ScCl₃, ScF₃, ScH₃, Se₈, SeH₂, SeO₂, SiCl₄, SiF₄, SiH₄, SiO₂, SiS₂, SnH₄, SnO, SnO₂, Sr₄, SrF₂, SrH₂, SrO, SrS, TaF₃, TaO₂F, Tc₂O₇, TcO₃F, TeH₂, TeO₂, TiCl₄, Ti(CO)₄, TiF₄, TiH₄, TiO₂, TiS₂, TlCl, TlCl₃, TiH, TiH₃, VH₅, W(CO)₆, WO₃, XeF₂, XeF₄, XeOF₄, YF, YF₃, Zn₂, ZnCl₂, ZnF₂, ZnH₂, Zn(CH₃)₂, ZrO, ZrO₂.
- [485] F. Weigend, M. Häser, H. Patzelt, and R. Ahlrichs, *Chem. Phys. Lett.* **294**, 143 (1998).
- [486] A. Hellweg, C. Hättig, S. Höfener, and W. Klopper, *Theor. Chem. Acc.* **117**, 587 (2007).
- [487] B. P. Pritchard, D. Altarawy, B. Didier, T. D. Gibson, and T. L. Windus, *J. Chem. Inf. Model.* **59**, 4814 (2019).
- [488] Basis Set Exchange library ver2, BSE Library v0.8.12, <https://www.basissetexchange.org/> (retrieved December 24, 2020).
- [489] J. Gauss, *Chem Phys. Lett.* **191**, 614 (1992).

- [490] J. Gauss, *J. Chem. Phys.* **99**, 3629 (1993).
- [491] M. Kollwitz and J. Gauss, *Chem. Phys. Lett.* **260**, 639 (1996).
- [492] M. Kollwitz, M. Häser, and J. Gauss, *J. Chem. Phys.* **108**, 8295 (1998).
- [493] C. Hättig, *Phys. Chem. Chem. Phys.* **7**, 59 (2005).
- [494] H. Eshuis, J. Yarkony, and F. Furche, *J. Chem. Phys.* **132**, 234114 (2010).
- [495] Basis sets available from the Dirac program web site, <http://dirac.chem.sdu.dk> (retrieved December 4, 2020).
- [496] ccRepo of the Hill group, <http://www.grant-hill.group.shef.ac.uk/ccrepo/> (retrieved December 23, 2020).
- [497] Sapporo segmented gtf basis set factory, <http://sapporo.center.ims.ac.jp/sapporo/> (retrieved November 9, 2019).
- [498] S. Grimme, J. Antony, S. Ehrlich, and H. Krieg, *J. Chem. Phys.* **132**, 154104 (2010).
- [499] M. Gerken, P. Hazendonk, J. Nieboer, and G. J. Schrobilgen, *J. Fluor. Chem.* **125**, 1163 (2004).
- [500] C. Jameson, "The Noble Gases," in *Multinuclear NMR*, edited by J. Mason (Springer US, New York, USA, 1987) Chap. 18, pp. 463–477.
- [501] U. Ekström, L. Visscher, R. Bast, A. J. Thorvaldsen, and K. Ruud, *J. Chem. Theory Comput.* **6**, 1971 (2010).
- [502] R. Ahlrichs and K. May, *Phys. Chem. Chem. Phys.* **2**, 943 (2000).
- [503] T. D. Crawford, K. W. Springer, and H. F. Schaefer, *J. Chem. Phys.* **102**, 3307 (1995).
- [504] M. Kaupp, C. van Wüllen, R. Franke, F. Schmitz, and W. Kutzelnigg, *J. Am. Chem. Soc.* **118**, 11939 (1996).
- [505] D. A. Dixon, W. A. de Jong, K. A. Peterson, K. O. Christe, and G. J. Schrobilgen, *J. Am. Chem. Soc.* **127**, 8627 (2005).
- [506] K. A. Peterson, D. A. Dixon, and H. Stoll, *J. Phys. Chem. A* **116**, 9777 (2012).
- [507] D. Andrae, U. Häußermann, M. Dolg, H. Stoll, and H. Preuß, *Theor. Chim. Acta* **77**, 123 (1990).
- [508] V. T. Tran and M. F. A. Hendrickx, *J. Chem. Phys.* **135**, 094505 (2011).
- [509] W. Huang, P. Pyykkö, and J. Li, *Inorg. Chem.* **54**, 8825 (2015).
- [510] B. N. Figgis, R. G. Kidd, and R. S. Nyholm, *Proc. Royal Soc. Lond. A* **269**, 469 (1962).
- [511] K. Reiter, M. Kühn, and F. Weigend, *J. Chem. Phys.* **146**, 054102 (2017).
- [512] C. Elschenbroich, *Organometallics*, 6th ed. (Vieweg+Teubner, Wiesbaden, Germany, 2008) p. 330.
- [513] B. Mann, "The Cinderella Nuclei," in *Annual Reports on NMR Spectroscopy*, Vol. 23, edited by G. Webb (Academic Press, San Diego, USA, 1991) pp. 141–207.
- [514] J. Banck and A. Schwenk, *Z. Phys. B* **20**, 75 (1975).

- [515] S. F. Gheller, T. W. Hambley, J. R. Rodgers, R. T. C. Brownlee, M. J. O'Connor, M. R. Snow, and A. G. Wedd, *Inorg. Chem.* **23**, 2519 (1984).
- [516] R. L. Keiter and D. G. V. Velde, *J. Organomet. Chem.* **258**, C34 (1983).
- [517] D. Sundholm, P. Pyykkö, and L. Laaksonen, *Mol. Phys.* **56**, 1411 (1985).
- [518] K. P. Huber and G. H. Herzberg, *Constants of Diatomic Molecules* (Van Nostrand Reinhold, New York, USA, 1979) see also <https://webbook.nist.gov/> (retrieved December 24, 2020).
- [519] L. Visscher, T. Enevoldsen, T. Saue, and J. Oddershede, *J. Chem. Phys.* **109**, 9677 (1998).
- [520] R. A. Kendall, T. H. Dunning, and R. J. Harrison, *J. Chem. Phys.* **96**, 6796 (1992).
- [521] A. J. Sadlej, *Collect. Czech. Chem. Commun.* **53**, 1995 (1988).
- [522] W. T. Raynes, J. Geertsen, and J. Oddershede, *Chem. Phys. Lett.* **197**, 516 (1992).
- [523] E. Ebsworth, S. Frankiss, and A. Robiette, *J. Mol. Spectrosc.* **12**, 299 (1964).
- [524] N. Flitcroft and H. D. Kaesz, *J. Am. Chem. Soc.* **85**, 1377 (1963).
- [525] W. Brügel, *Handbook of NMR Spectral Parameters*, Vol. 13 (Heyden, London, United Kingdom, 1979).
- [526] A. L. Wilkins, P. J. Watkinson, and K. M. Mackay, *J. Chem. Soc., Dalton Trans.*, 2365 (1987).
- [527] P. Fowler, *Mol. Phys.* **43**, 591 (1981).
- [528] S. M. Bass, R. L. DeLeon, and J. S. Muenter, *J. Chem. Phys.* **86**, 4305 (1987).
- [529] M. A. L. Marques, M. J. T. Oliveira, and T. Burnus, *Comput. Phys. Commun.* **183**, 2272 (2012).
- [530] S. Lehtola, C. Steigemann, M. J. T. Oliveira, and M. A. L. Marques, *SoftwareX* **7**, 1 (2018).
- [531] F. Jensen, *J. Chem. Theory Comput.* **2**, 1360 (2006).
- [532] E. Van Lenthe and E. J. Baerends, *J. Comput. Chem.* **24**, 1142 (2003).
- [533] B. Wrackmeyer, K. H. von Locquenghien, E. Kupče, and A. Sebald, *Magn. Reson. Chem.* **31**, 45 (1993).
- [534] V. Petrosyan, A. Permin, O. Reutov, and J. D. Roberts, *J. Magn. Reson.* **40**, 511 (1980).
- [535] V. Petrosyan, *Prog. Nucl. Magn. Reson. Spectrosc.* **11**, 115 (1977).
- [536] C. Schumann and H. Dreiskamp, *J. Magn. Reson.* **3**, 204 (1970).
- [537] W. McFarlane, *J. Chem. Soc. A*, 1630 (1968).
- [538] T. Birchall and A. Pereira, *J. Chem. Soc., Chem. Commun.*, 1150 (1972).
- [539] R. J. Forder, I. S. Mitchell, G. Reid, and R. H. Simpson, *Polyhedron* **13**, 2129 (1994).
- [540] M. Balmer, Y. J. Franzke, F. Weigend, and C. von Hänisch, *Chem. Eur. J.* **26**, 192 (2020).
- [541] C. van Wüllen, *J. Comput. Chem.* **32**, 1195 (2011).
- [542] U. Benedikt, A. A. Auer, and F. Jensen, *J. Chem. Phys.* **129**, 064111 (2008).

- [543] D. Flaig, M. Maurer, M. Hanni, K. Braunger, L. Kick, M. Thubauville, and C. Ochsenfeld, *J. Chem. Theory Comput.* **10**, 572 (2014).
- [544] P. Lantto and J. Vaara, *J. Chem. Phys.* **127**, 084312 (2007).
- [545] Y. Wang, Y. Xie, M. Y. Abraham, R. J. Gilliard, P. Wei, H. F. Schaefer, P. v. R. Schleyer, and G. H. Robinson, *Organometallics* **29**, 4778 (2010).
- [546] A. Doddi, M. Peters, and M. Tamm, *Chem. Rev.* **119**, 6994 (2019).
- [547] M. Balmer, F. Weigend, and C. von Hänisch, *Chem. Eur. J.* **25**, 4914 (2019).
- [548] E. Caldeweyher, C. Bannwarth, and S. Grimme, *J. Chem. Phys.* **147**, 034112 (2017).
- [549] K. Izod, P. Evans, P. G. Waddell, and M. R. Probert, *Inorg. Chem.* **55**, 10510 (2016).
- [550] K. Izod, D. G. Rayner, S. M. El-Hamruni, R. W. Harrington, and U. Baisch, *Angew. Chem. Int. Ed.* **53**, 3636 (2014).
- [551] C. J. Jameson, A. De Dios, and A. Keith Jameson, *Chem. Phys. Lett.* **167**, 575 (1990).
- [552] K. Wiberg, *Tetrahedron* **24**, 1083 (1968).
- [553] D. Nikolova, C. von Hänisch, and A. Adolf, *Eur. J. Inorg. Chem.* **2004**, 2321 (2004).
- [554] A. T. Balaban, P. v. R. Schleyer, and H. S. Rzepa, *Chem. Rev.* **105**, 3436 (2005).
- [555] L. Kürti and B. Czakó, *Strategic applications of named reactions in organic synthesis* (Elsevier Academic Press, London, United Kingdom, 2005) pp. 176–179.
- [556] A. Kekulé, *Liebigs Ann. Chem.* **137**, 129 (1866).
- [557] A. Kekulé, *Liebigs Ann. Chem.* **162**, 77 (1872).
- [558] E. C. Crocker, *J. Am. Chem. Soc.* **44**, 1618 (1922).
- [559] J. W. Armit and R. Robinson, *J. Chem. Soc., Trans.* **127**, 1604 (1925).
- [560] H. E. Armstrong, *J. Chem. Soc., Trans.* **51**, 258 (1887).
- [561] A. A. Frost and B. Musulin, *J. Chem. Phys.* **21**, 572 (1953).
- [562] A. D. McNaught and A. Wilkinson, *IUPAC. Compendium of Chemical Terminology (the “Gold Book”)*, 2nd ed. (Blackwell Scientific Publications, Oxford, United Kingdom, 1997) online version (2019-) created by S. J. Chalk, available at <https://doi.org/10.1351/goldbook> (retrieved May 6, 2021).
- [563] L. Pauling, *J. Chem. Phys.* **4**, 673 (1936).
- [564] P. v. R. Schleyer, C. Maerker, A. Dransfeld, H. Jiao, and N. J. R. v. E. Hommes, *J. Am. Chem. Soc.* **118**, 6317 (1996).
- [565] Y. J. Franzke, D. Sundholm, and F. Weigend, *Phys. Chem. Chem. Phys.* **19**, 12794 (2017).
- [566] A. Sekiguchi, T. Matsuo, and H. Watanabe, *J. Am. Chem. Soc.* **122**, 5652 (2000).
- [567] R. Wehrmann, H. Meyer, and A. Berndt, *Angew. Chem. Int. Ed.* **24**, 788 (1985).

- [568] F. De Proft, P. W. Fowler, R. W. A. Havenith, P. v. R. Schleyer, G. Van Lier, and P. Geerlings, *Chem. Eur. J.* **10**, 940 (2004).
- [569] J. Jin, G. Wang, M. Zhou, D. M. Andrada, M. Hermann, and G. Frenking, *Angew. Chem. Int. Ed.* **55**, 2078 (2016).
- [570] M. Unverzagt, G. Subramanian, M. Hofmann, P. von Ragué Schleyer, S. Berger, K. Harms, W. Massa, and A. Berndt, *Angew. Chem. Int. Ed. Engl.* **36**, 1469 (1997).
- [571] C. Präsang, M. Hofmann, G. Geiseler, W. Massa, and A. Berndt, *Angew. Chem. Int. Ed.* **41**, 1526 (2002).
- [572] A. Maier, M. Hofmann, H. Pritzkow, and W. Siebert, *Angew. Chem. Int. Ed.* **41**, 1529 (2002).
- [573] K. Takanashi, V. Y. Lee, and A. Sekiguchi, *Organometallics* **28**, 1248 (2009).
- [574] R. Gleiter, *Angew. Chem. Int. Ed. Engl.* **20**, 444 (1981).
- [575] C. F. Buchholz, *Gehlen's Neues J. Chem.* **3**, 3 (1804).
- [576] R. J. Gillespie and J. Passmore, *Acc. Chem. Res.* **4**, 413 (1971).
- [577] F. Kraus, J. C. Aschenbrenner, and N. Korber, *Angew. Chem. Int. Ed.* **42**, 4030 (2003).
- [578] N. Korber and M. Reil, *Chem. Commun.*, 84 (2002).
- [579] J. O. C. Jiménez-Halla, E. Matito, J. Robles, and M. Solà, *J. Organomet. Chem.* **691**, 4359 (2006).
- [580] A. Velian and C. C. Cummins, *Science* **348**, 1001 (2015).
- [581] O. J. Scherer, *Angew. Chem. Int. Ed. Engl.* **29**, 1104 (1990).
- [582] X.-W. Li, W. T. Pennington, and G. H. Robinson, *J. Am. Chem. Soc.* **117**, 7578 (1995).
- [583] X.-W. Li, Y. Xie, P. R. Schreiner, K. D. Gripper, R. C. Crittendon, C. F. Campana, H. F. Schaefer, and G. H. Robinson, *Organometallics* **15**, 3798 (1996).
- [584] R. J. Wright, M. Brynda, and P. P. Power, *Angew. Chem. Int. Ed.* **45**, 5953 (2006).
- [585] X. Li, A. E. Kuznetsov, H.-F. Zhang, A. I. Boldyrev, and L.-S. Wang, *Science* **291**, 859 (2001).
- [586] A. E. Kuznetsov, A. I. Boldyrev, X. Li, and L.-S. Wang, *J. Am. Chem. Soc.* **123**, 8825 (2001).
- [587] B. Twamley and P. Power, *Angew. Chem. Int. Ed.* **39**, 3500 (2000).
- [588] A. E. Kuznetsov, J. D. Corbett, L.-S. Wang, and A. I. Boldyrev, *Angew. Chem. Int. Ed.* **40**, 3369 (2001).
- [589] L. Yong, S. D. Hoffmann, T. F. Fässler, S. Riedel, and M. Kaupp, *Angew. Chem. Int. Ed.* **44**, 2092 (2005).
- [590] M. Gausa, R. Kaschner, H. Lutz, G. Seifert, and K.-H. Meiwes-Broer, *Chem. Phys. Lett.* **230**, 99 (1994).
- [591] A. I. Boldyrev and L.-S. Wang, *Chem. Rev.* **105**, 3716 (2005).
- [592] X. Cao, M. Dolg, and H. Stoll, *J. Chem. Phys.* **118**, 487 (2003).
- [593] B. Metz, H. Stoll, and M. Dolg, *J. Chem. Phys.* **113**, 2563 (2000).

- [594] F. Sondheimer, R. Wolovsky, and Y. Amiel, *J. Am. Chem. Soc.* **84**, 274 (1962).
- [595] Z. Zhu, X. Wang, M. Olmstead, and P. Power, *Angew. Chem. Int. Ed.* **48**, 2027 (2009).
- [596] A. Cisar and J. D. Corbett, *Inorg. Chem.* **16**, 2482 (1977).
- [597] S. C. Critchlow and J. D. Corbett, *Inorg. Chem.* **23**, 770 (1984).
- [598] A. R. Eulenstein, Y. J. Franzke, N. Lichtenberger, R. J. Wilson, H. L. Deubner, F. Kraus, F. Weigend, and S. Dehnen, *Nat. Chem.* **13**, 149 (2021).
- [599] S. F. Boys, *Rev. Mod. Phys.* **32**, 296 (1960).
- [600] L. Martins, F. Jorge, and S. Machado, *Mol. Phys.* **113**, 3578 (2015).
- [601] K. G. Dyall, *Theor. Chem. Acc.* **117**, 491 (2007).
- [602] P. Nava, M. Sierka, and R. Ahlrichs, *Phys. Chem. Chem. Phys.* **5**, 3372 (2003).
- [603] A. R. Eulenstein, Y. J. Franzke, P. Bügel, W. Massa, F. Weigend, and S. Dehnen, *Nat. Commun.* **11**, 5122 (2020).
- [604] C. Donsbach, K. Reiter, D. Sundholm, F. Weigend, and S. Dehnen, *Angew. Chem. Int. Ed.* **57**, 8770 (2018).
- [605] N. Flocke and V. Lotrich, *J. Comput. Chem.* **29**, 2722 (2008).
- [606] H.-P. Baron, *Entwicklung eines Programms zur Berechnung chemischer Verschiebungen*, Diploma thesis, University of Karlsruhe (TH), Germany (1991).
- [607] M. Abramowitz and L. A. Stegun, eds., *Handbook of Mathematical Functions*, 10th ed. (Dover, New York, USA, 1972).
- [608] I. N. Bronshtein, K. A. Semendyayev, G. Musiol, and H. Mühlig, *Handbook of Mathematics*, 6th ed. (Springer, Berlin, Heidelberg, Germany, 2015).
- [609] W. Gautschi, *ACM Trans. Math. Softw.* **20**, 21 (1994).
- [610] F. Furche, R. Ahlrichs, C. Wachsmann, E. Weber, A. Sobanski, F. Vögtle, and S. Grimme, *J. Am. Chem. Soc.* **122**, 1717 (2000).
- [611] E. Lindroth and S. Salomonson, *Phys. Rev. A* **41**, 4659 (1990).
- [612] J. Autschbach, D. Peng, and M. Reiher, *J. Chem. Theory Comput.* **8**, 4239 (2012).
- [613] W. Zou, M. Filatov, and D. Cremer, *J. Chem. Phys.* **137**, 084108 (2012).
- [614] D. Goebel and U. Hohm, *J. Chem. Soc., Faraday Trans.* **93**, 3467 (1997).

Acknowledgments

Firstly, I thank Florian Weigend for his generous support and mentoring throughout the years. I am very grateful for your continuous support, supervision, and helpful discussions since 2015. You gave me the chance and the freedom to work on my own projects and supported me during difficult times. You helped me to grow as a scientist and human being. Thank you very much!

Secondly, I am grateful to Filipp Furche for the opportunity to work with his group at the University of California, Irvine and for many fruitful discussions, which really helped me a lot. I want to thank all members of his group for their friendliness, interesting conversations, and ongoing collaborations. I am especially grateful to Saswata Roy and Scree Ganesh Balasubramani for their kind support and help. Furthermore, I thank Brian D. Nguyen, Luke Nambi Mohanam, and Jason M. Yu for interesting discussions. I learned so much during that (short) stay. Thank you!

Moreover, I am grateful to Wim Klopper and the members of the Theoretical Chemistry Group at KIT for the scientific and computational resources as well as interesting scientific and non-scientific discussions. To name only a few, I would like to thank Michael Harding, Christof Holzer, Max Kehry, Stephan Kohaut, Fabian Mack, Ansgar Pausch, Patrik Pollak, Florian Rehak, Kevin Reiter, and Timo Schulz for their help and stimulating conversations. I am further grateful to Tobias M. Pazdera and Robert Treß for their contribution to the NMR-tailored basis sets.

Besides the named ones, a lot of people contributed to my scientific publications. I thank all co-authors for interesting discussions. Of course, I would also like to express my gratitude to all experimental collaborators for the uncomplicated and very fruitful interdisciplinary work: Stefanie “Steffi” Dehnen, Carsten von Hänisch, Florian Kraus and the members of their groups, especially Armin R. Eulenstein and Markus Balmer, as well as John F. Corrigan, Werner Massa, and Rudolphe Cl  rac.

I thank all of my chemistry and physics teachers at school and the respective lectures at KIT for fostering my interest in chemistry and physics. I am especially thankful to Dage Sundholm for introducing me to the fascinating topic of magnetic properties during my research stay at the University of Helsinki.

Furthermore, I am grateful to Fonds der Chemischen Industrie (German Chemical Industry Funds), the German Academic Exchange Service (Deutscher Akademischer Austauschdienst, DAAD), and TURBOMOLE GmbH for financial support.

I thank Christof Holzer, Max Kehry, Fabian Mack, Ansgar Pausch, Kevin Reiter, and Timo Schulz for proofreading the drafts of this work and many helpful comments. Thank you very very much!

Finally, I would like to thank my family and friends, who supported me throughout the years and made this thesis possible!